Galaxy alignments from multiple angles

Fortuna, M.C.

Citation

Fortuna, M. C. (2021, November 25). *Galaxy alignments from multiple angles*. Retrieved from https://hdl.handle.net/1887/3243460

GALAXY ALIGNMENTS FROM MULTIPLE ANGLES

MARIA CRISTINA FORTUNA

Galaxy alignments from multiple angles

Proefschrift

ter verkrijging van
de graad van doctor aan de Universiteit Leiden,
op gezag van rector magnificus prof.dr.ir. H. Bijl,
volgens besluit van het college voor promoties
te verdedigen op donderdag 25 november 2021
klokke 10:00 uur

door

Maria Cristina Fortuna
geboren te Assisi (PG), Italië
in 1991

Promotiecommissie

Promotors: Prof. dr. H. Hoekstra
                    Prof. dr. K.H. Kuijken

Overige leden: Prof. dr. M. Franx
                    Prof. dr. C. Heymans (Ruhr University Bochum, University of Edinburgh)
                    Prof. dr. H.J.A. Röttgering
                    Prof. dr. J. Schaye
                    Dr. E.N. Chisari (Utrecht University)

Contents

1 | Introduction

A century ago, in 1920, the astronomy community was engaged in the so-called 'the great debate': did the entire Universe consist of just our Galaxy, the Milky Way, or were the observed nebulae non-local objects, being themselves galaxies similarly to our own?[1]

Three years later, at the Mount Wilson Observatory, where the most powerful telescope of the time, the 100-inch Hooker Telescope, was operating, Edwin Hubble put an end to the controversy. Studying the photographic plates, Hubble was able to measure the distance of M31 (Andromeda), finding that it was about a million light-years away. A few years before, Harlow Shapley had measured the size of the Milky Way, assessing a width of about 300 000 light-years (Shapley 1918). This meant that M31 was outside the Milky Way, establishing a new view of the Universe, and opening the door to extragalactic astrophysics and modern cosmology[2].

In 1990, the Hubble Space Telescope was launched. In 1995 it produced one of the highest impact images of astronomy: the Hubble deep field (Fig. 1.1). This high-quality image contains more than 3000 galaxies in just $\sim 0.19 \deg^2$, and the light of some of these has travelled for 10 billion years to reach us.

In just one century, our perception of the dimensions of Universe had completely changed.

---

[1] A transcript of the debate can be found at `https://apod.nasa.gov/diamond_jubilee/1920/cs_nrc.html`. For further material, see for example Shapley (1919); Shapley & Curtis (1921)

[2] Our current best estimates of the size of the Milky Way stellar disk and of M31 distance are, respectively, ~ 100000 light years and ~ 2.54 million light years.

Figure 1.1: The Hubble Ultra Deep Field 2012, an improved version of the Hubble Ultra Deep Field image featuring additional observation time. Credit: NASA, ESA, R. Ellis (Caltech), and the HUDF 2012 Team

1.1 A new view of the Universe

In the following years, the measurements of the distances and the velocities of several distant galaxies allowed Hubble to show that they were moving away from our own, and that their recessional velocities were linearly related to their distances: a relation now known as the Hubble-Lemaître law (Hubble 1929; Hubble & Humason 1931; Smith 1979, for a historical review). This was the experimental proof that the Universe was expanding, as already independently predicted a few years before by Friedmann and Lemaître (Friedmann 1922; Lemaître 1931). Due to the expansion of the Universe, the light of distant galaxies is red-shifted (i.e. it is observed at a longer wavelength) and thus we use the redshift, z, as a measure of distance and time; $z = 0$ corresponds to the present Universe, and it increases as we look back in the past.

Our modern view of the Universe is rooted in those years of great discoveries and on the fundamental theoretical works of Einstein, Lemaître, Robertson, Walker and other theorists who contributed to defining the geometrical description of the Universe we rely on. Our current model of the Universe is based on three fundamental assumptions: that we are not located at any special location in the Universe and that on large scales the Universe is isotropic and homogeneous. Starting from these hypotheses and using the theory of General Relativity, it is possible to build a specific class of metrics (Robertson-Walker metrics) and to derive a set of equations that describes the dynamical evolution of our Universe (Friedmann 1924).

Nowadays, the ΛCDM model is the standard cosmological model of reference, which gets its name from the dominant ingredients the Universe is composed of today: an unknown form of energy, called dark energy, that enters into the dynamical equations of the Universe in the form of a cosmological constant called Λ ($\sim 70\%$)[3], and (invisible) cold dark matter (CDM, $\sim 25\%$), originally inferred by its effect on the dynamics of visible matter (Zwicky 1933; Rubin et al. 1980, among others). The remaining components are the ordinary (baryonic) matter ($\sim 5\%$), followed by photons and neutrinos, which together account for less than $\sim 0.01\%$.

The question of what is the nature of dark matter and what is driving the acceleration parametrised by the dark energy are the most fundamental questions in modern cosmology. These involve theoretical as well as

---

[3]This is required to justify the observation of the late-time acceleration of the expansion of the Universe (Riess et al. 1998; Perlmutter et al. 1999)

experimental investigations (see for example Arun et al. 2017; Kafedžić-Briga & Džaferović-Mašić 2021, for some recent reviews). At the same time, while remaining agnostic on the intrinsic nature of such components, measuring the parameters of the cosmological model with as much precision and accuracy as possible is the main effort of observational cosmology (see Sect. 1.2.2).

In this Thesis, we focus on some specific techniques to infer the cosmological parameters with the main focus on how to control the systematic effects that would lead to incorrect estimates of these. Our subject of study is the alignments of galaxies. These can be intrinsic to the galaxy (what we call intrinsic alignment, IA, see Sect. 1.4) and provide information on the galaxy-dark matter connection, or apparent: in this case we refer to them as gravitational lensing, which we introduce in Sect. 1.3. Gravitational lensing is a powerful probe to explore the dark content of the Universe, as it uses the apparent distortion of galaxy shapes to infer the amount and the spatial distribution of dark matter, dark energy and the geometry of the Universe itself. We focus on modelling possible contaminants to lensing (Chapter 2 and 4) and to exploit lensing to learn more on IA (Chapter 3).

1.2   The Standard Cosmological Model

One of the main consequences of the expansion of the Universe is that it must have been much smaller in the past: in the hypothesis of mass conservation, also the density of the Universe was significantly higher. Thus, the Universe has experienced different phases across its life-time, and, winding back its history, we can reach a moment where the entire space-time was confined in a singularity: the so called Big Bang[4]. From the Big Bang until now, the Universe has continued to expand and cool down: from an initial stage where it was extremely hot and radiation-dominated, and all the particles were in the form of an opaque plasma, to the formation of the first nuclei in what is called the Big Bang Nucleosynthesis. This was followed by the decoupling of matter and radiation and the formation of the first neutral atoms[5] (Gamow 1946, 1948; Alpher & Herman 1948; Alpher et al. 1948). From here, baryonic matter started to assembly due to its grav-

---

[4]Strictly speaking, there are possible solutions to the Lemaître-Friedmann equations that would admit an ever expanding Universe, but these are excluded by specific observations and constraints on the cosmological parameters at certain redshifts (Boerner & Ehlers 1988).

[5]It is slightly before this point that the Universe entered the matter-dominated era.

itational attraction, forming the first stars and the first galaxies.

A fundamental evidence of the early stage of the Universe consists of the Cosmic Microwave Background (CMB), a relic radiation at the current temperature of ~ 2.725 K which originated at the moment of photon decoupling. The CMB was first predicted by Alpher & Herman (1948) and later detected by Penzias and Wilson (Penzias & Wilson 1965).

It is important to stress that the early Universe was not homogeneous at small scales: the origin of such anisotropies is still unknown, although the theory of inflation (Guth 1981) is generally accepted as the standard paradigm. Early after the equivalence between matter and radiation, matter started to condensate, as an effect of gravitational attraction. However, only dark matter was able to grow: this, not being affected by the electromagnetic radiation, was free to start its collapse, while the baryonic matter (all the visible matter) continued to interact with the surrounding photons. Once matter and radiation decoupled, these dark matter overdensities acted as seeds for structure formation: having higher density than the surrounding matter distribution, they attracted the surrounding baryonic matter (White & Rees 1978). In the standard model of structure formation, the assembly of matter is still driven by the most abundant and simplest form of matter, the collisionless dark matter. This shows the deep connection between dark and visible matter: dark matter forms the cosmic web, providing the gravitational wells where galaxies form and live. Baryonic matter, however, is able to cool via electromagnetic interactions, and can thus contract further, forming denser object such as stars and galaxies. The process of structure formation starts from small objects, which then merge to form larger and more massive ones, in a bottom-up scenario.

1.2.1 The galaxy-halo connection

The dark matter regions that are dense enough to decouple from the cosmic expansion form bounded objects that we refer to as haloes. The most massive haloes sit at the knots of the cosmic web (clusters) and host many galaxies, while less massive ones populate the filaments, and the galaxies they host are referred to as field galaxies (see Fig. 1.2 for a representation of the cosmic web from a N-body simulation). In general, the more massive is a halo, the more galaxies it hosts. In a simplified picture, the first galaxy to be born in a halo sits at its centre; depending on the characteristics of the proto-galaxy and on the surrounding tidal field, the galaxy can orient its major axis (or its spin axis) accordingly to the quadrupole of the gravitational field (see Joachimi et al. 2015; Kiessling et al. 2015, for a re-
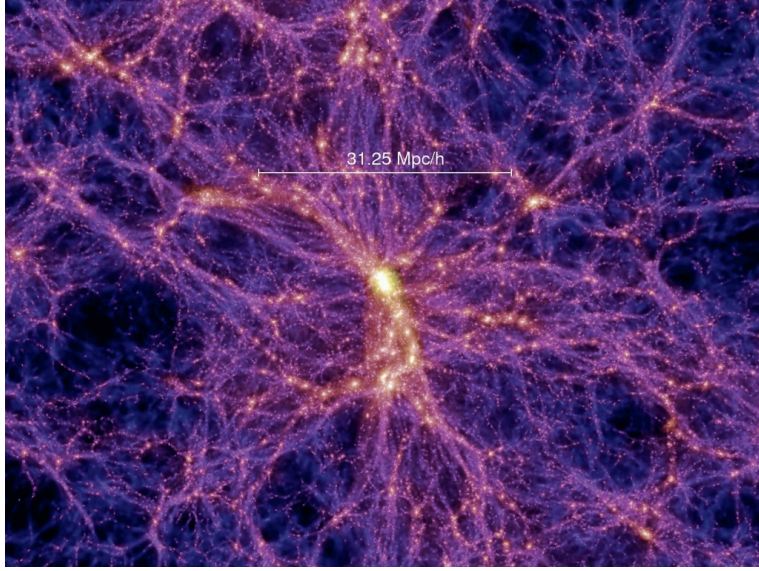
Figure 1.2: A zoom-in on a slice from the Millennium Simulation. A cluster is visible in the centre, surrounded by filaments. Image credit: Springel et al. (2005).

view). Interacting with the surrounding environment, a massive halo keeps attracting smaller structures from the neighbourhood, which become substructures and start orbiting around the halo centre; these sub-haloes can host galaxies themselves: we refer to these galaxies as satellites. Part of these satellites will be tidally stripped, either forming intra-cluster light or accreting onto the central galaxy, which is typically the most massive one in the halo. All of these processes affect the properties of satellites, from their star formation activity to their morphology and their angular momentum, either increasing or destroying the tendency of their major axes to point in the direction of the central galaxy. As the mergers continue, the central galaxy grows, the halo keeps attracting matter from the surrounding filaments, and becomes bigger and bigger: while at large scales the Universe expands, at small scales structures aggregate, contrasting locally the Hubble flow.

The complexity of the relation between galaxies and dark matter makes it impossible to have an exact analytical formalism to describe it. However, their ensemble properties can be captured using a statistical approach. There are several ways to parametrise the galaxy-halo connection: in this Thesis we focus on the halo model and the Halo Occupation Distribution (HOD)

(see Cooray & Sheth 2002, for a review). The halo model provides a way to describe the statistical properties of the dark matter haloes, such as their clustering. Dark matter haloes can have different masses: if a halo is massive enough, it can reach virial equilibrium, forming a bounded object, which can then host galaxies. Using N-body simulations, Navarro et al. (1996) showed that the dark matter distribution has a universal profile, with a decreasing density from the core to the outskirts of the halo (NFW profile). An alternative parametrisation which has also shown to fit well the simulations and lensing data is the Einasto profile (e.g. Gao et al. 2008; Mandelbaum et al. 2008). Combining the linear matter density distribution, the distribution of matter within the halo as predicted by the NFW profile and the number density of haloes of a given mass, as predicted by the halo mass function (HMF, Press & Schechter 1974) – now based on N-body simulations (e.g. Jenkins et al. 2001; Lukić et al. 2007; Despali et al. 2016) – it is possible to model the matter density field and predict its 2-point function, the matter power spectrum. The HOD then provides a link between the galaxies and the dark matter haloes, in the form of a probabilistic description of how the galaxies populate the halo. This is based on some observable quantities such as their luminosity and colour, and distinguishes between their type (central/satellites). These models have shown to provide a good fit to a number of observables (e.g. Zheng et al. 2007; Zehavi et al. 2011; More et al. 2011) and can be used to fit cosmological models via combined probes (Cacciato et al. 2013). The halo model is largely used in this Thesis, to link the observed correlation between galaxies and dark matter, for different observables (Chapter 2, 4, 5).

Based on their morphology, galaxies can be broadly divided in two main classes: elliptical and spiral galaxies. Elliptical galaxies are believed to be the result of one or more galaxy mergers, they are characterised by an elliptical shape, old stellar population (emitting more in the red part of the electromagnetic spectrum) and are gravitationally supported by the random motion of their stellar content. Spiral galaxies have a disc-like shape, a young population (emitting more in bluer wavelengths) and are rotationally supported. Due to their typical rest-frame optical wavelength emissions, we will often refer to these two class of objects, respectively, as red and blue galaxies. Cluster galaxies are typically red, as well as the central massive galaxy of big groups. A large fraction of satellite galaxies is also typically red and this correlates with the morphology of the central galaxy (Weinmann et al. 2006). Among the mechanisms responsible for quenching, there are mergers, Active Galactic Nuclei (AGN) and Supernova (SN)
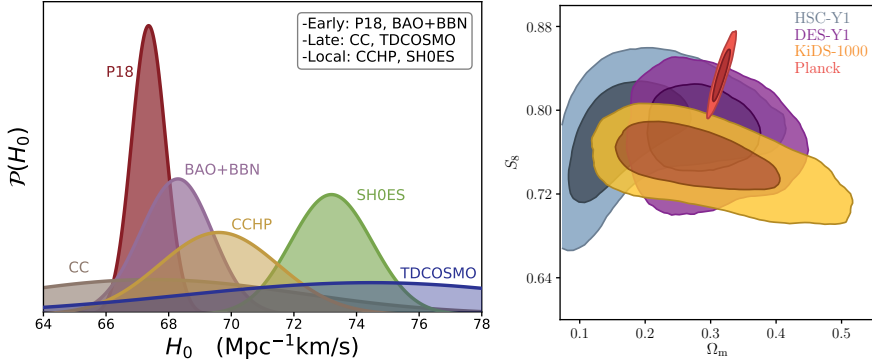
Figure 1.3: *Left:* The posterior distribution of the H_0 parameter as constrained by different analyses. The family of measurements can be broadly divided in three categories: those which rely on measurements of the early physics, such as the CMB (Planck Collaboration et al. 2020) and the Baryonic Acoustic Oscillations (Schöneberg et al. 2019, BAO); those which infer the Hubble constant from the late Universe, using relative galaxy ages (Jimenez & Loeb 2002; Haridasu et al. 2018, Cosmic Chronometers, CC) and the strong lensing of distant quasars (Chen et al. 2019, TDCOSMO); and finally those which measured the value of H_0 in the local universe, via the SNIa, either calibrated using the tip of Red Giant Branch (Freedman et al. 2020, CCHP) or the Cepheids (Riess et al. 2019, SH0EES).Image credit: José Luis Bernal et al. 2020. *Right:* Marginalised constraints for the joint distributions of $S_8 \equiv \sigma_8 \, (\Omega_{\mathrm{m}}/0.3)^{0.5}$ and Ω_{m} obtained by different lensing studies (HSC-Y1, DES-Y1, KiDS-1000) and *Planck*. The contours show the 68% and 95% credible regions. Image credit: Asgari et al. 2021

feedback and ram pressure stripping (Gabor et al. 2010; Zinger et al. 2018, among others).

In this Thesis, we will focus on the dark matter-halo interaction in the late-time Universe, from $z \sim 1.5$ to $z \sim 0.1$, spanning a range of time where the Universe has grown to double its size and has gone from the matter-dominated era to the Λ-dominated one. Our main scientific goal is to use observational data and models of how visible and invisible matter are spatially distributed and oriented to help infer the amount of matter present in the Universe, how it has expanded and clumped over this range of time. This contributes to the main question outlined at the beginning of this introduction, i.e. what are the exact values of the cosmological parameters, to confirm or challenge our current view of the Universe.

1.2.2   The era of precision cosmology and arising tensions

With the advent of space telescopes and the improvement of ground-based facilities, cosmology is facing a new challenge: to constrain the cosmolog-

ical model to high-precision and accuracy. With the decrease of the statistical error, any systematic effect becomes important and the limits of any model adopted to interpret the data are pushed to their boundaries[6].

In recent years, independent experiments have measured the cosmological parameters with increasing precision. Each experiment is typically able to constrain some parameters better than others, and it is subjected to different systematic effects. The outcomes of these experiments have shown some emerging tension between the different results. The most relevant one involves the expansion rate of the Universe, H_0, as summarised in Fig. 1.3 (left panel). Most notably, the largest tension $- 4.2\sigma -$ occurs between the value inferred from the analysis of the CMB, and thus of the very early Universe (Planck Collaboration et al. 2020) and a local measure which employs the SNIa as standard candles, calibrated using Cepheids (Riess et al. 2019, SH0ES). These might both point to unknown systematics in the data or new physics, and both directions are current area of research (see Di Valentino et al. 2021, for a recent review on possible solutions to the H_0 tension).

This is, however, not the only tension in the ΛCDM model: *Planck* results are also in mild tension with measurements of the amplitude of matter fluctuations at low redshifts, as constrained by the measurement of the apparent distortion of distant galaxy shapes (e.g. Heymans et al. 2013; Hildebrandt et al. 2017; Troxel et al. 2018; Hikage et al. 2019; Asgari et al. 2021). The light of these galaxies travels across the Universe and gets lensed by the distortion in the space-time due to the presence of matter distribution along the line-of-sight, a phenomenon called weak gravitational lensing (see Sect. 1.3). This can be used to infer the amount of matter in the Universe and by performing a tomographic slicing along the redshift direction to study the evolution of the amplitude of the large scale structures. These two quantities are summarised, respectively, by the cosmological parameters Ω_m and σ_8[7]. It is important to note that, as for the H_0 tension, the results from different groups provide different levels of tension, some of

---

[6]There is an important distinction between *precision* and *accuracy*: precision regards the size of the error bars and it is improved by the increase in the amount of data; accuracy reflects our ability to recover the *true* value of a parameter, i.e. our ability to model possible sources of biases that would shift the best fit value. Often researchers model our ignorance on systematic effects by adding free parameters that can potentially absorb the bias at the expense of the precision of the constrains: these are called nuisance parameters and the process is called marginalisation.

[7]The parameter σ_8 is defined as the amplitude of the (linear) matter power spectrum, parametrised by the root mean square fluctuations in spheres with a radius of $8h^{-1}\mathrm{Mpc}$ and it has important implications on the growth of fluctuations in the early Universe.

which are compatible with the *Planck* result, as summarised in the right panel of Fig. 1.3.

1.3   Weak Gravitational Lensing

Weak lensing is an extremely powerful probe to investigate the dark content and the geometry of the Universe. Most importantly, it is an orthogonal probe to galaxy clustering. The combined analysis of galaxy clustering and galaxy lensing is the primary goal of current and future cosmological surveys (see also Sect. 1.5).

In light of upcoming surveys which will measure the cosmological parameters with a precision below a per-cent, it is fundamental to understand the possible source of systematics and identify the best approaches to mitigate them. This is also crucial in light of the current tension with *Planck*, as seen in the previous section, in order to ensure a robust estimation of the cosmological parameters and to advocate for the need of an extension to the current cosmological model.

1.3.1   Fundamentals of Gravitational Lensing

Let us first briefly revisit the fundamentals of weak gravitational lensing. General Relativity predicts that a mass distribution distorts the local geometry of the space-time. We know from Fermat's principle that a light ray finds the fastest route in space-time to connect two points: in the absence of any deformation, in a Euclidean geometry, the path followed by the light ray will be a straight line. However, if light is travelling in the proximity of a mass distribution, it will follow a curved trajectory due the distortion of the space-time itself caused by the presence of the mass. In analogy with the distortion in the light-ray trajectory due to the refractive index of a glass lens, we call this process *gravitational lensing*: the mass distribution is the *lens*, while the object from which the light ray is emitted is called *source*. For a review on gravitational lensing, we refer to Bartelmann & Schneider (2001). Typically, the sources are distant galaxies, located behind the lens along the line-of-sight, i.e. $z_s > z_l$, with z_s and z_l the redshift of the source and the lens, respectively. Since in the majority of cases the distortion is very small[8], we study the induced distortions on an ensemble of source-

---

[8]This is not the case for strong gravitational lensing, a specific configuration in space that generates a very strong lensing effect. This is a rare phenomenon compared to weak lensing. It is also a promising way to infer cosmological parameters (e.g. Bartelmann &

lens pairs, in a statistical way. Although there is a family of applications to weak lensing (CMB lensing, lensing by clusters, ...), in here we will focus only on two main cases: the lensing effect generated by massive galaxies, which we refer to as galaxy-galaxy lensing (GGL) and the one of the matter distribution along the line-of-sight, which is called cosmic shear. Typically, GGL is used to infer the properties of the class of galaxies used as lenses, such as their total mass and their mass profile (i.e. including the dark matter component), while cosmic shear provides information on the overall matter distribution, growth of structures and the varying of the dark energy parameter, and it can thus be used to infer cosmological parameters, as discussed in the Sect. 1.2.2.

Gravitational lensing acts on the entire image of the background source: it distorts the ensemble of light rays coming from the distant galaxy, which in turn are perceived by the observer as the final (distorted) image of the galaxy. The effect of gravitational lensing is twofold: because the sources are extended objects, the differential deflection of light distorts the images tangentially around the centre of the lens (shearing), and at the same time it magnifies their observed flux due to the local stretch of the space-time, which dilates the image without changing its surface brightness (this is a consequence of the fact that during the process photons are neither absorbed nor emitted). We remind the reader that here we are focusing on weak lensing and thus all of these distortion are small ($\sim 1\%$ of the original light profile).

In the limit of weak gravitational field, the field equations of General Relativity can be linearised: this means that we can treat the deflection induced by an ensemble of point masses as the linear sum of the individual deflections. This provides the framework to treat the deflection caused by an extended mass distribution, which we can treat as the sum of infinitesimal mass elements dm of volume dV and volume density $\rho(\mathbf{r})$. Without entering in the details of the derivation, we report here the final expression of the deflection angle $\hat{\alpha}(\xi)$ generated by a mass distribution as sketched in Fig. 1.4, with $\xi = (\xi_1, \xi_2)$ the impact parameter (see e.g. Bartelmann & Schneider 2001, for the full derivation):

$$\hat{\alpha} = \frac{4G}{c^2} \int d^2\xi' \int dr'_3 \rho(\xi'_1, \xi'_2, r'_3) \frac{\xi - \xi'}{|\xi - \xi'|} \tag{1.1}$$

$$= \frac{4G}{c^2} \int d^2\xi' \Sigma(\xi') \frac{\xi - \xi'}{|\xi - \xi'|} \, , \tag{1.2}$$

Schneider Che), as discussed in Sect. 1.2.2
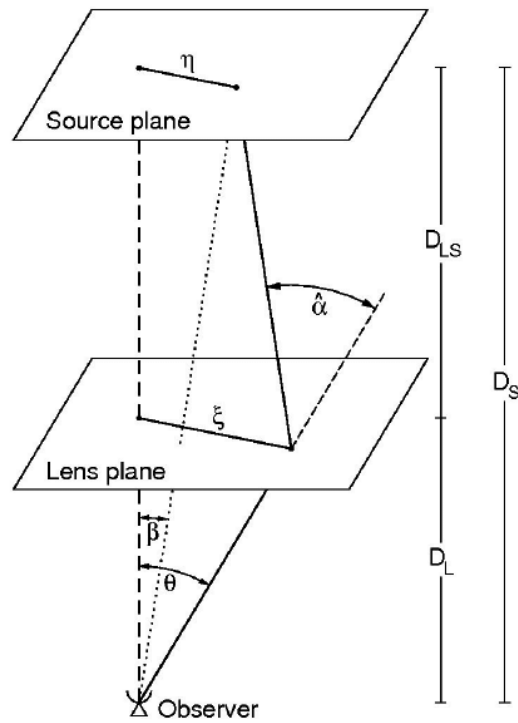
Figure 1.4: Sketch of a typical lensing system. Image credit: Bartelmann & Schneider (2001)
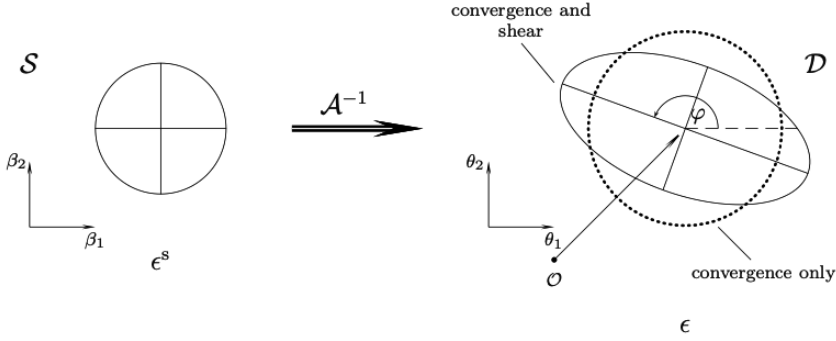
Figure 1.5: A circular source is transformed by the inverse of the Jacobian matrix $\mathcal{A}$: the convergence dilates the image, while the shear changes the axes ratio. Image credit: M. Bradac, from Schneider (2005)

where we have introduced the surface mass density $\Sigma(\xi) \equiv \int dr_3 \rho(\xi_1, \xi_2, r_3)$, defined as the mass density projected on the plane perpendicular to the line-of-sight.

Let us indicate as β the true angular position of a source galaxy at angular distance D_s from the observer, lensed by a mass distribution located at angular distance D_{ds} from the source (D_d from the observer). The source will be observed at a new angular position θ given by the vectorial sum of the original position β and the scaled deflection angle $\alpha(\theta)$, as described by the *lens equation*:

$$\beta = \theta - \frac{D_{ds}}{D_s} \hat{\alpha}(D_d \theta) \equiv \theta - \alpha(\theta) . \tag{1.3}$$

To get the final distorted image of an extended object such a galaxy, one should solve the lens equation for each light ray of the image. At first order, a convenient way to visualise the mapping between the original and the observed image is in terms of the Jacobian matrix $\mathcal{A}$, which is the derivative of the original position β with respect to the lensed position θ:

$$
\begin{aligned}
\mathcal{A} = \frac{\partial \beta}{\partial \theta} = \mathbb{I} - \frac{\partial \alpha}{\partial \theta} &= \begin{pmatrix} 1 - \kappa - \gamma_1 & -\gamma_2 \\ -\gamma_2 & 1 - \kappa + \gamma_1 \end{pmatrix} \\
&= (1 - \kappa) \begin{pmatrix} 1 & 0 \\ 0 & 1 \end{pmatrix} - |\gamma| \begin{pmatrix} \cos 2\phi & \sin 2\phi \\ \sin 2\phi & -\cos 2\phi \end{pmatrix} .
\end{aligned}
\tag{1.4}
$$

Here κ is the convengence, which encodes the isotropic focusing and thus quantifies the changes in size of the image; $\gamma = \gamma_1 + i\gamma_2 = |\gamma| \exp(i2\phi)$ is

the complex shear: it quantifies the anisotropic focusing, which yields the distortion in the image. The shear is a spin-2 quantity, i.e. it is invariant under a rotation of 180 deg, as evident from the factor 2 in the phase. From eq. 1.4 follows that a circle would transform into an ellipse, with minor and major axes given by the inverse of the eigenvalues of A. The eigenvectors of $\mathcal{A}$ provide instead the orientation of the ellipse. An illustration of the effect of convergence and shear in a galaxy image is shown in Fig. 1.5. The magnification is the inverse of the determinant of $\mathcal{A}$, $\mu = \frac{1}{\det \mathcal{A}}$.

1.3.2   Cosmic shear

Cosmic shear is the study of the weak cosmological lensing, i.e. of the continuous deflection of a light ray due to the matter inohomegeneities along the line-of-sight. It allows to probe the large scale structures (LSS) by studying the projected correlation of galaxy shapes. As we have seen in the previous section, the presence of matter along the line-of-sight tidally distorts the apparent shapes of the background galaxies and the final image that we receive is the result of the multiple deflections occurred along the way from the emitter to the observer. The formalism to describe cosmic shear has many analogies with the one presented in the previous section and, for the scope of this introduction, we consider it sufficient: the interested reader can refer to e.g. Kilbinger (2015) for a review.

Galaxies are typically non-round objects: we can indicate their intrinsic ellipticity as ϵ_s. This is modified by cosmic shear via the introduction of what is called *reduced shear*, g, which is a function of the shear and the convergence acting on the image, $g \equiv \gamma/(1-\kappa)$. In the weak lensing limit, however, since both $|\gamma|$ and κ are $\ll 1$, this simplifies and we can simply consider the distortion as purely due to the shear. The observed ellipticity, ϵ, is thus

$$\epsilon = \frac{\epsilon_\mathrm{s} + g}{1 + \epsilon_\mathrm{s} g^*} \approx \epsilon_\mathrm{s} + \gamma \ . \tag{1.5}$$

The observed ellipticity can be measured from galaxy images with dedicated algorithms and needs to be corrected for the effect of atmospheric blurring and noise. There are several techniques to do this (e.g. by using high fidelity image simulations to calibrate the bias in the recover shape or by using a meta-calibration approach, see for example Mandelbaum (2018) for a review). The observed ellipticity is measured with respect to a reference axis and, as the shear, it can be expressed as a complex quantity: $\epsilon = \epsilon_1 + i\epsilon_2 = |\epsilon|\mathrm{e}^{i2\phi}$ (see Fig. 1.6 for an illustration of the total ellipticity as a function of its two components). In this notation, the absolute value of
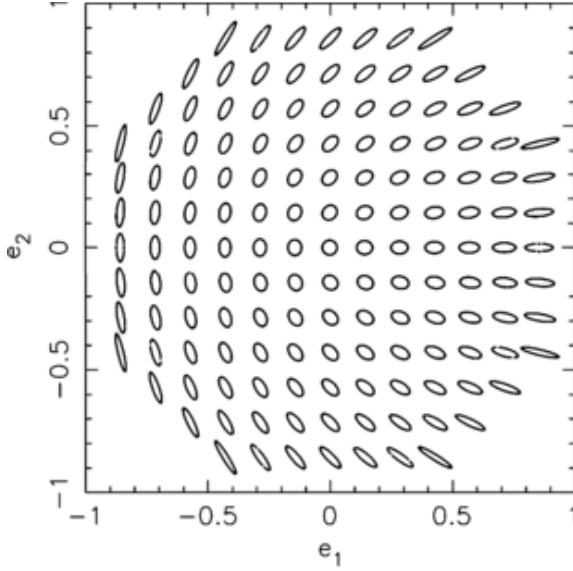
Figure 1.6: The effect of the shear distortions on a circular galaxy, as parametrised by the e_1 and e_2 components. Image credit: Bridle et al. (2009).

the ellipticity is defined as $|\epsilon| = (a-b)/(a+b)$, with a, b the major and minor axes of the ellipse, respectively. In the lack of preferential directions, the ensemble average of the intrinsic shapes would be $\langle \epsilon_s \rangle = 0$ and the observed ellipticity would be an unbiased estimator of the shear. This assumption is, however, violated by any intrinsic alignment (IA), i.e. by the tendency of galaxies to exhibit preferential directions in the sky, as a consequence of their interactions with the LSS. Galaxies form and live embedded in dark matter haloes whose tidal field imprints a preferred alignment to their major axis, as discussed in Sect. 1.2.1. These alignments, being sourced by the LSS, are correlated and are an important contaminant to cosmic shear. IA is the main focus of this work and it is the topic of the next Section.

The efficiency of the lensing depends on the distance between the galaxy and the lens, via a quantity called lensing efficiency:

$$q(\chi) = \int_{\chi}^{\chi_{\text{hor}}} d\chi' n(\chi') \frac{f_K(\chi' - \chi)}{f_K(\chi')}, \tag{1.6}$$

where χ is the comoving distance, χ_{hor} is the horizon distance, i.e. χ evaluated at infinite redshift; $n(\chi)$ is the source galaxy probability distribution and f_K is the comoving angular distance, which for a flat universe is simply $f_K(\chi) = \chi$. This shows that the lensing efficiency is a function of the

ratio D_{ls}/D_s and the source galaxy distribution $n(\chi)\mathrm{d}\chi = n(z)\mathrm{d}z$. The lensing efficiency is broad and most sensitive to the mass distributions located half-way between the observer and the source.

Because the lensing kernel is a function of comoving distance, it is convenient to split the galaxy sample into tomographic redshift bins, which provide lensing measurements with different weights. By measuring the correlation of galaxy shapes in different z-bins, it is possible to probe the evolution of the Universe at different times. However, to be competitive and to increase the signal-to-noise ratio (S/N), cosmic shear needs to measure galaxy shapes for very wide areas (Amara & Réfrégier 2007), making it impossible to get spectra for all galaxies. Moreover, because the luminosity function increases towards the faint end, the most abundant source objects are typically faint blue galaxies: measuring the spectra of these galaxies is extremely time consuming, and thus different techniques have been developed over time to estimate their redshifts via multi-band photometry. These exploit the redshift-colour relations and are calibrated over subsamples of galaxies for which spectroscopic redshifts are available (see e.g. Wright et al. 2020; Myles et al. 2020, for some recent applications). Weak lensing is mainly sensitive to the mean and the width of the bin redshift distribution (Amara & Réfrégier 2007), however other systematics can depend on other properties (see for example Appendix E in Chapter 2, where we show the impact of the catastrophic outliers on the IA signal), although this is a second order effect, which is not a concern for current surveys but might become important for future ones.

The photo-z provide the 3D spatial distribution of the galaxies, which, at the same time, indicate the time when the light has been emitted. By simultaneously fitting the signal for the different tomographic bins, cosmic shear can probe the growth of structures. However, even if the weights are different for different redshift tomographic bins, these are highly correlated due to the broad kernel of the lensing efficiency and the fact that part of the LSS is in common to all of the bins. Moreover, the uncertainty in the photometric redshifts introduces an overlap between different bins, due to the galaxies that are incorrectly assigned. These factors in practise limit the number of bins one can efficiently obtain, which is typically around five or six in a redshift baseline of $z < 1.2$.
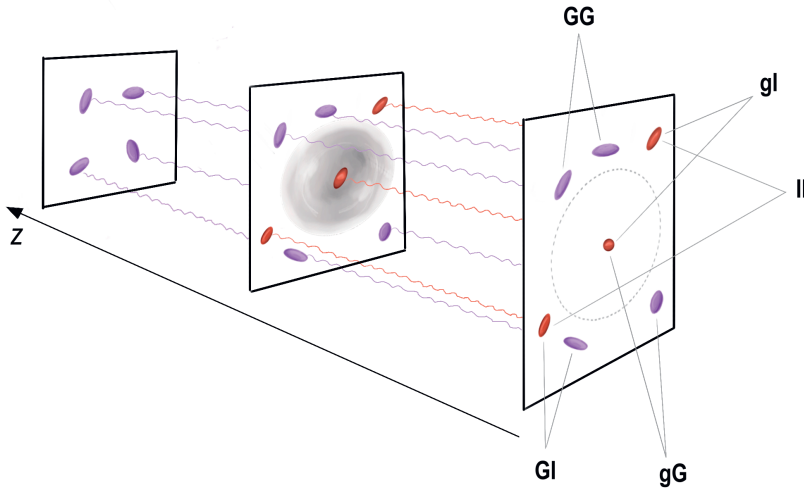
Figure 1.7: A schematic picture of the different terms that arise when correlating galaxy shapes (GG, II, GI), and when correlating galaxy positions and galaxy shapes (gI, gG). Starting from the panel on the left: the light of distant galaxies travels along the line-of-sight and is lensed by a matter overdensity at intermediate redshift (middle panel, indigo ellipses) which align the apparent shapes tangentially to the matter distribution. The galaxies that forms close to the same overdensity are instead intrinsic aligned to the major axis of the halo (red ellipses in the middle panel). The light of all of these galaxies is collected at $z = 0$ where we observe the projected shapes and correlate them to measure either shape-shape correlations, $\langle \epsilon\epsilon \rangle$, or shapes-number density correlations, $\langle \epsilon n \rangle$. For the purpose of illustrating the position-shape correlations, the central galaxy is shown as a circular point in the rightmost panel.

1.4   Intrinsic Alignment

As mentioned in the previous section, IA is the tendency of galaxies to have an intrinsic orientation imprinted at the moment of galaxy formation and evolved over time due to the continuous interaction with the surrounding tidal fields (Catelan et al. 2001). We have seen in Sec. 1.2.1 that galaxies form inside dark matter haloes and inherit from them their angular momenta and orientations via complex mechanisms that happen at the level of the proto-galaxy (see Joachimi et al. 2015; Kiessling et al. 2015; Kirk et al. 2015, for dedicated reviews). Our knowledge of these mechanisms is still limited and we mainly rely on hydrodinamical simulations to get insights. We can broadly distinguish two main regimes: the alignment of central galaxies, which dominates at large scales, and the one of satellite galaxies, which becomes important at small scales (Schneider & Bridle 2010). These two have an intrinsically different nature due to their different formation history and their location within the halo. Moreover, a clear distinction between the alignment of blue, disc-like galaxies and red, elliptical galaxies has also emerged both in observations (Hirata et al. 2007; Joachimi et al. 2011; Mandelbaum et al. 2011; Singh et al. 2015; Johnston et al. 2019) and simulations (Chisari et al. 2015b; Velliscig et al. 2015b; Tenneti et al. 2016), with the former showing no alignment within current precision, while the latter have a clear alignment signature, which further depends on secondary galaxy parameters, such as their luminosity, as we will discuss later.

In terms of its role as contaminant to weak lensing, we identify two IA correlations that contribute to the final observed measured in cosmic shear (see Fig. 1.7): the alignment between intrinsic galaxy shapes (intrinsic-intrinsic term, II), $\langle \epsilon_{\mathrm{s}} \epsilon_{\mathrm{s}} \rangle$, which is sourced by the tendency of galaxies that form close to a same overdensity to share the same alignment, and the correlation between the intrinsic shape of a galaxy an the shear of another galaxy, $\langle \gamma \epsilon_{\mathrm{s}} \rangle$. The latter is called the gravitational-intrinsic term (GI), and it is caused by a matter overdensity that simultaneously shears a background galaxy and aligns a foreground one, close to the mass distribution itself. It is the predominant contamination since it acts between galaxies that are separated in redshift (cross-terms in the projected correlation), while the II is only relevant when galaxies have similar redshifts, as they need to be physically connected to generate such term. The observed correlation is the sum of all of the terms:

$$\langle \epsilon \epsilon \rangle = \langle \gamma \gamma \rangle + \langle \epsilon_{\mathrm{s}} \epsilon_{\mathrm{s}} \rangle + \langle \gamma \epsilon_{\mathrm{s}} \rangle \ . \tag{1.7}$$

Here, $\langle\gamma\gamma\rangle$ is the term sourced by cosmic shear: it is clear that in order to recover the correct cosmic shear signal from the observed correlation we need to model the other two terms and account for them in the cosmological parameter inference.

Similarly, when measuring the galaxy position - shape correlation, as in the galaxy-galaxy lensing, we have

$$\langle\epsilon n\rangle = \langle\gamma n\rangle + \langle\epsilon_{\mathrm{s}} n\rangle \, , \qquad (1.8)$$

i.e. we need to account for the correlation between the position of a galaxy and the intrinsic orientation of another, nearby one. In this case, for the IA to be significant, the galaxies need to be physically connected and thus a cut in the lens-source pair separation is typically sufficient to remove the contamination.

Measuring IA poses the same challenges as measuring lensing: we have to deal with noisy, point-spread function (PSF)-convolved data, and we need to remove from the signal the contribution from lensing. To measure galaxy shapes there are different algorithms available, employing different methods (Kaiser et al. 1995; Kaiser, Squires & Broadhurst Mil; Melchior et al. 2011, e.g.). In this Thesis we focus on two methods and in Chapter 3 we compare their effect on the associated IA signal.

To measure the IA signal, it is convenient to look at the projected correlation function between galaxy positions and galaxy orientations, since it has a better S/N compared to the II signal and can be considered a proxy to the GI signal. It is fundamental to have good estimates of the galaxy positions to ensure that the galaxy pair is truly physically connected and minimise the lensing contribution: this is one of the main limitations to IA studies. For this reason, it is in general preferred to work with spectroscopic redshifts. In this thesis we investigate the signal in a photometric sample (KiDS-1000 LRGs, Chapter 3), which requires a full modelling of the possible contaminants (lensing and magnification).

Because the selection function of a survey implicitly selects galaxies with different properties (typically because of cuts in apparent magnitude, but it can also be in colours, or due to the presence of fibre/slits) the average properties of the galaxy sample will differ from survey to survey, and even more importantly will possibly change along the redshift baseline. It is thus of crucial importance to study how IA depends on observable galaxy properties such colour and luminosity, and to try to trace back the underlying physical relation, such as the formation history, the mass of the halo and the orbital time. Most of this Thesis tries to deal with such complexity, by
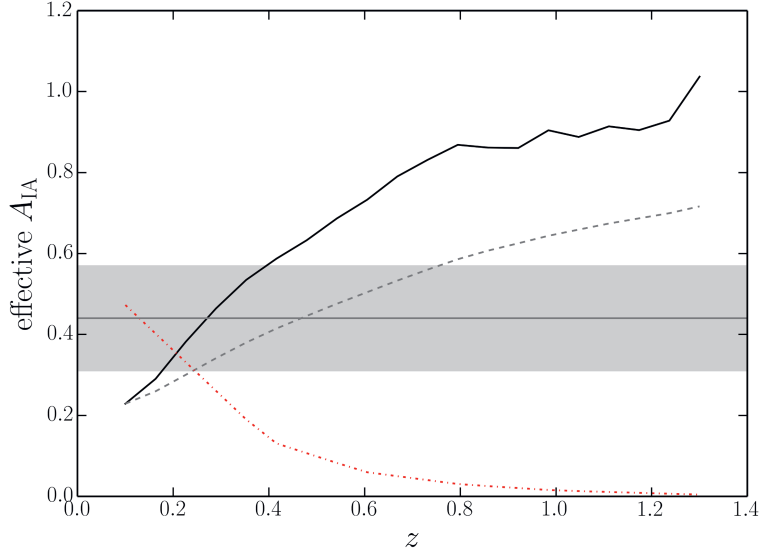
Figure 1.8: The effective IA signal input in the data vector (solid black line) and recovered by the NLA model (gray band). The dashed gray line shows the cumulative mean of the input IA signal, while the red dash-dotted line the ratio of IA over lensing at different redshifts (see the text for more details). Image credit: Robertson et al. (2020)

both informing the models with direct observation of intrinsic alignment of specific galaxy sub-samples (Chapter 3), and trying to connect them to the properties of the halo they reside on (Chapter 4). We dedicate a full analysis of how these differences propagate in the contamination of a lensing survey in Chapter 2.

It is interesting to note that even though a typical lensing survey – which is flux-limited – selects galaxies with a stronger IA signal at high redshifts (IA is typically stronger for luminous red central galaxies), the IA impact on cosmic shear is strongest in the low-redshift bins, where lensing is less efficient (see Sec. 1.3.2). We investigate this effect in Robertson et al. (2020) and present it in Fig. 1.8. Here we compare the best-fit amplitude for a KiDS-like analysis (grey band) from the model presented in (Fortuna et al. 2021a) and the input IA signal in the data vector (see Chapter 2 for more details). The best-fit value is lower than the mean IA signal and broadly corresponds to the signal present only in the low-redshift bins. This can be understood by considering the lensing efficiency over redshift: at high$-z$ the relative importance of IA over lensing decreases significantly, as we can see from the red dot-dashed line, which shows the ratio of the projected an-

gular power spectra $C_{\text{IA}}^{(ij)}(\ell)/C_{\text{GG}}^{(ij)}(\ell)$ evaluated at the multipole $\ell = 1000$ as a function of the redshift of the foreground bin j. Hence, although the actual IA signal is larger in the high-z tomographic bins, it impacts the best fit parameters less, because an error in the estimated IA signal there has a negligible effect on the inferred $C(\ell)$.

This is an important finding for CMB lensing studies, as it shows that although their results are sensitive to the IA amplitude, they can expect a minor contribution at the redshift probed by their analysis. Similarly, this might suggest that removing the first tomographic bin might be a safer choice for cosmic shear surveys.

1.5 Data

In the context of cosmology, it is common to divide the surveys into categories based on their constraining power. We refer to the ongoing surveys as Stage-III and the next generation surveys as Stage-IV. Currently there are three ongoing weak lensing surveys: the Kilo Degree Survey (KiDS, Kuijken et al. 2019), the Dark Energy Survey (DES, Abbott et al. 2021) and the Hyper Supreme-Cam Survey (HSC, Aihara et al. 2018). In this Thesis we focus on KiDS, which we use both as a reference to simulate a generic Stage-III survey on Chapter 2, and to investigate in depth the properties of one sub-sample of galaxies, the LRGs, in Chapter 3 and 4. We measure the shapes of these galaxies to study its IA signal using a moment-based algorithm, from which we measure the shapes as second-moments of the surface brightness. A full characterisation of this sample is then performed in Chapter 3, via the use of a halo model fit.

Stage-IV surveys include both space-based and ground-based surveys, which are designed to be synergic in their observing strategies. These are *Euclid* (Laureijs et al. 2011), the Vera C. Rubin Observatory, previously known as the Large Synoptic Survey Telescope (LSST, Abell et al. 2009) and the Nancy Roman Space Telescope, previously known as Wide Field InfraRed Survey Telescope (WFISRT, Spergel et al. 2015). A substantial part of the cosmology community is currently involved in forecasting the abilities of Stage-IV surveys to constrain the cosmological parameters and on identifying strategies to mitigate the systematic errors. We dedicate two chapters to these analyses, for both a generic Stage-IV survey (Chapter 2) and an LSST-like survey (Chapter 5). An extended version of the pipeline developed for these two projects is currently used by the Euclid-IA working group to forecast the impact of IA in *Euclid* and to provide a self-calibration

strategy to mitigate it. The pipeline is specifically designed to interface with CosmoSIS (Zuntz et al. 2015) a software for cosmological parameter fitting. The pipeline is fully modular, such that any ingredient of the model (the concentration-mass relation, the halo mass function etc...) can be replaced by the user with minimal editing. The pipeline allows to compute all the 2-point functions in Fourier space which enter into the clustering, IA and their cross-correlation statistics.

1.6   This Thesis

The main goal of this Thesis is to investigate the IA of galaxies to mitigate its impact on cosmic shear. Based on previous observations that IA depends on galaxy properties such as galaxy colour, type (central/satellite) and luminosity, in **Chapter 2** we study the impact of not accounting for the variety of IA signatures in the data when analysing cosmic shear signal and assessing the level of bias that would arise for Stage-III and Stage-IV surveys. We also provide an analytical prescription of how it should be modelled to fully account for such complexity and identify a minimal model that would at least capture the variation of the IA contamination across the tomographic redshift bins, as a consequence of the evolution on the composition of the galaxy population in a flux-limited survey. We find that the IA contamination is largest at low redshift, where lensing is less efficient and that the behaviour of the luminosity dependence at faint luminosities is crucial to assess the level of contamination. That was, however, the regime where less data were available and thus we provide a double scenario forecast, extrapolating over the most extreme regimes allowed by the data.

In **Chapter 3** we use the high quality data from KiDS and we focus on exploring the IA dependence luminosity and redshift for a highly S/N sample with precise photometric redshifts, the luminous red galaxies (LRGs). This sample is ideal to cover part of the unconstrained range of the luminosity dependence, and the high S/N allows us to completely disentangle the luminosity and the redshift dependence of the IA signal with specific cuts. We found the data to favour a broken power-law scenario for the luminosity dependence with a knee at $L \lesssim 3.2 \times 10^{10} h^{-2} L_\odot$ in the r-band; they also do not exhibit any redshift dependence from $z = 0.2$ to $z = 0.8$.

In **Chapter 4** we extend the investigation of the galaxy sample used in Chapter 3 to constraint IA and we explore the dark matter properties of these galaxies to provide a more direct link between the halo mass and the IA signal. We use GGL to infer the mass profile of the LRGs and to assess

the fraction of satellites in the sample. This is also crucial information to properly model the IA signal, since it is observed that centrals and satellites exhibit different IA signals (Johnston et al. 2019). To link the visible and invisible component of the galaxy and infer the galaxy properties we make use of the halo model, with the halo occupation distribution based on the conditional luminosity function (Yang et al. 2003). We also measure the IA signal sourced by the background galaxies which are physically connected to the LRGs, selecting only the sources for which $|z_l - z_s| < 0.2$.

In **Chapter 5** we focus on the other main effect of lensing which is often neglected: magnification. We consider the hypothesis of improving the cosmological constraints by including the effect of magnification and provide a forecast for the LSST. We include the large scale IA in the model and make use of the same halo model formalism as in Chapter 4. For this project, I developed a pipeline for the theoretical prediction of the clustering and the luminosity function. This includes the modelling of how the luminosity function is affected by the photometric redshift uncertainty. We find that the improvement in the recovered cosmological parameters by adding the magnification is negligible, while the effect of ignoring magnification can severely bias the cosmological parameters.

2 | The halo model as a versatile tool to predict intrinsic alignments

M.C Fortuna*, H. Hoekstra, B. Joachimi, H. Johnston, N.E. Chisari, C. Georgiou, C. Mahony 2021, MNRAS, 501*

Intrinsic alignments (IAs) of galaxies are an important contaminant for cosmic shear studies, but the modelling is complicated by the dependence of the signal on the source galaxy sample. In this paper, we use the halo model formalism to capture this diversity and examine its implications for Stage-III and Stage-IV cosmic shear surveys. We account for the different IA signatures at large and small scales, as well for the different contributions from central/satellite and red/blue galaxies, and we use realistic mocks to account for the characteristics of the galaxy populations as a function of redshift. We inform our model using the most recent observational findings: we include a luminosity dependence at both large and small scales and a radial dependence of the signal within the halo. We predict the impact of the total IA signal on the lensing angular power spectra, including the current uncertainties from the IA best-fits to illustrate the range of possible impact on the lensing signal: the lack of constraints for fainter galaxies is the main source of uncertainty for our predictions of the IA signal. We investigate how well effective models with limited degrees of freedom can account for the complexity of the IA signal. Although these lead to negligible biases for Stage-III surveys, we find that, for Stage-IV surveys, it is essential to at least include an additional parameter to capture the redshift dependence.

2.1 Introduction

As the light of distant galaxies travels towards us, it is deflected by matter inhomogeneities. The cumulative effect of these small distortions leads to a preferential apparent alignment of galaxy shapes, a phenomenon called weak lensing. The resulting correlation of galaxy shapes (*cosmic shear*) provides direct information on the matter distribution in the Universe as well as the effect of dark energy on the geometry and the growth of structures (e.g Bartelmann & Schneider 2001; Kilbinger 2015). However, extracting cosmological parameter estimates from weak lensing surveys is challenging due to a number of systematic errors it is prone to. On the measurements side, the main sources of bias come from the uncertainty in the source redshift distributions and the actual shape measurements, for which great improvements have been achieved in the last decades, due to advances in both image simulations and shape measurement algorithms (Kannawadi et al. 2019; Mandelbaum 2018, for a dedicated review).

On the modelling side, a naive interpretation of cosmic shear would relate the observed correlations between galaxy orientations as solely arising from the lensing effect of matter. In reality, galaxies form and live inside dark matter haloes and they are continuously exposed to the gravitational interaction with the surrounding matter distribution. This leads to the coherent alignment induced by the underlying tidal field on physically near galaxies, the so-named intrinsic alignment (IA) (Joachimi et al. 2015; Kiessling et al. 2015; Kirk et al. 2015; Troxel & Ishak 2015, for extensive reviews). If not properly accounted, IA can affect the inferred properties of the matter distribution from lensing. In the perspective of high precision surveys such as Euclid[1] (Laureijs et al. 2011) and LSST[2] (Abell et al. 2009), which aim to measure cosmological parameters with an accuracy better than a percent, it is crucial to properly model the impact of IA and to quantify the level of precision required in our models and IA constraints (Joachimi & Bridle 2010; Kirk et al. 2010; Krause et al. 2016).

One of the challenges in mitigating the effect of IA comes from the differences between the samples employed in studies of IA and in cosmic shear. Pressure supported (red/elliptical) galaxies are more subjected to the effect of tidal fields and tend to stretch their shapes in the direction of the matter overdensities (Catelan et al. 2001). This turns into a non-negligible IA signal, observationally constrained by a number of works (e.g.

---

[1]https://www.euclid-ec.org
[2]https://www.lsst.org

Mandelbaum et al. 2006; Hirata et al. 2007; Okumura & Jing 2009; Joachimi et al. 2011; Singh et al. 2015; Johnston et al. 2019, hereafter J19). On the other hand, disc, rotationally supported (blue) galaxies preferentially align their spins through a torque mechanism. Although this has been observed in simulations, there is no consensus on the final predictions due to the different implementations of hydrodynamics and baryonic feedback (e.g. Chisari et al. 2015b; Tenneti et al. 2016; Codis et al. 2018; Kraljic et al. 2020). From an observational point of view, the alignment of blue galaxies has not been detected yet, neither at low and intermediate redshifts (Mandelbaum et al. 2011; Blazek et al. 2012; Samuroff et al. 2019, J19), nor at high redshifts (Tonegawa et al. 2018).

For this reason, to maximise the signal-to-noise ratio, the majority of IA analyses focus on low redshift red galaxies, while cosmic shear surveys typically span a much broader range in redshift and do not make any colour selection. A proper re-scaling of IA predictions, weighted by the fraction of red galaxies in the sample, is then required in order to correctly account for the alignment contribution to the signal.

While the aforementioned alignment mechanisms describe the behaviour of the central galaxies well, the picture at small scales is complicated by the intra-halo tidal fields, galaxy mergers and halo assembly history, as well as AGN feedback and winds (Soussana et al. 2020; Tenneti et al. 2017). Pereira et al. (2008) and Pereira & Bryan (2010) investigated the satellite halo alignment in simulations, finding an overall tendency of satellites to point radially towards the centre of the host halo, due to a continuous torquing mechanism that aligns their major axes in the direction of the gravitational potential gradient during their orbits. Motivated by their findings, a halo model description of this alignment term was developed by Schneider & Bridle (2010, hereafter SB10). However, Sifón et al. (2015) did not find observational evidence for satellite alignment in clusters. Similarly, Chisari et al. (2014) explored the alignment signal around stacked clusters and found it to be consistent with zero. Huang et al. (2018) pointed out that the signal depends on the shape algorithm used, a feature further confirmed by Georgiou et al. (2019b, hereafter G19).

Recently, J19 and G19 investigated the alignment signal in the overlapping region between the Kilo Degree Survey[3] (KiDS, de Jong et al. 2013; Kuijken et al. 2019) and the Galaxy and Mass Assembly survey (GAMA, Driver et al. 2011). The detected IA signal provides evidence that a simple dichotomy between red and blue galaxies is not sufficient to capture

---

[3]http://kids.strw.leidenuniv.nl

the entire physics of the IA signal. In particular, G19 observed a scale dependence of the satellite alignment, with satellite shapes radially aligned at small radii and a vanishing signal towards larger scales. As a consequence, the tendency of satellites to be randomly orientated at large scales suppresses the the overall IA signal, as observed by J19. Therefore, even in the linear regime, where the IA signal can be modelled through the linear alignment model (LA, Hirata & Seljak 2004), the evolution of the satellite fraction in the sample can imprint a varying amplitude to the signal, a feature never explored by any forecasting analysis so far.

Cosmic shear analyses employ tomographic binning to investigate the growth of structures and better constrain cosmological parameters. Since these surveys are flux-limited, the tomography imprints an indirect galaxy selection, including only the most luminous galaxies in the high-redshift bins. As satellites are intrinsically fainter, this turns into a satellite cut at high redshifts. Satellites contribute predominantly a random signal at large scales and therefore can induce a modulation of the IA signal over the bins, suppressing it at large scales and boosting it at small scales, at low redshifts. Similarly, the fraction of red galaxies varies with redshift. The extrapolation of the results from IA studies then requires some care, since the majority of them limit their analyses to low-to-intermediate redshifts.

In addition, a luminosity dependence of the IA signal is currently under debate. While it has been observed for large luminous galaxies (Mandelbaum et al. 2006; Hirata et al. 2007; Joachimi et al. 2011; Singh et al. 2015), J19 has found no evidence for any luminosity scaling, hinting towards a more complex sample dependence. Similarly, two studies suggest a different behaviour for the satellite alignment signal, with Huang et al. (2018) detecting a more prominent alignment for the brightest satellites located close to the central galaxy, while G19 do not observe any luminosity trend in galaxy groups, but confirm a radial dependent signal. As for the large scales, a luminosity dependence of the satellite alignment can significantly change the contamination for a lensing survey, where the low redshift tomographic bins are dominated by faint satellites.

Understanding the sample dependence in the IA mechanism is a key feature to properly model it in the broader case of a cosmic shear galaxy sample. In this paper we investigate the impact of satellite galaxy alignment both at large and small scales. We provide a unified framework to incorporate all of the sample dependencies that emerged from observations, through the halo model formalism. We also explore the areas of tension between different measurements in the literature, trying to incorporate all

of the available information as well as the current uncertainties in our pre-
dictions. We base our model on SB10, including the scale dependent signal
measured in G19 and the luminosity dependence suggested by Huang et al.
(2018).

The paper is organised as following. In Sect. 2.2 we describe the mock
data we use to simulate a cosmic shear survey, for which we employ the
Marenostrum Institut de Ciències de l'Espai Simulations (MICE). We build
our mock to resemble a Stage III survey, mainly inspired by the final data
release of KiDS. Sect. 2.3 introduces our model at large scales. We explore
the possibility that part of the tension around the luminosity scaling of the
IA signal is caused by neglecting the satellite fraction in the samples while
modelling the signal. We provide a model that accounts for both the role
of satellites and the differences between different data sets: we investigate
the compatibility of the measurements in the literature within this frame-
work. In Sect. 2.4 we address the behaviour of satellites at small scales. We
re-analyse the G19 measurement in the context of a red/blue distinction of
the galaxy population, and model the satellite alignment including both a
radial and luminosity dependence. In Sect. 5.6 we show the predicted IA
signal and illustrate the impact on cosmic shear studies. We investigate
the impact of adopting simplistic IA models when performing cosmologi-
cal analysis and address the level of bias expected for a Stage-III (current
generation) and a Stage-IV (next generation) surveys. In Sect. 4.8 we draw
our conclusions.

Throughout this paper we assume the MICE cosmology as our cosmo-
logical model of reference: a spatially flat ΛCDM model with $h = 0.7$, $\Omega_m =
0.25$, $\Omega_b = 0.044$, $\Omega_\Lambda = 0.75$, $n_s = 0.95$, $\sigma_8 = 0.8$. We use $\bar{\rho}_m$ as the present
day mean matter density of the Universe. We provide our predictions and
measurements in units of h. Absolute magnitudes are always given assum-
ing $h = 1$.

2.2   MICE simulation

To investigate the impact of red and satellite fractions on the IA signal, we
need a realistic representation of the galaxy sample that populates a cos-
mic shear survey. Krause et al. (2016) has shown that one of the major
sources of uncertainties in forecasting IA for future cosmic shear surveys
comes from the uncertainty in the luminosity function modelling, which
determines the red/blue fraction of galaxies in the analysis. In this work,

we make use of the MICECATv2.0 [4] simulation (Fosalba et al. 2015b) as a realisation of our Universe and select galaxies based on the typical values of redshift, magnitude and area for a Stage III survey. We use the simulations as our reference cosmic shear survey, for which we can extract all the necessary information.

MICECAT is a public catalogue, now at its second data release, created to reproduce a number of local observational constraints and it is for this reason particularly suitable for our purposes. The mock galaxy catalogue is obtained from an N-body simulation containing 7×10^{10} dark matter particles in a $(3072 h^{-1} \mathrm{Mpc})^3$ comoving volume (Fosalba et al. 2015b) and then populated using a hybrid implementation of Halo Occupation Distribution (HOD) and Sub-Halo Abundance Matching (SHAM) (Crocce et al. 2015; Carretero et al. 2015).

Given the importance of having robust satellite fractions per luminosity and redshift bin and a representative colour distribution for our analysis, we report here the most relevant features adopted in Carretero et al. (2015) to build the galaxy catalogue. The HOD parametrisation employed to populate the haloes is inspired by Zheng et al. (2005), with some modifications that we briefly describe here. The HOD provides the probability $P(N_\mathrm{g}|M_\mathrm{h})$ that a halo of a given mass M_h contains N_g galaxies of a certain type (central, satellite). To assign galaxies to a halo, a sharp mass-threshold is adopted, such that every halo more massive than M_min contains at least one (central) galaxy. The number of satellite galaxies follows a Poisson distribution with mean $\langle N_\mathrm{sat} \rangle = [M_\mathrm{h}/M_1]^\alpha$. The slope of the power law is chosen to be $\alpha = 1$, as constrained by observations (e.g Kravtsov et al. 2004; Zehavi et al. 2011), while the mass threshold for satellite galaxies, M_1, is modelled to be a function of M_min and the halo mass M_h. The parameters of the functions that relate M_1 to M_min are those that best reproduce the observed galaxy clustering as a function of luminosity in the SDSS (Zehavi et al. 2011). Galaxy luminosities are assigned using abundance matching, based on the observed luminosity function from Blanton et al. (2003) and Blanton et al. (2005) for the faint end. Note that by construction, satellite galaxies are forced to be fainter than 1.05 times the luminosity of their central galaxy. Colours are assigned following an approach similar to Skibba & Sheth (2009): the colour-magnitude diagram is parametrised using three Gaussians, corresponding to the red, green and blue population; the mean and standard deviations vary as a function of luminosity. The colour of a galaxy is then drawn from these distributions, taking into account its type

---

[4]MICECAT v2 is publicly available at `https://cosmohub.pic.es/home`

(satellite or central). The colour-assignment process is calibrated to reproduce the clustering as a function of colour and luminosity in the SDSS (Zehavi et al. 2011). In our analysis we combine the green and blue population, isolating the red sequence with a different cut than what is reported in Carretero et al. (2015), as discussed in Section 2.2.1.

The second release of MICE increases the luminosity range by populating halos/groups with a fewer number of particles with respect to the v1, up to haloes composed by only two particles. Although the abundance of these small groups is not representative of the abundance of haloes at the equivalent halo mass, this is then corrected by the abundance matching.

2.2.1 Galaxy mocks

We generate two galaxy mocks: the first one reproduces a generic Stage III survey and is employed as our fiducial cosmic shear-like galaxy distribution. A second mock is constructed for a comparison to the results of J19 and G19 in KiDSxGAMA, and therefore is designed to reproduce the KiDSxGAMA galaxies used in their analysis. We use that mock to understand and interpret our results at small scales, where we use the measurements as input for our cosmic shear analysis. If not specified otherwise, we always refer to the Stage III mock in this work.

We select 58 485 848 galaxies from MICECAT v2, covering an area of $1049 \deg^2$ in a redshift range $0.1 < z < 1.3$. We impose a magnitude cut in the SDSS $r-$band $r < 24$. We split the sample into six redshift bins with $\Delta z = 0.2$, as shown in Fig. 2.1a. We correct the magnitudes to take into account the passive evolution of galaxies, as recommended in the MICE readme.

As discussed in the previous section, MICE is complete down to $M_r - 5\log(h) \sim -14$. With our selection, we are close to this limit (the faintest galaxy in our catalogue has a magnitude of $M_r - 5\log(h) = -13.4$). However, since IA is mainly affected by red galaxies, which are typically brighter than this value, even a small incompleteness should not significantly impact our results.

MICE provides colours in the filters $^{0.1}r$ and $^{0.1}g$. To be consistent with the data-set we aim to compare the mocks to, namely GAMA and the SDSS Main sample used by J19 and G19, which select their galaxies using the $g - r$ colour at $z = 0$, we correct the MICE $g - r$ colour to be at $z = 0$ (F.J. Castander, private communication). We verify that by selecting GAMA-like and SDSS-like mock galaxies from the MICE simulation, imposing the same area coverage, redshift ranges and flux-limit cut, we can reproduce
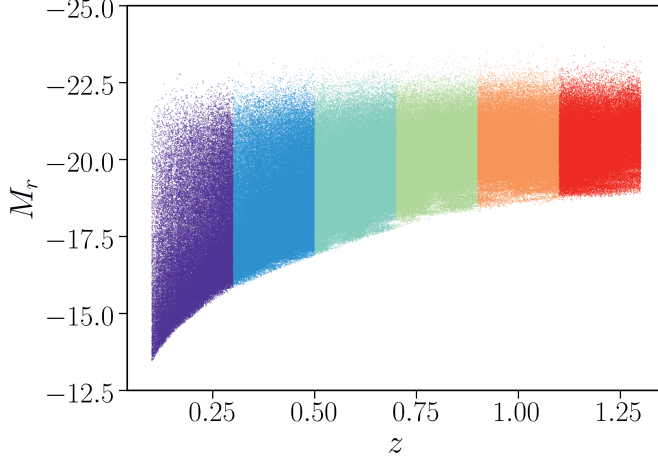
((a))
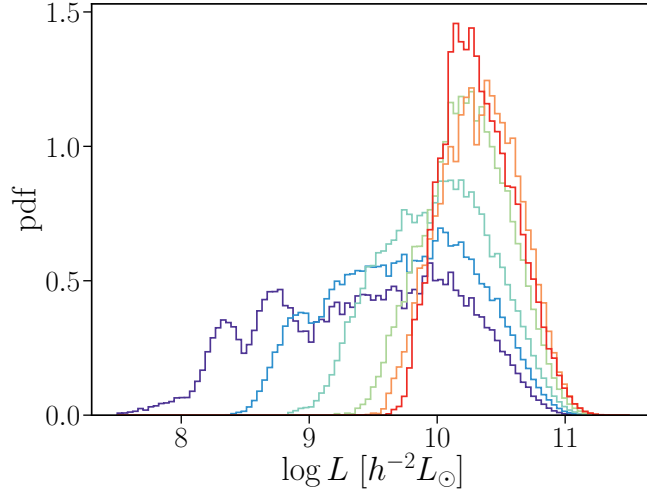
((b))

Figure 2.1: (a): The distribution in redshift and magnitudes of the sample we select from MICE, with the imposed cut in apparent magnitude at $r < 24$. The figure illustrates the samples used in our analysis for the six redshift bins listed in Table 2.1. The plot shows a random selection of 1% of the galaxies in the catalogue. (b): The luminosity distribution of the red central galaxy samples for the six redshift bins, colour coded as in (a).

Table 2.1: Properties of the five tomographic bins used in our analysis: the redshift range of each bin ($z_{\mathrm{min}}, z_{\mathrm{max}}$), the number of galaxies (N_{gal}), the mean luminosity of the red central galaxies in terms of a fiducial luminosity L_0 ($\langle L_{\mathrm{cen}}^{\mathrm{red}}\rangle/L_0$), the fraction of satellites in the given bin (f_{sat}) and the fraction of red galaxies (f_{red}), selected as shown in figure 2.2. The fiducial luminosity L_0 is chosen to be the luminosity corresponding to $M_r = -22$.

Bin	z_{min}	z_{max}	N_{gal}	$\langle L_{\mathrm{cen}}^{\mathrm{red}}\rangle/L_0$	f_{sat}	f^{red}	$f_{\mathrm{sat}}^{\mathrm{red}}$	$f_{\mathrm{sat}}^{\mathrm{blue}}$
1	0.10	0.30	7 633 382	0.17	0.41	0.15	0.10	0.31
2	0.30	0.50	12 445 504	0.24	0.37	0.22	0.14	0.23
3	0.50	0.70	12 453 204	0.33	0.33	0.27	0.16	0.17
4	0.70	0.90	9 863 462	0.48	0.28	0.28	0.15	0.13
5	0.90	1.10	8 003 975	0.58	0.23	0.25	0.12	0.11
6	1.10	1.30	8 086 321	0.55	0.22	0.26	0.13	0.09

the redshift and magnitude distribution of the samples, the colour-magnitude diagram and the relative galaxy fractions (Appendix A1). We therefore conclude that MICE galaxies provide a realistic mock for our analysis.

To select red galaxies we apply a cut at $g - r > 0.61 - 0.0125(M_r + 19)$, as shown in Fig. 2.2. The cut qualitatively reproduces the choice in J19. Table 2.1 summarises the characteristics of our cosmic shear-like galaxy sample in each redshift bin. Due to the flux limit imposed on our sample, the fraction of satellite galaxies drops from low to high redshifts. The red fraction increases for the first three bins, since the faint population is dominated by blue satellites, while it decreases for the last two bins, due to the overall increase of blue galaxies at higher redshifts.

2.3   The impact of satellites at large scales

Intrinsic galaxy alignment generates two types of 2-point statistic observables that are relevant in the context of cosmic shear contamination: the correlation between the shapes of two galaxies (II, where 'I' stands for Intrinsic) and the correlation between the gravitational shear induced by the lensing effect of a matter inhomogeneity and the intrinsic shape distorted by the same gravitational source (GI, where 'G' stands for Gravitation). The final observable is then given by the sum of the cosmic shear power spectrum (GG), which is the one of interest for cosmological studies, and the IA contributions, II and GI.
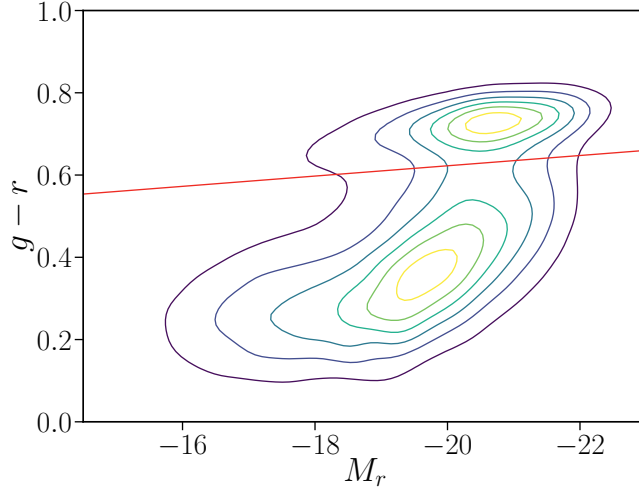
Figure 2.2: The colour-magnitude distribution of the sample. The red line shows the cut at $g - r > 0.61 - 0.0125(M_r + 19)$ we employ to isolate the red sequence.

2.3.1   The linear alignment model

It is well established that at large scales elliptical galaxies can be modelled through the linear alignment model (Catelan et al. 2001; Hirata & Seljak 2004), which predicts the shape distortion of a galaxy to be proportional to the strength of the tidal field at the moment of its formation. In Fourier space, the matter-intrinsic and the intrinsic-intrinsic power spectra can thus be written as

$$P_{\delta\mathrm{I}}^{\mathrm{LA}}(k, z) = -A_{\mathrm{IA}} C_1 \rho_c \frac{\Omega_m}{D(z)} P_\delta^{\mathrm{lin}} \,, \tag{2.1}$$

$$P_{\mathrm{II}}^{\mathrm{LA}}(k, z) = \left(A_{\mathrm{IA}} C_1 \rho_c \frac{\Omega_m}{D(z)} \right)^2 P_\delta^{\mathrm{lin}} \,, \tag{2.2}$$

where C_1 is a normalisation constant, ρ_c the critical density of the Universe today, $D(z)$ the linear growth factor, normalised to unity at $z = 0$, and P_δ^{lin} the linear matter power spectrum. We set $C_1 = 5 \times 10^{-14} M_\odot^{-1} h^{-2} \mathrm{Mpc}^3$ based on the IA amplitude measured at low redshifts using SuperCOSMOS (Brown et al. 2002). The free amplitude A_{IA} captures any variation with respect to this reference power spectrum. The SuperCOSMOS norm is a common choice in the literature, making the interpretation of our results and any comparison easier.

A successful modification of this theory replaces the linear matter power spectrum with the non-linear one (Bridle & King 2007), so named non-linear linear alignment (NLA). The reason behind the use of the non-linear power spectrum is to partially capture the nonlinear tidal field and it has been shown to fit the measurements better (for example, Blazek et al. 2011; Joachimi et al. 2011; Singh et al. 2015; Johnston et al. 2019). Although more sophisticated treatments of the non-linear scales have been developed in recent years (Tonegawa et al. 2018; Blazek et al. 2019; Vlah et al. 2020), and Samuroff et al. (2019) have found hints for quadratic alignments in measurements from the Dark Energy Survey (DES), a proper combination of perturbative approaches with the halo model is beyond the scope of this paper. To capture the IA signal at intermediate scales, we therefore use the NLA model (see also Appendix A2 for a discussion on the halo exclusion problem in this context).

2.3.2 From observations to models: how satellite galaxies complicate the picture

As direct measurements of the correlation between the density field and the shear field (δI) are not possible, IA studies typically focus on the correlation between the position of a galaxy and the shape of another one, the so called gI term (where 'g' stands for galaxy). At large scales, the galaxy position - shear and the matter - shear power spectra are related by the large scale bias, galaxies being tracers of the underlying matter distribution. For central galaxies, the relation between gI and δI is simply given by the linear galaxy bias, such that $P_{\mathrm{gI}}(k) = b_g \, P_{\delta\mathrm{I}}$

A complication arises when interpreting the gI term in the presence of satellite galaxies. Satellites tend to preferentially lie along the major axis of the central galaxy (Huang et al. 2016, J19, G19), which in turn is a proxy for the halo major axis. This anisotropic distribution of satellite positions boosts the satellite position - central shape (sc) correlation not only at small scales, but also in the two-halo regime, i.e. when correlating the shape of a central galaxy with the position of a satellite that belongs to a different halo.

In the context of contamination to lensing, however, such a boost is not expected to have the same importance. Since cosmic shear analyses only correlate shapes, the spatial segregation of satellites is not sufficient to induce a GI signal (where GI is the projected matter - shear power spectrum, i.e. the one that directly contaminate lensing), as satellites need to be coherently oriented to produce a shape correlation (for a discussion on this

in simulations, see for example Chisari et al. 2015b).

The impact of the anisotropic distribution of satellites has been explored in simulations by Samuroff et al. (2020b), who found a significant enhancement of the signal at small scales and a constant, redshift independent shift at large scales. They found that for an LSST-like (Stage-IV) survey, in the 'pessimistic' case (see their section 5.2), this can lead to a shift in the best constrained parameters $\Delta S_8 = 1.4\sigma$, $\Delta w = 1.5\sigma$. The recent results from G19, however, show that at large scales satellite galaxies are randomly oriented with respect to the brightest galaxy in the group, which can be considered as a proxy for the central galaxy, while within the halo their radial alignment is limited to the innermost galaxies. J19 also found a similar trend when looking at the projected satellite position - shape correlation and central position - shape correlation (their Fig. 7, right panels), suggesting satellites to only coherently orient their shapes in the intra halo regime. Using the same estimator as G19, $\langle \epsilon_+ \rangle$, Sifón et al. (2015) found a radial alignment consistent with zero in clusters. Although every detection depends on the choice of the shape measurement algorithm employed, those results suggest that at large scales satellite alignment is a minor contributor compared to the central galaxy alignment. At small scales the picture might be significantly different: we refer the reader to Section 2.4 for a discussion on the contribution of satellites at small scales.

While the relative positions of satellites within the halo have a strong impact on the gI correlation, from the argument above, they are not expected to be important in the correlation between the lensed background galaxies and the intrinsically aligned galaxies in the foreground. In this regard, the anisotropic distribution of satellites within the halo complicates the translation of gI measurements to GI, so care has to be taken when adopting informative priors for IA that come from gI measurements. An analysis of this contamination is outside the scope of this paper, and we leave a full modelling of the gI term that can disentangle the two contributions to a forthcoming paper. Given the argument above, we assume that at first order satellites do not contribute to the IA signal at large scales.

2.3.3   A weighted linear alignment model

We have seen in the previous section that, for the sake of accounting for IA contamination in cosmic shear analyses, the role played by satellites is small at large scales. In this sense, central galaxies provide a more consistent picture as they follow the linear alignment mechanism, while the contribution of satellites is mainly to add noise to the measurements. In

this context, we can assume that the majority of the contamination comes from the alignment of red central galaxies, while blue central galaxies are expected to add a minor although still very uncertain contribution.

Motivated by the need of priors for our signals, we decide here to use the NLA model for both red and blue galaxies. In this way, we can directly link our predictions to observational constraints, for which the NLA model has been used to fit the signal (J19). In principle, if the linear alignment mechanism is truly responsible for the alignment of blue galaxies, a cross term between red and blue galaxies should arise. However, theory suggests that blue galaxies gain their alignment from a torquing mechanism that aligns their spins (Catelan et al. 2001; Crittenden et al. 2001), also known as the Quadratic Alignment Model (Hirata & Seljak 2004). The lack of observational constraints leaves the question of the driving mechanism of blue galaxy alignment open. Our use of the NLA model for blue galaxies should thus be considered as an effective description. We omit the cross term, and consider this approximate treatment sufficient for the scope of the paper, but note that future studies might need to revisit this assumption. The large scale power spectra thus read:

$$P_{\delta I}^{2h}(k, z) = f_{\text{cen}}^{\text{red}} P_{\delta I, cc}^{2h, \text{red}}(k, z) + f_{\text{cen}}^{\text{blue}} P_{\delta I, cc}^{2h, \text{blue}}(k, z) \,, \qquad (2.3)$$

$$P_{\text{II}}^{2h}(k, z) = (f_{\text{cen}}^{\text{red}})^2 P_{\text{II}, cc}^{2h, \text{red}}(k, z) + (f_{\text{cen}}^{\text{blue}})^2 P_{\text{II}, cc}^{2h, \text{blue}}(k, z) \,, \qquad (2.4)$$

where we have introduced the superscript $2h$ to indicate that these power spectra describe the alignment in the two-halo regime, i.e. for galaxies that do not belong to the same halo (large scale alignment). Similarly, the subscript cc indicates that the correlation only involves central galaxies. $f_{\text{cen}}^{\text{red/blue}}$ is the fraction of red/blue central galaxies in the sample, and we have $f^{\text{blue}} = 1 - f^{\text{red}}$, $f_{\text{cen}}^{\text{red}} + f_{\text{cen}}^{\text{blue}} = f_{\text{cen}}$ of the entire sample. Note that these rescalings are necessary when converting between any two samples with different characteristics.

Figure 2.3 shows the competing effect of blue and satellite galaxies in suppressing the signal at high and low redshift respectively. Assuming a constant IA signal with amplitude $A = 1$, it illustrates how the change of the red and the satellite fractions across the tomographic bins can affect the IA amplitude at large scales. The purple solid line shows the total amplitude (equation 2.3): the evolution of the fraction of red central galaxies induces a sample-dependent redshift evolution of the *measured* IA signal. Weighting the signal by the (red) central galaxies only significantly reduces the amplitude of the predicted IA.
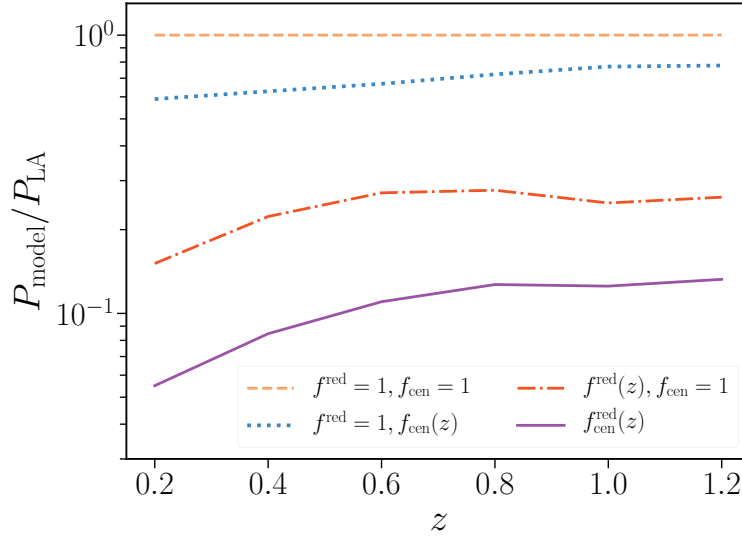
Figure 2.3: An illustration of the redshift dependence of the IA power spectrum at large scales (2-halo regime) due to the change of the fraction of red and satellite galaxies over the z-bins for our simulated cosmic shear survey. We plot the ratio of a 'weighted' GI power spectrum and the standard LA one. We assume a constant signal with amplitude $A = 1$ (gold dashed line); incorporating the satellite fraction decreases the overall amplitude; at high redshift the fraction of satellites drops (see table 2.1), with a consequent increase of the signal (blue dotted line). At high redshift blue galaxies become important, suppressing the signal (red dot-dashed line). In this toy model, only red central galaxies are expected to contribute to the total signal (purple solid line).

2.3.4   Luminosity dependence of the IA signal

A luminosity dependence of the IA signal has been explored in the context of the large scale alignment of elliptical galaxies in a number of works (Hirata et al. 2007; Joachimi et al. 2011; Singh et al. 2015, J19). A common approach to model this is to follow the parametrisation in Joachimi et al. (2011):

$$A_{\mathrm{IA}} \mapsto A_\beta \left(\frac{L}{L_0} \right)^\beta \qquad (2.5)$$

where L_0 is a pivot luminosity, assumed to correspond to $M_r = -22$.

The value of β is, however, being debated: while Joachimi et al. (2011) in the MegaZ-LRG + SDSS LRG + L4 + L3 samples - hereafter simply MegaZ - and Singh et al. (2015) in LOWZ find similar values ($A_{\mathrm{MegaZ}} = 5.76^{+0.60}_{-0.62}$ $\beta_{\mathrm{MegaZ}} = 1.13^{+0.25}_{-0.27}$; $A_{\mathrm{LOWZ}} = 4.5^{+0.6}_{-0.6}$, $\beta_{\mathrm{LOWZ}} = 1.27^{+0.27}_{-0.27}$), J19, fitting to red galaxy alignments in the GAMA + SDSS Main samples, find $A_{\mathrm{G+S}} = 3.17^{+0.55}_{-0.54}$ and $\beta = 0.09^{+0.32}_{-0.33}$5. As pointed out by J19, the galaxies employed in their study contain a larger fraction of satellites compared to the MegaZ and LOWZ samples; the way this can impact the luminosity dependence is, however, non-trivial.

Since cosmic shear surveys span a range in luminosity much broader than what is used in those analyses, the impact of a luminosity dependence can be important in modulating the signal over the redshift bins. Different values of β can lead to a significantly different contamination of lensing measurements (Chisari et al. 2015a). To illustrate this, we consider the case of a population of red central galaxies with an input amplitude of $A_\beta \sim 5$, and vary the value of β (Fig. 2.4). The typical luminosity of the different redshift tomographic bins causes a redshift dependence in the signal. We also note that the typical luminosity of the red central sample per z-bin in our mock survey is always below the pivot luminosity of $M_r = -22$ (Table 2.1), such that the effect of the luminosity dependence is to reduce the effective IA amplitude. To evaluate the average luminosity scaling $\langle (L/L_0)^\beta \rangle$ for our comic shear-like sample, we integrate over the pdf shown in Fig. 2.1b.

Since the impact of an evolving signal would not be captured by a fixed IA amplitude, as often done in weak lensing analyses, it is important to understand whether a luminosity dependence exists in the data. A way

---

[5]Mismatched definitions of the pivot luminosity L_0, between SDSS Main and GAMA, prompted us to recompute MCMC chains for the A_β, β constraints, such that they differ slightly from those reported in J19 – the updated constraints are consistent in all cases and conclusions from that work remain unchanged.
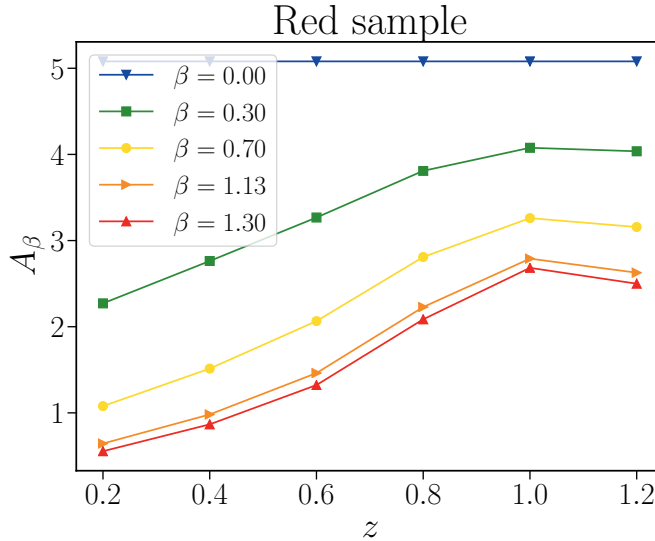
Figure 2.4: The IA signal for different values of the slope of the power law β. The observed $z-$dependence of the signal is only caused by the different galaxy samples that populate the redshift bins. Here, we only consider the luminosity of the red central population in our simulation.

around is to introduce a $z-$dependence in the alignment model, which can effectively capture the alignment variation across the $z-$tomographic bins. We do not include any *intrinsic* redshift evolution in our IA model as, currently, there are only weak constraints on it (Joachimi et al. 2011; Samuroff et al. 2019) but we consider its effectiveness in capturing the sample-induced redshift dependence in Sect. 5.6.

We point out that since the luminosity dependence has only been observed in the context of red galaxy alignment, in the rest of this section we limit the discussion to the red population only.

The case of GAMA galaxies

The GAMA survey is a highly complete spectroscopic survey (>98 per cent in the r-band down to $r = 19.8$), which overlaps with ~ 180 deg^2 of KiDS data. The KiDS data provide high-quality galaxy images, from which Georgiou et al. (2019a) has measured the shapes with the DEIMOS (DEconvolution In MOments Space) shape algorithm (Melchior et al. 2011). This shape catalogue is employed in J19 and G19 for IA studies.
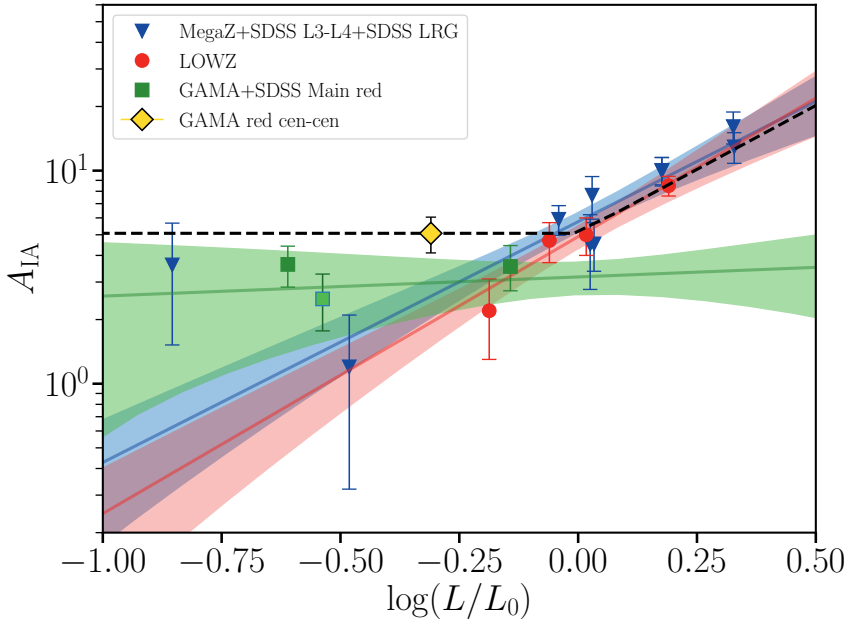
Figure 2.5: Overview of different estimates of the IA amplitude as a function luminosity. The best-fit relation from Joachimi et al. (2011) (blue line) for the MegaZ, SDSS L3 and L4 and SDSS LRG samples (blue downward facing triangles); Singh et al. (2015) best-fit (red line) on LOWZ (red circles) and the revised best-fit to GAMA+SDSS Main from J19 reported in the text (green line). The three individual samples used by J19 are shown as green squares (GAMA) and limegreen (SDSS Main sample). The yellow diamond indicates our best fit amplitude for the GAMA red central galaxies.

J19's fit of β is obtained using three samples of red galaxies: the SDSS Main, and two samples from the GAMA, cut at $z = 0.26$ in two equally populated redshift bins, Z1 and Z2. The individual fits to these samples are shown in Fig. 2.5. In this section, we explore whether the discrepancy on the value of β can be due to the presence of satellites in their samples. We focus on the GAMA samples only, for which we can obtain an estimate of the fraction of satellites through the GAMA Group Catalogue[6].

GAMA ($h = 0.7$) data-points from J19 must be shifted in the $\log(L/L_0)$ axis by a factor h^{-2} in order to align conventions for the pivot luminosity L_0 with SDSS ($h = 1$); a re-analysis of the J19 luminosity dependence, with L_0 convention homogenised for all of their samples, does not significantly change the slope of their best-fit relation[7]. Here, we follow the $h = 1$ convention, such that all the ratios reported are assuming $L_0 = 4.69 \times 10^{10} L_\odot h^{-2}$. Interestingly, this means that the measurements from J19 cover a region of the parameter space different from Joachimi et al. (2011) and Singh et al. (2015).

As mentioned in Section 2.3, satellite galaxies tend to randomly orient their shapes at large scales, not contributing to a alignment signal. At the same time, they preferentially lie along the major axis of their central galaxy, contributing to the satellite position - central shape correlation. In a halo model fashion, we can think of any possible contribution to sum up linearly (i.e. central position - central shape, central position - satellite shape, satellite position - central shape, satellite position - satellite shape), weighted by the fraction of galaxies that contribute to each term, together yielding the final signal that we measure.

The individual fits to the alignment signals of the Z1 and Z2 samples in J19 show roughly a similar amplitude ($A_{Z1} = 3.63^{+0.79}_{-0.79}$, $A_{Z2} = 3.55^{+0.90}_{-0.82}$) corresponding to galaxies of different luminosity ($\langle L/L_0 \rangle_{Z1} = 0.25$, $\langle L/L_0 \rangle_{Z2} = 0.72$), compatible with their finding of no luminosity dependence. However, at low redshift the fraction of satellite galaxies in their red population is roughly 0.36, which decreases to $f_{\mathrm{sat}} \sim 0.27$ in the second redshift bin.

We have seen in Sect. 2.3.2 that the net effect of satellites is to lower the measured amplitude. To get a sense of how this might affect our data points, we up-weight the signal by the fraction f_{sat} in each given bin: this increases the signal, which maintains the same flat relation, without sig-

---

[6]`http://www.gama-survey.org`

[7]We also note that the fiducial σ_8 in J19 was misquoted as 0.8, and should in fact be 0.73. Their IA model constraints are unaffected, though their best-fit galaxy biases should be rescaled by $0.73/0.8 \sim 0.91$ to compare with a $\sigma_8 = 0.8$ cosmology.

nificant tilts. We note that this up-weighting procedure is not quite correct and therefore should not be considered as the underlying *true* shape signal, because the gI correlation contains two terms that suppress the amplitude (i.e. those for which the satellites act as shape tracers) and two where they contribute positively to the final amplitude (the central-central correlation and the satellite position - central shape correlation). Our re-weighting does not consider the positive contribution of the satellite position - central shape correlation and thus overestimates the suppression induced by the satellites. Nevertheless, it gives us a sense of the overall shift and can be considered as an upper-limit to the expected central-only alignment amplitude.

To further explore the role played by the satellites, we measure the IA amplitude of the red central sample only in GAMA (cc correlation). The mean luminosity of this sample is $\langle L/L_0 \rangle = 0.46$, for which we find a best fit amplitude $A_{\mathrm{GAMA},cc} = 5.08^{+0.97}_{-0.95}$, with a reduced $\chi^2 = 2.0$ ($N_{\mathrm{dof}} = 4$).

This measurement does not agree with the curve predicted by MegaZ and LOWZ, which would correspond to $2.40^{+0.59}_{-0.47}$ at that given luminosity (assuming MegaZ best-fit parameters), as illustrated in Fig. 2.5. Our new measurement is displayed as a yellow diamond, while the predicted best fit luminosity dependent IA amplitude measured by MegaZ and LOWZ are shown as blue and red curves, respectively. Note that the MegaZ best fit curve also includes a z–dependent power law that was poorly constrained in that work. We do not include it here, as recent studies have not found evidence for an intrinsic z-dependence of alignment strength, so the curve reported in Fig. 2.5 is only the luminosity dependent part of their fit.

A central-only luminosity dependent signal

The complexity of the arising picture does not allow for a direct interpretation of the role of satellites in the context of the luminosity dependence, but we can at least identify two main scenarios.

1. Central galaxies follow a single power law as observed in Joachimi et al. (2011) and Singh et al. (2015) on MegaZ and LOWZ galaxies. The lack of such luminosity dependence detection in J19 can be accounted by the non-negligible presence of satellites in their sample. The fact the measurement of the central-central galaxy alignment from GAMA does not coincide with the MegaZ/LOWZ predictions can point towards a shallower relation than what was measured by those samples. This can be a consequence of satellites also contaminating the

MegaZ and LOWZ samples.

2. Bright central galaxies follow the luminosity dependence in Joachimi et al. (2011) and Singh et al. (2015), while faint galaxies are characterised by a different slope, in a double power law scenario. Given the current measurements in this part of the parameter space, the most extreme case is a flat luminosity dependence for $L < L_0$ ($\beta_{L<L_0} = 0$).

In all of these cases, we are restricting the IA luminosity dependence at large scales to central galaxies, a choice that finds a natural theoretical frame in the context of the linear alignment mechanism, where the intrinsic shear power spectrum can be expressed as a power of the mass of the hosting halo (Piras et al. 2018). This can in turn be related to the luminosity of its central galaxy. In the rest of the paper, we assume that in the 2-halo regime, the luminosity dependence is only caused by the central galaxy population and that the bright-end of such relation is well described by the best-fit values from MegaZ and LOWZ analyses. At the faint-end, we allow for both scenarios described above: our case (i) corresponds to the luminosity dependence from MegaZ and LOWZ, such that the luminosity dependence is described by a single power law,

$$P_{\delta\mathrm{I}}^{\mathrm{red}}(k,z,L) = f_{\mathrm{cen}}^{\mathrm{red}} P_{\delta\mathrm{I}}(k,z) \left\langle \left(\frac{L_{\mathrm{cen}}^{\mathrm{red}}}{L_0} \right)^{\beta} \right\rangle \qquad (2.6)$$

and

$$P_{\mathrm{II}}^{\mathrm{red}}(k,z,L) = (f_{\mathrm{cen}}^{\mathrm{red}})^2 P_{\mathrm{II}}(k,z) \left\langle \left(\frac{L_{\mathrm{cen}}^{\mathrm{red}}}{L_0} \right)^{\beta} \right\rangle^2 , \qquad (2.7)$$

while in our case (ii) we consider a broken power law that passes through the best fitting amplitude of the central-central correlation, flat for $L < L_0$ and then assuming the form of a power law with index $\beta = 1.2$ for $L > L_0$. This is shown with a black dashed line in Fig, 2.5. Any intermediate slope of the luminosity dependence of faint galaxies would be in between these two cases, and thus we can have an estimate of the range of impact of this term in the lensing contamination from IA.

Although the alignment of central galaxies with luminosities $L \geqslant L_0$ seems to be captured better by the LOWZ/MegaZ best fit curve, we caution that LOWZ and MegaZ are not pure central galaxy samples (for example, LOWZ has roughly a fraction 11% of satellites, see Singh et al. (2015), Sect. 3.3), which also contaminates the results, particularly at the faint end

of the curve. At low luminosities, the contribution of satellite galaxies to the final signal is more important, as satellites are predominantly faint. This implies that as we move from left to right in Fig. 2.5, we observe a simultaneous increase of the IA signal due to the increase of the galaxy luminosity and a depletion of the satellite suppressing contribution. If we assume that MegaZ and LOWZ measurements also suffer from the presence of satellites in their low luminosity bins, the net effect would be a lower value of β, and thus a less steep relation.

This scenario remains possible as we lack a proper normalisation for this term. As bright galaxies are in general not abundant and at high luminosities the sample is not significantly contaminated by satellites, this scenario is only relevant in the intermediate luminosities around L_0. Below L_0 this falls between the two cases we are considering. Future IA studies that aim to constrain the IA signal using observations and simulations should focus on the impact of satellites on the value of β, as galaxies at $L/L_0 \sim 1$ are already expected to have $\geqslant 10\%$ of satellites (based on $f_{\mathrm{sat}}(L)$ in our GAMA sample).

2.3.5   Colour dependence

A key aspect of our approach is that we weight the alignment signal by the fraction of galaxies that contributes to that specific amplitude. We have seen that the IA alignment is strongly morphology dependent: this implies that the weighting by the red fraction plays a significant role in the prediction of the final signal. The different measurements compared in the previous section have been measured on samples selected with different red cuts. However, Singh et al. (2015) has explored the dependence of the IA signal on colour, finding no evidence for a colour-dependence in the data. Since J19 provide IA amplitudes for both the red and blue samples, and we have shown that their measurements agree with the results in MegaZ and LOWZ once restricting the analysis to the central sample only, we adopt J19 amplitude for the blue population and consistently apply a red cut similar to the one in their work (see Sect. 2.2.1).

2.4   The impact of satellites at small scales

To model the impact of satellite alignment at small scales, we revisit the halo model formalism by SB10 to take into account new observational results. The spherical halo approximation should capture most of the small-
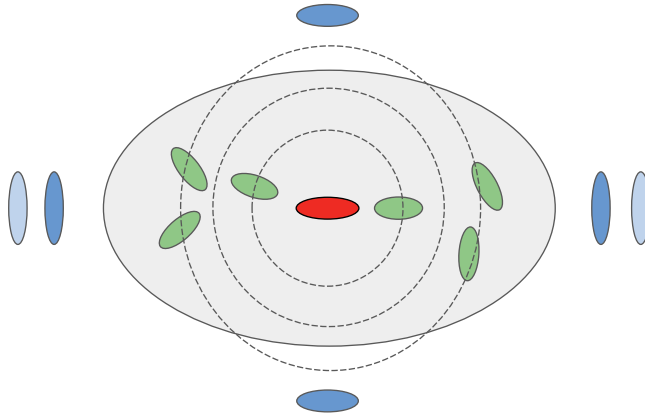
Figure 2.6: A cartoon showing the current picture of satellite alignment provided by observations. Satellite galaxies (green ellipses) tend to preferentially segregate along the direction of the central galaxy (red ellipse) major axis; the closest satellites to the centre of the halo show a preferential alignment in the direction of the central galaxy major axis. The source galaxies (blue ellipses) are tangentially aligned with respect to the halo shape, resulting in an opposite alignment with respect to the aligned satellites and the central galaxy. We can expect source galaxies to be lensed more along the halo major axis, due to the excess of matter in that direction. The dotted circles illustrate the way a spherical halo model can describe this alignment signal.

scale GI signal. As discussed in Sect. 2.3, the anisotropic distribution of satellites boosts the signal of the gI correlation, so a spherical model would underestimate w_{g+}. How it propagates exactly in the context of the GI contamination is not trivial. The satellite segregation along the central galaxy major axis is expected to source a large 1-halo satellite position - satellite shear correlation, confirmed in J19, but also of an opposite satellite-satellite II term, for which we do not have any observational measurement. Moreover, if only the innermost satellites are aligned in the direction of the central galaxy, as observed in G19, the impact on GI should be significantly reduced compared to gI. For an illustration of these terms, see the cartoon in Fig. 2.6. Although further study is needed, we use the spherical halo model formalism because we expect it to capture the leading contribution, providing a fair sense of the amplitude of the satellite alignment.

2.4.1   The halo model formalism for satellite alignment

Following SB10 we adopt an effective radial satellite alignment and describe galaxy orientations inside the halo through the stick approximation.

In this approximation, the two minor axes of the elliptical galaxy have equal lengths on average and the length and the orientation of the stick correspond to those of the galaxy major axis.

Defining a Cartesian reference system centred on the halo and with the $z-$axis along the line of sight, the position of a satellite galaxy inside the halo is identified by the vector $\mathbf{r} = (r, \theta, \phi)$. The orientation of the satellite major axis can then be expressed through the unit vector

$$\hat{e} = (\sin \theta_e \cos \phi_e, \sin \theta_e \sin \phi_e, \cos \phi_e), \qquad (2.8)$$

where θ_e and ϕ_e are, respectively, the polar and azimuthal angles that the satellite major axis forms with the radial vector $\mathbf{r}$.

In principle, we expect satellite galaxies to follow a distribution of angles between their major axes $\hat{e}$ and the radial vector $\mathbf{r}$. However, SB10 showed that the main effect of including this term is simply to reduce the amplitude of the correlation functions with respect to the case of perfect radial alignment, independently of the halo mass. Thus, we can simply consider the case of perfect radial alignment, absorbing any misalignment into the amplitude of the intrinsic alignment signal. In this case, $\theta_e = \theta$ and $\phi_e = \phi$. In a sense, the perfect radial alignment configuration can be considered as an effective description: we can only measure the tendency of galaxies to point in a certain direction, so the length of the sticks – which determines the amplitude of the signal – quantifies the combination of the amplitude of the misalignment angle and the intrinsic ellipticity of the galaxy. This provides a direct map between the formalism of the stick model and the measured alignment $|\epsilon|\langle\cos(2\phi)\rangle$, where $|\epsilon|$ is the modulus of the ellipticity and ϕ is the misalignment angle.

Calling $\bar{\gamma}$ the length of the stick, and assuming the alignment to be a function of the distance to the halo centre and the mass of the halo, it follows that (SB10)

$$\gamma^I (\mathbf{r}, M, c) = \bar{\gamma}(r, M, c) \sin \theta e^{i2\phi}. \qquad (2.9)$$

Here, $\bar{\gamma}(r, M) \sin \theta$ is the observed length of the stick, corresponding to the projection of the major axis along the line of sight. In principle, this quantity can also depend on the halo concentration, but we assume a deterministic relation between mass and concentration (see also Sect. 2.5) and so we omit such dependence in the following.

Since we only measure the IA signal at galaxy locations, it is necessary to introduce a density weighting in the model (Hirata & Seljak 2004), $\tilde{\gamma}^I = \gamma^I (1 + \delta_g)$. Following SB10, we weight the 3D projected ellipticity by the

number of galaxies inside the halo, N_g and the normalised matter density profile $u(\mathbf{r}|M) = \rho(r|M)/M$:

$$\tilde{\gamma}^I_{1-\mathrm{halo}}(\mathbf{r}, M) = \bar{\gamma}(r, M) \sin \theta^{2i\phi} N_g u(\mathbf{r}|M), \qquad (2.10)$$

where we identify the density-weighted shear with a tilde (Hirata & Seljak 2004, SB10).

Having defined the density-weighted ellipticity $\tilde{\gamma}^I$ for a given halo, we can construct a continuous intrinsic ellipticity field by summing up the contributions from each individual halo i, in the usual halo model fashion:

$$\tilde{\gamma}^I_s(\mathbf{r}) = \frac{1}{\bar{n}_g} \sum_i \gamma^I(\mathbf{r} - \mathbf{r_i}, M_i) N_{g,i} u(\mathbf{r} - \mathbf{r_i}, M_i)$$

$$= \sum_i \int \mathrm{d}M \int \mathrm{d}^3 r' \, \delta_D(M - M_i) \delta^{(3)}_D(\mathbf{r} - \mathbf{r_i}) \frac{N_{g,i}}{\bar{n}_g}$$

$$\times \gamma^I(\mathbf{r} - \mathbf{r}', M) u(\mathbf{r} - \mathbf{r}', M) \,,$$

where $\bar{n}_g$ is the galaxy number density per unit of volume, which is a function of redshift. The subscript s indicates that this density weighted shear only refers to satellites.

We calculate the correlation functions of interest for IA by correlating $\tilde{\gamma}^I_s(\mathbf{r})$ with itself and with the matter density contrast δ_m. In Fourier space, the E and B modes of the IA are defined as

$$\tilde{\gamma}^I_E(\mathbf{k}) = \cos(2\phi_k)\tilde{\gamma}^I_1(\mathbf{k}) + \sin(2\phi_k)\tilde{\gamma}^I_2(\mathbf{k}) \qquad (2.11)$$

$$\tilde{\gamma}^I_B(\mathbf{k}) = \sin(2\phi_k)\tilde{\gamma}^I_1(\mathbf{k}) - \cos(2\phi_k)\tilde{\gamma}^I_2(\mathbf{k}) \,, \qquad (2.12)$$

where

$$\tilde{\gamma}^I(\mathbf{k}, M) \equiv \int \mathrm{d}^3 \mathbf{r} \, \tilde{\gamma}^I_j(\mathbf{r}, M)^{i\mathbf{k}\cdot\mathbf{r}}. \qquad (2.13)$$

is the Fourier transform of the complex density-weighted shear, with $j = 1, 2$ being the two components. Thus,

$$\langle \tilde{\gamma}^{I*}_E(\mathbf{k}, z)\tilde{\gamma}^I_E(\mathbf{k}', z)\rangle = (2\pi)^3 \delta^{(3)}_D(\mathbf{k} - \mathbf{k}') P^{EE}_{\tilde{\gamma}^I}(\mathbf{k}, z) \qquad (2.14)$$

and

$$\langle \delta^*(\mathbf{k}, z)\tilde{\gamma}^I_E(\mathbf{k}', z)\rangle = (2\pi)^3 \delta^{(3)}_D(\mathbf{k} - \mathbf{k}') P_{\delta, \tilde{\gamma}^I}(\mathbf{k}, z) \qquad (2.15)$$

Without loss of generality, we can rotate our reference system such that $\gamma^I_1 = \gamma^I_+$, where γ^I_+ is the tangential component of the shear. This corresponds to fixing $\phi_k = 0$ in equations 2.11 and 2.12, transforming EE into II.

For computational reasons, it is convenient to separate the radially dependent part of the density-weighted shear, which is affected by the Fourier transform, from the terms that are only mass dependent. We then define:

$$\hat{\gamma}_s^I(\mathbf{k}, M) \equiv \mathcal{F}\left(\gamma^I(\mathbf{r}, M)\, u(\mathbf{r}, M)\right). \tag{2.16}$$

We now have the ingredients to compute all of the possible IA power spectra. In a spherical halo model, the only terms that survive are: the II satellite-satellite power spectrum and the satellite-matter term for the δI power spectrum. These can be written as

$$P_{\delta\mathrm{I},1\mathrm{h}}^s(\mathbf{k}, z) = \int \mathrm{d}M\, n(M) \frac{M}{\bar{\rho}_m} f_s(z) \frac{\langle N_s|M\rangle}{\bar{n}_s(z)} |\hat{\gamma}_s^I(\mathbf{k}|M)| u(k, M) \tag{2.17}$$

and

$$P_{\mathrm{II},1\mathrm{h}}^{ss}(\mathbf{k}, z) = \int \mathrm{d}M\, n(M) f_s^2(z) \frac{\langle N_s(N_s-1)|M\rangle}{\bar{n}_s^2(z)} |\hat{\gamma}_s^I(\mathbf{k}|M)|^2 \tag{2.18}$$

where $n(M)$ is the halo mass function, $f_s(z)$ is the fraction of satellite galaxies as a function of redshift and $\langle N_s|M\rangle$ is the halo occupation distribution of satellite galaxies.

The power spectra in equations 2.14-2.15 are functions of (k, θ_k). However, θ_k only modulates the strength of the amplitude of the signal. In the rest of the paper, we decide to fix $\theta_k = \pi/2$ (Limber approximation; for a more detailed discussion of the angular dependence of the power spectra, see Appendix A3).

2.4.2 Radial dependent satellite alignment

We use the mean radial alignment signal $\langle \epsilon_+ \rangle$ measured in G19 to model the satellite alignment in Eq. 2.10, $\bar{\gamma}(\mathbf{r}, M)$. They measured a satellite alignment in bins of projected distance of the satellite from the group's brightest galaxy, r_{sat}/r_{200} and found a radially dependent signal. It is well-fitted by a power law of the form $\langle \epsilon_+ \rangle = A(r_{\mathrm{sat}}/r_{200})^b$. The slope is chosen to be fixed at $b = -2$ and the amplitude is fit for the different galaxy samples. G19 do not detect any mass dependence, so we do not include it in our parametrisation.

The estimator $\langle \epsilon_+ \rangle$ is related to the shear via

$$\gamma_+ = \frac{\langle \epsilon_+ \rangle}{\mathcal{R}}, \tag{2.19}$$

where $\mathcal{R}$ is the shear responsivity and quantifies the response of the ellipticity to a small shear[8]. Rounded object are easier to shear than highly elliptical objects. Here, we assume a typical value of $\mathcal{R} \approx 1 - \sigma_\epsilon^2 = 0.91$ to convert ϵ_+ to γ^I.

In order to prevent unphysiscal behaviour at very small scales, we adopt a piecewise function of the form

$$\bar{\gamma}(r) = \begin{cases} a_{1h}\left(\frac{0.06}{r_{\mathrm{vir}}}\right)^b, & \text{if } r < 0.06 \text{ Mpc}/h \\ a_{1h}\left(\frac{r}{r_{\mathrm{vir}}}\right)^b, & \text{if } r > 0.06 \text{ Mpc}/h , \end{cases} \tag{2.20}$$

where a_{1h} is the amplitude of the power law. We further impose that $\bar{\gamma}(r)$ never exceeds 0.3, which corresponds to a perfect alignment. We choose to set $r = 0.06$ Mpc/h based on the minimum angular separation for a shape measurement, which we assume to be $\theta_{\max} = 4$ arcsec for a ground-based telescope. At high redshifts, the largest separation that can be resolved is around 60 kpc/h. At low redshifts, the spatial resolution is much smaller, but the light coming from the central galaxy, in particular for the most massive ones, can contaminate the measurements up to this scale (Sifón et al. 2018). A cut at 0.06 Mpc/h slightly suppresses the signal of the low mass galaxies, for which the satellite alignment is expected to be small. A space-based telescope such as *Euclid* will be able to resolve objects down to a smaller separation, but the physical extent and the contamination from the central galaxy still impose a truncation at small scales. Reducing the transition scale increases the amplitude of the signal, as satellites get more and more aligned as we approach the centre of the group/cluster. We experimented with different values of the truncation parameter and we find the impact to be subdominant with respect to the other source of uncertainties considered in this paper. However, future lensing studies that aim to include very small separations have to cope with an increasing IA contamination, in a regime where we do not have observations to properly calibrate its impact.

The measurements by G19 are performed in projection, which means that we can easily relate the projected shear γ^I to $\langle \epsilon_+ \rangle$. However, the radial position within the halo in our framework requires the 3d position, while G19 measure the signal in projected distance. For $r > 0.06$ Mpc/h, this

---

[8]Our definition of ellipticity is $|\epsilon| = (1 - q)/(1 + q)$, where q is the semi-minor to semi-major axis ratio and thus we do not need to double the responsivity in eq. 2.19, as in the case of shapes measured via polarisation.

introduces a $\sin^b \theta$ term in our expression of γ^I (see also Appendix A3),

$$\gamma^I(r, \theta) = \bar{\gamma}(r) \sin \theta = a_{1\mathrm{h}} \left(\frac{r \sin \theta}{r_{\mathrm{vir}}} \right)^b . \qquad (2.21)$$

As for the large scale signal, we distinguish between the alignment of red and blue satellites, for which G19 find a different amplitudes.

2.4.3 Luminosity dependence of the satellite galaxy alignment

In the spirit of including any observational insights into our model, we focus here on the luminosity dependence of satellites. This was detected in Huang et al. (2018) in the SDSS redMaPPer galaxies but not confirmed by G19 in galaxy groups. The same dependence was explored in clusters by (Sifón et al. 2015), who did not find any evident trend with the given S/N.

Addressing whether a luminosity dependence of satellites exists is particularly important for the IA contamination of the lensing signal in the low redshift bins, where the satellite population is more abundant and spans a large range in luminosities. In particular, the lowest redshift bins of a typical lensing survey do not reflect the satellite population employed in G19, containing a larger fraction of faint blue satellites, while their sample peaks at $M_r - 22$ and has an equivalent fraction of red and blue satellites. If faint satellites are characterised by a different alignment behaviour with respect to the bright ones, extrapolating their findings might largely overestimate the IA impact on such bins.

We focus on the SDSS-redMaPPer and GAMA+KiDS analyses here. Huang et al. (2018) observed that when using the re-Gaussianization shape algorithm, the satellites with $^{0.1}M_r < -21$, located closer to central galaxies, show a more prominent signal. Since the redMaPPer algorithm selects luminous red galaxies, one of the major differences between the galaxy samples used in the two studies is the colour of the satellites. G19 investigate the luminosity dependence only for the full sample, while Huang et al. (2018) focus on the red population only.

We re-analyse the galaxies in G19, looking for a luminosity scaling of the signal for the two separate cases of red and blue galaxies. We select red galaxies imposing the same cut as G19. We split the samples into two bins, cutting at $M_r = -22$ to ensure that the two bins have a comparable number of galaxies. We detect a luminosity dependence for both the red and blue sample. As before, we fit a power law with fixed index $b = -2$. Our results
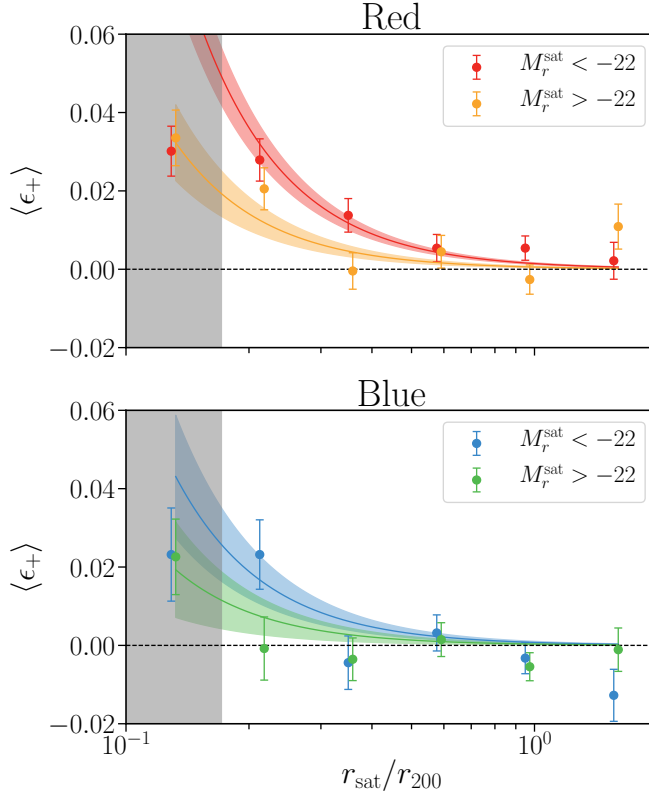
Figure 2.7: Mean tangential ellipticity components versus satellite projected distance from the brightest galaxy in the group, for the galaxy sample in G19. We separately consider the red (top panel) and blue (bottom panel) sample. We jointly fit the luminosity and radial dependence for each of the two samples, as in equation 2.22. The data points in the grey region are excluded from the fit. Our best fit is on top of the data points, with the $1 - \sigma$ uncertainty on the fit.

Table 2.2: Satellite luminosity dependence best fit amplitude (a_{1h}) for the red and blue sample. The samples are split in two luminosity bins, L1 (bright) and L2 (faint), with a cut at $M_r = -22$. In all of the fits, we assume a radial dependence with the form of a power law with slope -2, as in G19. In the joint fit, the luminosity dependence is modelled with a power law with slope ζ, as in eq. 2.22.

Sample		N_{gal}	a_{1h}	ζ	χ^2/dof
Individual sample fits:					
Red	L1	7505	0.0014 ± 0.0002	-	0.59
	L2	6618	0.0008 ± 0.0002	-	1.76
Blue	L1	5989	0.0008 ± 0.0004	-	1.97
	L2	8778	-0.0002 ± 0.0003	-	0.67
Joint fit:					
Red	all		0.0009 ± 0.0001	0.7 ± 0.2	1.02
Blue	all		0.0006 ± 0.0002	0.5 ± 0.4	1.50

are summarised in Table 2.2. Following G19, we do not include the first radial bin in our fits, since the light from the brightest galaxy of the group biases the shapes.

Although the signal-to-noise ratio does not allow for a definitive constraint on the luminosity dependence of the satellite alignment, we can draw the following conclusions: the faint blue satellites do not show any alignment signal, while the bright sample shows an alignment signal only for the innermost radial bin. The red satellites show a more prominent signal for both the faint and the bright samples. While the bright sample of the blue and the red satellites are still consistent with each other within the error bars, what drives the main difference in the red and blue satellite alignment is the behaviour of the faint bin.

To model the luminosity dependence, we decide to follow the parametrisation adopted for the red central galaxies, a power law in L/L_0, where L is now the luminosity of the satellite sample under consideration and L_0 is the pivot luminosity, corresponding to a magnitude of $M_r = -22$. We perform a joint fit of the radial and luminosity dependence for the red and blue sample separately, assuming the functional form:

$$\langle \epsilon_+ \rangle (r_{\text{sat}}, L) = a_{1h} \left(\frac{L}{L_0} \right)^\zeta \left(\frac{r_{\text{sat}}}{r_{\text{vir}}} \right)^b . \tag{2.22}$$

As for the rest of the analysis, we do not fit for b, which is chosen to be $b = -2$. Table 2.2 reports our best fit values of a_{1h} and ζ for the two samples, and Fig. 2.7 shows our best fit curves on top of the data points.

2.5   Halo model setup

To inform our model about the properties of the galaxy sample for which we predict the IA signal, we extract the HODs of central and satellites from our Stage III survey mock. We checked that this procedure gives us number densities of galaxies that match those measured in the simulations in redshift bins.

We define dark matter haloes as spheres with an average density of $200\bar{\rho}_m$. The mass of the haloes provided by MICE is based on the Friends-of-Friends (FoF) algorithm. The two definitions slightly differ from each other, in particular at high redshifts. We employ MICE masses only when computing the HODs, which enter in the small scales of the model. Those scales are important at low redshift only, so this mass-definition discrepancy is expected to not have a major impact for our analysis. This is further confirmed by the fact that we can recover compatible measured galaxy number densities within our halo model setup. In the following, we always use the M_{200} definition.

We assume that dark matter haloes follow the Navarro-Frenk-White distribution (Navarro et al. 1996), with a concentration-mass relation from Duffy et al. (2008) and that satellite galaxies are spatially unbiased with respect to the dark matter particles[9]. For the halo mass function and for the halo bias function we adopt the functional forms from Tinker et al. (2010). For the implementation of the former we make use of the public available python package HMF[10] (Murray 2014).

The total IA power spectra are given by the sum of the contributions introduced in Sect. 2.3 eq. 2.6-2.7, describing the behaviour at large scales (2h regime), and at small scales, presented in Sect. 2.4, eq. 2.17-2.18. When evaluating the mass integrals we consider masses in the range $[10^{10.5}, 10^{15.5}]$ $h^{-1}M_\odot$ to match the observed one in our mocks. To weight the IA signal, we do not use the galaxy fractions that we directly measure from the simulations, but those computed as the integral of the HOD and the halo mass function. In this way we ensure that the large and small scales contain the same galaxy numbers and ratios. Our recovered fractions are overall more accurate for the red sample, with an error around 5% in the relevant bins, while for the blue sample, we recover the true values with an error of 15%. As blue galaxies have a smaller alignment amplitude, this is not a major

---

[9]We do not provide galaxy positions within the halo as implemented in MICE, but only the mean halo occupation, N_g given the mass of the halo.

[10]https://github.com/steven-murray/hmf

concern here. We have also tested that our main results are not affected by reasonable changes of the mass ranges.

As discussed in Sect. 2.3.4, to model the large-scale alignment of the red sample, we consider two cases:

1. Simple power-law: $A_{\mathrm{red}} = 5.33 \pm 0.6$ and a luminosity dependence with slope $\beta = 1.2 \pm 0.4$, given by the weighted mean of LOWZ and MegaZ best fit A_0 and β

2. Broken power-law: $A_{\mathrm{red}} = 5.08^{+0.97}_{-0.95}$, $\beta_{L<L_0} = 0$ and $\beta_{L\geqslant L_0} = 1.2 \pm 0.4$

For the blue galaxy alignment at large scales, we refer to the best fit amplitude in J19, who found $A_{\mathrm{blue}} = 0.21 \pm 0.37$[11]. For the satellite alignment we consider a combined radial and luminosity dependence, as discussed in Sect. 2.4.3. We de-project the signal as described in Sect. 2.4.2, so that our final γ^I is in terms of r rather than the projected separation r_{sat}. The radial dependence is described by 2.21, including the piece-wise term as in equation 2.20. Note that in the case of the luminosity dependence, L is the mean luminosity of the red/blue satellites for each redshift tomographic bin. The final parameters are summarised in Table 2.3.

2.6   Results

Figure 2.8 shows our predictions for the IA power spectra for case (i) (solid lines) and (ii) (dashed lines). Our fiducial power spectra correspond to the best fit values in Table 2.3. Here, we also plot the associated 1σ uncertainties, to illustrate the current uncertainties in our IA parameters. The one-halo parameters $a_{1\mathrm{h}}$ and ζ are modelled as a multivariate Gaussian with the covariance matrix computed in the fitting procedure outlined in Sect. 2.4.3. Since we do not have information on the covariance matrix between the parameters A_{IA}, β, we assume that they follow uncorrelated Gaussian distributions centred on the best fit values and with standard deviation given by the 1σ uncertainties. We then draw 300 Monte Carlo realisations of the model, and we derive the lower and upper uncertainties using, respectively, the 16th and the 84th percentiles of the resulting distributions.

For both our case (i) and (ii), at low redshift and small scales, we find a larger signal that decreases as the redshifts increase, due to the drop of

---

[11]We decided to use J19 best fit amplitude for the blue sample as input parameter for the IA signal of the central blue galaxies only. This is motivated by the fact that our sample is significantly fainter than the one used in J19 and we have seen that faint blue satellites to not show any alignment signal (Sect. 2.4.3).

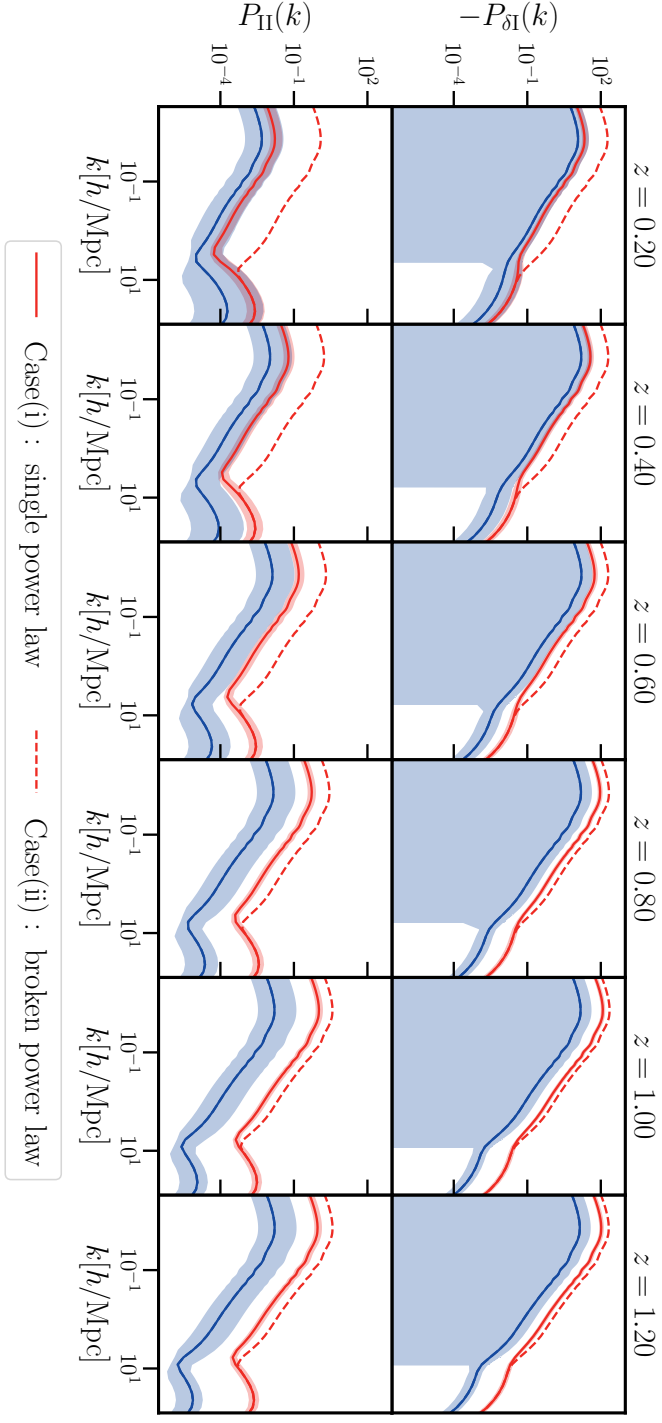**Figure 2.8:** The matter - intrinsic and the intrinsic-intrinsic shear power spectra for our case (i) (solid lines) and (ii) (dashed lines). The red curve corresponds to the red sample, the blue curve to the blue sample. The shaded areas corresponds to the 1σ uncertainties in the model as derived from the parameters uncertainties in Tab. (2.3). For the matter-intrinsic power spectra, we only plot the negative part.

Table 2.3: The IA parameters adopted in our model. In the 2-halo regime, we consider two different cases for the luminosity dependence of the central galaxy population: a single power law (case i) and a double (broken) power law (case ii).

Sample	Model	Parameter	Value
Red	2-halo (i)	A_β	5.33 ± 0.60
		β	1.2 ± 0.27
	2-halo (ii)	A_β	5.08 ± 0.97
		$\beta_{L \geqslant L_0}$	1.2 ± 0.27
		$\beta_{L < L_0}$	0
	1-halo	a_{1h}	0.0010 ± 0.0001
		ζ	0.7 ± 0.2
		b	-2
Blue	2-halo	A_{IA}	0.21 ± 0.37
		β	0
	1-halo	a_{1h}	0.0006 ± 0.0002
		ζ	0.5 ± 0.4
		b	-2

satellite galaxies at high redshifts imposed by the flux limit. The opposite happens for the large scales, where we observe an inverted trend in the redshift dependence: at high redshifts, where only bright galaxies are observed, the large-scale signal increases due to the luminosity dependence of the red central galaxy alignment. These trends are more pronounced for the single slope scenario (i), where we observe more variation among the different redshift bins. The power spectra of the red sample of our case (ii) maintains an almost constant effective amplitude, as expected for a luminosity distribution predominantly below L_0. The radial alignment of satellite galaxies shifts the contribution of the 1-halo term to larger k, reducing the impact of the IA at intermediate scales.

At small scales, the uncertainty in the luminosity dependence of the blue satellite alignment dominates our predictions. We note that the joint constrains on the luminosity and radial dependence of the faint blue sample do not fully capture the measurements, as the curve always remains slightly above the data points (Fig. 2.7). Indeed, the individual fit for the blue L2 sample is consistent with zero (Table 2.2). This is driven by the fixed slope of the radial dependence when performing the combined radial and luminosity dependence fit. We find that a steeper radial dependence can capture the measurements better, but given the limited S/N we decided

to not adopt separate dependencies for the red and blue samples.

2.6.1   Impact on lensing

To assess the contamination to the lensing measurements, we use the projected angular power spectra, $C(\ell)$, where ℓ is the 2D angular frequency. In the flat sky approximation, these can be written as:

$$C_{\mathrm{obs}}^{(ij)}(\ell) = C_{\mathrm{GG}}^{(ij)}(\ell) + C_{\mathrm{GI}}^{(ij)}(\ell) + C_{\mathrm{II}}^{(ij)}(\ell) \tag{2.23}$$

where

$$C_{\mathrm{GG}}^{(ij)}(\ell) = \int_0^{\chi_{\mathrm{hor}}} \mathrm{d}\chi \frac{q^{(i)}(\chi) q^{(j)}(\chi)}{\chi^2} P_{\delta\delta}\left(\frac{\ell}{\chi}, \chi\right), \tag{2.24}$$

$$C_{\mathrm{GI}}^{(ij)}(\ell) = \int_0^{\chi_{\mathrm{hor}}} \mathrm{d}\chi \frac{q^{(i)}(\chi) p^{(j)}(\chi) + p^{(i)}(\chi) q^{(j)}(\chi)}{\chi^2} P_{\delta\mathrm{I}}\left(\frac{\ell}{\chi}, \chi\right), \tag{2.25}$$

and

$$C_{\mathrm{II}}^{(ij)}(\ell) = \int_0^{\chi_{\mathrm{hor}}} \mathrm{d}\chi \frac{p^{(i)}(\chi) p^{(j)}(\chi)}{\chi^2} P_{\mathrm{II}}\left(\frac{\ell}{\chi}, \chi\right). \tag{2.26}$$

Here, χ denotes the comoving distance, χ_{hor} the comoving distance to the horizon, $p^i(\chi)\mathrm{d}\chi$ the distribution of source galaxies in the sample i, normalised to $\int \mathrm{d}\chi \, p^i(\chi) = 1$, and $q(\chi)$ is the lensing efficiency, defined as

$$q^{(i)}(\chi) = \frac{3H_0^2 \Omega_m}{2c^2} \int_\chi^{\chi_h} \mathrm{d}\chi' \, p^{(i)}(\chi') \frac{\chi' - \chi}{\chi'}. \tag{2.27}$$

We compute the power spectra $P(k, z)$ for the *true* redshifts and then integrate over the $n(z)$ of six photo-z bins with ranges reported in Table 2.1. To simulate the effect of photometric scatter we generate six Gaussian redshift distributions with a scatter $\sigma_z = 0.05(1 + z)$, as described in Chisari et al. (2019). We assume a total shape dispersion of $\sigma_\epsilon = 0.35$.

We compute a fully analytical covariance matrix, as described in Hildebrandt et al. (2020). To be consistent with current cosmic shear analyses, we do not include the IA contribution in the covariance matrix. To generate our predictions, we make use of the latest version of the public available software CosmoSIS[12] (Zuntz et al. 2015). Our results are shown in Fig. 2.9. For clarity, here we do not show the 1σ contours derived from the uncertainty in the IA parameters. In practise, when it comes to the contamination to lensing, the unknown luminosity dependence of the IA of faint

---
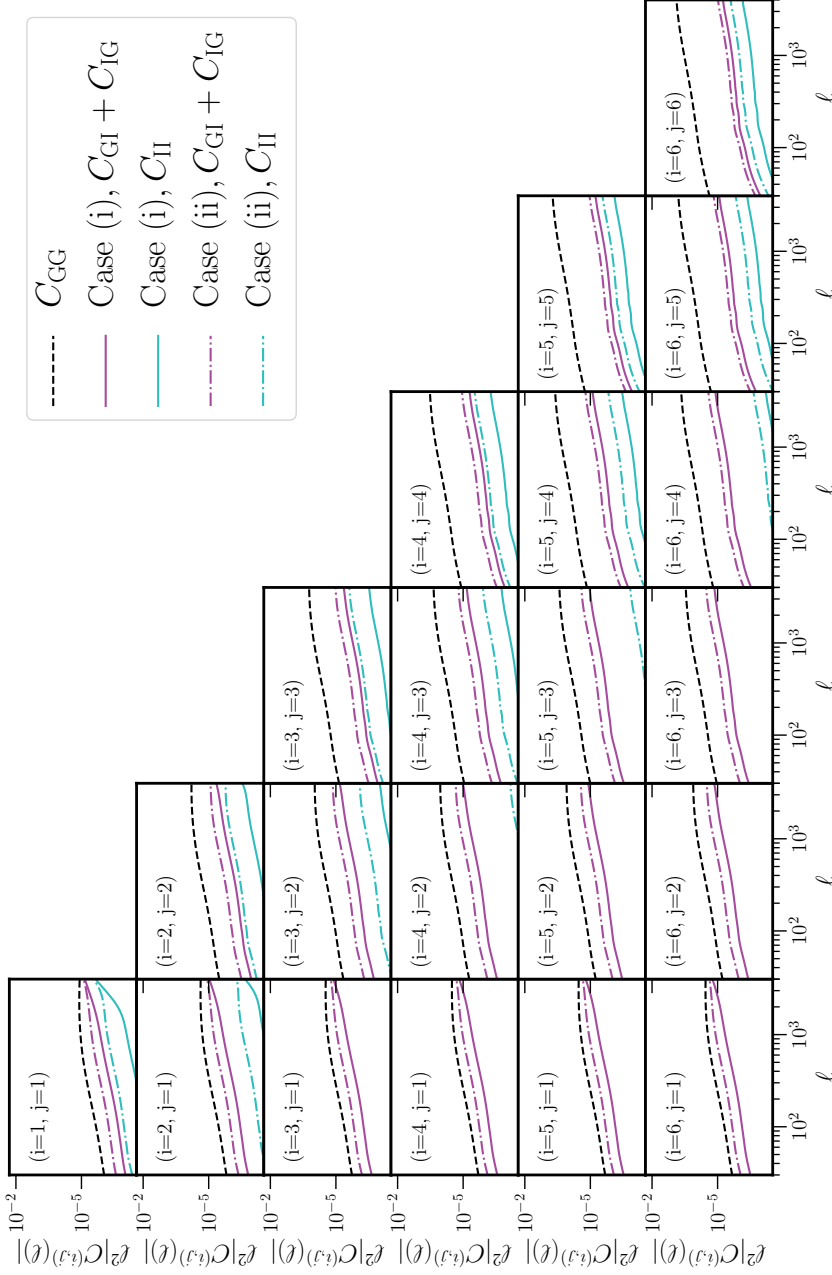
[12]`https://bitbucket.org/joezuntz/cosmosis`

Figure 2.9: Predictions for the projected angular power spectra: solid lines correspond to case (i), the dash-dotted lines to case (ii). The black dashed line shows the lensing power spectrum.

galaxies dominates our uncertainty, being the distance between the curves labelled as (i) and (ii) larger than the individual uncertainties in the fits of the IA signal of the specific sub-samples.

At low redshift, the large fraction of satellite galaxies is reflected in the IA signal, which becomes important. As expected, the II term is only relevant in the auto-correlation bins, while the GI is larger in all of the off-diagonal terms. Overall, the relative contamination from IA is larger at low redshifts, where also lensing is less efficient.

2.6.2   The impact of the modelling choice on the cosmological parameter estimate

The main goal of this paper is to investigate whether the emerged complexity of satellite contribution in the IA signal can lead to a bias in the Stage-III cosmological parameter estimate if not properly accounted. To explore this, we consider two cases of a generic cosmic shear analysis: in the first we simply assume the NLA model to hold for the full sample, without splitting in red and blue galaxies and without considering any luminosity dependence - so with only one free parameter, the amplitude A_{IA}; in the second case we introduce a power law to capture the redshift evolution of the signal due to the IA dependence on the galaxy sample:

$$P_{\delta\mathrm{I}}(k, z) = \left(\frac{1+z}{1+z_0}\right)^{\eta} P_{\delta\mathrm{I}}^{\mathrm{NLA}}(k, z) \tag{2.28}$$

and

$$P_{\mathrm{II}}(k, z) = \left(\frac{1+z}{1+z_0}\right)^{2\eta} P_{\mathrm{II}}^{\mathrm{NLA}}(k, z), \tag{2.29}$$

where we choose $z_0 = 0.3$. We refer to this model as NLA-z.

To do so, we generate a data vector of angular correlation functions $\xi_{\pm}(\theta)$ with the setup discussed in Sect. 2.5 and analyse it assuming the NLA and NLA-z as typically done in most of the Stage-III analyses. In this way, we have perfect knowledge of the signal injected and we can isolate the impact of marginalisation.

We perform the analysis in real space, using the projected correlation functions $\xi_{\pm}$, which we derive from the angular power spectra $C(\ell)$ using the implementation available in CosmoSIS (Kilbinger et al. 2009). The minimum and maximum angular scales adopted in this analysis are, respectively: $\theta_+^{\min} = 3'$, $\theta_+^{\max} = 72'$, $\theta_-^{\min} = 6'$ and $\theta_+^{\max} = 153'$, based on the KV450 (Hildebrandt et al. 2020) cosmic shear analysis.

We limit our interest to the cosmological parameters to which lensing is most sensitive, Ω_m, σ_8 and w. Instead of σ_8, we sample the logarithm of the scalar amplitude $\ln(10^{10}A_s)$, so our final parameter vector is $\lambda = \{\Omega_m, \ln(10^{10}A_s), w\}$ and one (two) nuisance parameter(s), A_{IA} (A_{IA}, η). We adopt uniform priors $\Omega_m = [0.1, 0.8]$, $\ln(10^{10}A_s) = [1.5, 5]$, $w \in [-5.0, 0.33]$, $A_{IA} = [-6, 6]$ ($\eta = [-5, 5]$). To sample the parameter space we make use of the Emcee sampler (Foreman-Mackey et al. 2013). The same analysis is performed for both scenarios; we only change the IA recipe while generating the data vector.

Our results show that for Stage-III surveys the NLA model provides an adequate description. For both scenarios the redshift dependence of the IA signal caused by the variation of the galaxy sample is not large enough to induce a bias in the cosmological parameters, with only marginal shifts in both S_8 and w for our case (ii). The recovered IA amplitudes are instead, as expected, different. In our case (i) we find a $A_{IA,(i)} = 0.14 \pm 0.14$, while for our case (ii) we find $A_{IA,(ii)} = 0.44 \pm 0.13$.

When adopting the NLA$-z$ model as the reference, in both cases the cosmological parameters are correctly recovered, but the η parameter remains unconstrained in our case (i) and it is very weakly constrained in our case (ii).

Our low IA amplitude for case (i) is in line with the best fit NLA amplitude found in J19 for the full GAMA sample, while their best fit value for the joint GAMA+SDSS Main has an amplitude of $A_{IA} \sim 1$, compatible with the fact that SDSS Main contains a larger fraction of red galaxies and fewer satellites to lower the signal at large scales. The comparison is, however, complicated by the fact that J19's results are based on the gI correlations. Compared to the KV450 IA amplitude, $A_{IA} = 0.981^{+0.694}_{-0.678}$, we find our case (i) to provide a lower value for a similar galaxy sample. However, different redshift distributions are adopted in the two works. We note that the full shape of the $n(z)$ is critical for the accurate modelling of the IA contribution (see Appendix A4). The redshift distributions of KV450 are more peaked and with more prominent tails, which increase the impact of the II in real data: as a consequence, since II and GI have opposite contributions, the IA balance changes. The way this effect can couple with the IA sample dependence is not obvious, as calibration errors in the final $n(z)$ can be absorbed by the A_{IA} amplitude during the fit (Li et al. 2021). In addition to this, a luminosity dependence of the signal reduces the presence of IA in the data (Joachimi et al. 2011; Krause et al. 2016): if the faint end of the luminosity dependence of red central galaxies is significantly shallower than what

we assumed in our case (i), the final amplitude would increase, as already suggested by our case (ii) setup. Similarly, our predictions are based on the assumption that the blue central galaxy population does not significantly contribute to the signal ($A_{\mathrm{IA}}^{\mathrm{blue}} = 0.21$), a constraint that suffers from large uncertainties. Our results (i) and (ii) point toward a lower amplitude to what is preferred by the cosmic shear analysis in DES data, for both their results with the NLA and NLA$-z$ models (Troxel et al. 2018), although we observe the same increase of the overall IA amplitude as a function of red-shift. Samuroff et al. (2019) find a lower IA amplitude in DES galaxies when simultaneously fitting for the cosmology and the IA amplitude in a 3x2pt statistics ($\gamma\gamma + \delta_g\gamma + \delta_g\delta_g$, $A_{\mathrm{NLA}} = 0.49^{+0.15}_{-0.15}$), which is in closer agreement with our findings. We want to stress that the aim of these comparisons is only to provide a sense of the ranges of the IA amplitudes currently con-strained by lensing analyses: we should not interpret the IA amplitudes as stand-alone quantities, without taking into account the best fit cosmologi-cal parameters and the exact $n(z)$.

Stage-IV

Given our results on a Stage-III setup, we investigate whether in the case of a Stage-IV survey we still recover the right cosmological parameters. We leave our setup unchanged, and only replace the covariance matrix to ac-count for the larger area (15 000 deg^2) and double the number density per redshift bin. We note that we do not modify our HODs, resulting in an un-derestimate of the satellite number density. Thus, our results have to be considered a lower limit on the possible induced biases.

Fig. 2.11 illustrates our findings for the NLA model. Overall, we find that case (i) leads to a lower level of bias in all the cosmological parameters compared to case (ii); this is expected, given the lower IA signal present in the data when assuming a steep luminosity dependence. In our case (i) we observe a 1σ bias in Ω_m only, while for case (ii) all parameters are biased by more than 1σ, with the bias in Ω_m exceeding 2σ. We note that the NLA A_{IA} amplitude recovered by the fits is dominated by the effective amplitude of the low redshift bins. The relative importance of IA over lensing is indeed strongest when the foreground galaxies are at low redshift (see the first columns of Fig. 2.9) and thus, even if the data contain a significantly higher alignment signal at high redshift, the fit is not particularly sensitive to these bins.

We also explore the performance of the NLA$-z$ model for the same se-tups. We find the flexibility of the NLA$-z$ sufficient to recover the cos-

Figure 2.10: Constraints on the cosmological parameters Ω_m, $S_8 = \sigma_8\sqrt{\Omega_m/0.3}$ and w, marginalising over the IA amplitude, for a Stage-IV survey. We inject the IA signal as predicted by the full halo model formalism assuming at larger scales a steep luminosity dependence (i: indigo) or a broken power law with constant amplitude for faint galaxies (ii: plum) - Table 2.3 lists the IA parameters used for constructing the data vectors. We perform the analysis assuming a NLA model with no distinction between red and blue galaxies. The orange lines and the square markers indicate the fiducial values of the cosmological parameters.
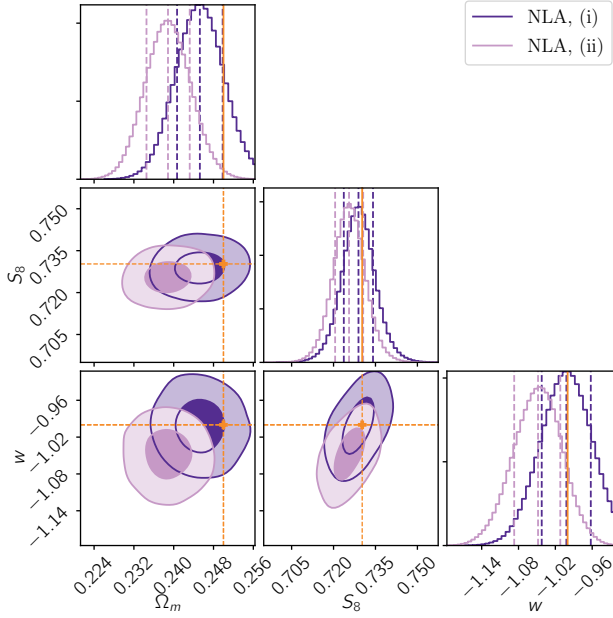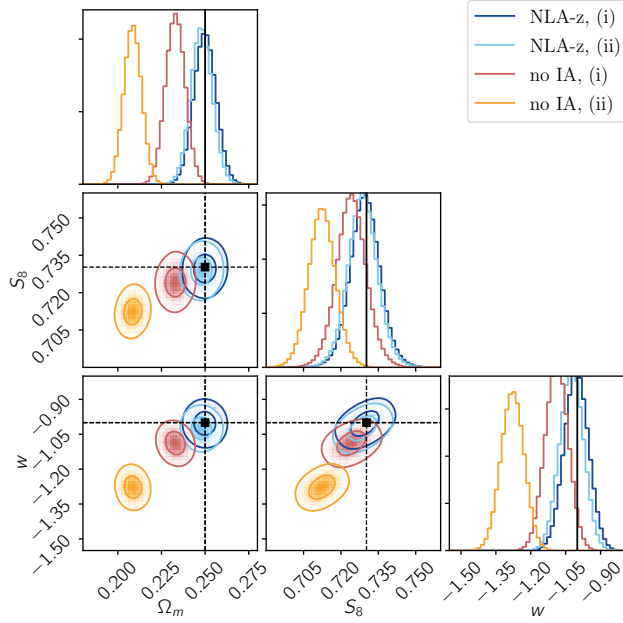
Figure 2.11: Constraints on the cosmological parameters Ω_m, $S_8 = \sigma_8\sqrt{\Omega_m/0.3}$ and w, marginalising over the IA amplitude, for a Stage-IV survey. We distinguish between two IA scenarios at large scales, as detailed in Table 2.3. We perform the analysis assuming no distinction between red and blue galaxies and assume either a NLA$-z$ model (dark blue ellipse for the IA signal as in case (i) and light blue ellipse for the case (ii)) or no IA (red for the IA signal based on (i), orange for the (ii)). The black lines and the square markers indicate the fiducial values of the cosmological parameters.

mological parameters for both our case (i) and (ii), with best-fit values: $A_{\mathrm{IA},(i)} = 0.16^{+0.02}_{-0.02}$, $\eta_{(i)} = 2.91^{+0.68}_{-0.73}$ and $A_{\mathrm{IA},(ii)} = 0.42^{+0.02}_{-0.02}$, $\eta_{(ii)} = 2.21^{+0.22}_{-0.23}$. The predicted redshift dependence of the signal for our sample can be captured by its power-law scaling, while the scale dependence introduced by the 1-halo term is not recovered. Because the amplitude of the 1-halo term is small and we remove the smallest scales in our fit with the cuts presented in Sec. 2.6.2, this remains a subdominant effect compared to the redshift variation in the IA signal induced by the galaxy sample selection across the redshift tomographic bins. In this case, we also note that the fits are driven by the low-z bins, with a worse recovery of the large scale alignment at high redshifts. This is more pronounced for case (ii), where the double power-law induces a more complex redshift scaling in the IA signal.

Given the precision of a Stage-IV survey, any specific choice in the setup can impact the results. We identify as the most significant ingredient the treatment of the halo exclusion. We caution that our implementation of the halo exclusion is not based on simulations, but merely aims to avoid the double counting at small scales, due to the use of the NLA$-\beta$ model for the 2-halo term. While this is sufficient for a Stage-III survey, we observe that the bias in the cosmological parameters is affected by the specific implementation of the halo exclusion for a Stage-IV. In general, a smoother transition that would remove more power at the intermediate scales would result in less bias in Ω_m and more bias in S_8 and w. The IA amplitude is instead weakly affected by the specific choice of the halo exclusion recipe. We also note that a full double counting at the small scales does not significantly change our results. We conclude that a proper modelling of the intermediate scales is more important than the exact amplitude of the 1-halo term.

2.7   Conclusions

We have performed a comprehensive analysis of the contamination by IA in cosmic shear surveys, with a particular focus on modelling the satellite contributions at small and large scales, based on the most recent observational IA findings. We proposed a new model to describe the IA signal, which explicitly accounts for the fact that only central galaxies contribute to the alignment signal at large scales. We introduced a satellite alignment signal at small scales, modelled through the halo model formalism, which includes a radial and luminosity dependence. We also differentiated the contribution from the red and blue population at all scales.

At large scales, we investigated whether limiting a luminosity dependence of the IA signal to the central galaxy sample provides a unified picture for all the measurements in the literature. Although in this scenario the slope measured by MegaZ/LOWZ seems to be favoured at high luminosities, the current uncertainty in the measurements does not allow for a definitive constraint on the luminosity dependence at low luminosities. For this reason, we decided to follow two alternative scenarios for all our forecasts: a single power law with slope $\beta = 1.2$ and a double power law with a faint end characterised by a flat slope, $\beta_{L<L_0} = 0$, and a bright-end with same slope as case (i), $\beta_{L\geqslant L_0} = 1.2$. Future IA studies should focus on constraining the faint end of Fig. 2.5, where uncertainties dominate. Upcoming surveys such as the Physics of the Accelerating Universe Survey[13] (PAUS; Eriksen et al. 2019; Padilla et al. 2019) can help gaining insight into our understanding of the faint central galaxy alignment, a key feature to properly predict the IA contamination in cosmic shear surveys.

At small scales, we model the satellite alignment with a power law for the radial dependence, as recently measured by G19 in groups. We reanalyse the G19 data splitting the sample in red and blue, and we found that in this case a cut at $M_r = -22$ suggests a luminosity dependence in the signal. We jointly fitted the radial and luminosity dependence assuming a double power law, and used this result as input for our forecasting model. More data are needed to tightly constrain the luminosity dependence of satellites, as the statistical uncertainties in the measurements might play a role in constraining the amplitude of the power law. It is also relevant to note that since red and blue satellites show a different alignment amplitude, it is important to model them separately, as their relative fraction depends on the magnitude cut of the specific survey.

Although satellites do not share the same alignment mechanisms as central galaxies, the dichotomy in morphology observed at large scales is reflected also in their alignment mechanism. A different radial dependence of red and blue satellites might reveal a more complex alignment mechanism for the two populations and/or probe the galaxy in-fall history. With current measurements it is not possible to further investigate this possibility, but future dedicated high resolution hydrodynamical simulations might shed light in the understanding of the intra-halo alignment. Such simulations can also improve the modelling of intermediate scales, to which the lensing signal is most sensitive, but where our model is relatively simplistic. A proper calibration of the IA alignment in this intermediate regime

---

[13]https://www.pausurvey.org

is of primary importance for the interpretation of data from Stage-IV surveys.

Our predicted power spectra show two opposite trends at high and low redshifts, as shown in Fig. 2.8. While at low redshift the small scales have a larger IA signal, due to the presence of satellites, the large scales are dominated by the alignment of red central galaxies. The large scale signal becomes stronger as we go to higher redshifts, due to the survey magnitude cut: this selects brighter galaxies, which are those that carry most of the IA signal, due to the observed luminosity dependence of the red central galaxy alignment. The opposite happens to the small scales, which are almost completely washed out by the suppression of satellites in the high redshift bins. These trends are enhanced when considering the single power law for the luminosity dependence.

In this work we have not accounted for the anisotropic distribution of satellites within the halo, which is also known to contaminate lensing measurements. In the context of cosmic shear analyses, this is expected to be important only at small and intermediate scales. The satellite segregation along the central galaxy major axis complicates the interpretation of IA measurements performed using the central galaxy position - satellite shear correlation (gI), and future studies should focus on modelling it, in order to have a clear mapping between gI and GI. However, our spherical model can be considered as an *effective* model: in the perspective of a direct fit of IA to data, the free amplitude in the 1-halo term can potentially capture to first order the extra correlation due to the anisotropic term.

While direct IA measurements provide unique insights into the IA mechanisms and amplitudes, translating those results into informative priors for cosmic shear analyses requires a full modelling of the sample dependence of the IA signal. This aspect has often been underestimated in lensing studies, adopting simplistic models that do not distinguish between the different IA signatures of different galaxy populations, and adopting broad, uninformative priors. We investigated what is the impact of this choice for the IA signal that we expect for a cosmic shear survey given our model. We considered the case of a Stage-III analysis on a simulated data vector, built to reproduce our best knowledge of the IA, and then analysed it using simple NLA and NLA$-z$ models. Limiting our analysis to Ω_m, S_8 and w, we find both models to be sufficient to capture the IA signal without biasing in the cosmological parameters. This is no longer true for Stage-IV surveys, where we observe a bias in Ω_m that exceeds 2σ bias when adopting a simple NLA model. Including a power-law redshift dependence, the NLA$-z$ model

is able to recover our input cosmological parameters in the presence of a sample-dependent IA signal. Hence we recommend the use of a flexible redshift dependent model of IA for Stage-IV surveys.

In all cases the recovered IA amplitudes are smaller than 1, similar to typical values obtained by current cosmic shear studies. The amplitude depends on the specific IA model assumed: we find the broken power law for the red central galaxy luminosity dependence to provide a larger effective amplitude. This is a consequence of the larger amplitude assumed for the faint population in this setup, which dominates our overall alignment, as faint galaxies are more abundant than bright galaxies. We find the IA signal to be smaller than what was assumed in previous works: this is driven by the central galaxy weighting at large scales which significantly reduces the effective IA amplitude. This has implications for the inferred level of bias in the cosmological parameters. These findings are, however, based on several assumptions that represent our best extrapolation of the current picture of IA as emerging from dedicated studies. Future studies on the behaviour of faint central and satellite galaxies are needed to confirm these results. However, the model is extremely flexible and any new findings can be easily incorporated.

We find our fits to be driven by the low-z bins, where IA dominates over cosmic shear, whereas at high-z a bias in IA barely affects the results. We also note that the redshift dependence of the signal is more important than the scale dependence introduced by the 1-halo term. This is a consequence of the small satellite alignment we adopt in the model, based on current observational constraints. The inclusion of a term for the anisotropic distribution of the satellites might change this conclusion.

As the impact of IA is larger for the lowest redshift bin, excluding it can mitigate the impact of uncertainties in the modelling of the IA signal. Alternatively, improving the constraints at low-z, with a focus on faint galaxies, will be essential.

We want to stress that these model predictions are based on idealised redshift distributions and so our results cannot be directly compared with the best fit parameters inferred by cosmic shear studies. At higher redshifts and lower luminosities, the mocks might suffer from a larger uncertainty, as the luminosity is calibrated locally and then evolved to high redshifts. This has to be considered as part of the uncertainty in the model predictions, which requires additional data to be assessed. Upcoming surveys that aim to use the model can use clustering information in their data and the observed luminosity function to further constrain these parameters.

In light of future cosmological analyses, this model can be used to account for the IA signatures on different galaxy populations allowing for a direct map between IA observations and cosmic shear contamination. The model can be used to predict the IA signal in a given cosmic shear based on its galaxy composition at different redshifts: provided that the galaxy mocks are sufficiently representative of the data, it is possible to provide priors for different IA models. We caution that the current uncertainty in the luminosity dependence of the signal currently prevents the use of tight priors; instead the range covered by both our (i) and (ii) scenarios should be considered. Given a halo occupation distribution model for the red and blue galaxy populations, this model can be employed to jointly fit the clustering, IA and lensing observables.

Acknowledgements

Figure 12: The satellite galaxy fractions in our mocks compared to those in the GAMA sample. We select the galaxies in the mocks to reproduce the same redshift-magnitude selection as GAMA.

A1   Satellite galaxy fractions in MICE

We investigate here how well MICE reproduces the GAMA survey in the corresponding redshift and magnitude space, because we use that sample as input for our study. Our reference GAMA catalogue is obtained by matching the StellarMassLambda-v2 catalogue, from which we obtain photometric information, and the G3CGal, which contains the group information. We identify the satellite population by imposing RankBCG>1.

We build a GAMA-like sample from MICE in the following way. We select from our mock all galaxies brighter that $r < 19.8$, the flux-limit of our GAMA catalogue, and limited the analysis to a sub-patch of $\sim 180 \deg^2$, which is the size of the overlapping region with the KiDS survey employed by J19, C19 and in this work. With only these conditions, we find a very good agreement with the colour and magnitude distributions of the GAMA galaxies.

Given the compatibility in the colour-magnitude space, we select red galaxies in GAMA by applying the same cut as used in the rest of the paper (2.2.1). We then measure the galaxy fraction for all the sub-samples that enter in the halo model, to quantify the accuracy of our mocks. Fig. 12 illustrates our findings. We observe a remarkable agreement for the red galaxy population. For the blue sample, MICE exhibits a larger satellite fraction at low redshift and the opposite behaviour at high redshifts; however, the absolute difference between the fractions found in MICE and GAMA is 0.065 at maximum.

A2   Halo exclusion and intermediate scales

One of the limitations of the halo model is its lack of a proper treatment of the intermediate, mildly non-linear scales. In particular, the configuration with radially dependent satellite alignment pushes the one-halo term to very small scales ($k < 6h/\mathrm{Mpc}$). This implies that the intermediate scales do not arise as a simple sum of the 1h and 2h terms, with the one halo term being too small in this regime. Current observations of the IA signal show a much stronger alignment at intermediate scales than what is predicted by this model. However, a further complication comes from the fact that the intermediate scales are significantly affected by the central-satellite correlation, which is known to be large in the context of gI, due to the anisotropic distribution of satellites within the halo. Since direct IA measurements are performed correlating galaxy positions with galaxy shapes, we lack a proper reference for this term in the case of the matter-shear and shear-shear correlations. A proper treatment of this problem requires a dedicated calibration with simulations, which we defer to future work.

To compensate the lack of power at intermediate scales, we use the non-linear power spectrum as done in the context of the NLA model. This leads, however, to double counting at the level of the 1-halo term. To avoid this, we truncate the 2-halo term at $k_{2\mathrm{h}} = 6h/\mathrm{Mpc}$, roughly corresponding to a

halo of $1\,\mathrm{Mpc}/h$, via a window function of the form:

$$f^{2\mathrm{h-trunc}}(k) = \exp\left[-(k/k_{2\mathrm{h}})^2\right] \ . \tag{30}$$

Similarly, we truncate the 1-halo term to $k_{1\mathrm{h}} = 4h/\mathrm{Mpc}$ applying

$$f^{1\mathrm{h-trunc}}(k) = 1 - \exp\left[-(k/k_{1\mathrm{h}})^2\right] \ . \tag{31}$$

We allow for a small overlap of the signal at intermediate scales, where the aforementioned truncations gradually reduce both the 1h and 2h terms.

A3 The angular part of the satellite alignment density run

We compute the satellite alignment following the formalism developed in Schneider & Bridle (2010), assuming a perfect radial alignment scenario. We report here our expansion for f_l and the main steps to derive it. We have tested our results against the analytical solution for the first two non-zero multipoles ($l_{\max} = 4$), finding excellent agreement.

The complex phase in equation 2.13 can be re-written through the plane wave expansion:

$$\exp(i\mathbf{k} \cdot \mathbf{r}) = \sum_{l=0}^{\infty} i^l (2l+1) P_l(\cos\gamma) j_l(kr) \ , \tag{32}$$

where $P_l(x)$ are the Legendre polynomials of order l and $\cos\gamma$ is the angle between $\mathbf{r} = (r, \theta, \phi)$ and $\mathbf{k} = (k, \theta_k, \phi_k)$,

$$\cos\gamma = \sin\theta_k \sin\theta \cos(\phi_k - \phi) + \cos\theta_k \cos\theta \ . \tag{33}$$

We can rewrite the Legendre polynomials through the identity

$$P_l(x) = 2^l \sum_{m=0}^{l} x^m \binom{l}{m} \binom{\frac{l+m-1}{2}}{l} \ , \tag{34}$$

where $x = \cos\gamma$. We can express $(\cos\gamma)^m$ using the binomial theorem, such that all of the terms on the right in equation 33 are of the form a^j and those on the left b^{m-j}, where j goes from 0 to m. Separating the integrals on ϕ and θ, we have that the azimuthal part reduces to

$$\int_0^{2\pi} \mathrm{d}\phi \begin{pmatrix} \cos(2\phi) \\ \sin(2\phi) \end{pmatrix} (\cos\phi_k \cos\phi + \sin\phi_k \sin\phi)^j \ , \tag{35}$$

where the integrals over ϕ are all zeros for odd j, while the even terms are

$$g_{j=2n} = \left\{0, \frac{\pi}{2}, \frac{\pi}{2}, \frac{15\pi}{32}, ...\right\} \text{ for n=1,2,3, ...} \tag{36}$$

The terms in ϕ_k can be rearranged to be of the form $e^{i2\phi_k}$. The integral over the polar angle θ gives instead

$$\int_{-1}^{1} d\cos\theta \sin^{j+1}\theta \cos^{m-j}\theta = \int_{-1}^{1} d\cos\theta \left(1 - \cos^2\theta\right)^{\frac{j+1}{2}} \cos^{m-j}\theta$$
$$= I(j+1, m-j), \tag{37}$$

where, following SB10, we have defined

$$I(a, b) = \int_{-1}^{1} dx(1 - x^2)^{\frac{a}{2}} x^b. \tag{38}$$

Collecting all the terms together, we get

$$f_l(\theta_k, \phi_k) = e^{i2\phi_k} 2^l \sum_{m=0}^{l} \binom{l}{m} \binom{\frac{l+m-1}{2}}{l} \sum_{j=0}^{m} \binom{m}{j} g_j$$
$$\times I(j+1, m-j) \sin^j\theta_k \cos^{m-j}\theta_k. \tag{39}$$

Since the $E-$ and $B-$ modes of the intrinsic alignment are invariant under rotation in the plane of the sky, we can choose without loss of generality to fix $\phi_k = 0$. The polar angle θ_k defines the projection of the wave vector $\mathbf{k}$ on the plane of the sky: modes perpendicular to the line of sight are identified by $\theta_k = \frac{\pi}{2}$, for which we have the strongest alignment signal, as illustrated in Fig. 13. Indeed, the angular part of $\hat{\gamma}(\mathbf{k}, M)$ is dominated by the lowest term of the expansion, $l = 2$, which peaks at $\theta_k = \pi/2$. The main effect of θ_k is to change the amplitude of $\hat{\gamma}(\mathbf{k}, M)$ (Fig. 13). We decide to assume $\theta_k = \frac{\pi}{2}$ throughout our analysis, i.e. to only consider the modes perpendicular to the line of sight, and to truncate the expansion at $l_{\max} = 6$.

Note that we decide to not adopt the definition of the density-weighted shear in SB10, $w(k|M)$ and instead work with their original definition (their equation 7), from which we can naturally derive the expression for the radially dependent case. Here, we normalise the density-weighted shear with the NFW mass, as originally in eq. 7 of SB10.

In our work, the intrinsic shear has the form

$$\gamma^I(r, \theta, L) \equiv \bar{\gamma}(r, L) \sin\theta = a_{1h}(L) \sin^b\theta \left(\frac{r}{r_{\text{vir}}}\right)^b, \tag{40}$$
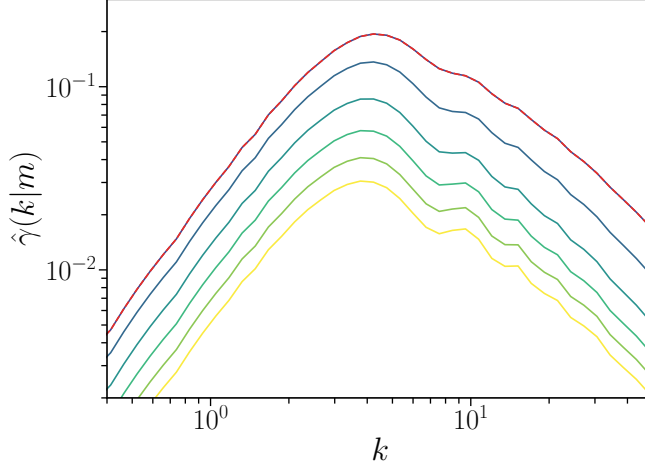
Figure 13: The Fourier transform of the density-weighted shear (eq. 2.13) for $\phi_k = 0$ and $\theta_k \in \left[\frac{\pi}{2}, \pi\right]$, in the case of constant radial dependence. For clarity, we normalise the curves by the input amplitude, $a_{1\mathrm{h}}$. The amplitude of the curves decreases as we go from $\theta_k = \frac{\pi}{2}$ (red) to $\theta_k = \pi$. Note that $f(\theta_k)$ is symmetric around $\theta_k = \pi/2$, so the curves from $\left[0, \frac{\pi}{2}\right]$ coincide with the ones plotted here, with increasing amplitude for increasing values of θ_k.

where the $\sin^b \theta$ in the right-hand side comes from the de-projection of the satellite separation from the BCG. This brings $\sin \theta \mapsto \sin^b \theta$ and only affects the integral in $\mathrm{d}\cos\theta$, such that $I(j+1, m-j) \mapsto I(j+b, m-j)$ in eq. 39. To avoid singularities along the line-of-sight, we perform the integral in the range $[-1 + \varepsilon, 1 - \varepsilon]$, with $\varepsilon = 10^{-10}$.

A4 Intrinsic alignment dependence on photometric redshift distributions

We illustrate here the impact on the choice of $n(z)$ in predicting the IA signal. As discussed in Sect. 5.6, the specific choice of the $n(z)$ distribution plays an important role in enhancing the II term, changing the balance between the different IA components. Here, we try to disentangle which feature has the largest impact on modulating the magnitude of the II term and its scale dependence. For this exercise, we use the IA model referred as (i), where the IA dependence on the red central galaxy luminosities is modelled as a single power law. We generate three different distributions (14), which progressively include a new feature. Fig. 15 illustrates our findings. We
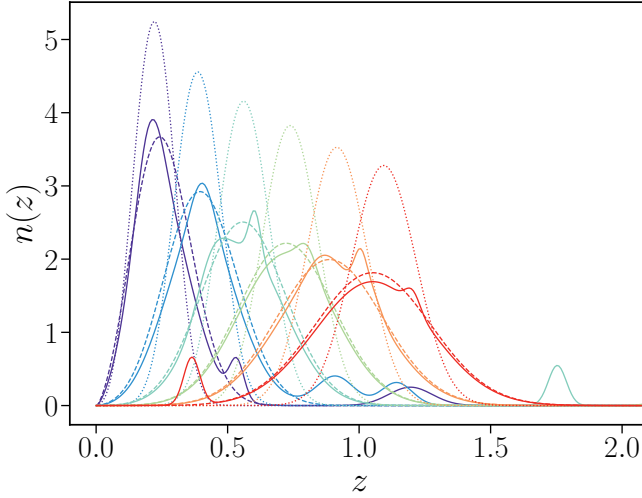
Figure 14: Two of the four different $n(z)$ adopted in our comparison. The dotted curves refer to the case of Gaussian photometric distributions with $\sigma_z = 0.05(1 + z)$ as discussed in the text (see Sect. 2.6.1), the dashed curves to broader Gaussians ($\sigma_z = 0.1(1+z)$), while the solid lines are the $n(z)$ built from the broader Gaussians with the inclusion of 'catastrophic outliers' and more pronounced peaks in the distributions.

start with the Gaussian distributions adopted in the paper and presented in Sect. 2.6.1 (solid orange lines), then we broaden them by increasing the standard deviation per bin, $\sigma_z^{\text{broad}} = 0.1(1 + z)$ (dashed green lines): this increases the amplitude of the II power spectra in the off-diagonal terms, due to the overlap of the tails of the distributions from different adjacent bins; on the diagonal terms, the broadening slightly reduces the II power spectrum. We then introduce 'catastrophic outliers', which we generate as Gaussian islands centred on random points extracted from the original dN/dz, with a similar approach as Samuroff et al. (2020b). The presence of the outliers increases the II contribution (dash-dotted magenta lines): this is particular prominent at low redshift, for highly separated z–bins, where the outliers introduce correlated pairs between bins that would otherwise been uncorrelated.
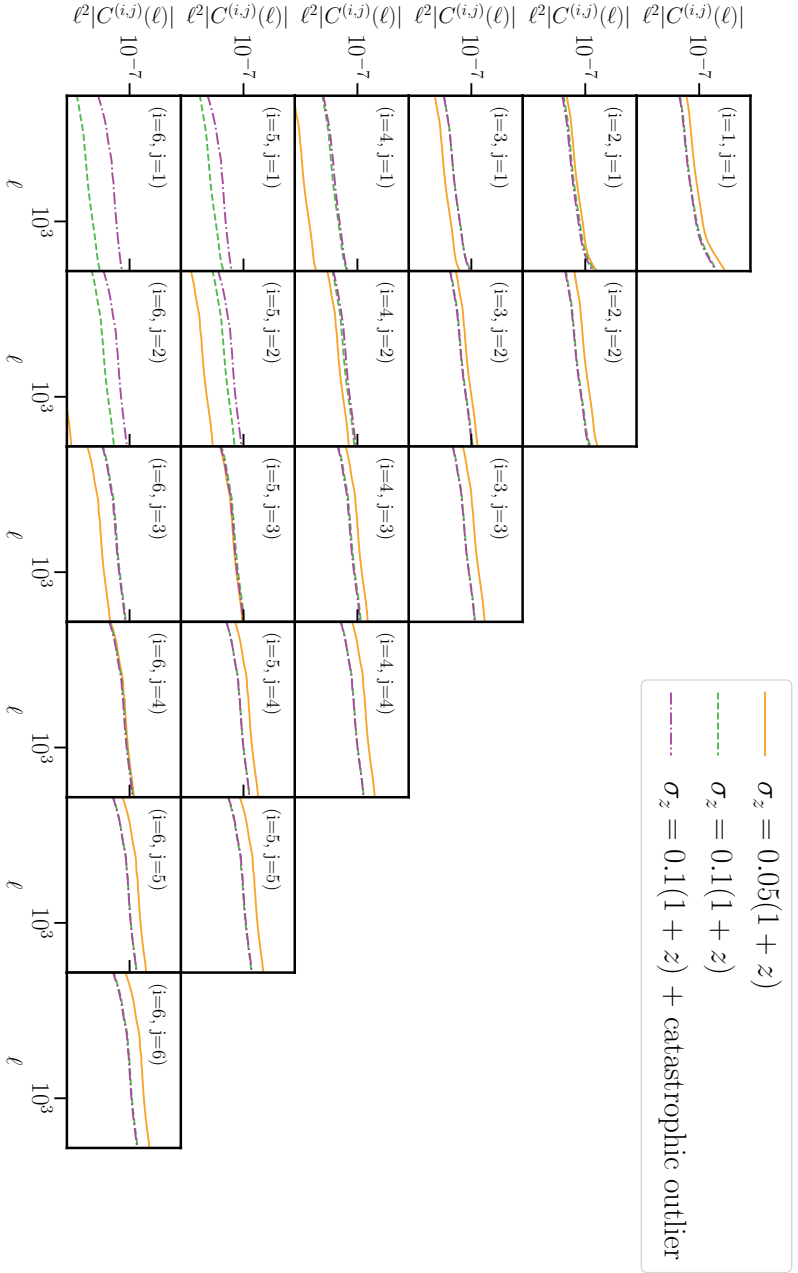
Figure 15: The impact of the $n(z)$ on the projected II angular power spectrum. The IA is generated assuming the same setup as 2.3, while the $n(z)$ are respectively: the fiducial Gaussian $n(z)$ adopted in the rest of the paper (solid orange lines), broader Gaussian distributions (dashed green lines) and broader Gaussians with the superpositions of 'catastrophic outliers' and peaks (dash-dotted magenta lines).

3 | KiDS-1000: Constraints on the intrinsic alignment of luminous red galaxies

M.C Fortuna, *H. Hoekstra, H. Johnston, M. Vakili, A. Kannawadi, C. Georgiou, B. Joachimi, A. H. Wright, M. Asgari, M. Bilicki, C. Heymans, H. Hildebrandt, K. Kuijken, M. Von Wietersheim-Kramsta 2021, A&A, 654, A76*

We constrain the luminosity and redshift dependence of the intrinsic alignment (IA) of a nearly volume-limited sample of luminous red galaxies selected from the fourth public data release of the Kilo-Degree Survey (KiDS-1000). To measure the shapes of the galaxies, we used two complementary algorithms, finding consistent IA measurements for the overlapping galaxy sample. The global significance of IA detection across our two independent luminous red galaxy samples, with our favoured method of shape estimation, is $\sim 10.7\sigma$. We find no significant dependence with redshift of the IA signal in the range $0.2 < z < 0.8$, nor a dependence with luminosity below $L_r \lesssim 2.9 \times 10^{10} h^{-2} L_{r,\odot}$. Above this luminosity, however, we find that the IA signal increases as a power law, although our results are also compatible with linear growth within the current uncertainties. This behaviour motivates the use of a broken power law model when accounting for the luminosity dependence of IA contamination in cosmic shear studies.

3.1   Introduction

Galaxies that form close to a matter over-density are affected by the tide induced by the quadrupole of the surrounding gravitational field, and the distribution of stars will adjust accordingly. This process, which starts during the initial stages of galaxy formation (Catelan et al. 2001), can persist over their entire lifetime, as galaxies have continuous gravitational interactions with the surrounding matter (e.g. Bhowmick et al. 2020), and leads to the intrinsic alignment (IA) of galaxies.

This tendency of neighbouring galaxy pairs to have a similar orientation of their intrinsic shapes is an important contaminant for weak gravitational lensing measurements (e.g. Joachimi et al. 2015). The matter distribution along the line-of-sight distorts the images of background galaxies, resulting in apparent correlations in their shapes. Intrinsic alignment contributes to the observed correlations, complicating the interpretation. To infer unbiased cosmological parameter estimates it is therefore crucial to account for the IA contribution. This is particularly important in the light of future surveys, such as *Euclid*[1] (Laureijs et al. 2011) and the Large Synoptic Survey Telescope (LSST)[2] at the Vera C. Rubin Observatory (Abell et al. 2009), which aim to constrain the cosmological parameters with sub-percent accuracy (for a forecast of the IA impact on current and upcoming surveys see Kirk et al. 2010; Krause et al. 2016, among others). Some recent results on current weak lensing studies are available in, for example, Aihara et al. (2018); Asgari et al. (2021); DES Collaboration et al. (2021).

To provide informative priors to lensing studies, it is essential to learn as much as possible from direct observations of IA. It is, however, also important that such results can be related to the properties of galaxies that give rise to the alignment signal in cosmic shear surveys (Fortuna et al. 2021a). Intrinsic alignment studies are typically limited to relatively bright galaxies, which often sit at the centre of their own group or cluster, and it is thus possible to connect their alignment to the underlying dark matter halo alignment via analytic models (Hirata & Seljak 2004). The picture becomes more complicated when considering samples that contain a significant fraction of satellite galaxies: The alignment of satellites arises as a result of the continuous torque exercised by the intra-halo tidal fields while the satellite orbits inside the halo (Pereira et al. 2008; Pereira & Bryan 2010). This leads to a radial alignment, which also depends on the galaxy

---

[1] https://www.euclid-ec.org
[2] https://www.lsst.org

distance from the centre of the halo (Georgiou et al. 2019b). At the same time, satellites fall into halos through the filaments of the large-scale structure, and this persists as an anisotropic distribution within the halo, which has been detected both in simulations (Knebe et al. 2004; Zentner et al. 2005) and observations (West & Blakeslee 2000; Bailin et al. 2008; Huang et al. 2016; Johnston et al. 2019; Georgiou et al. 2019b). The combination of these two effects complicates the picture. At small scales, where the satellite contribution is expected to be important, their signal may be described using a halo model formalism (Schneider & Bridle 2010; Fortuna et al. 2021a), but their contribution to IA on large scales remains poorly constrained (Johnston et al. 2019); although it is expected that they are not aligned, they do affect the inferred amplitude because they contribute to the overall mix of galaxies. This prevents a straightforward interpretation of any secondary sample dependence of the IA signal sourced by the central galaxy population, such as the dependence on luminosity or colour, in mixed samples where the fraction of satellites is relevant.

Observational studies have found discordant results regarding the presence of a luminosity dependence of the IA signal, with the bright end being well described by a steep power law with index ~ 1.2 (Hirata et al. 2007; Joachimi et al. 2011; Singh et al. 2015), while less luminous galaxies do not show any significant dependence of the IA signal with luminosity (Johnston et al. 2019). A recent investigation using hydrodynamic simulations by Samuroff et al. (2020a) supports a flatter slope, in agreement with Johnston et al. (2019) and Fortuna et al. (2021a) at low luminosities but in tension with previous studies that probe more luminous galaxies. The interpretation of these results is also affected by the presence of satellites, whose fraction varies with luminosity and depends on the specific selection function of the data. At low redshift, a cosmic shear survey is dominated by faint galaxies, and improving our understanding of the IA signal at low luminosities is one of the most urgent questions for IA studies.

Another relevant aspect that is often neglected is the dependence of IA on the shape measurement method (Singh & Mandelbaum 2016). The tendency to align in the direction of the surrounding tidal field is a function of galaxy scale (Georgiou et al. 2019b), with the outermost parts – which are more weakly gravitationally locked to the galaxy – showing a more severe twist. It increases the IA signal associated with shapes measured via algorithms that assign more importance to the galaxy outskirts. In contrast, lensing studies typically prefer shape methods that give more weight to the inner part of a galaxy. Accounting for this discrepancy is potentially

relevant for future cosmic shear studies.

In this work we focus on investigating the luminosity dependence of the IA signal in the least constrained regime, $M_r \gtrsim -22$. We employ two different samples, which differ in mean luminosity and number density. We limit the analysis to the large-scale alignment, for which a theoretical framework is already available and where the luminosity dependence is known to play a crucial role (Fortuna et al. 2021a). We also provide estimates of the satellite fractions present in our samples in order to guide future work on the modelling of satellite alignment at large scales. We also explore the dependence of our signal on the shape measurement algorithm used to create the shape catalogue. We compare the signal as measured by two complementary algorithms: DEIMOS (DEconvolution In MOment Space; Melchior et al. 2011), which has been widely used in IA studies (Georgiou et al. 2019a; Johnston et al. 2019; Georgiou et al. 2019b), and *lens*fit (Miller et al. 2007, 2013) which has been used for the cosmological analysis of the Canada-France-Hawaii Telescope Lensing Survey (Heymans et al. 2013, CFHTLenS;) and the Kilo-Degree Survey (KiDS; see Asgari et al. 2021, and references therein).

One of the main limitations for measuring IA is the necessity of simultaneously relying on high-quality images and precise redshifts to properly identify physically close pairs of galaxies that share the same gravitational tidal shear. Wide field image surveys provide high-quality images, but the uncertainty in the photometric redshifts is too large for useful IA measurements. Fortunately, using a specific selection in colours, it is possible to obtain a sub-sample of galaxies with more precise photometric redshifts: the luminous red galaxies (LRGs). At any given redshift, LRGs populate a well-defined region in the colour-magnitude diagram, known as the red-sequence ridgeline. Using this unique property, it is possible to design a specific algorithm to select LRGs in photometric surveys, which results in both precise and accurate redshifts (Rozo et al. 2016; Vakili et al. 2019, 2020). Luminous red galaxies have also been shown to be strongly affected by the surrounding tidal fields, making them an extremely suitable sample for exploring the behaviour of IA at different redshifts and as a function of secondary galaxy properties, such as luminosity and type (central or satellites).

Joachimi et al. (2011) first studied the IA signal of an LRG sample with photometric redshifts. In this paper we follow their main approach but use a catalogue of LRGs selected by Vakili et al. (2020) using the KiDS fourth public data release (KiDS-1000 Kuijken et al. 2019).

The paper is structured as follows. In Sect. 3.2 we describe our data and the characteristics of our two main samples. In Sect. 3.3 we introduce the two shape measurement methods employed in the analysis and present the strategy adopted to calibrate the bias in the measured shapes. Section 3.4 presents the estimators we use to extract the signal from the data, while Sect. 3.5 illustrates the theoretical framework we rely on when modelling the signal: the way the model accounts for the use of photometric redshifts as well as the way we account for astrophysical contaminants. Finally, we present our main results in Sect. 5.6 and conclude in Sect. 4.8.

Throughout the paper, we assume a flat Λ cold dark matter cosmology with $h = 0.7, \Omega_{\mathrm{m}} = 0.25, \Omega_{\mathrm{b}} = 0.044, \sigma_8 = 0.8$, and $n_{\mathrm{s}} = 0.96$.

3.2   KiDS

The Kilo-Degree Survey is a multi-band imaging survey designed for weak lensing studies, currently at its fourth data release (KiDS-1000; Kuijken et al. 2019). The data are obtained with the OmegaCAM instrument (Kuijken 2011) on the VLT Survey Telescope (VST; Capaccioli et al. 2012). This combination of telescope and camera was designed specifically to produce high-quality images in the $ugri$ filters, with best seeing-conditions in the $r-$band, and a mean magnitude limit of ~ 25 (5σ in a $2''$ aperture). These measurements are combined with results from the VISTA Kilo-degree INfrared Galaxy survey (VIKING; Edge et al. 2013), which surveyed the same area in five infrared bands ($ZYJHK_{\mathrm{s}}$). This resulted in high-quality photometry in nine bands across approximately $1000\ \mathrm{deg}^2$ imaged by the fourth data release[3]. The VIKING data are important for the LRG selection at high redshift (Vakili et al. 2020): the Z band is included in the red-sequence template and improves the constraints on the redshift of the high-redshift galaxies, while the K_{s} band allows for a clean separation between galaxies and stars in the $(r - K_{\mathrm{s}}) - (r - z)$ colour-colour space.

3.2.1   The LRG sample

Red-sequence galaxies are characterised by a tight colour-redshift relation, so that at any given redshift they follow a narrow ridgeline in the colour-magnitude space. This relation can be exploited to select red galaxies from photometric data and obtain precise photometric redshifts. Here we use the catalogue of LRGs presented in Vakili et al. (2020). It uses a variation of

---

[3]The survey was recently completed, imaging a final total of 1350 deg^2.
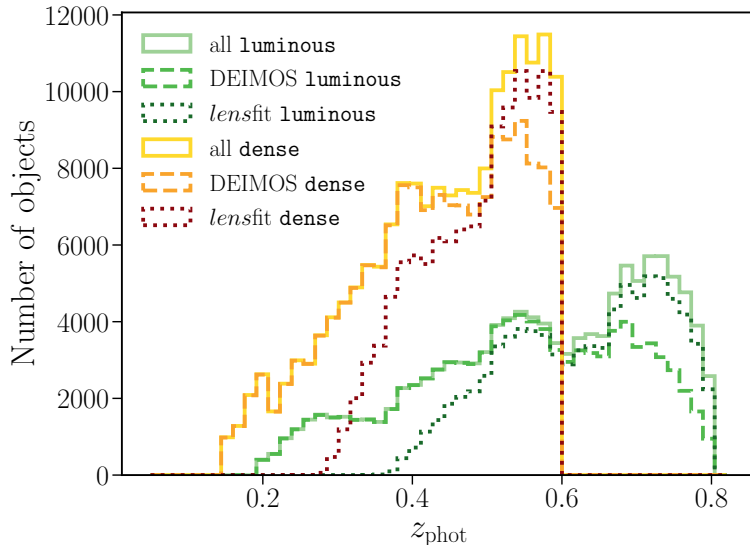
Figure 3.1: Photometric redshift distributions for our density (all) and shape catalogues (*lens*fit and DEIMOS; see text for details). The orange histograms show the distribution for the dense samples, which is limited to $z_{\mathrm{phot}} < 0.6$, whereas the luminous sample (green) is restricted to $z_{\mathrm{phot}} < 0.8$.

the redMagiC algorithm (Rykoff et al. 2014) to select LRGs from the KiDS-1000 data. As detailed in Vakili et al. (2019) and Vakili et al. (2020), the red-sequence template is calibrated using the regions of KiDS that overlap with a number of spectroscopic surveys: SDSS DR13 (Albareti et al. 2017), 2dFLenS (Blake et al. 2016), GAMA (Driver et al. 2011), together with the GAMA G10 region, which overlaps with COSMOS (Davies et al. 2015).

The algorithm is designed to return a sample of LRGs with a constant comoving number density. It achieves this by imposing a redshift-dependent magnitude cut that depends on $m_r^{\mathrm{pivot}}(z)$, the characteristic r-band magnitude of the Schechter (1976) function, assuming a faint-end slope $\alpha = 1$ (for more details, see Vakili et al. 2019, sect. 3.1). We use this to define two samples that differ from each other in terms of their minimum luminosity relative to the luminosity $L_{\mathrm{pivot}}(z)$. We refer to them as our luminous sample (high luminosity, low number density, $L_{\mathrm{min}}/L_{\mathrm{pivot}}(z) = 1$) and dense sample (lower luminosity, higher number density, $L_{\mathrm{min}}/L_{\mathrm{pivot}}(z) = 0.5$). To ensure that the two samples are separate, we removed the galaxies in the dense sample that also belong to the luminous one. However, this does not mean they do not overlap in their physical properties. In particular,
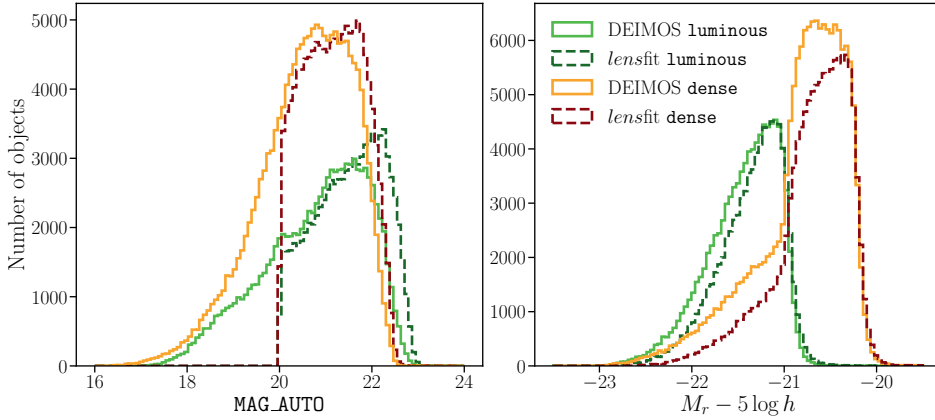
Figure 3.2: The magnitude distributions of the samples used in the analysis. *Left panel:* Histograms of the apparent magnitude, `MAG_AUTO` in the r-band for the galaxies in the `dense` (orange lines) and `luminous` (green lines) samples with shapes measured by *lens*fit (darker colours) and DEIMOS (lighter colours). *Right panel:* Histograms of the absolute magnitudes in the r-band ($K + e$ corrected) for the same samples.

they overlap partially in luminosity, a feature that we will exploit later in the paper.

As shown in Fig. 3.1, the two samples also span different redshift ranges. The `luminous` sample extends from $z = 0.2$ to $z = 0.8$. After applying a conservative mask to select only objects with a high probability to be red-sequence galaxies (corresponding to objects with a clear separation from the star sequence in the colour-colour diagram), we are left with $117\,001$ galaxies, which comprise our density sample. By density sample—not to be confused with the `dense` sample described above—we refer to the sample used to trace galaxy positions, as opposed to the shape sample, which is the sample used for the measurement of galaxy orientations and is composed by the galaxies of the corresponding density sample for which a given shape measurement algorithm is able to measure the galaxy shape. The density and shape samples used in this analysis are visible in Fig. 3.1, where the density samples of the `luminous` and `dense` samples are referred to as 'all' galaxies. The `dense` sample is obtained with the same strategy, but we further impose $z < 0.6$ to ensure the completeness and purity of the sample (see Fig. 4 in Vakili et al. (2020)). This leads to a final sample of $173\,445$ galaxies. As shown in Vakili et al. (2020), the redshift errors are well described by a Student's t–distribution. The width of the distribution increases slightly with redshift, with typical values around $\sigma_z \sim 0.014 - 0.019$.

For further details on the sample selection and redshift estimation, we refer the interested reader to Vakili et al. (2020).

We infer galaxy absolute magnitudes using Lephare[4] (Arnouts & Ilbert 2011), assuming the dust extinction law from (Calzetti et al. 1994) and the stellar population synthesis model from Bruzual & Charlot (2003). We correct our magnitudes to $z = 0$; the K-correction is provided by Lephare and the correction for the evolution of the stellar populations (e−correction) is computed with the python package EzGal[5] (Mancone & Gonzalez 2012), assuming Salpeter initial mass function (Chabrier 2003) and a single star formation burst at $z = 3$. These corrections are based on the magnitudes used to define the colours (`MAG_GAAP`), which are measured using Gaussian apertures (Kuijken et al. 2019). Although ideal for colour estimates, these underestimate the flux and should not be used to compute the luminosity. For that purpose we correct[6] them using the Kron-like `MAG_AUTO` measured from the r-band images by SExtractor (Bertin & Arnouts 1996).

The left panel of Fig. 3.2 shows the distribution in apparent magnitude `MAG_AUTO` for galaxies in the `dense` and `luminous` samples for which shapes were determined by *lens*fit or DEIMOS. In Sect. 3.3 we describe the two shape measurement methods and explain the difference in their number counts. We note that the LRGs are much brighter than the limiting magnitude of KiDS in the r-band. The corresponding distributions in absolute magnitude in the rest-frame r filter, K+e corrected to $z = 0$, are presented in the right panel of Fig. 3.2. This shows that the `dense` sample overlaps somewhat with the `luminous` sample in terms of luminosity, as a consequence of the photometric redshift uncertainty[7].

---

[4]https://www.cfht.hawaii.edu/~arnouts/LEPHARE/lephare.html

[5]http://www.baryons.org/ezgal

[6]The total flux in the x filter can be computed using $m_x = $ `MAG_AUTO`$_r$ + (`MAG_GAAP`$_x$ − `MAG_GAAP`$_r$), which implicitly assumes that colour gradients are negligible.

[7]The selection through the redshift-dependent apparent magnitude cut results in an overlap in apparent magnitudes of the `dense` and `luminous` samples. Because the cut is redshift-dependent, this implies a threshold in luminosity: In the case of perfect redshifts, this would result in a disjoint sample, because we removed the galaxies from the `dense` sample that overlap with the `luminous` one. The photometric redshift uncertainty, however, assigns to galaxies with the same apparent magnitude different luminosities, and thus a portion of the `dense` sample extends above the luminosity threshold of the `luminous` sample.

3.2.2   Satellite galaxy fraction estimation

Observations suggest that satellite galaxies are only weakly aligned (see e.g. Georgiou et al. 2019b, for recent constraints) and thus suppress the IA signal at large scales. We do not take this into account in our analysis but provide here an estimate of the fraction of satellites we expect in our samples. Such information will be useful for future modelling studies.

    We used the publicly available G3GGal and G3GFoFGroup catalogues (Robotham et al. 2011) from the GAMA survey (Driver et al. 2009, 2011; Liske et al. 2015). Since KiDS overlaps with GAMA, these catalogues provide group information for a subset of our galaxies, obtained with a Friends-of-Friends algorithm. We cross-matched our LRG samples with the G3GGal catalogue and selected galaxies with $z < 0.21$ ($z < 0.32$), which provide a roughly volume-complete match to the dense (luminous) sample. With the information in both group catalogues, we identify both the brightest group galaxies and ungrouped galaxies as centrals, and the rest as satellites. With this strategy, we obtain $f_{\mathrm{sat}} = 0.34$ for our dense×GAMA sample and $f_{\mathrm{sat}} = 0.23$ for the luminous×GAMA[8]. Since our samples are selected to resemble the same galaxy populations at different redshifts, these estimates should be fairly representative beyond the redshift range probed by our direct comparison.

3.3   Shape measurements

In addition to precise redshifts, a successful IA measurement requires accurate shape measurements. In this work, we compare two different algorithms, DEIMOS and *lens*fit both in terms of their ability to recover reliable ellipticity measurements and the resulting IA signal. Exploring the dependence of the IA signal on the shape measurement algorithm is important if one aims to provide informative priors to lensing studies (Singh & Mandelbaum 2016). Both algorithms have been used to analyse KiDS data: DEIMOS to provide the shape catalogue (Georgiou et al. 2019a) for a number of IA studies, while *lens*fit was used for cosmic shear analyses (see Giblin et al. 2021, for the most recent shape measurements).

---

[8]These estimates refer to the full samples, but should be representative for the shape samples as well.

3.3.1   DEIMOS

DEIMOS (Melchior et al. 2011) is a moment-based shape measurement algorithm designed to measure the moments of the surface brightness distribution from an image, which are subsequently used to estimate the ellipticity. The main features of DEIMOS are its rigorous treatment of the PSF moments to arbitrary order, the lack of model assumptions and the flexibility in changing the size of the weight function so that it is possible to assign more importance to different parts of a galaxy while performing the shape measurement (bulge or outskirts).

The unweighted moments of the surface brightness $G(\vec{x})$ are defined as

$$Q_{ij} \equiv \{G\}_{ij} = \int G(\vec{x}) \, x^i y^j \, \mathrm{d}x \, \mathrm{d}y \,, \tag{3.1}$$

where (x, y) are the Cartesian coordinates with origin at the galaxy's centroid. The complex ellipticity is then defined in terms of the second-order moments as

$$\epsilon \equiv \epsilon_1 + \mathrm{i}\epsilon_2 = \frac{Q_{20} - Q_{02} + 2\mathrm{i}\,Q_{11}}{Q_{20} + Q_{02} + 2\sqrt{Q_{20}\,Q_{02} - Q_{11}^2}} \,. \tag{3.2}$$

In practice, unweighted moments cannot be used because of noise in the images, and weighted moments have to be employed instead. We will return to this issue later. Moreover, the galaxy images are smeared and distorted by the atmospheric blurring and the telescope optics, so that the observed image, G^*, is convolved with the PSF kernel $P(\vec{x})$,

$$G^*(\vec{x}) = \int G(\vec{x}') \, P(\vec{x} - \vec{x}') \, \mathrm{d}\vec{x}' \,. \tag{3.3}$$

The DEIMOS algorithm estimates the unweighted moments by correcting the observed weighted moments of the galaxy surface brightness for the convolution by the PSF. The underlying mathematical framework is a deconvolution in moment space. In order to measure the moments in Eq. (3.1) we then need to deconvolve them. This can easily be achieved in Fourier space, where the convolution becomes a product. Using the Cauchy product, we can write (Melchior et al. 2011):

$$\{G^*\}_{ij} = \sum_k^i \sum_l^j \binom{i}{k}\binom{j}{l} \{G\}_{kl}\{P\}_{i-k,j-l} \,, \tag{3.4}$$

which shows that the $(i + j)$-order convolved moments are determined by the same- or lower-order moments of the galaxy and the PSF kernel. The deconvolution procedure to estimate the galaxy moments is to invert the above hierarchical system of equations, starting from the zeroth order.

As mentioned above, it is necessary to introduce a weight function to avoid noise dominating the second-order moments outside the galaxy light profile. In this work, we adopt an elliptical Gaussian weight function with size $r_{\mathrm{wf}} = r_{\mathrm{iso}}$, where r_{iso} is the isophotal radius, defined as $r_{\mathrm{iso}} = \sqrt{A_{\mathrm{iso}}/\pi}$, following Georgiou et al. (2019a). The area A_{iso} of the galaxy's isophote is computed using the `ISOAREA_IMAGE` by SExtractor (Bertin & Arnouts 1996). The shape measurement procedure is the same as described in Georgiou et al. (2019a) and we point the interested reader to their Section 2 for a detailed description of the algorithm. In Appendix A1 we report our analysis of the measured shape bias for different setups, which led to our final choice reported above.

Using DEIMOS, we successfully measured the shapes of 96 863 galaxies from the `luminous` sample, $\sim 83\%$ of the corresponding density sample, and 152 832 shapes from the `dense` sample, roughly $\sim 88\%$ of its density sample. The shape measurements mainly fail[9] for the faintest galaxies in the sample.

3.3.2 *lens*fit

The second shape catalogue is obtained using the self-calibrating version of *lens*fit (Miller et al. 2013), described in more detail in Fenech Conti et al. (2017). It is a likelihood-based model-fitting method that fits a PSF-convolved two-component bulge and disk galaxy model. This is applied simultaneously to the multiple exposures in the KiDS-1000 r-band imaging, to get an ellipticity estimate for each galaxy.

*lens*fit provides shapes for 84 785 galaxies from the `luminous` sample (72% of the density sample), and for 121 500 galaxies from the `dense` sample (70% of the density sample). The lower completeness with respect to DEIMOS is largely explained by the fact that *lens*fit has been optimised for cosmic shear studies, where the signal is maximised for high-redshift galaxies, which are typically small and faint. Whilst *lens*fit could determine ellipticity measurements for the large bright galaxies with `MAG_AUTO` < 20, this model-fitting algorithm becomes prohibitively slow given the large number

---

[9]We only considered shapes with `flag_DEIMOS==0000`, corresponding to measurements that do not raise any flag (see Georgiou et al. 2019a).

of pixels that these bright galaxies span. Therefore, the *lens*fit catalogue only contains galaxies fainter than `MAG_AUTO` > 20 (hence the sharp cut-off in apparent magnitude in Fig. 3.2). It performs better than DEIMOS for relatively faint and low signal-to-noise (S/N) galaxies. As these are preferentially found at higher redshifts, this also explains the different redshift distributions, as illustrated in Fig. 3.1.

3.3.3   Image simulations

We want to measure the shapes of galaxies from images that are corrupted by noise and blurred by the atmosphere and telescope optics. These bias the inferred shapes and thus need to be carefully corrected for. Although both DEIMOS and *lens*fit are designed to do so, residual biases remain. These can be expressed as (Heymans et al. 2006)

$$\epsilon_i^{\mathrm{obs}} = (1 + m_i)\epsilon_i^{\mathrm{true}} + c_i , \qquad (3.5)$$

with $i \in \{1, 2\}$ the ellipticity components introduced in 3.2. Here $\epsilon_i^{\mathrm{true}}$ is the true ellipticity, while $\epsilon_i^{\mathrm{obs}}$ is the output of the shape measurement algorithm; m_i is the multiplicative bias and c_i is the additive bias. Differently from what is done in lensing studies (e.g. Kannawadi et al. 2019), here we calibrated the ellipticity rather than the shear. Our aim is to determine the biases in our shape measurements using realistic image simulations, with a precision that is better than the statistical error on our IA signal.

We stress that although it is important to start with an algorithm that does not lead to a large bias in the first place, what matters the most is to calibrate the residual bias on realistic image simulations in order to properly account for galaxy blending and the different observing conditions (Hoekstra et al. 2017; Kannawadi et al. 2019; Samuroff et al. 2018; MacCrann et al. 2020). We use dedicated image simulations generated with the COllege pipeline (COSMOS-like lensing emulation of ground experiments; Kannawadi et al. 2019). These simulations reproduce the observations from the Cosmic Evolution Survey (COSMOS, Scoville et al. 2007), for which we have both KiDS imaging (KiDS-COSMOS) and deeper images from the *Hubble* Space Telescope (HST). We use the HST observations to generate our input catalogue and simulate the KiDS observations by varying the observation conditions. Under the assumption that COSMOS is representative of our galaxy sample (in practice we only require that it covers the S/N and size parameter space, while we do not need the galaxy distributions to match) we study the m−bias properties of the LRGs in our KiDS-COSMOS

((a))

((b))
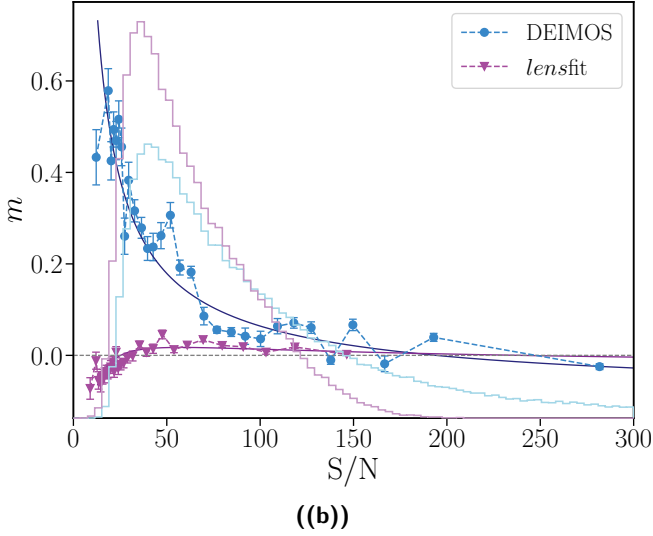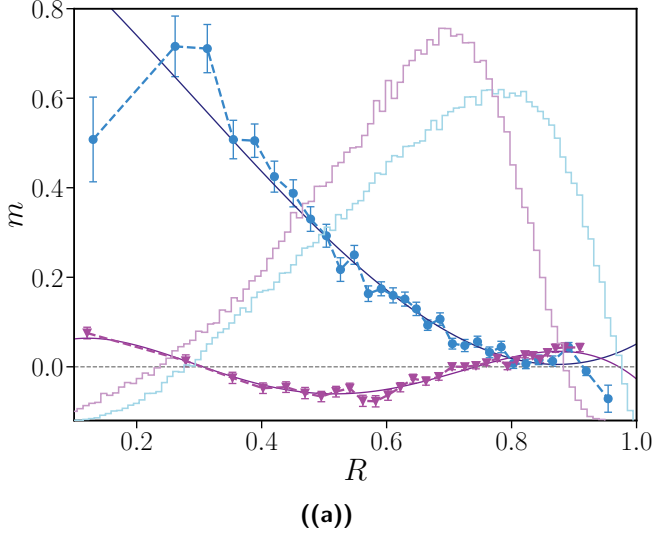
Figure 3.3: Average multiplicative bias, $m = (m_{\epsilon_1} + m_{\epsilon_2})/2$, as a function of (a) the galaxy resolution, R, and (b) the signal-to-noise ratio, S/N. Each point is measured on the same number of simulated galaxies and the error bars are estimated using bootstraps. For a comparison we also display in the background the weighted distribution of the two definitions of R and the S/N in the real data for the dense shape samples (pink: *lens*fit; blue: DEIMOS). The solid lines show the polynomial fit to $m(R)$ and $m(\text{S/N})$, which guided the construction of the two-dimensional bias surface.

field and use the bias model obtained from this set of galaxies to calibrate our full sample.

The image simulations used in this work differ slightly from those presented in Kannawadi et al. (2019) because we required a larger number of simulated LRGs for our calibration. To achieve this, we adopted the ZEST catalogue (Zurich Estimator of Structural Type; Scarlata et al. 2007; Sargent et al. 2007) for the input galaxy parameters. We generated 52 KiDS-like images by varying the observing conditions and rotating the galaxies. We used 13 different PSF sets and four rotations per each image. Since our underlying galaxy selection is identical for both the *lens*fit and DEIMOS shape catalogues, we employed the same suite of simulations for both calibrations.

The shape measurement bias depends on the size, S/N, radial surface brightness profile and ellipticity of the galaxy, as well as the observing conditions. Of these, the size and S/N are the most relevant, and we use these to capture the dependence of the bias for our set of simulated galaxies. Rather than the intrinsic size of the galaxy, we use a proxy for how well it is resolved: R quantifies the relative size of the PSF compared to the size of the galaxy. Here, we adopt two slightly different definitions, depending on the shape algorithm employed. For DEIMOS we use

$$R^{\mathrm{DEIMOS}} = 1 - \frac{T^{\mathrm{PSF}}}{T^{\mathrm{gal}}} \,, \tag{3.6}$$

where $T^{\mathrm{PSF}} = Q_{20}^{\mathrm{PSF}} + Q_{02}^{\mathrm{PSF}}$ and $T^{\mathrm{gal}} = Q_{20}^{*\mathrm{gal}} + Q_{02}^{*\mathrm{gal}}$, where $Q_{ij}^{*\mathrm{gal}}$ are the unweighted moments of the PSF-convolved surface brightness profile (see Eqs. 3.4 and 3.1). In the case of *lens*fit we use

$$R^{lens\mathrm{fit}} = 1 - \frac{r_{\mathrm{PSF}}^2}{\left(r_{\mathrm{ab}}^2 + r_{\mathrm{PSF}}^2\right)} \,, \tag{3.7}$$

where $r_{\mathrm{PSF}}^2 = \sqrt{P_{11}P_{22} - P_{12}^2}$ and $r_{\mathrm{ab}} = r_{\mathrm{e}}\sqrt{q}$. Here, P_{ij} are the *lens*fit PSF weighted quadrupole moments (see Eq. (2) in Giblin et al. 2021), measured with a circular Gaussian function of size 2.5 pixels; r_{e} is the half-light radius measured along the major axis of the best-fit elliptical profile by *lens*fit, which is an estimate of the true galaxy size before PSF-convolution, while q is the axis ratio, such that r_{ab} is the azimuthally averaged size of the galaxy. As we can see, R can in practice only assume values between 0 and 1, where 1 corresponds to galaxies with sizes that are much larger than the PSF.

We evaluate the multiplicative bias m in bins of S/N and R that contain an equal number of galaxies and the error bars are computed using 500 bootstrap realisations. The resulting biases are presented in Fig. 3.3 for both *lens*fit and DEIMOS. We find that the two components $\epsilon_{1,2}$ show similar dependencies, and, therefore, we calibrate the bias for the two components jointly. The additive bias for both components is consistent with zero, and thus we do not consider it further in our calibration.

For both $m(\mathrm{S/N})$ and $m(R)$, we find that *lens*fit has a small bias and thus also our correction is small; in general, it performs better than DEIMOS for poorly resolved galaxies and low S/N. It is, however, prohibitively slow when measuring shapes for large galaxies, limiting the *lens*fit sample to galaxies with $m_r > 20$. In contrast, DEIMOS shows a large bias for low values of R: the galaxy size correlates with its ellipticity, and we find that removing the highly elliptical galaxies significantly reduces the bias. However, once we calibrate the shapes of those galaxies, we recover a very similar signal for the full shape sample and the one cut in ellipticity. Similarly, we have also tested that adding inverse-variance weights to account for these noisy galaxies does not significantly improve our signal. This motivates our choice to keep all galaxies in our sample and not to introduce additional weighting; we assume that the measurements are dominated by shape noise only.

We can see that $m(R)$ for both DEIMOS and *lens*fit is well described by a polynomial curve, which we truncate at degree 3 and 4, respectively, while $m(\mathrm{S/N})$ is well described by the expansion: $d(\mathrm{S/N}) = d_1/\sqrt{\mathrm{S/N}} + d_2/(\mathrm{S/N})$. We combine the two individual bias dependencies into a single bias surface as detailed in Appendix A1. The specific functional forms for the two shape methods differ to better adapt the surface to our observed bias. We use these empirical relations to infer the m-bias associated with each galaxy, given its S/N and R.

To ensure that our empirical correction performs well on our sample, we selected sets of galaxies from the image simulations that resemble our LRG samples by reproducing the observed distributions in S/N and R. We measured the residual biases for these samples, defined as the difference in the estimated m-bias (inferred using our model for the bias) and the bias measured directly from the simulations for the given set of galaxies. For the DEIMOS shape method, we find an average residual of -0.002 ± 0.007 for the `dense`-like sample, while this is -0.002 ± 0.008 for the `luminous`-like sample. Similarly, in the case of *lens*fit the residuals for the `luminous`-like and `dense`-like galaxies are, respectively, -0.0014 ± 0.0013 and -0.0019 ± 0.0020.
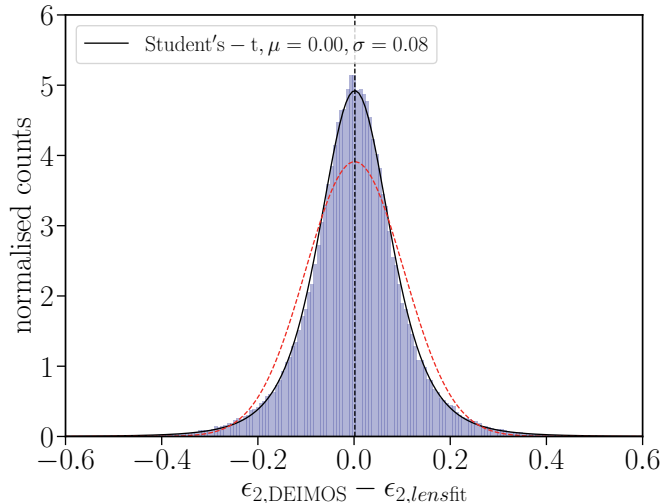
Figure 3.4: Histogram of the difference of the ϵ_1 component of the ellipticity measured by the two shape measurement algorithms, *lens*fit and DEIMOS, on a common sub-sample of galaxies, after applying the m−bias correction as described in the text. The ϵ_2 component shows the same behaviour. The distribution is more peaked than a Gaussian (red dashed line) and is best described by a Student's t−distribution with $\nu = 4.3$, and a width $\sigma = 0.08$ with zero mean (black solid line).

As we will see later, this is much smaller than the uncertainty in the IA measurements: the average bias introduced by the shape measurement process is subdominant and does not affect our best estimate of the IA amplitude.

The LRGs are relatively bright and we thus expect the shape measurements to be shape noise-dominated. This also implies that the DEIMOS and *lens*fit measurements are correlated. To quantify this, we show the distribution of the difference between the m−corrected ellipticities measured by the two algorithms in Fig. 3.4. The distribution is more peaked than a Gaussian, and well described by a Student's t−distribution centred on zero, with $\nu = 4.30$ (degrees of freedom) and with scale parameter $\sigma = 0.08$. This is to be compared to the intrinsic ellipticity of galaxies, which is about $\epsilon_{\rm rms} = 0.12$ based on DEIMOS measurements for galaxies with apparent magnitude $m_r < 20$. It is interesting to note that our sample is considerably rounder than a typical cosmic shear sample, as expected for an LRG sample (see for example van Uitert et al. 2012); this implies that it might be affected differently by a weighting scheme in a lensing analysis. The differences between the DEIMOS and *lens*fit measurements are caused by differences in how each method deals with noise in the images.

3.4 Correlation function measurements

We measured the IA signal using the two-points statistic w_{g+}, defined as the projection along the line-of-sight of the cross-correlation between galaxy positions and galaxy shapes. It measures the tendency of galaxies to point in the direction of another galaxy as a function of their comoving transverse separation, r_p, and comoving line-of-sight separation, Π. To quantify the alignment signal in our data, we employed the estimator presented in Mandelbaum et al. (2006)[10],

$$\hat{\xi}_{g+}(r_p, \Pi) = \frac{S_+ D - S_+ R_D}{R_S R_D},$$ (3.8)

where R_D and R_S are catalogues of random points designed to reproduce the galaxy distribution of the density and shape samples, respectively. We indicate with D the density sample that provides the galaxy positions, while S_+ is the shape sample, such that the quantity

$$S_+ D = \sum_{i \neq j} \gamma_+(i|j),$$ (3.9)

gives us the tangential shear component of the galaxy pair (i, j), $\gamma_+(i|j)$, where i is extracted from the shape sample and j from the density sample. γ_+, in turn, is defined as

$$\gamma_+(i|j) = \frac{1}{\mathcal{R}} \mathfrak{R} \left[\epsilon_i \exp(-2i\phi_{ij}) \right],$$ (3.10)

where $\mathfrak{R}$ denotes the real part; ϵ_i is the complex ellipticity associated with the galaxy i, $\epsilon_i = \epsilon_{1,i} + i\epsilon_{2,i}$, whose components 1,2 are measured by the shape measurement algorithms presented in Sect. 3.3; ϕ_{ij} is the polar angle of the vector that connects the galaxy pair; $\mathcal{R} = \partial\epsilon/\partial\gamma$ is the shear responsivity and it quantifies by how much the ellipticity changes when a shear is applied: for an ensemble of sources, $\mathcal{R} = 1 - \epsilon_{rms}^2$.

The galaxy clustering signal is computed with the standard estimator (Landy & Szalay 1993),

$$\hat{\xi}_{gg}(r_p, \Pi) = \frac{DD - 2DR_D - R_D R_D}{R_D R_D}.$$ (3.11)

---

[10] Instead of normalising by $R_S R_D$, we actually normalise by the density - randoms vs. shapes pair count, $R_D D_S$. This significantly speeds up the computation and has been tested to have negligible impact (Johnston et al. 2019).

To measure our clustering and IA signals, we used uniform random samples that reproduce the KiDS footprint, accounting for the masked regions; to these we assigned redshifts randomly extracted from the galaxy unconditional photometric redshift distributions. For each sample, we constructed the random sample to match their redshift distribution.

To account for the spatial variation in the survey systematics, we applied weights to the galaxies when computing the signal, as discussed in Vakili et al. (2020). These weights are designed to remove the systematic-induced variation in the galaxy number density across the survey footprint. For a detailed discussion of how the weights are generated and tested, we refer to Sect. 4 in Vakili et al. (2020). To capture the variation in the survey systematics along the line-of-sight, we split each sample into three redshift bins and assigned the weights to those sub-samples. We tested that this procedure does not induce a correlation between the galaxy weights and the redshifts themselves. We also verified that the impact of the weights is very small and can be neglected when considering the split in luminosity of the samples (see Sect. 3.6.1). We applied such weights to both the density and shape samples.

In this work, we measured the clustering and IA signals using an updated version of the pipeline presented in Johnston et al. (2019), which makes use of the publicly available software Treecorr (Jarvis et al. 2004)[11] for clustering correlations. $\xi_{\mathrm{g+}}$ and ξ_{gg} are then projected by integrating over the line-of-sight component of the comoving separation, Π,

$$\hat{w}_{gi}(r_{\mathrm{p}}) = \int_{-\Pi_{\max}}^{\Pi_{\max}} \mathrm{d}\Pi \, \hat{\xi}_{gi}(r_{\mathrm{p}}, \Pi) \quad i = \{+, g\} \,. \tag{3.12}$$

The largest scales probed in this analysis are limited by the effective survey area (~ 777 deg^2). We set a maximum transverse separation of $60 \, h^{-1}\mathrm{Mpc}$ and measure the signal in 10 logarithmically spaced bins, from $r_{\mathrm{p,min}} = 0.2 \, h^{-1}\mathrm{Mpc}$.

We performed the measurements for three different setups: we adopt $\Pi_{\max} = 120 \, h^{-1}\mathrm{Mpc}$ as the fiducial case, but repeated the analysis for $\Pi_{\max} = 90 \, h^{-1}\mathrm{Mpc}$ and $\Pi_{\max} = 180 \, h^{-1}\mathrm{Mpc}$ (see Appendix A5). We always bin our galaxies in equally spaced bins with $\Delta\Pi = 10 \, h^{-1}\mathrm{Mpc}$. We observe an extended signal to $\Pi > 180 \, h^{-1}\mathrm{Mpc}$, but the signal is comparable to the noise at those distances.

---

[11]https://github.com/rmjarvis/TreeCorr

Our choice of Π_{max} is conservative since the uncertainties in the photometric redshifts are $\sigma_z < 0.02(1 + z)$ for both the `dense` and `luminous` samples (Vakili et al. 2020), and if we choose Π_{max} based on the 1σ uncertainty in the photometric redshifts (Joachimi et al. 2011), we could potentially reduce Π_{max} to $70\,h^{-1}\mathrm{Mpc}$. However, this might be too optimistic given that the error on σ_z increases with redshift. The choice of Π_{max} is motivated by two opposite necessities: to maximise the S/N, we want to minimise the amount of signal that we discard, whilst we also want to avoid adding uncorrelated pairs that would increase the noise. To find the best balance, we calculate the S/N of our signal as a function of (r_p, Π) by dividing the measured $w_{gg}(r_p, \Pi)$ by the root-diagonal of the jackknife covariance. We truncate at Π_{max} based on the $10\,\sigma$ detection, which roughly corresponds to $\Pi_{max} = 120\,h^{-1}\mathrm{Mpc}$. In addition to these considerations, there is a further motivation to limit the integral to modest line-of-sight separations: as discussed in Appendix A3, the contamination from galaxy-galaxy lensing has a shallower dependence on the line-of-sight separation; as we move along the Π direction, we see an increase in the contamination with a mild increase in the IA signal, until lensing dominates.

The error bars are computed via a delete-one jackknife re-sampling of the observed volume. The covariance matrix is constructed as

$$\mathrm{Cov}_{jack.} = \frac{N-1}{N} \sum_{\alpha=1}^{N} (w^\alpha - \bar{w})(w^\alpha - \bar{w})^\top, \qquad (3.13)$$

where w^α is the signal measured from jackknife sample α, while $\bar{w}$ is the average over N samples; $\top$ denotes the transpose of the vector.

The number of regions N is ultimately set by the size of the survey and the scales we aim to probe. A maximum value of $r_p = 60\,h^{-1}\mathrm{Mpc}$ corresponds to an angular separation of ~ 8 degrees (`dense` sample) and ~ 6 degrees (`luminous` sample) at the lowest redshifts probed in the analysis. However, to increase the number of jackknife regions, we decided to set the minimum angular scale to 5 degrees, which strictly satisfies our requirement only for $z \gtrsim 0.2$. This is motivated by the fact that the majority of our galaxies are at high redshift and hence only $\lesssim 5\%$ of our galaxies have unreliable error estimates in the last r_p–bin. The total number of jackknife regions that we are able to obtain for our samples is $N = 37$. We corrected our inverse covariance matrices, which enter into our likelihood estimations, as recommended in Hartlap et al. (2007): because of the presence of noise, the inverse of a covariance matrix obtained from a finite number of jackknife (or bootstrap) realisations is a biased estimator of the true inverse

covariance matrix.

3.5 Modelling

The linear alignment model (Catelan et al. 2001; Hirata & Seljak 2004) predicts a linear relation between the contribution to the shear induced by IA and the quadrupole of the gravitational field responsible of the tidal effect. This can be expressed as

$$\gamma^{\mathrm{I}} = (\gamma^{\mathrm{I}}_{+}, \gamma^{\mathrm{I}}_{\times}) = -\frac{C_1}{4\pi G}(\partial_x^2 + \partial_y^2, \partial_x\partial_y)\Phi_{\mathrm{p}} \,, \tag{3.14}$$

where the partial derivatives are with respect to comoving coordinates and provide the tangential and cross components of the shear with respect to the x-axis; Φ_{p} is the gravitational potential at the moment of galaxy formation, assumed to take place during the matter-dominated era (Catelan et al. 2001); C_1 is a normalisation constant and G is the gravitational constant.

Using Eq. (3.14), by correlating the intrinsic shear with itself or with the matter density field δ, we can construct the relevant equations for the IA correlation functions (Hirata & Seljak 2004). In Fourier space, the matter density-shear power spectrum (δI) becomes

$$P_{\delta\mathrm{I}}^{\mathrm{LA}}(k, z) = A_{\mathrm{IA}}C_1\rho_{\mathrm{c}}\frac{\Omega_m}{D(z)}P_{\delta\delta}^{\mathrm{lin}}(k, z) \,. \tag{3.15}$$

Here, $D(z)$ is the linear growth factor, normalised to unity at $z = 0$, ρ_{c} is the critical density of the Universe today, and $P_{\delta\delta}^{\mathrm{lin}}$ is the linear matter power spectrum. We set $C_1 = 5 \times 10^{-14}h^{-2}M_{\odot}^{-1}\mathrm{Mpc}^3$ based on the IA amplitude measured at low redshifts using SuperCOSMOS (Hartlap, Simon & Schneider Bro), which is the standard normalisation for IA power spectra.

Galaxies are biased tracers of the matter density field, and at large scales this relation is linear, $\delta_{\mathrm{g}} \sim b_{\mathrm{g}}\delta$. We can thus relate the galaxy position–intrinsic shear power spectrum to the matter density–intrinsic shear power spectrum via the galaxy bias b_{g}:

$$P_{\mathrm{gI}}^{\mathrm{LA}}(k, z) = b_{\mathrm{g}}P_{\delta\mathrm{I}}^{\mathrm{LA}}(k, z) \,, \tag{3.16}$$

which is the power spectrum of interest for our analysis.

A successful modification of the LA model replaces the linear matter power spectrum in Eq. (3.15) with the non-linear one, to account for the non-linearities arising at intermediate scales (Bridle & King 2007). This

so-called NLA model was succesfully employed in a number of studies (e.g. Blazek et al. 2011; Joachimi et al. 2011) and here we follow the same approach to model our signal. More sophisticated treatments of the IA signal, which include the modelling of the mildly or fully non-linear scales, have been developed in the last decade (Schneider & Bridle 2010; Blazek et al. 2019; Fortuna et al. 2021a), but given the scales probed in our analysis (see Sect. 3.5.3) and the homogeneous characteristics of the galaxy population studied, the NLA model provides a sufficient description for this work. Unless stated otherwise, in the following we always assume the NLA model as our reference choice. To generate the linear matter power spectrum we use CAMB[12] (Lewis et al. 2000; Lewis & Bridle 2002), while the non-linear modifications are computed using Halofit (Smith et al. 2002) with the implementation presented in Takahashi et al. (2012). In the rest of the paper, we simply refer to the non-linear matter power spectrum as $P_{\delta\delta}(k, z)$.

3.5.1 Incorporating the photometric redshift uncertainty into the model

The use of photometric redshifts results in an uncertainty in the estimated distance of the galaxies, which has to be included in the model. In particular, if we express the correlation function ξ_{gI} in terms of the two components of the galaxy separation vector $\mathbf{r}$, (r_{p}, Π), we can map the redshift probability distribution into the probability that the true values of r_{p} and Π correspond to their photometric estimates. Here, we follow the approach derived in Joachimi et al. (2011) and use their approximated expression,

$$\xi_{\mathrm{gI}}^{\mathrm{ph}}(\bar{r}_{\mathrm{p}}, \bar{\Pi}, \bar{z}_{\mathrm{m}}) = \int \frac{\mathrm{d}\ell\,\ell}{2\pi} J_2\left(\ell\theta(\bar{r}_{\mathrm{p}}, \bar{z}_{\mathrm{m}})\right) C_{\mathrm{gI}}\left(\ell; \bar{z}_1(\bar{z}_{\mathrm{m}}, \bar{\Pi}), \bar{z}_2(\bar{z}_{\mathrm{m}}, \bar{\Pi})\right) \ . \quad (3.17)$$

The observables are: $\bar{z}_1$ and $\bar{z}_2$, the photometric redshift estimates of the pair of galaxies for which we are measuring the correlation, and their angular separation θ. These can be related to $(\bar{r}_{\mathrm{p}}, \bar{\Pi}, \bar{z}_{\mathrm{m}})$, through the approximate relations

$$z_{\mathrm{m}} = \frac{1}{2}(z_1 + z_2) \ , \tag{3.18}$$

$$r_{\mathrm{p}} \approx \theta\chi(z_{\mathrm{m}}) \ , \tag{3.19}$$

$$\Pi \approx \frac{c}{H(z_{\mathrm{m}})}(z_2 - z_1) \ , \tag{3.20}$$

---

[12]https://camb.info

where $\chi(z_{\rm m})$ and $H(z_{\rm m})$ are, respectively, the comoving distance and the Hubble parameter at redshift z_m, and c is the speed of light.

The conditional redshift probability distributions are incorporated into the angular power spectrum $C_{\rm gI}$, which can be expressed in terms of the three-dimensional power spectrum $P_{\rm gI}(k, z)$,

$$C_{\rm gI}(\ell, \bar{z}_1, \bar{z}_2) = \int_0^{\chi_{\rm hor}} {\rm d}\chi' \frac{p_n(\chi'|\chi(\bar{z}_1)) p_\epsilon(\chi'|\chi(\bar{z}_2))}{\chi'^2}$$
$$\times P_{\rm gI}\left(\frac{\ell + 1/2}{\chi'}, z(\chi')\right) \quad (3.21)$$

where we have implicitly assumed the flat-sky and Limber approximations, and n and ϵ indicate the density and shape sample respectively. $p(\chi'|\chi)$ are the conditional comoving distance probability distributions, which are related to the redshift distributions via $p(\chi'|\chi){\rm d}\chi = p(z|\bar{z}){\rm d}z$. When computing our predictions, we bin our photometric data and compute the corresponding $p(z|\bar{z}) \equiv p(z_{\rm spec}|z_{\rm phot})$ per each bin; z_1 and z_2 in Eq. (3.18) corresponds to the mean values of the probability distribution with z_1 being the mean of the i-th bin and z_2 of the j-th bin. In Appendix A2 we show the redshift distributions entering our analysis. We refer the interested reader to appendices A.2 and A.3 in Joachimi et al. (2011) for the full derivation of equation 3.21. The exact same formalism can then be applied to the clustering signal, where $C_{\rm gI} \to C_{\rm gg}$, $J_2 \to J_0$ and the redshift distributions are those corresponding to the density sample.

The projected correlation functions $w_{\rm g+}$ and w_{gg} can then be obtained as:

$$w_{\rm g+}(r_{\rm p}) = \int {\rm d}\bar{\Pi} \int {\rm d}z_{\rm m} \mathcal{W}(\bar{z}_{\rm m}) \xi_{\rm gI}^{\rm ph}(\bar{r}_{\rm p}, \bar{\Pi}, \bar{z}_{\rm m}) \quad (3.22)$$

and

$$w_{\rm gg}(r_{\rm p}) = \int {\rm d}\bar{\Pi} \int {\rm d}z_{\rm m} \mathcal{W}(\bar{z}_{\rm m}) \xi_{\rm gg}^{\rm ph}(\bar{r}_{\rm p}, \bar{\Pi}, \bar{z}_{\rm m}) , \quad (3.23)$$

where the redshift window function $\mathcal{W}(z)$ is defined as (Mandelbaum et al. 2011):

$$\mathcal{W}(z) = \frac{p_i(z)p_j(z)}{\chi^2(z){\rm d}\chi/{\rm d}z} \left[\int {\rm d}z \frac{p_i(z)p_j(z)}{\chi^2(z){\rm d}\chi/{\rm d}z}\right]^{-1} , \quad (3.24)$$

where $p_{i,j}(z)$ with $i, j \in S, D$ are now the unconditional redshift distributions for the shape and density samples, and $\chi(z)$ is the comoving distance to redshift z.

3.5.2   Contamination to the signal

All possible two-point correlations between galaxy shapes and positions contribute to the estimator in Eq. (3.12). Following the notation in Joachimi & Bridle (2010), here we consider: the correlation between the intrinsic shear and the galaxy position (g+), which is the quantity we aim to constrain; but also the correlation between gravitational shear and galaxy position, sourced by the galaxy lensing of a background galaxy by a foreground galaxy (gG); and the apparent modification of the galaxy number counts due to the effect of lensing magnification, which affects both the correlations with the intrinsic shear and the gravitational shear (mI and mG).

Among these effects, galaxy-galaxy lensing is the main contaminant to our signal. While IA requires physically close galaxies, galaxy-galaxy lensing occurs between galaxies at different redshifts. This implies that the level of contamination depends on our ability to select close pairs of galaxies, which ultimately depends on the photometric redshift precision. For this reason, the width and the tails of the redshift distributions play an important role in the amount of contamination. Since our $p(z^{\mathrm{spec}}|z^{\mathrm{phot}})$ are quite narrow (see Appendix A2) we do not expect this to be a major effect in our data. Nevertheless, we fully model both lensing and magnification effects, and account for them when interpreting the signal. We note that the sign of the gI and gG terms are opposite, such that adding the lensing to the model allows us to remove its suppressing contribution and capture the true IA signal.

It is convenient to write the various correlations in terms of the projected angular power spectra: indicating with n the density sample (that provides the galaxy positions) and with ϵ the shape sample, we have

$$C_{n\epsilon}^{(ij)}(\ell) = C_{\mathrm{gI}}^{(ij)}(\ell) + C_{\mathrm{gG}}^{(ij)}(\ell) + C_{\mathrm{mI}}^{(ij)}(\ell) + C_{\mathrm{mG}}^{(ij)}(\ell) , \qquad (3.25)$$

where, in a flat cosmology, these read

$$C_{\mathrm{gG}}^{(ij)}(\ell) = b_g \int_0^{\chi_{\mathrm{hor}}} \mathrm{d}\chi \frac{p_n^{(i)}(\chi)q_\epsilon^{(j)}(\chi)}{\chi^2} P_{\delta\delta}\left(\frac{\ell+1/2}{\chi},\chi\right) , \qquad (3.26)$$

$$C_{\mathrm{mI}}^{(ij)}(\ell) = 2(\alpha^{(i)} - 1)C_{\mathrm{IG}}^{(ij)}(\ell), \qquad (3.27)$$

and

$$C_{\mathrm{mG}}^{(ij)}(\ell) = 2(\alpha^{(i)} - 1)C_{\mathrm{GG}}^{(ij)}(\ell) . \qquad (3.28)$$

Here $\alpha^{(i)}$ is the slope of the faint-end logarithmic luminosity function[13]. The lensing weight function, q_X, $X \in \{n, \epsilon\}$ is defined as

$$q_X(\chi) = \frac{3H_0^2 \Omega_m}{2c^2} \frac{\chi}{a(\chi)} \int_0^{\chi_{\mathrm{hor}}} \mathrm{d}\chi' p_X(\chi') \frac{\chi' - \chi}{\chi'} . \qquad (3.29)$$

$C_{\mathrm{IG}}^{(ij)}$ is the intrinsic-shear power spectrum. It models the correlation between the shearing of source galaxies by a foreground matter overdensity and the simultaneous IA of galaxies located near that overdensity:

$$C_{\mathrm{IG}}^{(ij)}(\ell) = \int_0^{\chi_{\mathrm{hor}}} \mathrm{d}\chi \frac{p_n^{(i)}(\chi) q_\epsilon^{(j)}(\chi)}{\chi^2} P_{\delta\mathrm{I}} \left(\frac{\ell + 1/2}{\chi}, \chi \right) ; \qquad (3.30)$$

$C_{\mathrm{GG}}^{(ij)}$ is instead defined as:

$$C_{\mathrm{GG}}^{(ij)}(\ell) = \int_0^{\chi_{\mathrm{hor}}} \mathrm{d}\chi \frac{q_n^{(i)}(\chi) q_\epsilon^{(j)}(\chi)}{\chi^2} P_{\delta\delta} \left(\frac{\ell + 1/2}{\chi}, \chi \right) . \qquad (3.31)$$

We note that with respect to the usual shear power spectrum, we require here that one of the samples refers to the density sample, n.

   To account for these sources of contamination in the fit, we replace ξ_{gI} with $\xi_{n\epsilon}$, which can be obtained from Eq. (3.25). The prediction for ξ^{obs} is then used to constrain the measured signal $\hat{w}_{\mathrm{g+}}$. In Appendix A3 we expand further on the impact of lensing on our measurements, while in Appendix A4 we describe our strategy to measure the values of $\alpha^{(i)}$ in our data.

3.5.3   Likelihoods

We perform the fits to the data using a Markov Chain Monte Carlo (MCMC) that samples the multi-dimensional parameter posterior distributions and finds the set of parameters that maximise the likelihood. We assume a Gaussian likelihood of the form $\mathcal{L} \propto \exp(-\chi^2/2)$, where

$$\chi^2 = \chi^2_{w_{\mathrm{gg}}} + \chi^2_{w_{\mathrm{g+}}} \qquad (3.32)$$

and we simultaneously fit for the galaxy bias, b_{g} and the IA amplitude, A_{IA}.

---

[13]Formally, the magnification of the *lens*fit sample is also affected by the slope of the luminosity function at the bright end of $m_r = 20$. We ignore such complexity: we find magnification to be a subdominant effect for the faint distant galaxies, thus the contribution of low-redshift galaxies is expected to be negligible for our analysis.

To correct for the effects of a partial-sky survey window, we also introduce an integral constraint, IC, when modelling the clustering, signal,

$$w_{\mathrm{gg}} \rightarrow w_{\mathrm{gg}} + \mathrm{IC} \ . \tag{3.33}$$

This term, which becomes important only on large scales, has the function of capturing the bias that arises from a mis-estimation of the global mean density (Roche & Eales 1999). We treat this term as a nuisance parameter, such that our parameter vector reads

$$\lambda = \{b_g, A_{\mathrm{IA}}; \mathrm{IC}\} \ . \tag{3.34}$$

We limit our fits to the quasi-linear regime, $r_{\mathrm{p}} > 6\,h^{-1}\mathrm{Mpc}$, to ensure that the linear bias approximation is satisfied and the IA signal is well described by the NLA model. To perform our fits, we make use of the Emcee (Foreman-Mackey et al. 2013) package as implemented in the cosmology software CosmoSIS[14] (Zuntz et al. 2015). When analysing the chains, we exclude the first 30% of samples for a burn-in phase.

3.6   Results

The left panels in Fig. 3.5 show the measurements of the projected position-shape correlation function $w_{\mathrm{g+}}$ for the `luminous` (top panel) and `dense` (bottom panel) samples. We present results for both the *lens*fit (dark green triangles) and DEIMOS (light green squares) shape catalogues. As described in Sect. 3.5.3, we simultaneously fit the IA and the clustering signals. We show the resulting best-fit models to measurements with $r_{\mathrm{p}} > 6\,h^{-1}\mathrm{Mpc}$ of $w_{\mathrm{g+}}$ and w_{gg} as solid lines in the figures. The estimates from the two shape measurement algorithms are fit independently, but given that the corresponding clustering signal is the same, here we only show the best-fit curve for the DEIMOS fit. The clustering measurements use the full density samples, and thus do not rely on a successful shape measurement.

We observe similar signals for the DEIMOS and *lens*fit samples, with the *lens*fit measurements having a lower S/N, because of the lack of shape measurements for galaxies with $m_r < 20$. We note that we do not necessarily expect to observe the same signal, because DEIMOS contains more bright, low-redshift galaxies, whereas the *lens*fit sample includes fainter, distant galaxies (see Figs. 3.1 and 3.2). If the alignment signal depends

---

[14]`http://bitbucket.org/joezuntz/cosmosis/wiki/Home`
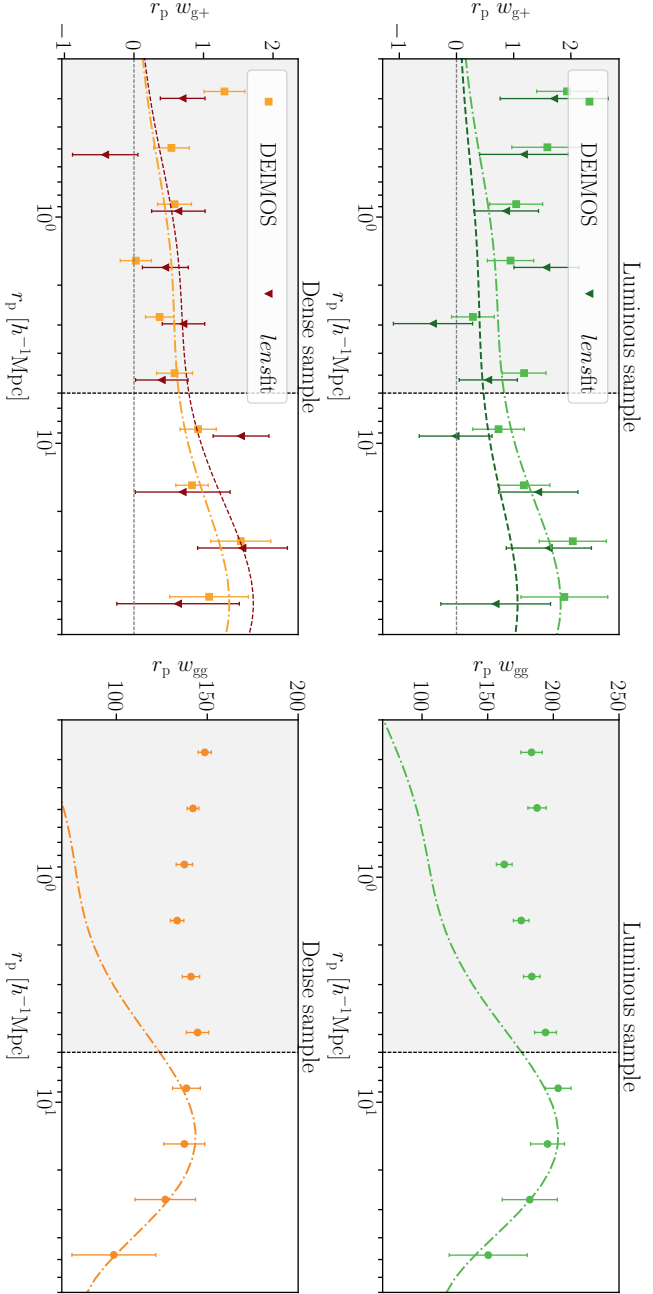
Figure 3.5: Projected correlation functions (IA and clustering signal) measured in this work and the best-fit curve predicted by our model. *Left*: Projected position-shape correlation function, w_{g+}, measured for our luminous (top panel) and dense (bottom panel) samples. We show results for shapes measured with DEIMOS (light squares) and *lensfit* (dark triangles). The best-fit models to the data with $r_p > 6\,h^{-1}\mathrm{Mpc}$ (indicated by the vertical dashed line), are shown as well, with the same colour scheme (DEIMOS: dash-dotted lines, *lensfit*: dashed lines). For clarity, the *lensfit* results have been slightly offset horizontally. *Right*: Projected clustering signal, w_{gg}, of the dense and luminous samples. The dot-dashed lines corresponds to the best-fit models. As we do not include a scale-dependent bias in our model, the mismatch between data and prediction at small scales is expected.

Table 3.1: Properties of the individual galaxy samples used in our analysis and the corresponding best-fit galaxy bias (b_g) and IA amplitude (A_{IA}) as constrained by our model.

Samples	$\langle z \rangle$	N_D	N_S	$[L_{min}, L_{max}]$	$\langle L \rangle / L_0$	b_g	A_{IA}	χ^2_{red}
DEIMOS								
dense	0.44	173 445	152 832		0.38	$1.59^{+0.04}_{-0.04}$	$3.69^{+0.66}_{-0.65}$	0.78
luminous	0.54	117 001	96 863		0.64	$2.06^{+0.04}_{-0.04}$	$4.03^{+0.81}_{-0.79}$	1.19
D1	0.41	173 445	39 108	[0.09, 1.13]	0.21	$1.60^{+0.04}_{-0.04}$	$3.02^{+1.53}_{-1.48}$	1.00
D2	0.42	173 445	39 322	[1.13, 1.43]	0.27	$1.60^{+0.04}_{-0.04}$	$1.21^{+1.63}_{-1.64}$	0.91
D3	0.43	173 445	39 229	[1.43, 1.92]	0.35	$1.59^{+0.04}_{-0.04}$	$4.11^{+1.48}_{-1.48}$	1.05
D4	0.45	173 445	19 333	[1.92, 2.81]	0.49	$1.59^{+0.04}_{-0.04}$	$3.02^{+2.37}_{-2.33}$	1.52
D5	0.45	173 445	19 235	$\geqslant 2.81$	0.89	$1.59^{+0.04}_{-0.04}$	$8.39^{+1.04}_{-1.30}$	0.47
L1	0.53	117 001	48 588	[0.29, 2.66]	0.46	$2.06^{+0.04}_{-0.04}$	$1.80^{+0.96}_{-0.95}$	1.17
L2	0.55	117 001	24 208	[2.66, 3.51]	0.65	$2.06^{+0.04}_{-0.04}$	$4.95^{+1.24}_{-1.21}$	1.19
L3	0.56	117 001	24 067	$\geqslant 3.51$	1.00	$2.06^{+0.04}_{-0.04}$	$5.71^{+1.57}_{-1.60}$	2.03
lensfit								
dense	0.49	173 445	121 500		0.33	$1.60^{+0.04}_{-0.04}$	$4.94^{+1.24}_{-1.22}$	1.52
luminous	0.63	117 001	84 785		0.59	$2.06^{+0.04}_{-0.04}$	$2.95^{+1.49}_{-1.42}$	1.54
DEIMOS + *lensfit*								
Z1 ($z \leqslant 0.585$)	0.44	56 754	56 754		0.63	$2.01^{+0.06}_{-0.06}$	$3.84^{+1.10}_{-1.06}$	0.22
Z2 ($z > 0.585$)	0.70	57 613	57 613		0.61	$2.39^{+0.02}_{-0.08}$	$3.97^{+2.02}_{-2.04}$	2.43

The galaxy properties are summarised by: the mean redshift, $\langle z \rangle$; the number of galaxies in the density (shape) sample, N_D (N_S); the mean luminosity in terms of a pivot luminosity $L_0 = 4.6 \times 10^{10} h^{-2} L_\odot$; the bias, b_g. To compute the ratio $\langle L \rangle / L_0$, we only consider the galaxies in the corresponding shape sample. For our L–cuts sub-samples, we also provide the range in luminosity they probe, $[L_{min}, L_{max}]$, in units of $10^{10} h^{-2} L_\odot$. Similarly, we provide in brackets the cut adopted to split our sample in two redshift bins. When cross-correlating different samples, N_D refers to the density sample used in the correlation and the bias is the best-fit bias of the density tracer as obtained for that given measurement. All measurements are performed assuming $\Pi_{max} = 120 \, h^{-1}$Mpc. Since the best-fit parameters and the medians of the marginal posterior distributions are in agreement, we quote the marginal values, while the χ^2 refers to the maximum likelihood. In all cases, the degrees of freedom are 5; the p–values are all above 0.03, with the majority of them being in the range 0.3-0.7.
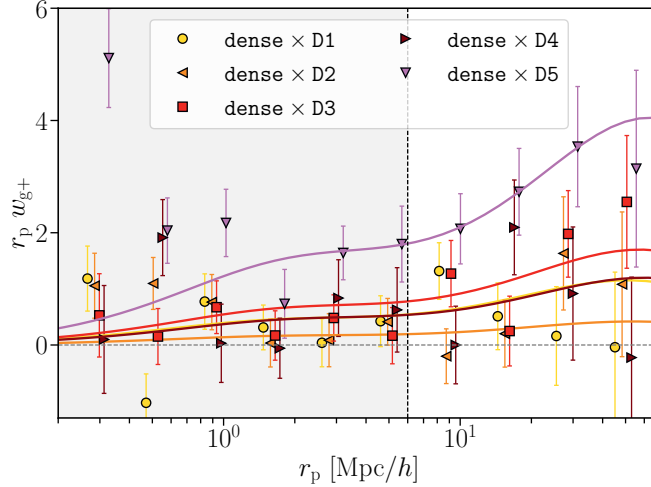
Figure 3.6: Projected correlation function, w_{g+}, measured for the different cuts in luminosity of the DEIMOS dense sample. The best-fit curves are plotted on top of the data points, and the fits are performed for $r_p > 6\,h^{-1}\mathrm{Mpc}$. All but the yellow points have been slightly offset horizontally; to better visualise the goodness of fit, the corresponding best-fit curves have been displaced accordingly.

on luminosity or redshift, the two shape samples would give different signals. In Appendix A6 we restrict the comparison to the sample of galaxies with shape measurements from both methods, and find that the average difference $\langle r_p \Delta w_{g+} \rangle = 0.003 \pm 0.13$ is negligible, especially compared to the amplitude of the IA signal quantified as $\langle r_p w_{g+} \rangle = 0.90 \pm 0.17$ (DEIMOS shapes; see Appendix A6 for details).

We also show the models that provide the best-fit to the combined w_{gg} and w_{g+} measurements in Fig. 3.5, and report the values for the bias b_g and IA amplitude A_{IA} in Table 3.1. The results for DEIMOS and *lens*fit are consistent.

Our constraints on the galaxy bias of the dense and luminous samples are in broad agreement with the values presented in Vakili et al. (2020): We find a larger bias for the luminous sample than for the dense one, as expected by its higher luminosity and the higher redshift baseline.

3.6.1   Luminosity dependence

Previous studies of LRGs (Joachimi et al. 2011; Singh et al. 2015) have found a significant dependence of their IA signal with luminosity, with

more luminous galaxies showing stronger alignments. On average our LRG sample probes somewhat lower luminosities than those earlier studies, but the overlap with these earlier works also enables a direct comparison. Thanks to the large range in luminosity it covers, the `dense` sample is particularly suited to explore the dependence with luminosity. To do so, we use the DEIMOS shape catalogue[15] and split the `dense` LRG galaxies in five sub-samples: `D1`, `D2`, and `D3`, correspond to the lowest three quartiles in luminosity; the remaining two, `D4` and `D5`, are obtained by splitting the highest luminosity quartile into two equally sized samples. The motivation to split the quartile with the highest luminosities is that it encompasses a very large range in luminosity, which complicates the interpretation if the signal depends on luminosity (see below). Relevant details for the sub-samples are listed in Table 3.1. We keep the `dense` and `luminous` samples separate, in order to better isolate the effect of the luminosity dependence from any redshift evolution of the sample itself. For instance, as listed in Table 3.1, the mean redshift of the sub-samples increases somewhat from `D1` to `D5`.

We cross-correlate the DEIMOS shape catalogues for the individual sub-samples with the positions of galaxies in the full `dense` sample. In this way, we can disentangle the luminosity dependence of the IA signal from the luminosity dependence of the density tracer (brighter galaxies are typically found in denser environments). The measurements and the best-fit models are presented in Fig. 3.6. In Table 3.1 we list the best-fit values for the galaxy bias b_{g} and IA amplitude A_{IA}, as well as the reduced χ^2, as before, using the measurements for $r_{\mathrm{p}} > 6\,h^{-1}\mathrm{Mpc}$. We also show the measurements in Fig. 3.7 as orange stars as a function of L/L_0, where $L_0 = 4.6 \times 10^{10} h^{-2} L_\odot$.

We repeat the same analysis for the `luminous` sample, which we divide in three bins, with a similar bin refining approach as for the `dense` sample (in this case `L1` contains half of the `luminous` galaxies, while `L2` and `L3` the remaining quarters). The best-fit amplitudes for these samples are reported in Table 3.1, and presented as green stars in Fig. 3.7. In the luminosity range where the `luminous` and `dense` samples overlap, we find the results between the two samples to be compatible. The `luminous` sample seems to show a more pronounced luminosity dependence compared to the `dense` sample, which can either be an effect of being brighter overall (from `L1` to `L3`, $L/L_0 = 0.46, 0.64, 1.01$) or due to the satellite fraction being lower (see Sect. 3.2.2), or a combination of the two. We note that the measure-

---

[15]The internal cut at $m_r < 20$ in *lens*fit makes it less suitable for this analysis, as we have fewer galaxies at high luminosities.
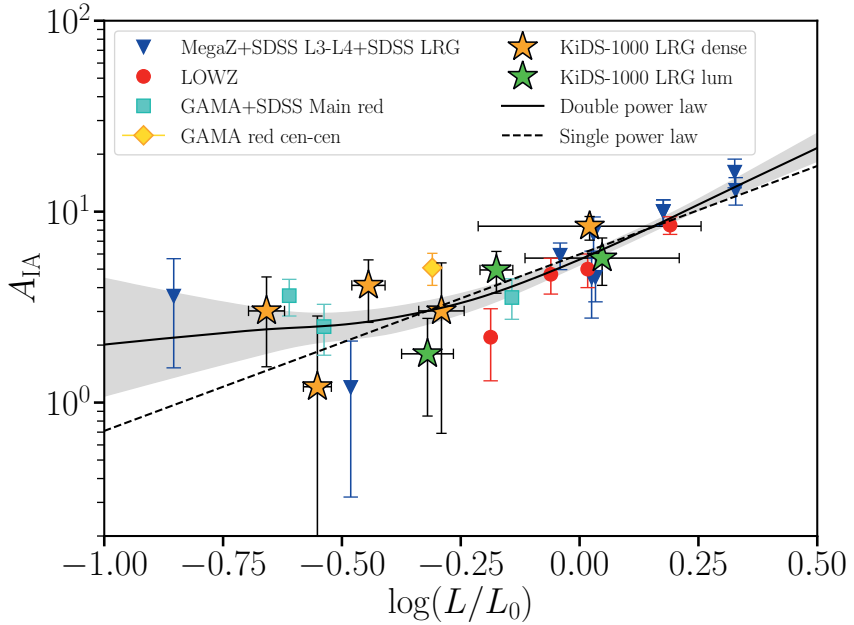
Figure 3.7: Luminosity dependence of the IA amplitude as measured by different observational studies (Joachimi et al. 2011; Singh et al. 2015; Johnston et al. 2019; Fortuna et al. 2021a); our new measurements on the LRG samples are shown as star markers. We provide horizontal error bars to indicate that the measurement is performed on a bin in luminosity, here plotted as the weighted standard deviation of the luminosity distribution of each sample, with the marker placed at the weighted mean. The solid (dashed) black line shows the median of the distribution of the MCMC sample associated with the double (single) power law; the shaded area corresponds to the 68% confidence region.

Figure 3.8: Constraints on the double power law parameters described in equation 3.35 by jointly fitting all the measurements in Fig. 3.7. The red crosses indicate the value of the parameters that maximise the likelihood, while the blue squares correspond to the medians.
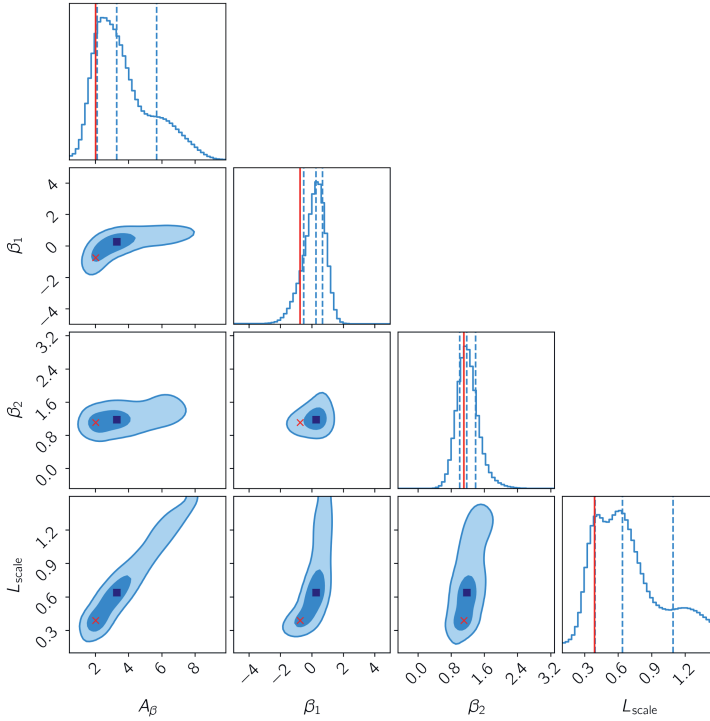
Table 3.2: Best-fit parameters of the single and double power law fit on the measurements in Fig. 3.7.

Model	A_β	β_1	β_2	L_{break}	χ^2/dof	dof
Double power law	$3.28^{+2.41}_{-1.17}$ (2.01)	$0.26^{+0.42}_{-0.77}$ (-0.75)	$1.17^{+0.21}_{-0.17}$ (1.11)	$0.64^{+0.45}_{-0.24} L_0$ ($0.39 L_0$)	1.36 (1.33)	22
Single power law	$5.98^{+0.27}_{-0.27}$ (6.0)	$0.93^{+0.11}_{-0.10}$ (0.92)	-	L_0	1.61 (1.61)	24

The listed values correspond to the medians of the marginal posterior distributions, and the associated errors correspond to the 16th and 84th percentiles, while in brackets we report the parameters that maximise the likelihood. The same scheme is adopted for the corresponding reduced χ^2. L_{break} is the pivot luminosity that enters in the denominator of the power law argument. For convenience, the slope of the single power law model is here reported as β_1.

ments of the L3 sample appear to scatter more than the covariance predicts, which results in higher χ^2. A similar issue is present in the D4 sample and it is visible in Fig. 3.6.

The horizontal error bars in Fig. 3.7 indicate the weighted standard deviation of the luminosity distribution within the bin for each sample, with the measurement placed at the luminosity-weighted mean of the bin. If the range is too large, and the IA signal varies within the bin, the resulting amplitude is difficult to interpret, and may even appear discrepant. For instance, when we combine the D4 and D5 samples we obtain $A_{\mathrm{IA}} = 6.70^{+1.15}_{-1.14}$. We note, however, that the luminosity range probed by this combined bin is particularly extended, and the high signal measured is mainly driven by the galaxies in the high luminosity tail of the bin (D5, $A_{\mathrm{IA}} = 8.39^{+1.04}_{-1.30}$). The other half of the bin has a relatively low signal with very large uncertainties (D4, $A_{\mathrm{IA}} = 3.02^{+2.37}_{-2.33}$). This is relevant because it suggests that the alignment of galaxies with luminosities below $L/L_0 \sim 0.60 - 0.70$ hardly depends on luminosity, and thus with a similar amplitude to D1 and D3, the smaller sample is less constraining. As soon as we exceed this approximate threshold, the signal increases significantly, suggesting a luminosity dependence. This overall picture is enhanced when we also consider previous results for LRGs (Joachimi et al. 2011; Singh et al. 2015; Johnston et al. 2019; Fortuna et al. 2021a)[16]. These are also shown in Fig. 3.7. We investigate how well the current measurements support the picture of a single or double power law by fitting the data points in Fig. 3.7, assuming them to be uncorrelated. For each data point, we only use the quoted L/L_0 as we do not have the underlying luminosity distribution for most of the measurements. We propose a double power law with knee at L_{break}, amplitude A_β and slopes $\beta_{1,2}$:

$$A(L) = A_\beta \left(\frac{L}{L_{\mathrm{break}}} \right)^\beta \text{ with } \begin{cases} \beta = \beta_1 & \text{for } L < L_{\mathrm{break}} \\ \beta = \beta_2 & \text{for } L > L_{\mathrm{break}} \end{cases} \tag{3.35}$$

and fit for

$$\lambda = \left\{ A_\beta, \beta_1, \beta_2, L_{\mathrm{scale}} \right\} , \tag{3.36}$$

where $L_{\mathrm{scale}} = L_{\mathrm{break}}/L_0$. We explore the parameter space using a MCMC and assuming a Gaussian likelihood. Figure 3.8 shows our parameter constraints, while the model prediction is shown in Fig 3.7 as a solid black line.

---

[16]The GAMA points (Johnston et al. 2019) have been adjusted to homogenise the units convention, as discussed in Fortuna et al. (2021a).

Our best-fit parameters are reported in Table 3.2[17]. We repeat the same analysis assuming a single power law, as parametrised in Joachimi et al. (2011). The best-fit parameters are also reported in Table 3.2. The larger χ^2/dof of the single power law compared to the double power law suggests that the latter is a better description of our current data, although the scatter between the points at low L is still too large to draw definitive conclusions and the data are also mildly inconsistent in that regime. The degeneracy between the parameters, and in particular between A_β and L_{scale}, shows that the data can weakly constrain the model. Nevertheless, the emerging picture seems to support more the broken power law scenario presented in Fortuna et al. (2021a), but with a transition luminosity around $0.4 - 0.6L_0$, also in line with the results from simulations by Samuroff et al. (2020a). The double power law is also supported by the fact that the alignment of redMaPPer clusters (van Uitert & Joachimi 2017; Piras et al. 2018), not included in this analysis, forms a smooth extension towards higher mass of the alignment observed for the high luminosity LRGs. This result is hard to reconcile with a single shallow power law, but finds a natural framework in the double power law scenario, where the slope of the relation at high luminosities recovers the trend in Joachimi et al. (2011); Singh et al. (2015).

We caution that this analysis does not aim to be fully comprehensive, but rather to provide a sense of the current trends. A proper analysis should jointly fit all of the measurements incorporating the full luminosity distributions of each sample, as well as accounting for the presence of satellites, which might suppress the signal at low luminosities.

3.6.2 Redshift dependence

Having assessed that the two shape measurements produce compatible IA signals and that their calibrations are robust, we merge the two shape catalogues to span the largest possible range in redshift. This allows us to extend the sample from the low-z, high S/N galaxies, where only DEIMOS provides shapes, to the high-z, low S/N galaxies, where we preferentially measure the shapes via *lens*fit. In the case of overlap between DEIMOS and *lens*fit, we select the DEIMOS shapes. We only focus on the `luminous` sample as we are interested in a long redshift baseline with the same luminosity cut. In this way, we can probe the redshift evolution of the sample, without confusing the results with any luminosity dependence.

---

[17]We note that the parameters that maximise the likelihood differ from the medians of the posterior distributions as a consequence of the degeneracies between the parameters. This is particularly evident for β_1, which has negative slope, $\beta_1 = -0.75$.
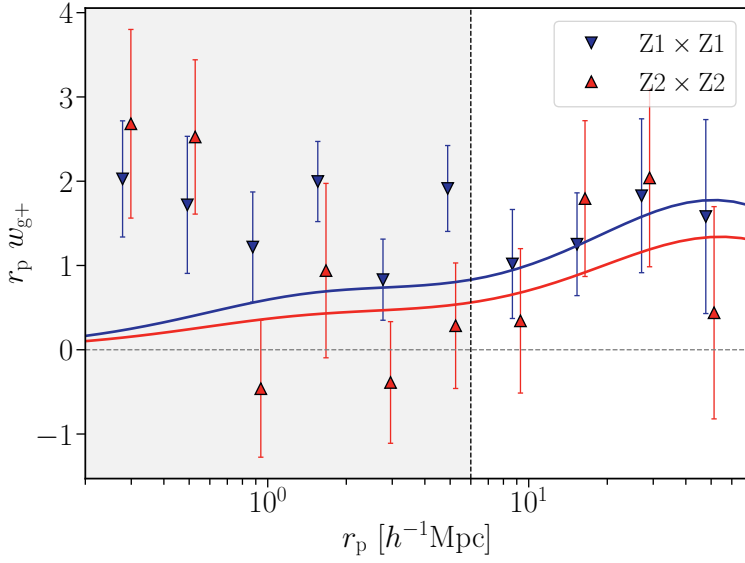
Figure 3.9: Projected correlation function, $w_{\mathrm{g+}}$, measured on our different cuts in redshift of the luminous sample. The best-fit curves are plotted on top of the data points, and the fits are performed for $r_{\mathrm{p}} > 6\,h^{-1}\mathrm{Mpc}$. The red points are slightly displaced for clarity and the corresponding best-fit curve has been displaced accordingly.
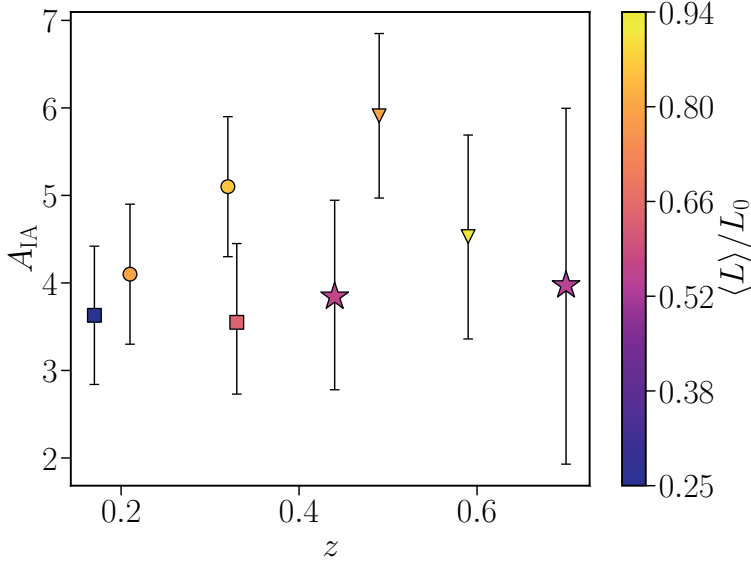
Figure 3.10: Intrinsic alignment amplitude, A_{IA}, as a function of redshift and luminosity for different best-fit values in the literature. Different markers refer to different studies and are colour-coded based on their luminosity: MegaZ (Joachimi et al. 2011) is shown as triangles, LOWZ (Singh et al. 2015) as circles, GAMA (Johnston et al. 2019) as squares and the LRG luminous sample Z1 and Z2 as stars.

Our final catalogue contains 115 322 galaxies that we split at $z = 0.585$, which roughly provides two equally populated bins. We call these two samples Z1 and Z2. The measurements for $w_{\mathrm{g+}}$ are presented in Fig. 3.9. The best-fit values for the two redshift bins are listed in Table 3.1 and agree within their error bars, despite their mean redshift being $\langle z \rangle = 0.44$ and $\langle z \rangle = 0.70$, respectively.

We note that the χ^2 of our Z2 sample is quite high: This is driven by the poor fit of the clustering signal. We attribute this to our photo$-z$, which at high redshift are less reliable. We note, however, that the uncertainty in the IA amplitude is large enough to absorb the inaccuracies in $p(z_{\mathrm{spec}}|z_{\mathrm{phot}})$, such that modifying the redshift distributions has little impact on the recovered IA amplitude.

Figure 3.10 compares our results with the best-fit amplitudes at various redshifts found by previous studies (Joachimi et al. 2011; Singh et al. 2015; Johnston et al. 2019). The colour of the data points reflects the lu-

minosity of the sample used to measure the signal[18]. As previously discussed, galaxies with different luminosities may manifest different levels of IA, and hence even with a lack of redshift dependence, we should still expect points at different amplitudes: the bottom part of the plot should be mainly populated by darker points and the upper part by brighter points. Figure 3.10 confirms this scenario: overall, the points exhibit a similar alignment and the scatter between the different points is consistent with the extra luminosity dependence. We can conclude that there is little evidence for a strong redshift dependence of the IA signal.

3.7   Conclusions

We have constrained the IA signal of a sample of LRGs selected by Vakili et al. (2020) from KiDS-1000, which images ~ 1000 deg^2. These data allowed us to investigate the luminosity dependence and the redshift evolution of the signal. To do so, we measured the shapes of the LRGs with two different algorithms, DEIMOS and *lens*fit. We used custom image simulations to calibrate and correct the residual biases that arise from measurements of noisy images.

We used the calibrated ellipticities to compute the projected position-shape correlation function w_{g+} and analyse the signals obtained by the two different algorithms independently, thus exploring the dependence of IA on the specific shape method employed. We found *lens*fit measurements to be overall noisier than the DEIMOS ones and we attributed this to the prevalence of faint galaxies in the sample, due to the internal magnitude cut in the *lens*fit algorithm. Because bright galaxies typically carry more alignment signal, this cut, which removes galaxies with $m_r < 20$, can potentially reduce the IA contamination in KiDS cosmic shear analyses, which employ *lens*fit as the shape method. For a sub-sample of galaxies, where both shape methods return successful measurements of the shapes, we find a remarkable agreement in the measured w_{g+}, with a difference in the signal of 0.003 ± 0.13 (amplitude of a fitted power law).

We explored the luminosity dependence and the redshift evolution independently, selecting our galaxies in such a way that ensures the two do not mix. Within the luminosity range probed by the measurements our re-

---

[18]The colour of the marker corresponds to the bin centre, which may not be sufficient if the range in luminosity is large, as it is typically the case for these samples. The information provided by the colour has therefore only qualitative meaning and should be considered as such.

sults agree with previous studies (Joachimi et al. 2011; Singh et al. 2015; Johnston et al. 2019). However, a single power law fit, as was used in Joachimi et al. (2011) and Singh et al. (2015) does not describe the measurements well. Instead, our results suggest a more complex dependence with luminosity: for $L_r \lesssim 2.9 \times 10^{10} h^{-2} L_{r,\odot}$ the IA amplitude does not vary significantly, whereas the signal rises rapidly at higher luminosity. This also has implications for the width of the luminosity binning, as the use of broad bins may complicate the interpretation of the measurements. Analyses that aim to combine these measurements to model the luminosity dependence should incorporate the underlying luminosity distributions to properly link the signal to the galaxy luminosity. Nevertheless, we provide a preliminary fit on the current measurements available in the literature and found that the data are best described by a broken power law. This result can already be used by cosmic shear analyses to improved their modelling of the IA carried by the red galaxy population. We remind the reader that this sample is not representative of the galaxy population. Different galaxy samples carry different alignment signals and should thus be individually modelled as described in Fortuna et al. (2021a).

To probe the redshift dependence of the IA signal with the largest baseline to date, we merged the DEIMOS and *lens*fit catalogues. We find no evidence for redshift evolution of the IA signal. This result is in line with previous studies of LRG samples (Joachimi et al. 2011; Singh et al. 2015), and it is consistent with the current paradigm that IA is set at the moment of galaxy formation. However, it is also possible that galaxy mergers counteract the evolution of the tidal alignment, such that the net signal does not change. Further improvements in the measurements are needed to distinguish between scenarios.

Acknowledgements

Author contributions: All authors contributed to the development and writing of this paper. The authorship list is given in three groups: the lead authors (MCF, HH, HJ, MV, AK, CG) followed by two alphabetical groups. The first alphabetical group includes those who are key contributors to both the scientific analysis and the data products. The second group covers those who have either made a significant contribution to the data products, or to the scientific analysis.

A1 m-bias calibration

In this Appendix, we detail our procedure to calibrate the m-bias in our shape measurements. We follow the same procedure for both DEIMOS and *lens*fit, but we present the results separately.

A1.1 DEIMOS

One of the key features of DEIMOS that was exploited by Georgiou et al. (2019b) is that the weight function that is used to measure the moments of the surface brightness distribution can be adjusted. As explained in Sect. 3.3, we follow Georgiou et al. (2019a) and adopt a Gaussian weight function with a width r_{iso}. However, not only the radial profile can be changed, but one can also choose between a circular or an elliptical weight function. Hence, before proceeding with the shape calibration, we investigate which choice of weight function would suit our data best.

In both cases, the weight function is centred on the centroid of the galaxy, with the size and ellipticity iteratively matched to those measured for the galaxy (see Georgiou et al. 2019a, for details). While an elliptical weight function matches the shape of an elliptical galaxy better, a circular one generally performs better on small and faint objects.

The circular weight function performs similar to the elliptical weight function for low-to-intermediate S/N (S/N< 60), but with an overall constant bias of ~ 0.2 as the S/N increases. Hence, the elliptical weight function performs significantly better for more than half of the (real) galaxy sample, which motivates our choice to adopt an elliptical weight function in our analysis.

DEIMOS measured the shapes of 13 301 simulated LRGs from our image simulations, and we use these to calibrate our ellipticity estimates. To do so, we first explore the dependence of the m-bias on the individual galaxy parameters S/N and R, as discussed in Sect. 3.3. Figure 3.3 indicates that $m(R)$ is well described by a polynomial curve, which we truncate at degree 3, $p(R) = p_1 R + p_2 R^2 + p_3 R^3$, while $c(\text{S/N})$ is well described by: $d(\text{S/N}) = d_1/\sqrt{\text{S/N}} + d_2/(\text{S/N})$.

We have tested different combinations of the two functions $m(\text{S/N})$ and $m(R)$, and explored if higher-order polynomials are needed: while the fit to $m(R)$ is indeed better described by a polynomial of degree 5, we stress that we are not interested to reproduce all of the noisy features in the data, but rather to capture the trend in the two components. We therefore keep

Table 3: Best-fit parameters for the empirical correction of the two-dimensional multiplicative bias surface (Sect. 3.3.3).

Parameter	DEIMOS	*lens*fit
b_0	−0.895	0.1794
d_1	5.238	−5.081
d_2	−0.006	1.292
p_1	−1.900	−0.972
p_2	5.147	0.669
p_3	−3.148	0.783
p_4	−	−0.698

the number of the parameters as low as possible. This is also motivated by the fact that the image simulations suffer from galaxy repetitions.

The final expression for our empirical correction for the DEIMOS measurements is then:

$$m(\text{S/N}, R) = b_0 + \frac{1 + d(\text{S/N})}{1 + p(R)} \ . \tag{37}$$

To find the best-fit parameters in 37, we re-computed the value of the m−bias by binning the data in 64 regions using the k−means algorithm[19]. We then measured the bias for the two components $\epsilon_{1,2}$ in each region, identifying the bin coordinate in S/N and R as their mean value within the bin. We then fit the average of the two components $(m_1 + m_2)/2$ with equation 37. Some of the galaxies have very small shape measurement errors, and to avoid them dominating the fit, we also added an intrinsic scatter σ_{int} to our error-bars. This accounts for the fact that the number of unique galaxies in our simulations is limited and mitigates the importance of the highly resolved ones. The intrinsic scatter σ_{int} is chosen such that the reduced χ^2 is ∼ 1. The best-fit parameters are reported in Table 3. We stress here that since we are only correlating shapes with positions, we are not interested in a perfect calibration of the bias per galaxy but rather want to ensure that the mean ellipticity of an ensemble is unbiased.

---

[19]`https://scikit-learn.org/stable/modules/generated/sklearn.cluster.KMeans.html`

A1.2 *lens*fit

In the case of *lens*fit we follow a very similar procedure to calibrate the residual m-bias. *lens*fit successfully measured the shapes of 17 573 simulated galaxies, which are used for the calibration. The dependence of the m-bias with S/N can be described by the same parametrisation that we used for the DEIMOS sample, $d(\text{S/N})$, while $m(R)$ is better described by a polynomial of degree four, $p(R) = p_1 R + p_2 R^2 + p_3 R^3 + p_4 R^4$.

   The combination that best reproduces our measurements of the m-bias in k-means cells of the two-dimensional space $(\text{S/N}, R)$ is

$$m(\text{S/N}, R) = b_0 + d(\text{S/N}) + p(R) \,, \tag{38}$$

with the specific values of the parameters reported in Table 3. We note that compared to DEIMOS, the *lens*fit-bias is small, and hence so is our correction.

A2   Redshift distributions

We describe here the redshift distributions, $p(z_{\text{spec}}|z_{\text{phot}})$, employed in our analysis as reported in Sect. 3.5 and which are used in the computation of the angular power spectra in Eq. (3.25). We bin the galaxies for which we have spectroscopic redshifts in bins of $\Delta z_{\text{phot}}^{\texttt{dense}} = 0.0146(1+z)$ and $\Delta z_{\text{phot}}^{\texttt{luminous}} = 0.0139(1 + z)$ with an iterative procedure; this constructs unequal binning whose size increases with z. The last bin is adjusted to avoid spurious results: If the maximum redshift found with the iterative procedure exceed the maximum redshift of the sample, we remove the last bin and extend the second-to-last up to z_{max}. In the case of the $\texttt{luminous}$ sample we further increase the scatter at high redshift to account for the increasing uncertainty of our photometric redshifts: for $z > 0.7$ we increase the bin width to $\Delta z_{\text{phot}}^{\texttt{luminous}} = 0.027$. We adopt the same approach for the Z1 and Z2 samples, for which we use, respectively, $\sigma_z = 0.0133$ and 0.0190. We use the resulting spec-z histograms in our analysis. We employ the same conditional redshift distributions for both our density and shape samples; while this is a very good approximation for DEIMOS, *lens*fit lacks bright galaxies that would populate our spec-z, and thus this approximation might partially be responsible for the worse fit of the model.

   We tested that our IA constraints are only marginally dependent on the width of the bins adopted, and the changes in the best-fit amplitude are subdominant to the statistical uncertainty.
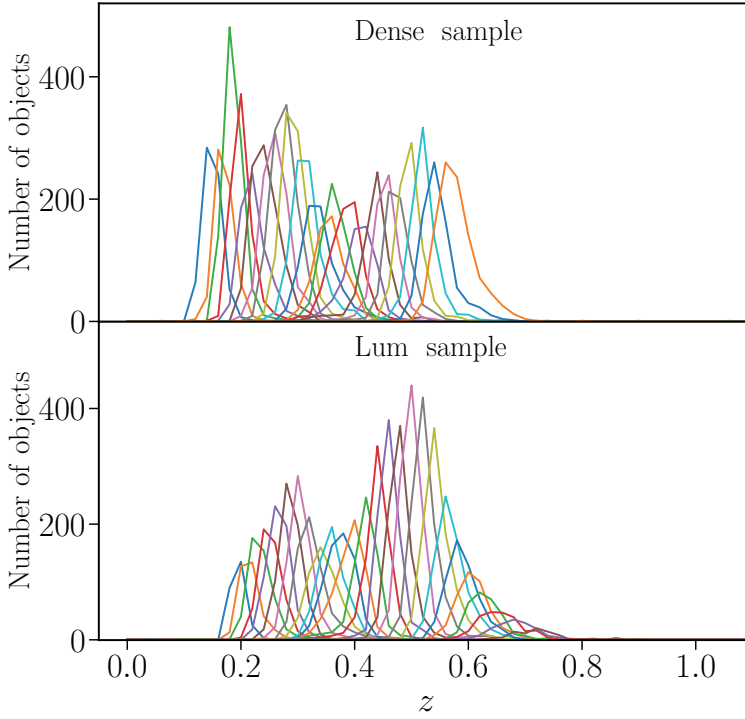
Figure 11: The $p(z_{\mathrm{spec}}|z_{\mathrm{phot}})$ of our `dense` and `luminous` samples.
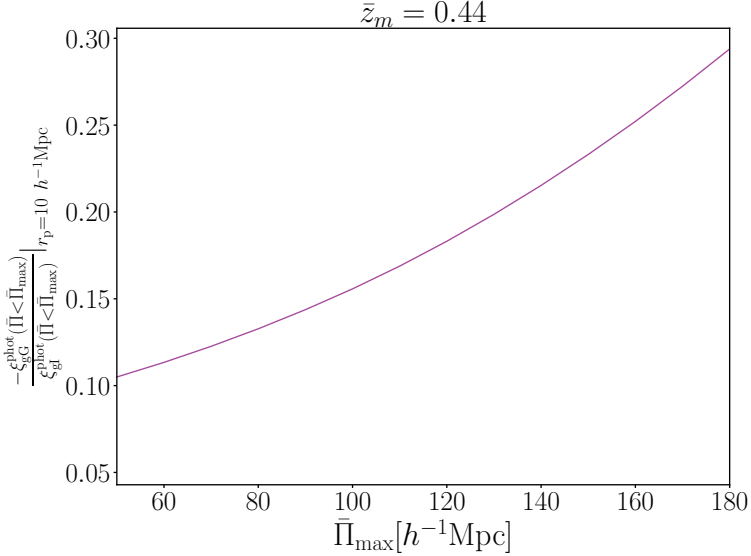
Figure 12: Ratio of the cumulative galaxy-galaxy lensing signal over the cumulative IA signal as a function of Π_{max} at the mean redshift of the `dense` sample, $z = 0.44$.

A3 Contamination from galaxy-galaxy lensing

As discussed in Sect. 3.5.2, galaxy-galaxy lensing is the main astrophysical contaminant to our signal. Here, we focus on its dependence on the line-of-sight integration range. The lensing and the IA signals scale differently with distance: this can be used to maximise the signal and avoid an excess of contamination. In this Appendix we therefore explore in more detail the modelling of the galaxy-galaxy lensing and how this has guided our choice for the value of Π_{max}.

Figure 12 shows the amount of lensing contamination as a function of the maximum Π used in the integral along the line-of-sight. We illustrate it by plotting the cumulative contribution of the galaxy-galaxy lensing over the one of IA for different values of the truncation, Π_{max}. To generate the signal, we used the $p(z_{\mathrm{spec}}|z_{\mathrm{phot}})$ associated with the `dense` sample and evaluated the correlation functions at the mean redshift of the sample, assuming the fiducial bias and IA amplitude reported in Table 3.2. The ratio is almost constant in r_{p}, thus we plot it for fixed $r_{\mathrm{p}} = 10\,h^{-1}\mathrm{Mpc}$. We also note that the lensing signal has negligible impact for negative Π because the source is in front of the lens in that case.

In principle, if one had perfect knowledge of the galaxy-galaxy lensing contribution, extending the integration up to very large line-of-sight separations would allow us recover the full IA signal from the measurements, without discarding any information. In practice, even though we fully model the galaxy-galaxy lensing contribution, we are limited by the accuracy of the lensing modelling we rely on, and thus it is safer to truncate the integral to values of Π that are not severely affected by it.

We use Fig. 12 to choose the fiducial Π_{max} that enters in Eq. (3.12): although the specific values of the ratio depend on the input parameters (b_g, A_{IA}), it provides a realistic estimate of the amount of contamination for our LRG samples. We chose as our fiducial setup a conservative value of $\Pi_{max} = 120 \, h^{-1} \mathrm{Mpc}$, which ensures that the mean contamination is below $\sim 20\%$ of the signal.

A4   Contamination from magnification

The changes in the galaxy number counts determined by lensing magnification arise as a result of two competing effects: on one hand, the lensing locally stretches the sky, diluting the observed number density; on the other hand, it enlarges the apparent sizes of the galaxies without modifying the surface brightness: at the faint end, this allows the detection of galaxies that are intrinsically fainter than the magnitude limit, enhancing the observed number density.

The theory of magnification for flux-limited surveys is well established and allows us to relate the changes in the number density to the differential galaxy count $n(m)$ over a given band magnitude range from m to $m + \mathrm{d}m$ (Bartelmann & Schneider 2001; Joachimi & Bridle 2010):

$$\alpha(m) = 2.5 \frac{\mathrm{d}\log[n(m)]}{\mathrm{d}m} \; . \tag{39}$$

The case of a non-flux-limited sample, such as our LRG sample, is more complicated and we lack a proper theoretical framework for the interpretation of α. Here, we follow von Wietersheim-Kramsta et al. (2021) and calibrate α using dedicated mocks, which we present in Appendix A7. We remind the reader that our samples are selected by imposing a luminosity threshold, which implies a redshift-dependent magnitude selection.

The calibration works as follows: the mocks provide the reference relation between the convergence κ and the slope α, which we can measure

as the difference in the number density of a 'magnified' sample and a 'non-magnified' one,

$$\frac{n(<m) - n_0(<m)}{n_0(<m)} \approx 2(\alpha - 1)\kappa \,. \tag{40}$$

Here, $n(<m)$ is the local number density of magnified sources with magnitudes below m, while $n_0(<m)$ is the underlying true number density without the enhancement due to the flux magnification and the simultaneous lensing dilution.

We used our mocks to measure α in Eq. (40), obtained as the mean value of κ on sufficiently small patches of the sky. To partition the sky we used the public available python module Healpy[20] (Zonca et al. 2019), based on the HEALPix pixellization of the sphere[21] (Górski et al. 2005). We used this value of α to calibrate the magnitude range over which the observable α in equation 39 best agrees with the *true* one obtained from equation 40. If the mocks reproduce the data selection function to good accuracy, this provides the optimal magnitude range to use to measure α via observable quantities (Eq. (39)) in the data.

To evaluate Eq. (39) we used the $r-$band magnitude and we ensured that the magnitude distribution of the mocks and the data agree to high accuracy. We find that, when applied to the data, the method results in values of α that depend somewhat on the binning scheme employed along the redshift baseline. While the values of α are robust against changing the bins at intermediate and high redshifts, the very low-z bins are poorly constrained by the method. However, at such low redshifts magnification is negligible, and our samples contain only a few galaxies, so it is reasonable to expect the same value of α to hold for the entire sample. Moreover, the LRG selection ensures a constant comoving number density, which reduces the sensitivity to magnification even further.

We find $\alpha \sim 1.5$ for both our `dense` and `luminous` sample. In Appendix A5 we show that the effect of including magnification is subdominant in our analysis.

Table 4: Reduced χ^2 statistics to assess the significance of our signals w_{g+} and $w_{g\times}$ against the null hypothesis.

Sample	Shapes	Signal	$\chi^2_{\nu,\text{null}}$	$p-$value
dense	DEIMOS	w_{g+}	8.01 (7.56)	4.88×10^{-13} (4.35×10^{-6})
		$w_{g\times}$	0.59 (0.36)	0.83 (0.83)
	*lens*fit	w_{g+}	3.52 (4.99)	0.0001 (0.0005)
		$w_{g\times}$	0.66 (0.64)	0.76 (0.63)
luminous	DEIMOS	w_{g+}	9.46 (5.85)	6.66×10^{-16} (0.0001)
		$w_{g\times}$	0.37 (0.33)	0.96 (0.85)
	*lens*fit	w_{g+}	2.48 (1.49)	0.006 (0.20)
		$w_{g\times}$	0.40 (0.40)	0.95 (0.81)

A detection of $w_{g\times}$ would hint at the presence of unaccounted systematics in the measurements. The numbers in brackets refer to the signal for $r_p > 6 \ h^{-1}\text{Mpc}$.

A5   Systematic tests and significance of the detection

To ensure the robustness of our analysis, we performed a number of tests for residual systematics. We present the results of these in this Appendix. Many of these are commonly used to test weak gravitational lensing signals.

In one of the most basic tests, the galaxy shapes are rotated by $45 \deg$ and the correlation between $\epsilon_\times$ and galaxy position, $w_{g\times}$ is measured. This correlation is expected to vanish, and any detection of a non-vanishing signal is therefore an indication of residual systematics. Table 4 reports the reduced $\chi^2_{\nu,\text{null}}$, which we used to assess the significance of the signal against the null hypothesis for both w_{g+} and $w_{g\times}$. We choose a significance level of 5%: for $p-$values below 0.05 we discard the null hypothesis. We can see that all of our $w_{g\times}$ measurements have a $p-$value above 0.05 and thus support the null hypothesis. In contrast, we observe a significant detection for all of our w_{g+} measurements, for both DEIMOS and *lens*fit shapes.

As a further look into possible systematics in the data, we measured the signal for a very large value of the line-of-sight truncation, $\Pi_{\text{max}} = 1000 \ h^{-1}\text{Mpc}$, using our dense sample. Extending the value of Π_{max} to very large separations introduces uncorrelated pairs into the estimator, and thus

---

[20]https://healpy.readthedocs.io/en/latest/
[21]http://healpix.sourceforge.net

we expect the IA signal to vanish, while the galaxy-galaxy lensing can potentially arise. We find a signal consistent with a null detection, with $\chi^2_{\nu,\text{null}} = 0.35$ and p−value of 0.96.

We also investigated the impact of specific choices for the setup of our modelling, with a particular focus on how our results depend on the value of the Π_{max} adopted in the analysis. To do so, we repeat our analysis of the `dense` sample using two different values of Π_{max}: 90 and 180 $h^{-1}\text{Mpc}$. Table 5 reports our results. We find compatible results that also agree with our fiducial value of $\Pi_{\text{max}} = 120\, h^{-1}\text{Mpc}$.

In Table 5 we also report the results when we include magnification in the modelling for the `dense` sample, or ignore it for the `luminous` sample. The resulting parameter estimates agree with the baseline results (also see Sect. 5.6), suggesting magnification is small in our data, as expected from theory (Unruh et al. 2020).

A6　IA dependence on the shape measurement method

Singh & Mandelbaum (2016) compared the IA signal measured with different shape methods and found that the signal depends on the specific algorithm employed. Georgiou et al. (2019a) explored this further, and used DEIMOS to show that the IA signal depends on the width of the weight function. Since different methods use different weight functions, the difference in the IA detection can be linked to the parts of the galaxies they probe.

In this Appendix, we therefore explore how the IA signal depends on the shape measurement methods used in our analysis. To ensure this is done consistently, we only selected galaxies that belong to both our DEIMOS and *lens*fit catalogues, irrespective whether they are part of the `luminous` or `dense` sample. We identify 173 499 galaxies in common between the two shape catalogues.

We measure $w_{\text{g+}}$ for this sub-sample for both shape catalogues, and show the difference in the signal, $\Delta w_{\text{g+}} = w_{\text{g+},\text{DEIMOS}} - w_{\text{g+},lens\text{fit}}$ (indigo squared markers) in Fig. 13. The error bars are computed via bootstrap; we are only interested in the shape noise contribution: We are measuring the difference of signals obtained using the same sample of galaxies and thus the sample variance should vanish. We generated 215 re-samplings with replacement of our input galaxies and provided the same input catalogue to both our DEIMOS and *lens*fit measurement of $w_{\text{g+}}$. The error

Table 5: Tests of the modelling setup.

Sample	b_g	A_IA	χ^2_red
DEIMOS			
dense (120, baseline)	$1.59^{+0.04}_{-0.04}$	$3.69^{+0.66}_{-0.65}$	0.78
dense (90)	$1.60^{+0.04}_{-0.04}$	$3.99^{+0.73}_{-0.72}$	0.67
dense (180)	$1.58^{+0.05}_{-0.05}$	$3.50^{+0.69}_{-0.70}$	0.71
dense (120, w/o magnification)	$1.59^{+0.04}_{-0.04}$	$3.67^{+0.66}_{-0.64}$	0.78
dense (120, w/o lensing and magnification)	$1.59^{+0.04}_{-0.04}$	$3.47^{+0.67}_{-0.66}$	0.78
luminous (120, baseline)	$2.06^{+0.04}_{-0.04}$	$4.03^{+0.81}_{-0.79}$	1.19
luminous (120, w/o magnification)	$2.06^{+0.04}_{-0.04}$	$4.01^{+0.82}_{-0.81}$	1.19
luminous (120, w/o lensing and magnification)	$2.06^{+0.04}_{-0.04}$	$3.84^{+0.80}_{-0.80}$	1.19

The value of Π_max adopted for the measurement is reported in brackets. The same value is assumed in the model. The tests are always performed using the DEIMOS shape catalogue.
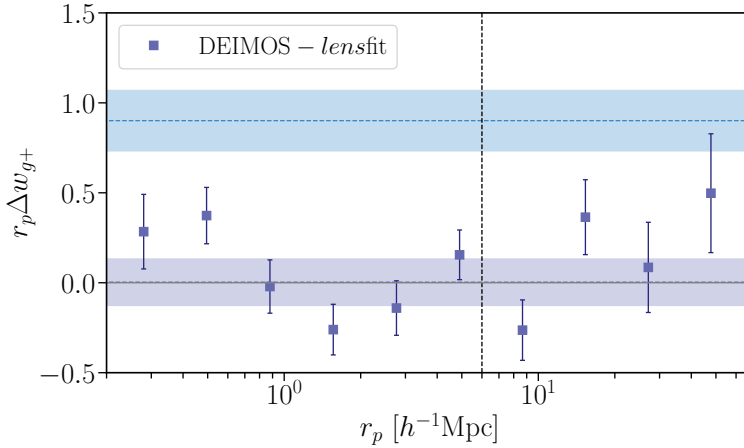
Figure 13: Difference in the w_{g+} measurements as measured by DEIMOS and *lens*fit. The indigo dashed line shows the best-fit amplitude of the difference, here parametrised as A/r_p. Similarly, the light blue dashed line illustrates the best-fit amplitude for the DEIMOS sample, both performed for $r_p > 6\,h^{-1}\mathrm{Mpc}$. The shaded areas delimit the 1σ contour of the fit.

Table 6: Parameters of the Student's t-distributions that best-fit the residuals $(z^{\mathrm{phot}} - z^{\mathrm{spec}})/\sigma_z$ of our samples.

Sample	ν	μ	s
dense	3.79	0.06	0.90
luminous	3.99	-5.43×10^{-6}	0.86

bars are then computed as the standard deviation of the difference in the measured signal for this ensemble.

To quantify the amplitude of the signal to the potential differences in measurement method, we fit both $w_{g+,\mathrm{DEIMOS}}$ and Δw_{g+} with a curve of the form $f(r_p) = A/r_p$, for $r_p > 6\,h^{-1}\mathrm{Mpc}$. The best-fit amplitudes are, respectively, 0.90 ± 0.17 and 0.003 ± 0.13, which means that we detect a signal that is more than six sigma above the uncertainty due to the choice in the shape measurement algorithm adopted.

A7   Mock catalogues

To investigate the impact of magnification bias on the interpretation of our measurements, we generated two mock catalogues that resemble our LRG samples. Our simulated catalogues are obtained from the KiDS photomet-

Figure 14: Comparison between the redshift distributions of the data and those reproduced by the mocks. *Left:* The photometric redshift distribution of our data is shown as an orange hatched histogram, while the solid red line shows the distribution of the photometric redshifts of the mock, obtained from the true ('spectroscopic') redshifts (blue solid line) as detailed in the text. *Right:* Comparison of the mock spectroscopic redshift distribution (solid blue line) and the estimated spectroscopic distribution of our data (light blue line).
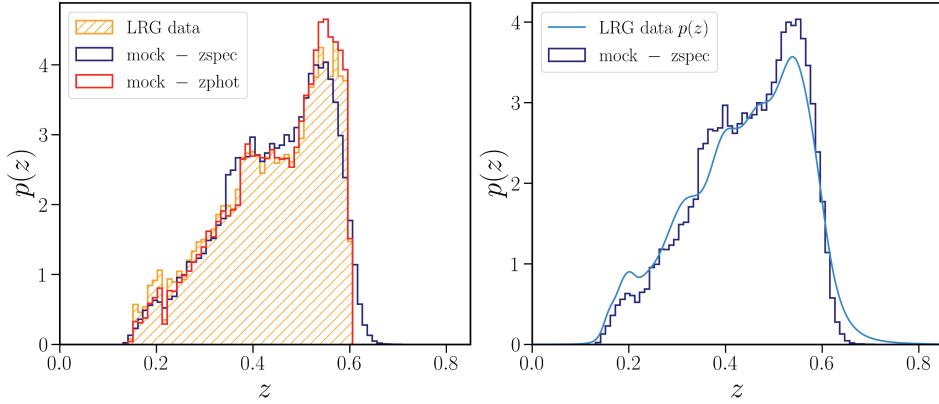
ric mock catalogue presented in van den Busch et al. (2020), which is based on the MICEv2 simulation[22] (Fosalba et al. 2015b; Crocce et al. 2015; Fosalba et al. 2015a; Carretero et al. 2017; Hoffmann et al. 2015) and is specifically designed to reproduce the KiDS photometry. We did not run the LRG selection algorithm on the mock, but rather used their observed location in the redshift-colour space ($u - g, g - r, r - i, i - z$) to select them in the mock.

We first apply a broad colour selection using the MICE `z_cgal` 'spectroscopic' redshift. After assigning the photo-z to our mocks, we repeat the selection replacing the spectroscopic redshift with the photometric one. The photometric redshifts are designed to reproduce the distributions reported in Sect. 3.3 of Vakili et al. (2020). To do so, we draw a random value from a Student's t–distribution centred on $z_{\text{spec}} - \mu\sigma_z$ and with the scale parameter equal to $s\sigma_z$, with μ, ν and s the Student's t–parameters fitted to the full distribution (of the real data). We remind the reader that ν defines the peakiness of the distribution, μ its mean and s sets the width. In the limit of the Student's t–distribution approaching a Gaussian ($\nu \to \infty$), s can be interpreted as the standard deviation of the distribution.

We note that our samples differ from Vakili et al. (2020), since we excluded the galaxies that overlap with the `luminous` sample from the `dense`

---

[22] http://maia.ice.cat/mice/

sample. We therefore recomputed the parameters of the Student's t–distributions specifically for our samples and report these in Table 6. Some care has to be taken when assigning σ_z to the mocks. The per-galaxy σ_z of the LRG samples correlates with the magnitude of the galaxy. We, therefore, identify the closest real galaxy in the (z, m_r) space to each galaxy in the mock, and assign it the corresponding σ_z. We repeat the process for one iteration, replacing the 'spectroscopic' redshift with the preliminary estimate of the photometric one. We note that this procedure results in multiple assignments of the same σ_z to the mock galaxies, but this is not a concern as we do not require it to be unique.

Since we require a high fidelity reproduction of the line-of-sight distribution of our galaxies, we divide our samples and their corresponding mock catalogues in thin redshift slices and match the galaxy number density per slice. At this step, we do not require a perfect match. In this way, we still have enough galaxies to apply the same $m_r^{\mathrm{pivot}}(z)$ cut as for our real data. We repeat these steps iteratively until the number densities are matched between the samples. We tested that the final $p(z^{\mathrm{spec}}|z^{\mathrm{phot}})$ of our mocks are in good agreement with the data $p(z^{\mathrm{spec}}|z^{\mathrm{phot}})$ (see Fig. 14) and that the resulting clustering signal at large scales reproduces the one in our data.

We generate two sets of mock catalogues: a magnified one and one without magnification. We use these for the calibration of α as discussed in Appendix A4.

4 | KiDS-1000: weak lensing and intrinsic alignment around luminous red galaxies

M.C Fortuna, *H. Hoekstra, A.Dvornik*

We study the properties of the Luminous Red Galaxies (LRGs) selected from the 4th data release of the Kilo Degree Survey (KiDS-1000) via galaxy-galaxy lensing of the background galaxies from KiDS-1000. We use a halo model formalism to model our measurements and obtain estimates of the halo masses and the satellite fractions of the LRGs. We use these to interpret the intrinsic alignment (IA) measurements in Fortuna et al. (2021b), who studied the tendency of the LRGs to point in the direction of other LRGs, via the galaxy shape-galaxy position correlation. Here, we directly link the observed IA of the (central) galaxy to the mass of the hosting halo, which is expected to be a fundamental quantity in establishing the alignment, and find that the dependence of the IA amplitude on halo mass is described well by a single power law. We also find that both red and blue galaxies from the source sample associated with the LRGs are oriented randomly with respect to the LRGs.

4.1   Introduction

The intrinsic alignment (IA) of galaxies, defined as the tendency of galaxies to point in a coherent direction, has gained attention in the last two decades as an important contaminant to lensing (Heavens et al. 2000; Crittenden et al. 2001; Kirk et al. 2010; Krause et al. 2016, among others). N-body simulations have explored the origin of the triaxility and angular momentum of dark matter haloes, and how they orient their major axis in the direction of matter overdensities, finding that the orientation also depends on the environment and the location on the large scale structure (Dubinski 1992; Croft & Metzler 2000; Hopkins et al. 2005; Hahn et al. 2007; Lee et al. 2008; Forero-Romero et al. 2014). Models of galaxy alignment predict that the galaxy inherits the orientation of its major axis from the orientation of the parent halo: such a relation is expected to be primarily sourced by the effect of tidal fields during galaxy formation (Catelan et al. 2001). These models predict a dichotomy in the alignment of elliptical, pressure-supported galaxies, and disc-like, rotationally supported galaxies (e.g. Catelan et al. 2001; Hirata & Seljak 2004), in agreement with results from observations (Hirata et al. 2007; Faltenbacher et al. 2009; Joachimi et al. 2011; Blazek et al. 2011; Singh et al. 2015; Johnston et al. 2019; Mandelbaum et al. 2011).

Observations have shown that luminous red galaxies (LRGs) are the main source of IA and that the dependence on luminosity can be described by a power law (Hirata et al. 2007; Joachimi et al. 2011; Singh et al. 2015). Fortuna et al. (2021b) extended observational constraints on the IA amplitude to samples of LRGs with significantly lower luminosities compared to previous studies, and found that the dependence with luminosity is shallower compared to the high-L samples. This points toward a more complex behaviour in the luminosity-alignment relation.

The relation between luminosity and halo mass itself is complex. Hence, a simple dependence with halo mass, as predicted by models of IA (Xia et al. 2017; Piras et al. 2018), would result in a complex dependence of the IA signal with luminosity. It is therefore interesting to explore the observational link between the IA of galaxies and the mass of the hosting halo. This could simplify the modelling and help generate synthetic galaxy catalogues that reproduce the observed IA using halo catalogues from N-body simulations (e.g. Carretero et al. 2017). A direct measure of IA as a function of halo mass avoids the intermediate step of calibrating IA on secondary galaxy properties that are not directly responsible for the alignment mechanism

and that have non-negligible scatter.

In this paper we determine the average halo mass for the samples used in Fortuna et al. (2021b), direct linking their IA signal and their halo mass. Singh et al. (2015); van Uitert & Joachimi (2017) and Piras et al. (2018) have addressed the same question using higher luminosity/higher mass samples, finding a single power law relation for the IA dependence on halo mass. Here, we extend the analysis to the faint-end, where the IA dependence on luminosity changes its slope. This allows us to address the question whether the observed flattening in the IA amplitude is a consequence of a similar flattening in the halo mass-luminosity relation.

To measure the halo masses, we employ weak gravitational lensing: light bundles of the distant galaxies are deflected by the matter distribution along the line of sight, which leads to an apparent correlation between the shape of a background galaxy (source) and the position of a foreground galaxy (lens). This galaxy-galaxy lensing (GGL) signal is an important tool to investigate the dark matter distribution around galaxies (e.g. Hoekstra et al. 2005; Mandelbaum et al. 2006; Velander et al. 2014; Miyatake et al. 2015; van Uitert et al. 2015; Dvornik et al. 2020; Bilicki et al. 2021).

In this paper, we use the halo model to connect the statistical properties of dark matter haloes to those of the galaxies. It is an analytical approach to predict observable quantities based on the link between the galaxy occupation statistics, the abundance, and the clustering of dark matter (Seljak 2000; Ma & Fry 2000; Cooray & Sheth 2002).

In this study, the lens sample consists of LRGs in the footprint of the 4th data release of KiDS (KiDS-1000, Kuijken et al. 2019), which were selected via a variation of the redMagiC algorithm (Rykoff et al. 2014), as presented in Vakili et al. (2020). To measure the lensing signal, we use the source sample presented in Giblin et al. (2021).

LRGs are typically the central galaxies in massive haloes, and are responsible for the alignment at large scales. The alignment at small scales is sourced by satellite galaxies: the intra-halo tidal fields align the satellites in a torquing mechanism that leads to a net radial alignment signal towards the halo centre (Pereira et al. 2008). In this paper, we investigate this signal by determining the alignment of galaxies in the source sample. These are selected to be physically close to the LRGs, so that the LRG can be considered a proxy for the halo centre. To do so, we employ an estimator that is similar to the one used GGL, following the approach presented in Blazek et al. (2012). When measuring the signal, we account for the lensing contamination and the lensing dilution that occurs between galaxies that are

physically associated. The IA of the sources presented here is complementary to the study of the IA signal in Fortuna et al. (2021b), who looked at the alignment signal of the LRG sample at large scales. Here, we constrain the small scale signal ($r_\mathrm{p} < 10h^{-1}\mathrm{Mpc}$) sourced by non-LRG galaxies. These results can thus be used to inform models such as the halo model.

The paper is organised as follows: in Sect. 4.2 we present the data employed in this work; in Sect. 4.3 we introduce the estimator used to measure the signal, while in Sect. 4.4 we present the model framework we use to interpret the measurements. In Sect. 4.5 we detail the fitting procedure and in Sect. 4.6 and Sect. 4.7 we present our results. In Sect. 4.8 we draw our conclusions.

Throughout the paper, we assume a flat ΛCDM cosmology with $h = 0.7, \Omega_\mathrm{m} = 0.25, \Omega_\mathrm{b} = 0.044, \sigma_8 = 0.8$ and $n_\mathrm{s} = 0.96$. Absolute magnitudes are computed assuming $h = 1$.

4.2 Data

The data employed in this work are collected by the Kilo Degree Survey (KiDS), a multi-band imaging survey that has mapped $1350\,\mathrm{deg}^2$ of the sky, divided in two equally sized patches, one in the equatorial region and one in the Southern hemisphere. The latest data release (DR4, hereafter KiDS-1000) covers $1006\,\mathrm{deg}^2$ and provides high quality images in the $ugri$ bands, obtained on the VLT Survey Telescope (VST; Capaccioli et al. 2012) with the OmegaCAM instrument (Kuijken 2011). By survey design, the best images are provided in the r–band, where the mean magnitude limit is $r \sim 25$ (5σ in a $2''$ aperture), and thus we will always refer to the r–band images in the rest of this work. Five infrared bands, $ZYJHK_\mathrm{s}$, obtained from the companion survey VISTA Kilo-degree INfrared Galaxy survey (VIKING; Edge et al. 2013), complement the data, allowing for a robust photometric redshift calibration (Wright et al. 2019; Hildebrandt et al. 2020).

4.2.1 The lens sample

The LRG sample is selected from KiDS-1000 using a variation of the red-MagiC algorithm (Rykoff et al. 2014), as presented in Vakili et al. (2019, 2020). Details of the sample properties can be found in Vakili et al. (2020). Here we summarise the most relevant ones. The sample is selected with a redshift-dependent magnitude cut to ensure a constant comoving number density. The parameter that regulates the selection is $m_r^{\mathrm{pivot}}(z)$, the char-

acteristic r-band magnitude of the Schechter (1976) function, assuming a faint-end slope $\alpha = 1$. The resulting luminous-threshold samples are defined by the ratio:

$$\frac{L}{L_{\mathrm{pivot}}(z)} = 10^{-0.4\left(m_r - m_{r,\mathrm{pivot}}(z)\right)} \, , \qquad (4.1)$$

where $m_r^{\mathrm{pivot}}(z)$ is evaluated using the EzGal (Mancone & Gonzalez 2012) implementation of Bruzual & Charlot (2003), assuming a Salpeter initial mass function (Chabrier 2003), a solar metallicity ($Z = 0.02$) and a single star formation burst at $z = 3$.

Two samples are obtained with the aforementioned strategy: a high luminosity ($L/L_{\mathrm{pivot}}(z) > 1$) and sparser sample ($\bar{n}_{\mathrm{g}} = 2.5 \times 10^{-4} h^3 \mathrm{Mpc}^{-3}$) named `luminous` sample and a denser ($\bar{n}_{\mathrm{g}} = 10^{-3} h^3 \mathrm{Mpc}^{-3}$) and less luminous one ($L/L_{\mathrm{pivot}}(z) > 0.5$), the `dense` sample. In this work, we follow Fortuna et al. (2021b) and use both samples for our analysis, but from the `dense` samples we removed the galaxies that are in common with the `luminous` sample. For a detailed explanation of why the two samples contain overlapping galaxies, we refer to Fortuna et al. (2021b). We also adopt the same luminosity-binning scheme as Fortuna et al. (2021b), with some minor variation as described in Sect. 4.6.

We quantify the scatter in the photometric-spectroscopic redshift relation using the scaled median absolute deviation of $(z_{\mathrm{phot}} - z_{\mathrm{spec}})/(1 + z_{\mathrm{spec}})$. This increases with redshift and it is tighter for the `luminous` sample. In particular, we find $\sigma_z = 0.0139$ for the `luminous` sample and $\sigma_z = 0.0146$ for the `dense` sample. This is also responsible for some overlap of the galaxy properties between the two samples, even when removing the overlapping galaxies.

The stellar masses and absolute magnitudes are obtained via LePhare (Arnouts & Ilbert 2011), assuming the stellar population synthesis model from Bruzual & Charlot (2003), the Chabrier (2003) initial mass function and Calzetti et al. (1994) dust-extinction law. We use the `MASS_BEST` output from LePhare as our best estimate of the mass to use for the point mass approximation (see Sect. 4.4). When computing the mean stellar mass per bin, we remove the galaxies for which the masses estimated as `MASS_MED` are flagged as bad (-99), indicating that the best fit was performed by a non-galaxy template[1].

---

[1]These galaxies are, however, used in the measurements, as our main focus is the luminosity-to-halo mass relation and the luminosity is robustly measured. We note that the change in the average mass is at the sub-percent level.
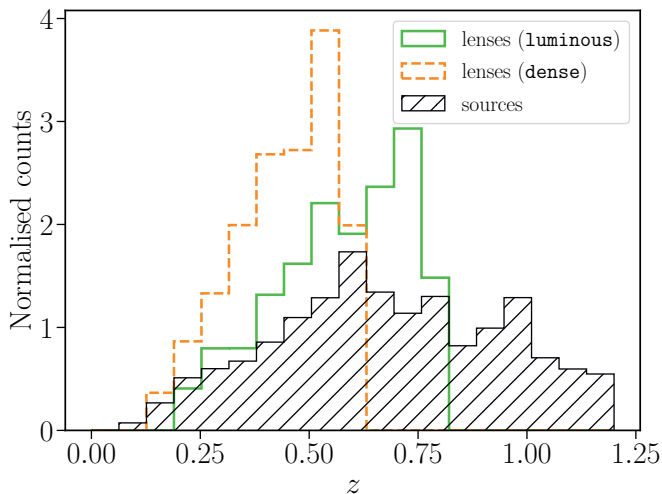
Figure 4.1: The photometric redshift distributions of the source and lens samples employed in the analysis. When computing the GGL signal, we only consider source galaxies at higher redshift than the lens, and with a minimum separation of $z_\epsilon = 0.2$.

We correct the absolute magnitudes for the passive evolution of the stellar population (e−correction). We use EzGal to compute it and follow the setup used in Vakili et al. (2020) to identify the limiting magnitude for the selection of the LRG candidates as described above.

4.2.2   The source sample

The shapes of our galaxies are computed via a self-calibrating version of *lens*fit (Miller et al. 2007, 2013; Fenech Conti et al. 2017; Kannawadi et al. 2019; Giblin et al. 2021)[2]. *lens*fit is a model-based algorithm that provides a measure of the ellipticity by fitting a PSF-convolved two-component bulge and disc model of a galaxy. It returns the ellipticity components $\epsilon = \epsilon_1 + i\epsilon_2$, with $|\epsilon| = (a-b)/(a+b)$, where a, b are, respectively, the major and minor axis. For each galaxy, the method returns also a weight, w_s, which accounts for the increase/decrease in the S/N due to the relative orientation of the galaxy with respect to the PSF and the overall S/N. Note that with this definition, the average ellipticity is an estimator of the shear, $\langle \epsilon \rangle = \gamma$.

The KiDS-1000 shear catalogue benefits from the improvement in the PSF treatment due to the available information provided by the *Gaia* mis-

---

[2]The catalogue is publicly available at `http://kids.strw.leidenuniv.nl/DR4/KiDS-1000_shearcatalogue.php`

sion (Gaia Collaboration et al. 2018). The shears are also calibrated to account for the multiplicative bias (m–bias) that arises as a further correlation between shear systematics: this is calibrated employing high fidelity image simulations based on deep images of the Cosmic Evolution Survey (COSMOS Scoville et al. 2007). We will discuss the m–bias again in Sec. 4.3, where we apply it to our lensing measurements. A full description of the catalogue and the systematic tests can be found in Giblin et al. (2021), while more details on the strategy to calibrate residual biases in described in Kannawadi et al. (2019).

The distributions of our photometric redshifts are illustrated in Fig. 4.1. These redshifts of the source galaxies are estimated based on deep spectroscopic catalogues that cover a sub-sample of the galaxies: these are then re-weighted using a self-organised map (SOM, Wright et al. 2020) to resemble the KiDS-1000 sample, and only sources that fill the SOM cells (a nine-dimensional magnitude-space volume) enter our final sample. The method is also validated by using a clustering–z algorithm. Details on the photometric redshift calibration can be found in Hildebrandt et al. (2021). We restrict our analysis to source galaxies in the redshift range $0.1 < z_s < 1.2$, based on the available calibration of their photometric redshift via the SOM, where z_s indicates the photometric redshift of the source galaxy.

4.3   Measuring the signal

The GGL signal is quantified by the tangential distortion in the shapes of background galaxies (sources) induced by the mass distribution of the foreground galaxies (lenses) along the line-of-sight. As the distortion for a single lens galaxy is small and we lack information on the intrinsic shape of the background galaxy, we perform a statistical analysis of the signal encoded by a large number of lens-source galaxy pairs and measure the mean tangential shear around each lens as a function of lens-source galaxy projected separation, $\langle \gamma_t(r_p) \rangle$. This is a direct measure of the enclosed mass, as we will see later. Note that the S/N of the lensing signal around individual lenses is too small to be detected, and thus we average the signals of an ensemble of lenses. Here, we are implicitly assuming the weak lensing regime, so that the effective shear of a background galaxy can be approximated by the sum of the shears of the individual galaxies in the foreground. We measure the signal of both the `dense` and `luminous` samples in bins of luminosity.

For each source-lens pair, we measure the tangential component of the

ellipticity: indicating with ϕ the angle between the $x-$axis and the lens-source separation vector, and using the ellipticity definition introduced in Sec. 4.2.2, we have

$$\begin{bmatrix} \epsilon_t \\ \epsilon_\times \end{bmatrix} = \begin{bmatrix} -\cos(2\phi) & -\sin(2\phi) \\ \sin(2\phi) & -\cos(2\phi) \end{bmatrix} \begin{bmatrix} \epsilon_1 \\ \epsilon_2 \end{bmatrix} . \quad (4.2)$$

Here, $\epsilon_\times$ is the cross-component of the ellipticity, which corresponds to a rotation of $45 \deg$. The cross-component is an important test of residual systematics and in our measurements we always ensure that the cross-component is compatible with noise.

The ensemble average of the ellipticities of all the sources – which we remind the reader is an estimator of the shear – at projected separation r_p from the lens is directly related to the the amount of matter that we observe around a galaxy, which is quantified by the excess surface mass density (ESD) profile:

$$\Delta\Sigma(r_p) = \bar{\Sigma}(< r_p) - \Sigma(r_p) = \gamma_t(r_p) \, \Sigma_{\text{crit}} . \quad (4.3)$$

The ESD is thus defined as the difference between the mean projected surface mass density enclosed in a projected radius r_p and the surface mass density at r_p. The critical surface mass density is a geometrical factor defined as

$$\Sigma_{\text{crit}} = \frac{c^2}{4\pi G (1 + z_l)^2} \frac{D(z_s)}{D(z_l) D(z_l, z_s)} , \quad (4.4)$$

where the factor $(1+z_l)^2$ at the denominator accounts for our use of comoving units (see also Dvornik et al. 2018, Appendix C for a discussion on this term). Here, z_l (z_s) is the redshift of the lens (source) galaxy, and $D(z_l)$, $D(z_s)$ and $D(z_l, z_s)$ are, respectively, the angular diameter distance to the lens, to the source and between the lens and the source galaxies.

As we rely on photometric redshifts, we need to integrate Eq. 4.4 for the redshift probability distributions of the source sample, $n(z_s)$, and the individual redshift probability distribution of each lens, $p(z_l)$. This provides an effective estimate of Σ_{crit}:

$$\Sigma^{-1}_{\text{crit,eff}} = \frac{4\pi G}{c^2} \int_0^\infty (1 + z_l)^2 D(z_l) \left(\int_{z_l}^\infty \frac{D(z_l, z_s)}{D(z_s)} n(z_s) \mathrm{d}z_s \right) p(z_l) \mathrm{d}z_l . \quad (4.5)$$

To model $p(z_l)$ we use a Gaussian centred on the photometric redshift of the given lens and with standard deviation given by the value of σ_z associated to the specific sample, as discussed in Sect. 4.2.1. The redshift probability

distribution of the source sample, $n(z_s)$, is instead obtained from the SOM as described in Sec. 4.2.2.

The lensing signal decreases as the distance between the lenses and the sources decreases (due to the $D(z_l, z_s)$ in Σ_{crit}^{-1}). In our case, while the lenses span a large range in redshift ($0.15 < z_l < 0.8$), the signal is limited by the source sample, for which we have robust redshift estimates only up to $z_s = 1.2$ (Wright et al. 2020). This means that our lensing efficiency peaks around $z_{ls} \sim 0.3$ and rapidly decreases as we approach high redshifts.

To each lens-source pair we also assign a weight determined by three components: a weight associated to the source sample, w_s, which down-weights the shears of the galaxies with low S/N, and that corresponds to the *lens*fit weight reported as `weight` in the KiDS-1000 shear catalogue (see Sect. 4.2.2); a weight associated to the lens galaxies, which is designed to remove residual correlations between the spatial galaxy number density and the survey observing conditions (Vakili et al. 2020); and a geometric term that down-weights lens-source pairs that are close in redshift, given by the square of the inverse critical mass surface density:

$$w_{ls,eff} = w_s w_l \left(\Sigma_{crit,eff}^{-1} \right)^2 .$$

(4.6)

Our estimator (here indicated with a hat) for the excess surface mass density thus reads:

$$\hat{\Delta\Sigma}_{ls}(r_p) = \left[\frac{\sum_{ls} w_{ls,eff} \, \epsilon_{t,s} \, \Sigma_{crit,eff}}{\sum_{ls} w_{ls,eff}} \right] \frac{1}{1+\bar{m}} \Bigg|_{r_p} ,$$

(4.7)

where we have included an average correction to the galaxy shear obtained from dedicated simulations, which quantifies the residual multiplicative bias in the estimate shear due to the presence of noise and blending in the images. The $m-$bias is a function of redshift (Kannawadi et al. 2019): here we rely on the calibration presented in Kannawadi et al. (2019) and evaluate it in narrow redshifts slices and weight it by $w' = w_s D(z_l, z_s)/D(z_s)$:

$$\bar{m} = \frac{\sum_i w'_i m_i}{\sum_i w'_i}$$

(4.8)

where i is the $i-$th redshift slice. The $m-$bias measured in our samples goes from -0.01 to -0.03.

4.3.1   Contamination from physically associated galaxies: boost factor and IA

Because galaxies tend to cluster and the clustering is a function of galaxy separation, there is an overdensity of sources that are physically associated with the lens. This has two implications: on one hand, these galaxies are not lensed, diluting the GGL signal at small scales; on the other hand, because these galaxies experience the local tidal field, some of them are intrinsically aligned towards the lens, that is, opposite to the lensing signal, further suppressing the signal. The former effect can be accounted by comparing the weighted number of pairs between the lens and source sample and the weighted number of pairs that a random distribution of lenses forms with the source sample, as a function of the projected separation r_p (Sheldon et al. 2004; Mandelbaum et al. 2005). This term is typically referred as boost factor:

$$B(r_\mathrm{p}) = \left.\frac{\sum_\mathrm{r} w_\mathrm{r}}{\sum_\mathrm{l} w_\mathrm{l}} \frac{\sum_\mathrm{ls} w_\mathrm{ls,eff}}{\sum_\mathrm{rs} w_\mathrm{rs,eff}}\right|_{r_\mathrm{p}} \tag{4.9}$$

where $w_\mathrm{rs,eff} = w_\mathrm{s} \left(\Sigma_\mathrm{crit,eff}^{-1}\right)^2$ and $w_\mathrm{r} = 1$.

Both the lensing dilution from unlensed galaxies and the negative contribution from IA can be removed by selecting only source galaxies that have separations larger than z_ϵ from the lens, with $z_\mathrm{s} - z_\mathrm{l} = z_\epsilon$ (Leauthaud et al. 2017). Although we also apply the boost factor, we make use of this cut when measuring the lensing signal, to ensure that any contamination is low and adopt $z_\epsilon = 0.2$.

4.3.2   Random subtraction

On top of the correction discussed in the previous section, we follow Singh et al. (2017) and subtract the signal around random points from the lensing signal. This ensures that residual additive biases, introduced by the survey edges and by the presence of masks are removed from our measurement. The random signal is obtained in exact analogy to Eq. 4.7, but measuring the lensing signal around points uniformly distributed over the survey footprint with removal of the masked regions. The final estimator is thus given by

$$\Delta\hat{\Sigma}(r_\mathrm{p}) = B(r_\mathrm{p})\Delta\hat{\Sigma}_\mathrm{ls}(r_\mathrm{p}) - \Delta\hat{\Sigma}_\mathrm{rs}(r_\mathrm{p}) . \tag{4.10}$$

4.3.3 Estimator for the IA signal

We are, however, also interested in measuring the IA signal of the source galaxies around the lenses. To this end, we only select galaxies within a small redshift separation from the lenses. We chose $\Delta z \equiv |z_{\mathrm{l}} - z_{\mathrm{s}}| < z_\epsilon$ with $z_\epsilon = 0.15$. The computation is analogous to the case of lensing, (Eq. 4.10): we label the resulting signal $\Delta\Sigma_{\Delta z}$ to denote the redshift range used for this measurement. The signal measured in this way is still affected by the lensing contamination, which can be removed using lensing signal measured for the 'lensing' sample. Focusing on physically associated galaxies, in this case it is crucial to correctly account for the boost factor.

The excess of lens-source pairs after the random subtraction described in the previous section causes the IA signal (as this corresponds to the clustered galaxies): the average critical surface density thus becomes:

$$\langle \Sigma_{\mathrm{crit,eff}} \rangle_{\mathrm{ex}} = \frac{\sum_{\mathrm{ls}} w_{\mathrm{ls,eff}} \Sigma_{\mathrm{crit,eff}}^{(\mathrm{ls})} - \sum_{\mathrm{rs}} w_{\mathrm{rs,eff}} \Sigma_{\mathrm{crit,eff}}^{(\mathrm{rs})}}{\sum_{\mathrm{ls}} w_{\mathrm{ls,eff}} - \sum_{\mathrm{rs}} w_{\mathrm{rs,eff}}} \ . \qquad (4.11)$$

Finally, the IA estimator is (Blazek et al. 2012):

$$\hat{\gamma}_{\mathrm{IA}}(r_{\mathrm{p}}) = \left. \frac{\Delta\hat{\Sigma}_{\Delta z} - \Delta\hat{\Sigma}_{\mathrm{lens}}}{(B_{\Delta z} - 1)\langle \Sigma_{\mathrm{crit,eff}}^{(\Delta z)} \rangle_{\mathrm{ex}} - (B_{\mathrm{lens}} - 1)\langle \Sigma_{\mathrm{crit,eff}}^{(\mathrm{lens})} \rangle_{\mathrm{ex}}} \right|_{r_{\mathrm{p}}} \ . \qquad (4.12)$$

Leonard et al. (2018) presented an improved version of this estimator which exploits the scale dependence of IA to better separate it from lensing. This requires multiple measurements of the source galaxy shapes, obtained with different shape estimates that weigh different galaxy scales differently. Here, we do not investigate this possibility, mainly motivated by the results in Georgiou et al. (2019b), who used very high S/N measurements and found that the scale dependence of IA is mainly limited to red satellites. The gain is therefore expected to be minimal in a mixed sample.

4.4 Modelling the signal with the halo model

The GGL signal captures the projected two-point correlation function between a galaxy position and a galaxy shear, which in turn is a measure of the three-dimensional correlation between matter and density distributions. Because lensing is sensitive to density contrasts, in practise we measure the difference between the projected mass density at a certain radius and the average mass density contained in that radius (eq. 4.3).

In order to model the signal, we need to provide an analytical expression for the projected surface mass density around galaxies. This is related to the three-dimensional correlation function via a projection integral. In the distant observer approximation, it can be expressed as an Abel transform

$$\Sigma(r_{\mathrm{p}}) = 2\bar{\rho}_m \int_{r_{\mathrm{p}}}^{\infty} \xi_{\delta\mathrm{g}}(r) \frac{r \, \mathrm{d}r}{\sqrt{r^2 - r_{\mathrm{p}}^2}} \; . \tag{4.13}$$

Here $\xi_{\delta\mathrm{g}}(r)$ is the correlation between the galaxy and the fractional matter density contrast, $\langle \delta(\mathbf{x})\delta_{\mathrm{g}}(\mathbf{x} + \mathbf{r})\rangle$, with $\delta(\mathbf{x}) = (\rho_X(\mathbf{x}) - \bar{\rho}_X)/\bar{\rho}_X$, $X \in \{\delta, \mathrm{g}\}$. In the following, we will always use the short-notation δ to indicate the dark matter and g for the galaxy. Since galaxies form inside dark matter haloes, the halo model is a natural framework to describe the matter-galaxy correlation function, $\xi_{\delta\mathrm{g}}(r)$. We present this formalism in the next section.

The projected mass contained within the radius r_{p} can be written as

$$\bar{\Sigma}(< r_{\mathrm{p}}) = \frac{2}{r_{\mathrm{p}}^2} \int_0^{r_{\mathrm{p}}} \Sigma(R')R'dR' \tag{4.14}$$

and from eq. 4.3 we can recover the ESD.

While this formalism strictly describes only the lensing effect due to the dark matter distribution, we also include the GGL due to the baryonic mass of the galaxy, here modelled as a point mass (pm),

$$\Delta\Sigma_{\mathrm{pm}} = \frac{\langle M_* \rangle}{\pi r_p^2} \; . \tag{4.15}$$

This approximation is motivated by the fact that the minimum scale we probe is $r_p = 60 \; h^{-1}\mathrm{kpc}$, much larger than the physical extent of the stellar component of a galaxy.

We evaluate the model at the effective redshift of the lenses, z_{eff}, given by the weighted mean of the lenses, with weight the lensing efficiency in equation 4.6. For the luminous sample, this corresponds to $z_{\mathrm{eff}} = 0.406$, while for the dense sample $z_{\mathrm{eff}} = 0.368$.

4.4.1   The halo model

The halo model (Seljak 2000; Ma & Fry 2000; van den Bosch et al. 2013; Cooray & Sheth 2002, for a review) is a well-established formalism for predicting and interpreting the clustering and lensing statistics of galaxies and dark matter. The key idea behind the halo model is that the mass of the

halo is the fundamental property that drives halo clustering statistics. It assumes that all dark matter in the Universe is bound in haloes and that dark matter haloes are fully described by a universal density profile.

The formalism is based on a set of ingredients: a density profile for the dark matter distribution; a halo mass function, that provides a prescription of how many haloes populate a given comoving volume at a given redshift; and a halo bias function, which quantifies the bias of the bounded haloes with respect to the underlying matter distribution. Then, galaxies can be included into the formalism through a prescription that provides the way galaxies occupy dark matter haloes. The halo occupation distribution (HOD), is a convenient way of doing that, assigning the number of galaxies N_g per a give halo of mass M, $\langle N_g | M \rangle$. We discuss in detail the model we adopt for the HOD in Sect. 4.4.3

We define dark matter haloes as spheres with an average density of 200 times the background density today, $\rho_h = 200 \rho_m$. We assume that the dark matter is spatially distributed following the Navarro-Frenk-White profile (NFW, Navarro et al. 1996), with a concentration-mass relation from Duffy et al. (2008). We also assume that satellite galaxies are spatially unbiased with respect to the dark matter particles, i.e. that their spatial distribution is described by $\rho_s(r, M) = \rho_h(r, M) \equiv M u(r, M)$, with $u(r, M)$ the normalised density profile of dark matter and r the distance from the centre of the halo. We allow central galaxies to have a different amplitude of the concentration-mass relation, which we parametrise as a free pre-factor f_c. For the halo mass function, $n(M)$, as for the halo bias function, $b_h(M)$, we adopt the functions presented in Tinker et al. (2010). We explicitly force the halo bias to be normalised at each redshift: the normalisation is obtained by integrating the halo bias function over a large range of masses ($10^2 - 10^{18} \ h^{-1} M_\odot$). We do not model the off-centering of central galaxies, i.e. we always assume that they sit at the centre of their halo.

4.4.2   The galaxy-matter power spectrum

Given a prescription for the HOD (Sect. 4.4.3) and the set of ingredients introduced in Sect. 4.4.1, it is possible to build the correlation functions between the matter density field and a continuous galaxy field, as well as their auto-correlations. As such relations involve convolutions, for computational reasons it is convenient to work in Fourier space and then transform the quantities back to real space. We thus present them in Fourier space, as they are implemented this way in the code.

One of the main advantages of the halo model is its separate treatment

of the correlation that arise between the galaxies/matter within the halo, which leads to the so called 1-halo term, and the correlation between those that belong to different haloes, the 2-halo term. As a general result, the full power spectrum is

$$P(k, z) = P^{1h}(k, z) + P^{2h}(k, z) \qquad (4.16)$$

regardless whether we are describing the clustering of galaxies, of dark matter or the matter-galaxy correlation.

In turn, we can split the contributions from central and satellite galaxies and model them individually. Denoting with 'c' the central-galaxy components, with 's' the terms which are sourced by the satellite population, and with δ those corresponding to matter, we have that any correlation is given by the sum of all of the possible correlations between these terms. In Fourier space, for the case of the galaxy-matter cross power spectrum, this reads:

$$P_{g\delta}(k, z) = f_c P^{1h}_{c\delta}(k, z) + f_s P^{1h}_{s\delta}(k, z) + f_c P^{2h}_{c\delta}(k, z) + f_s P^{2h}_{s\delta}(k, z) . \qquad (4.17)$$

Here f_X with $X \in \{c, s\}$ is the fraction of galaxies of a given type entering the correlation. These can be obtained from the galaxy number densities as predicted by the HOD as

$$f_X = \frac{n_X}{n_g} , \qquad (4.18)$$

where

$$n_X = \int_0^\infty \langle N_X | M \rangle \, n(M) \, \mathrm{d}M . \qquad (4.19)$$

It is convenient to introduce the functions $\mathcal{H}_X$, where $X = \{\delta, c, s\}$ and are thus associated to a given component:

$$\mathcal{H}_\delta(k, M) = \frac{M}{\rho_m} u(k, M) , \qquad (4.20)$$

$$\mathcal{H}_c(k, M) = \frac{\langle N_c | M \rangle}{n_g} \qquad (4.21)$$

and

$$\mathcal{H}_s(k, M) = \frac{\langle N_s | M \rangle}{n_g} u(k, M) . \qquad (4.22)$$

The 1-halo and 2-halo terms of the power spectrum thus read:

$$P^{1h}_{xy}(k) = \int_0^\infty \mathcal{H}_x(k, M) \mathcal{H}_y(k, M) \, n(M) \, \mathrm{d}M \qquad (4.23)$$

and

$$P_{xy}^{2h}(k) = P_{\text{lin}}(k) \int_0^\infty \mathrm{d}M_1\, \mathcal{H}_x(k, M_1) b_{\text{h}}(M_1) n(M_1)$$
$$\times \int_0^\infty \mathrm{d}M_2\, \mathcal{H}_y(k, M_2) b_{\text{h}}(M_2) n(M_2)\,. \tag{4.24}$$

A relevant quantity that we can predict via this formalism is the average mass mass of bounded haloes that host a central galaxy. This is defined as:

$$\langle M_{200} \rangle = \frac{1}{n_{\text{c}}(z_{\text{eff}})} \int \langle N_{\text{c}} | M \rangle n(M) M \mathrm{d}M\,. \tag{4.25}$$

4.4.3 The halo occupation distribution

Following Cacciato et al. (2009), we derived the HOD from the Conditional Luminosity Function (CLF) obtained for the SDSS by Yang et al. (2003). The CLF, $\mathrm{d}\Phi(L|M)\mathrm{d}M$, specifies the average number of galaxies with luminosity in the range $L \pm \mathrm{d}L/2$ that reside in a halo of mass M. Thus, integrating over a certain luminosity bin provides the number of galaxies with a certain luminosity $L \in [L_1, L_2]$ that reside in a halo of mass M,

$$\langle N_g | M, L_1, L_2 \rangle = \int_{L_1}^{L_2} \Phi(L|M)\mathrm{d}L \tag{4.26}$$

As in Cacciato et al. (2009), we split the CLF in two components,

$$\Phi(L|M) = \Phi_{\text{c}}(L|M) + \Phi_{\text{s}}(L|M), \tag{4.27}$$

where $\Phi_{\text{c}}(L|M)$ is the CLF associated with central galaxies, while $\Phi_{\text{s}}(L|M)$ is the CLF associated with satellite galaxies.

The central galaxy CLF is described by a log-normal function,

$$\Phi_{\text{c}}(L|M)dL = \frac{\log e}{\sqrt{2\pi}} \exp\left[-\frac{(\log L - \log L_{\text{c}})^2}{2\sigma_{\text{c}}^2} \right] \frac{\mathrm{d}L}{L}, \tag{4.28}$$

where

$$L_{\text{c}}(M) = L_0 \frac{(M/M_1)^{\gamma_1}}{[1 + (M/M_1))^{\gamma_1 - \gamma_2}]} \tag{4.29}$$

is the mean luminosity of central galaxies in a halo of mass M. M_1 is the characteristic mass scale at which $L_{\text{c}}(M)$ changes its slope ($L_{\text{c}} \propto M^{\gamma_1}$ for $M \ll M_1$ and $L_{\text{c}} \propto M^{\gamma_2}$ for $M \gg M_1$). Eq. 4.29 is one of the key relations we aim to constrain for the LRG sample (see Sec. 4.6).

Satellite galaxies obey

$$\Phi_s(L|M) = \Phi_s^* \left(\frac{L}{L_s^*}\right)^{\alpha_s+1} \exp\left[-\left(\frac{L}{L_{s^*}}\right)^2\right] \frac{\mathrm{d}L}{L}, \qquad (4.30)$$

where $L_{s^*}(M) = 0.562 L_c(M)$ and

$$\log[\Phi_s^*(M)] = b_0 + b_1(\log M_{12}) \qquad (4.31)$$

In total, our halo occupation distribution is described by nine parameters: $\log M_1, \log L_0, \gamma_1, \gamma_2, \sigma_c, f_c \alpha_s, b_0, b_1$.

4.5   Fitting procedure

We sample the parameter space via a Monte Carlo Markov Chain procedure, using the Emcee sampling[3] (Foreman-Mackey et al. 2013) sampler. We assume a Gaussian Likelihood of the form

$$\mathcal{L} \propto \exp\left[-\frac{1}{2}(\mathbf{D}_i - \mathbf{M}(\theta)_i)^{\mathrm{T}} \mathbf{C}_{ij}^{-1}(\mathbf{D}_j - \mathbf{M}(\theta)_j)\right], \qquad (4.32)$$

where $\mathbf{D}$ is the data vector, $\mathbf{M}(\theta)$ is the model evaluated for the set of parameters θ, and i, j refer to the radial bin under consideration, and $\mathbf{C}_{ij}^{-1}$ is the inverse of the data covariance matrix. We employ 120 walkers and check the convergence of the chains by visually inspecting the chains. The priors for the HOD parameters are reported in Table 4.1 and are based on previous results in literature. In particular, while we broadly follow the choice of the priors in Bilicki et al. (2021), we adopt more informative priors in the following cases: σ_c has been shown to be tightly constrained by current measurements as investigated in Cacciato et al. (2014, see e.g. their Fig. 6); γ_1 is expected to be poorly constrained by a luminous sample such as the LRGs: here we follow Cacciato et al. (2014), but rather than fixing it we provide an informative prior centred on the best-fit value in C13; the prior for γ_2 is typically extremely broad: however, the best-fit values obtained for different samples are all in good agreement and span the range $0.2 - 2.0$ (Cacciato et al. 2013, 2014; van Uitert et al. 2016a; Dvornik et al. 2018; Bilicki et al. 2021): we thus restrict the sample to the range $\mathcal{U}(0, 2)$. We also reduce the range of f_c based on some preliminary runs and exclude zero to avoid unphysical behaviour of the model.

---

[3]https://emcee.readthedocs.io/en/stable/

Table 4.1: The priors adopted in the fit and the corresponding fiducial values, here reported as the median of the marginal posteriors, while the best fit values are reported in brackets. The error bars correspond to the 16th and 84th percentiles. $\mathcal{N}(\mu, \sigma)$ indicates a normal distribution with mean μ and standard deviation σ.

Parameter	Prior	Fiducial
f_c	$[0.1, 1]$	$0.977^{+0.017}_{-0.054}$ (0.999)
$\log(L_0/[h^{-2}L_\odot])$	$[7, 13]$	$9.950^{+0.331}_{-0.577}$ (10.357)
$\log(M_1/[h^{-1}M_\odot])$	$[9.0, 14.0]$	$11.656^{+0.341}_{-0.434}$ (12.070)
γ_1	$\mathcal{N}(3.18, 2)$	$4.224^{+1.888}_{-1.863}$ (3.146)
γ_2	$[0, 2]$ (0.266)	$0.421^{+0.174}_{-0.140}$ (0.266)
σ_c	$[0.1, 0.3]$	$0.131^{+0.060}_{-0.022}$ (0.115)
α_s	$\mathcal{N}(-1.1, 0.9)$	$-1.734^{+0.524}_{-0.404}$ (-1.478)
b_0	$\mathcal{N}(0, 1.5)$	$-1.355^{+0.491}_{-0.456}$ (-1.607)
b_1	$\mathcal{N}(1.5, 2.0)$	$0.864^{+0.287}_{-0.359}$ (1.056)

4.6   Constraints on the lens sample properties

We measured the ESD signal of the `dense` and `luminous` samples in bins in luminosity, applying the cuts presented in Fortuna et al. (2021b) and labelled `D1`, `D2`, `D3`, `D4`, `D5`, `L1`, `L2`, `L3`. The D1 and L1 samples of this studies slightly differ from those in Fortuna et al. (2021b), because of the removal of the galaxies that reside in the tails of the distributions[4]. Removing the tail is crucial for the correct interpretation of the luminosity distributions by the model: the HOD modelling assumed here is designed for volume-complete samples. Given the lack of a selection function in the model, the long faint-tail would be populated by a large number of faint galaxies, as predicted by the modified Schechter function in Eq. 4.30. We explore how well our model can capture the luminosity distribution of our samples in Appendix A1.

The properties of the lens samples are reported in Table 4.2. We jointly fit all the samples with a single model and found a unique set of HOD parameters, which we report in Table 4.1. The reduced χ^2 is 1.05.

The best-fit HOD parameters agree within the error bars with the best-fit parameters of the red population of the KiDS-Bright sample (Bilicki et al. 2021). This is a sign that the two samples, albeit selected with different

---

[4]The tail is due to the photo-z scatter, such that a $m_r(z)$ cut does not translate into a sharp cut in absolute magnitudes. We also remove part of the high-L, with a cut at $M_r - 5\log(h) = -22.6$.
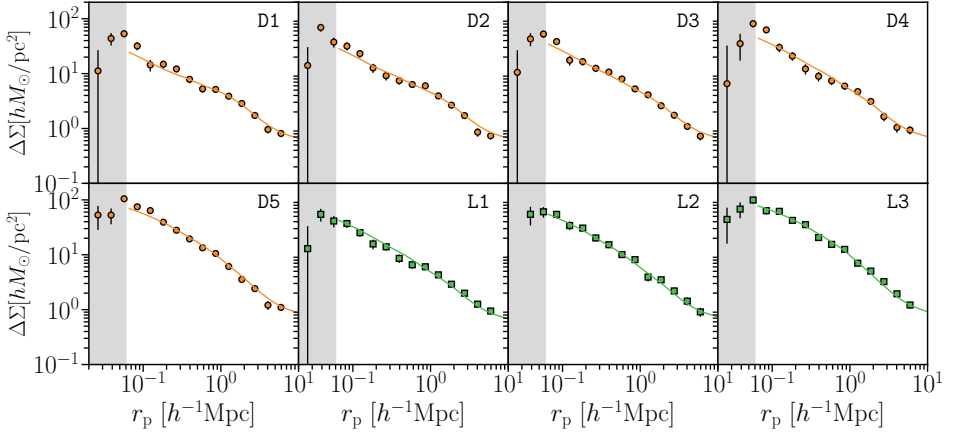
Figure 4.2: The ESD measurements for the samples listed in Table 4.2. We plot the best fit curves (Table 4.1) on top of the data points. The grey shadowed area is excluded from the fit. The reduced χ^2 of the fit is $\chi^2_{\rm red} = 1.05$.

cuts, are characterised by similar scaling relations. It is, however, surprising that the stellar-to-halo mass relation of the red galaxies of the Bright sample has a very similar scaling to the luminosity-to-halo mass relation of the LRG sample (see Sect. 4.6.1). We interpret this result as a consequence of the observed luminosity-to-stellar mass-relation for the LRGs, which is close to unity (see Tab. 4.2).

4.6.1   Luminosity-halo mass relation

For each sample, we derive the corresponding average halo mass, $\langle M_{200} \rangle$ (Eq. 4.25). These are reported in Table 4.2. At intermediate luminosity (D5, L2 L3), our results are in good agreement with previous studies (Mandelbaum et al. 2006; Miyatake et al. 2015; van Uitert et al. 2015), although at high luminosity the extrapolation of our best-fit curve is above the measurements from literature. Here, we only show the point from van Uitert et al. (2015) which are the closest to the effective redshift of our samples. We also note that Mandelbaum et al. (2006) use a different definition of halo mass, and thus the comparison has to be considered only qualitative. However, our samples are overall fainter than these, providing an extension to the $L - M$ towards lower luminosities. This is illustrated in Fig. 4.3, where we also plot the luminosity-halo mass relation for the central galaxies as predicted in Eq. 4.29. Given that the fraction of satellites is overall low (see Table 4.2), the qualitative agreement between the data
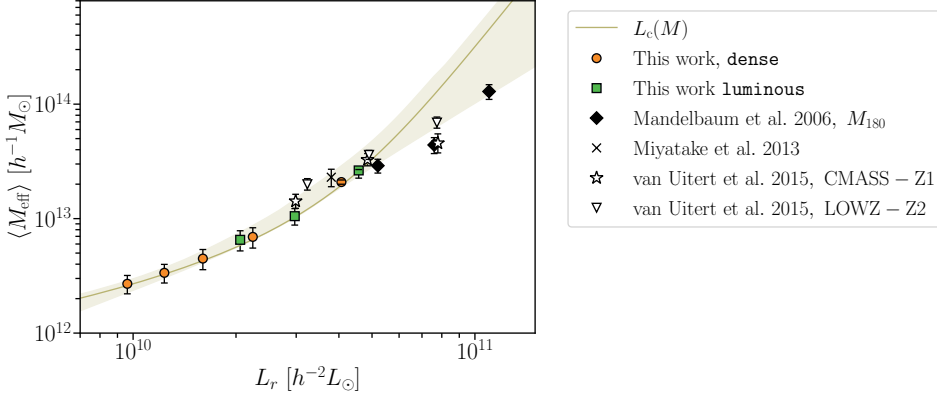
Figure 4.3: The luminosity-halo mass relation for the LRG sample (`dense` orange circles; `luminous` green squares), compared with similar measurements from different sample in the literature. The solid line shows the $L_c(M)$ relation predicted by our model.

Table 4.2: Properties of the lens samples.

Sample	$\langle \log L[h^{-2}L_\odot] \rangle$	$\langle \log M_*[h^{-2}M_\odot] \rangle$	$\langle \log M_{200}[h^{-1}M_\odot] \rangle$	f_s
D1	10.01	10.25	12.43 ± 0.05	0.29 ± 0.05
D2	10.20	10.35	12.53 ± 0.06	0.27 ± 0.04
D3	10.21	10.46	12.65 ± 0.07	0.24 ± 0.03
D4	10.35	10.62	12.84 ± 0.08	0.2 ± 0.02
D5	10.59	10.84	13.32 ± 0.03	0.13 ± 0.01
L1	10.33	10.63	12.81 ± 0.08	0.19 ± 0.02
L2	10.48	10.77	13.02 ± 0.07	0.16 ± 0.02
L3	10.65	10.94	$13.42^{+0.02}_{-0.05}$	0.11 ± 0.02

$\langle M_{200} \rangle$ and f_s are derived from the set of HOD parameters that maximise the likelihood. The error bars correspond to the 16th and 84th percentiles.
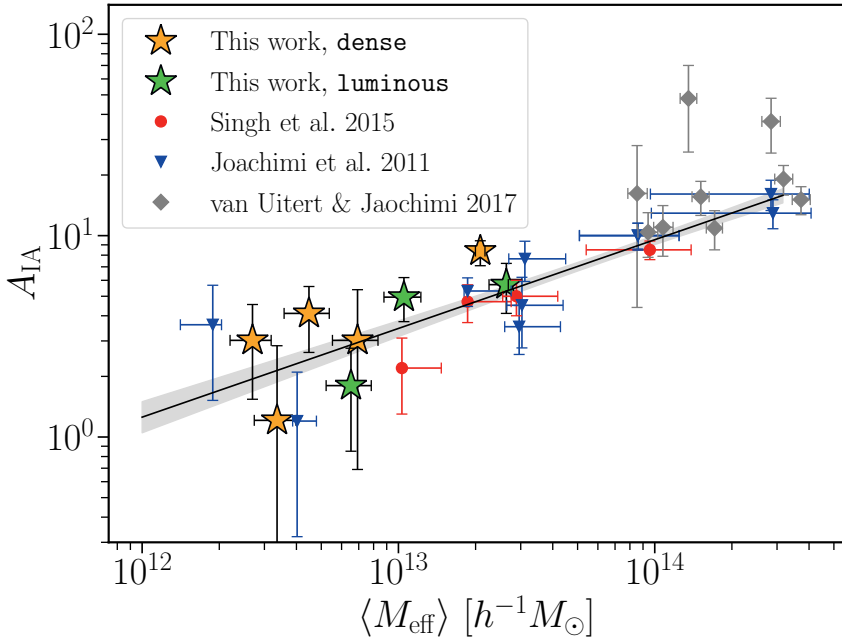
Figure 4.4: The dependence of IA on halo mass for different IA measurements. The halo masses, $\langle M_{\mathrm{eff}} \rangle$, are obtained as described in the text. We indicate our measurements with star markers (orange: `dense` sample, green: `luminous`); the other data points are taken from the literature. The solid black line shows the best fit curve of the $A_{\mathrm{IA}}(M)$ relation described by Eq. (4.33), while the shaded area delimits the 68% confidence region.

and the curve is expected and the curve provides a useful comparisons for simulations and the galaxy properties in mock catalogues.

4.6.2   IA dependence on halo mass

To explore the implications of the observed luminosity-to-halo mass relation for the IA signal of the LRGs, we use the measurements in Fortuna et al. (2021b) and place them into context using the estimates of the halo masses obtained in the previous section. Fortuna et al. (2021b) used a Non-Linear Linear Alignment model (Hirata & Seljak 2004; Bridle & King 2007), adapted to account for the photometric redshift uncertainty (Joachimi et al. 2011), to fit the IA signal at large scales ($r_{\mathrm{p}} > 6\,h^{-1}\mathrm{Mpc}$). The best-fit IA amplitudes, A_{IA}, of the different sub-samples are shown in Fig. 4.4 as orange (`dense`) and green (`luminous`) stars.

When combined with previous measurements in the literature, Fortuna

et al. (2021b) found that the IA dependence of the red galaxies can be described well by a double power law, with a break at $L_r \lesssim 3.2 \times 10^{10} h^{-2} L_{r,\odot}$, although the data show a large scatter at low-L. We are now in a position to investigate whether this dependence was primarily sourced by the halo mass, or if the relation is more complex and requires the addition of secondary galaxy properties. Interestingly, our measurements of $L(M)$ lie on the transition between the two regimes of the power law in Eq. 4.29. This means that the double power law in the IA-L plane reflects at least partially the double power law in the $L - M$ plane. We explore this further by showing the IA amplitudes in Fortuna et al. (2021b) as a function of weak lensing mass in Fig. 4.4. Although the scatter is too large to draw definitive conclusions, we note that the overall trend matches a single power law. To obtain a more complete picture, we also added the measurements from Joachimi et al. (2011) (MegaZ, SDSS LRGs, the L3 and L4 samples from the SDSS) and Singh et al. (2015) (LOWZ) to Fig. 4.4, which are based on LRGs and thus can safely be assumed to be mainly centrals[5] To do so, we converted the luminosity of each sample into an estimate of their halo mass, via the relation found in Sect. 4.6 and displayed in Fig. 4.3. Singh et al. (2015) provide estimates of the halo masses of their samples, but those are based on a different definition of halo mass and for ease of comparison we decided to use our scaling relation. Since van Uitert & Joachimi (2017) do not provide the luminosity of the clusters, but use the same definition of halo mass, we decided to use their halo mass estimate. We fit all the measurements in Fig. 4.4 with a single power law of the form:

$$A_{\mathrm{IA}}(M) = A \left(\frac{M}{M_0} \right)^{\beta_M} , \qquad (4.33)$$

with $M_0 = 10^{13.5} h^{-1} M_\odot$. We find a best fit amplitude of $A = 5.74^{+0.32}_{-0.32}$ and slope $\beta_M = 0.44^{+0.04}_{-0.04}$. The reduced χ^2 is 1.64 for 21 degrees of freedom. We stress, however, that some of the masses associated to these measurements lie beyond the range constrained by our data, and are thus an extrapolation. This is relevant because a small variation of the slope becomes significant at high-L. We test the impact of this by replacing our $L - M$ relation with the one in van Uitert et al. (2015) for the high-mass points (LOWZ, MegaZ and SDSS LRGs). This relation was also adopted in Piras et al. (2018) and includes a redshift dependence, which we do not consider in our model. When repeating the fit with this new set of data, we still find comparable

---

[5]For this reason, we decided to omit the measurements from Johnston et al. (2019), which are known to have a larger fraction of satellites.
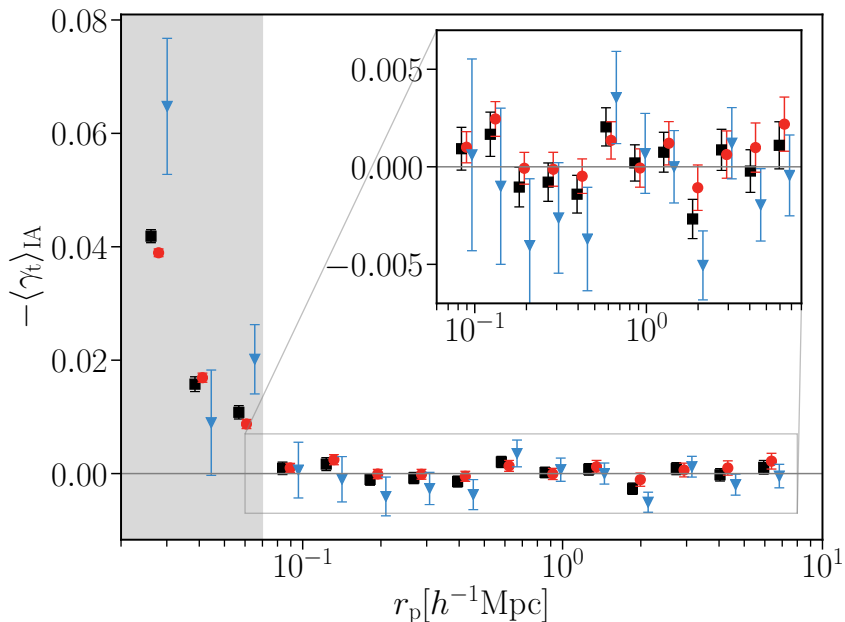
Figure 4.5: The IA signal of the source galaxy sample around the LRGs, selected for small redshift separations ($|z_l - z_s| < 0.15$). We consider the signal from the full source sample (black squares), and its split in red/blue (red circles/blue triangles). At separations below $0.06\ h^{-1}\mathrm{Mpc}$ (grey region) blending becomes important and thus we do not consider it in the analysis. For clarity, the red and blue points are shifted horizontally.

results within the model uncertainty although we notice an improvement in the reduced χ^2, which in this case is 1.19. We also tested the impact of the clustering measurements on our fit: the interpretation of their IA signal is indeed complicated by the fact that their shapes are obtained with a different technique than for the LRG samples (van Uitert & Joachimi 2017). We thus removed them from our data vector and repeated the fit: the result of this test is compatible with our fiducial setup.

4.7 Constraints on the IA of the source sample

To constrain the IA of the source galaxies we measured the $\langle \gamma_t \rangle$ signal in narrow bins in redshift ($\Delta z \equiv |z_l - z_s| = 0.15$)[6] and subtracted the lens-

---

[6]We note that with this definition, the galaxy-galaxy separation is a function of redshift. Here, we are primarily limited by the photometric redshift uncertainty, and thus consider

ing contribution as described in Sect. 4.3.3[7]. Selecting only galaxies with a small separation along the line-of-sight enhances the IA signal, while removing a substantial part of the lensing contribution. The different choice in z-binning is fully accounted for in the model through Σ_{crit}, which is computed according to the new galaxy selection. The average signal, $\langle \gamma_{\mathrm{t}}(r_{\mathrm{p}}) \rangle$ is computed as in Eq. 4.12 and thus is the average tangential ellipticity ϵ_{t}, weighted by the lensing efficiency. Hence, the IA signal is expressed in terms of the weighted intrinsic shear instead of the intrinsic ellipticity, as in Georgiou et al. (2019b).

Here, we only consider the lens galaxies from the `dense` sample, without any split in luminosity. In Appendix A2 we report the fraction of galaxies of the source sample that are physically associated to the LRGs. The results are presented in Fig. 4.5. We do not detect any intrinsic alignment for the full source sample, $\langle \gamma_{t,\mathrm{IA}} \rangle = -0.0001$ up to $10\,h^{-1}\mathrm{Mpc}$, with a χ^2 of the null-hypothesis of $\chi^2_{\mathrm{null}} = 1.67$. As for the GGL signal, we do not consider the data points below $0.06\ h^{-1}\mathrm{Mpc}$, where observational systematics become important. Although at small scales IA is expected to be radial dependent (Pereira et al. 2008; Pereira & Bryan 2010), having detected zero signal, we limit our fit to a constant value and do not consider more sophisticated models: we find $C = (-0.49 \pm 1.4) \times 10^{-4}$.

We explore now the possibility that the signal is washed out by the presence of blue galaxies in the sample, which are expected to be poorly or none aligned. We thus split the source galaxies based on their morphology. We follow Li et al. (2021) and use the parameter T_{B} from the BPZ photo-z code (Benítez 2000; Coe et al. 2006) as a proxy for the morphology: we identify the 'red' population (a combination of E1, Sbc, Scd types) as the galaxies satisfying $T_{\mathrm{B}} \leqslant 3$, while the 'blue' one is the complementary sample, selected by requiring $T_{\mathrm{B}} > 3$. The signal is displayed in Fig. 4.5. Also in this case we do not observe any alignment signal, with $\langle \gamma_{t,\mathrm{IA}}^{(\mathrm{red})} \rangle = -0.0007$ ($\chi^2_{\mathrm{null,red}} = 1.39$) and $\langle \gamma_{t,\mathrm{IA}}^{(\mathrm{blue})} \rangle = 0.0011$ ($\chi^2_{\mathrm{null,blue}} = 1.35$). We also report the best fit values of the constant fit, which in this cases are: $C^{(\mathrm{red})} = -0.0003 \pm 0.0002$ and $C^{(\mathrm{blue})} = 0.0003 \pm 0.0002$.

To measure the IA with the split in colour, we subtracted the same lensing signal as for the full sample. This is motivated by the fact that lensing does not depend on the source galaxy colour. We tested, however, that the residual IA that might contaminate the signal did not affect the results by

---

this effective treatment as sufficient.

[7]We stress that this IA signal differs from the one discussed in the previous section, which was obtained by using the two-point projected correlation function.

measuring the lensing signal only for the red source galaxies and measured the IA by subtracting this 'red lensing' ESD from $\Delta\Sigma_{\Delta z}^{(\text{red})}$. We found the results to be compatible within the statistical uncertainty with our fiducial setup.

Our results are in line with previous measurements (Hirata & Seljak 2004; Blazek et al. 2012; Chisari et al. 2014; Sifón et al. 2015). Dark matter only simulations predict satellite galaxies to be radially aligned towards the centre of the halo (Pereira et al. 2008; Pereira & Bryan 2010), but this signal is significantly washed out when considering the stellar component (Velliscig et al. 2015b), as a possible consequence of the misalignment between the luminous and the dark component of the galaxy (Velliscig et al. 2015a). Pereira & Kuhn (2005) and Faltenbacher et al. (2007) both detected a radial alignment signal, the fist in cluster galaxies and the second on red satellites in the SDSS galaxy group catalogue (Yang et al. 2007). In line with these findings, recently, Georgiou et al. (2019b) detected a radial signal for both red and blue satellites in galaxy groups selected from the Galaxy And Mass Assembly survey (GAMA, Driver et al. 2009). However, all of these studies rely on spectroscopic redshifts, and thus to a more robust assignment of the galaxies to their group: here, we considered all galaxies within a given redshift separation, which significantly degrades the signal. The uncertainty in photometric redshifts also contributes to dilute the signal due to the promotion of uncorrelated pairs within the selection as well as the removal of physically associated galaxies. Moreover, Velliscig et al. (2015a) find that IA depends on the subset of stars used to the signal: using all the stars bound in sub-haloes, the signal is significantly increased compared to the alignment of stars within the half-mass radius. In this latter case, they find compatible values for $\langle \epsilon_{g+} \rangle$ to Chisari et al. (2014); Sifón et al. (2015); Singh et al. (2015). This is in line with the finding in Georgiou et al. (2019b) that the alignment signal is a function of galaxy scale, with the outskirt of the galaxy being more aligned with the position of the central galaxy. In this sense, *lens*fit, which weighs more the inner part of the galaxy, might also contribute to the low signal observed in our samples.

4.8 Conclusions

We used weak gravitational lensing to measure the mass of a sample of LRGs for which the IA signal was measured in Fortuna et al. (2021b). We split the sample into bins based on their luminosity, and used a halo model to interpret our data. We fit the ESD measurements of all the luminos-

ity bins jointly, with a single model. We confirmed that the LRG sample consists mainly of central galaxies, as expected for this kind of galaxy population, and provide the satellite fraction for each L–bin. We ensured that the modelling recovers the true galaxy properties sufficiently well, by inspecting the luminosity distribution per each luminosity bin predicted by the model: we find good agreement between the predicted and the real distributions.

The best fit model predicts an increasing average halo mass with luminosity, which we model with a double power law, for which we obtain the following slopes: $\gamma_1 = 4.412$ and $\gamma_2 = 0.476$ (Eq. 4.29). We note, however, that our data mainly constrain the high mass-end of the double power law ($M > M_1$), which is reflected by the uncertainties in γ_1. Our results are in good agreement with previous studies at high luminosity and extend the luminosity-to-halo mass relation towards the faint-end (low mass).

We used these results to interpret the IA dependence with halo mass, starting from the luminosity dependence measured in the literature. The IA-halo mass relation can be parametrised by a single power law, as predicted by current models (Piras et al. 2018). This suggests that the flattening at low luminosity, hinted at by Fortuna et al. (2021b), may be caused by the double power law in the luminosity-to-halo mass relation. Although the scatter in the measurements remains large, this would imply that the halo mass is the driving source of the alignment.

We also measured the IA signal of the lensing source sample around the LRGs, by selecting only pairs with a maximum separation of $|z_l - z_s| = 0.15$. We considered three cases: the full source sample, and a split in red and blue. We did not detect any alignment signal, in none of the cases considered for $r_p > 0.06\,h^{-1}\mathrm{Mpc}$. We mainly attribute our null-detection to the photometric redshift selection of the galaxy pair: the use of better photo-z might revisit our conclusions.
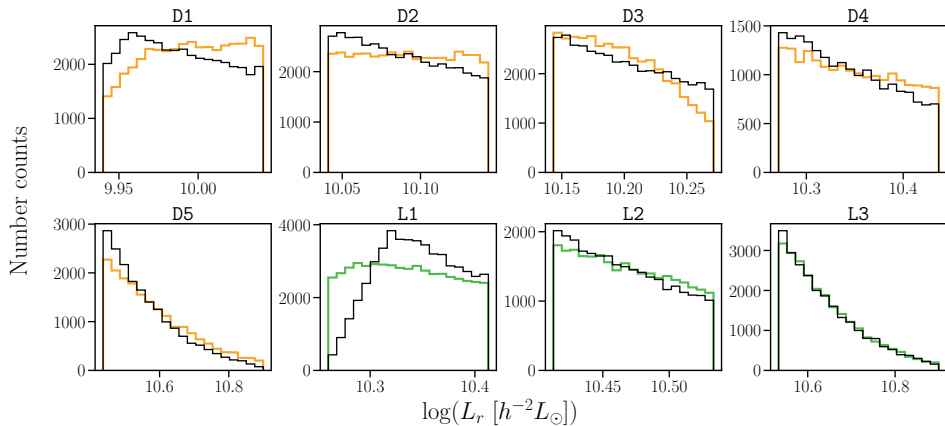
Acknowledgements

Figure 6: The real data number counts per luminosity bin (`dense`: orange, `luminous`:green) and the prediction from the best-fit model (black), normalised for the number of objects in the given bin.

Author contributions: All authors contributed to the development and writing of this paper. The authorship list is given in three groups: the lead authors (MCF, HH, AD) followed by two alphabetical groups. The first alphabetical group includes those who are key contributors to both the scientific analysis and the data products. The second group covers those who have either made a significant contribution to the data products, or to the scientific analysis.

A1 How well does the model predict the luminosity distribution of the galaxies?

The HOD modelling adopted in this work relies on the relation between the halo mass and the luminosity of the galaxies that populate it via the CLF. This allows us to test how well the best-fit model recovers the luminosity distributions of the galaxy samples, a quantity which is not directly used
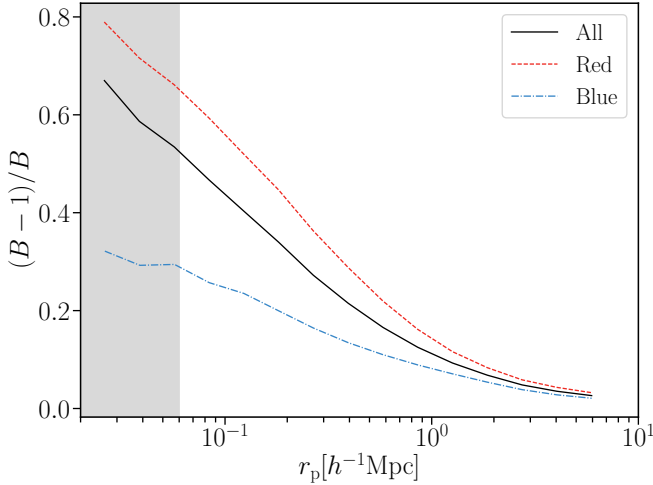
Figure 7: The fraction of source galaxies that are physically associated to the LRGs.

in the fit. This represents an independent test of the ability of the model to recover the properties of the lens galaxies. Fig. 6 shows our results. We use the predicted luminosity function (LF) at the z_{eff} of the corresponding sample to generate the model distributions (black solid line), while the orange/green lines show the underlying true number counts. Overall, the model reproduces sufficiently well the galaxy distribution per luminosity bin, with the exception of L1, where the distribution is significantly more peaked than the real one.

A2   Fraction of physically associated galaxies

In this Appendix we report the fraction of galaxies of the different source samples (all/red/blue) that are physically associated to the LRGs. The fractions are presented in Fig. 7 as a function of projected separation, and they are computed as $(B(r_{\mathrm{p}}) - 1)/B(r_{\mathrm{p}})$.

5 | Forecasting the potential of weak lensing magnification to enhance LSST large-scale structure analyses

C. Mahony, **M.C Fortuna**, *B. Joachimi, A. Korn, H. Hoekstra*

Recent works have shown that weak lensing magnification must be included in upcoming large-scale structure analyses, such as for the Vera C. Rubin Observatory Legacy Survey of Space and Time (LSST), to avoid biasing the cosmological results. In this work we investigate whether including magnification has a positive impact on the precision of the cosmological constraints, as well as being necessary to avoid bias. We forecast this using an LSST mock catalog, a halo model to calculate the galaxy power spectra and a multiplicative factor to account for systematic effects in the magnification measurement. We find that including magnification has little effect on the cosmological parameter constraints for an LSST galaxy clustering analysis. In particular, we find that for the LSST gold sample ($i < 25.3$) including weak lensing magnification only improves the galaxy clustering constraint on Ω_m by a factor of 1.03, and when using a deeper LSST mock sample ($i < 26.5$) by a factor of 1.3. Since magnification predominantly contributes to the clustering measurement and provides similar information to that of cosmic shear, this mild improvement would be further reduced for a combined galaxy clustering and shear analysis. We also confirm that not modelling weak lensing magnification will catastrophically bias the cosmological results from LSST. Magnification must therefore be included in LSST large-scale structure analyses even though it does not significantly enhance the cosmological constraints.

5.1   Introduction

As light from distant galaxies travels towards telescopes it is deflected gravitationally by intervening matter. This means that galaxy images appear distorted. On average, the distortions to individual galaxy images are very small, but when combined, they can be used to statistically map the matter distribution in the universe. This technique is called weak gravitational lensing.

Weak gravitational lensing distorts both the shape and size of galaxy images. Statistical measurements of the shape distortions are referred to as cosmic shear, and statistical measurements of the size distortions are referred to as magnification. Making a magnification measurement of the matter distribution in the Universe, which directly uses size information is challenging because there is a large intrinsic variation in the sizes of galaxies, and it is more prone to serious systematics (Hoekstra et al. 2017). However, Schmidt et al. (2011) achieved a simplified magnification measurement using the joint distribution of galaxy sizes and magnitudes, and there are developing techniques which anchor the size distribution using the fundamental plane of galaxies (Huff & Graves 2013; Freudenburg et al. 2019). Most magnification analyses therefore focus on making a magnification measurement using galaxy number density information (Scranton et al. 2005; Myers et al. 2005; Hildebrandt et al. 2009). In a flux limited survey, distortions to the sizes of galaxy images affect the observed number density of galaxies for two reasons:

1. Since surface brightness is conserved by lensing if the observed size of a galaxy is increased, so is its observed flux. This means that galaxies previously too faint to be observed by a galaxy survey become observable. The number density of galaxies is increased.

2. It is not only the observed size of individual galaxies that is increased by magnification, but the observed size of the whole patch of sky behind the lens. This means that the observable separation between galaxies behind the lens increases and there is a dilution in the number density of galaxies.

These two effects compete and contribute to an overall fluctuation in the number density of galaxies, as a result of weak lensing magnification (for the associated equations see section 5.3.1). Here we are concerned with how magnification can probe the total matter distribution, but it can also be used to constrain the mass of galaxy clusters (e.g. Tudorica et al. 2017).

Weak lensing using cosmic shear has been a highly successful technique. In recent years there have been increasingly precise results using cosmic shear from galaxy surveys such as the Kilo Degree Survey (KiDS) (van Uitert et al. 2018; Joudaki et al. 2018; Hildebrandt et al. 2020), the Dark Energy Survey (DES) (Abbott et al. 2018; Troxel et al. 2018) and the Hyper Suprime-Cam Survey (HSC) (Hikage et al. 2019). Weak lensing magnification has not been included in standard weak lensing analyses to date. All that has been included is the sensitivity of results to including a simplified magnification model (Abbott et al. 2019). The reasoning is that magnification provides similar information to that of cosmic shear and has a poorer signal-to-noise ratio (Bartelmann 2010). However, due to improvements in statistical precision, recent works have shown that cosmological results from upcoming surveys such as the Vera C. Rubin Observatory Legacy Survey of Space and Time (LSST) and *Euclid* will be biased if the effects of weak lensing magnification are not included (Duncan et al. 2014; Cardona et al. 2016; Lorenz et al. 2018; Thiele et al. 2019).

These works have shown that magnification must be included in future surveys to avoid bias, but the aim of this work is to determine whether including magnification as a complementary probe can also improve the final precision of the LSST weak lensing results. Duncan et al. (2014) and Lorenz et al. (2018) found no increase in precision from including magnification in a weak lensing analysis, however LSST is a special case, because it is a very deep ground based galaxy survey. This means that there will be a lot of very faint, small and distant galaxies, which will be poorly resolved. It will therefore not be possible to measure the shape of these galaxies, but it may be possible to count them for a weak lensing magnification analysis. This means that the potentially usable sample size for weak lensing magnification is significantly larger than that for cosmic shear, and as such it is worth investigating magnification's potential as a complementary probe in the case of LSST [1]. Particularly, as Nicola et al. (2020) showed that even with only approximately 100 square degrees, deep samples are already sensitive to magnification.

In summary, we wish to determine the effect of including weak lensing magnification on the precision of the final constraints from LSST weak lensing. We determine this using the Fisher matrix formalism introduced in section 5.2. We then describe the modelling of the observables (weak lensing power spectra and the galaxy luminosity function) in sections 5.3

---

[1]Lorenz et al. (2018) also considered LSST specifically, but did not include systematics or explore departures from the gold sample used for cosmic shear.

and 5.4. We describe the details of our LSST specific survey modelling in section 5.5; and present our results and conclusions in sections 5.6 and 5.7. We verify the stability of our Fisher matrices in appendix A2.

5.2   Fisher Analysis

The Fisher Information matrix summarises the expected curvature of the log-Likelihood function around its maximum,

$$F_{ij} = \left\langle \frac{-\partial^2 \ln L}{\partial \theta_i \partial \theta_j} \right\rangle , \tag{5.1}$$

where L is the likelihood and θ_i is a model parameter. If the likelihood function is sharply peaked for a given parameter, the parameter is tightly constrained by the data (Dodelson 2003). The marginal uncertainty on the model parameter θ_i can be calculated from the Fisher matrix as:

$$\Delta \theta_i \geqslant \sqrt{(F^{-1})_{ii}} . \tag{5.2}$$

The greater than or equal relation is in reference to the Cramér-Rao inequality, which specifies that the Fisher matrix gives the minimum possible uncertainty on an unbiased model parameter (Tegmark et al. 1997).

The Fisher information matrix can be calculated without data and is therefore a useful tool for forecasting best case parameter constraints. In the case of a Gaussian likelihood function and a parameter independent covariance matrix the Fisher matrix is given by:

$$F_{ij} = \sum_{\ell} \frac{\partial C_{\ell}}{\partial \theta_i} \, \mathrm{Cov}^{-1} \, \frac{\partial C_{\ell}}{\partial \theta_j} , \tag{5.3}$$

where C is the theory datavector and Cov is the associated covariance (Tegmark et al. 1997). In this work we consider two component Fisher matrices, which we then add together since they concern separate observables: the Fisher matrix where the theory datavector consists of the weak lensing observables (detailed in section 5.3) and the Fisher matrix where the theory datavector consists of the galaxy luminosity function (detailed in section 5.4). There may be a small correlation between the observables due to cosmic variance, but we do not consider this in this forecast. The associated covariances are detailed in sections 5.5.4 and 5.5.5 respectively.

5.3 Weak Lensing Observables

The two observable quantities used in this weak lensing analysis are the shape, often referred to as ellipticity, and the number density of galaxy images. Since weak lensing is a local effect, the mean ellipticity ϵ and fluctuation in the number density of galaxies n, resulting from weak lensing, is equal to zero when averaged over large scales. Therefore, the key statistical quantity used in weak lensing analyses is the two-point correlation function. There are three two-point correlation functions commonly considered in large-scale structure and weak lensing analyses: cosmic shear (ellipticity-ellipticity), angular galaxy clustering (number density-number density) and galaxy-galaxy lensing (number density-ellipticity). These two-point correlation functions can be considered as individual probes or combined together into a joint analysis, commonly referred to as '3x2pt'. Performing a joint analysis is desirable as it helps to control uncertainties in the measurement, since the two-point functions are subject to different systematic effects and have different sensitivity to the cosmological parameters.

The Fourier transform of the two-point correlation function for cosmic shear is given by:

$$\langle \tilde{\epsilon}^i(\boldsymbol{\ell}) \tilde{\epsilon}^j(\boldsymbol{\ell}') \rangle = (2\pi)^2 \delta^{(2)}(\boldsymbol{\ell} + \boldsymbol{\ell}') C^{ij}_{\epsilon\epsilon}(\ell) \,, \tag{5.4}$$

where $\tilde{\epsilon}$ is the Fourier transform of the ellipticity, $\boldsymbol{\ell}$ is the angular frequency, $\delta^{(2)}$ is the two-dimensional Dirac delta function and $C^{ij}_{\epsilon\epsilon}$ is the projected ellipticity power spectrum between redshift bins i and j (Joachimi & Bridle 2010). It is useful to work in Fourier space because it simplifies linking to the theory predictions. The galaxy samples used for weak lensing are often split into redshift bins; a technique called redshift tomography. This binning enables weak lensing to probe the evolution of the power spectrum with time, through auto- and cross-correlations between the different redshift bins, and hence study the expansion of the universe and dark energy.

The Fourier space two-point correlation function for angular galaxy clustering is given by:

$$\langle \tilde{n}^i(\boldsymbol{\ell}) \tilde{n}^j(\boldsymbol{\ell}') \rangle = (2\pi)^2 \delta^{(2)}(\boldsymbol{\ell} + \boldsymbol{\ell}') C^{ij}_{\mathrm{nn}}(\ell) \,, \tag{5.5}$$

where $\tilde{n}$ is the Fourier transform of the number density contrast and C^{ij}_{nn} is the projected number density power spectrum between redshift bins i and j. The Fourier space two-point correlation function for galaxy-galaxy

lensing and is given by:

$$\langle \tilde{n}^i(\boldsymbol{\ell}) \tilde{\epsilon}^j(\boldsymbol{\ell}') \rangle = (2\pi)^2 \delta^{(2)}(\boldsymbol{\ell} + \boldsymbol{\ell}') C_{n\epsilon}^{ij}(\ell) , \qquad (5.6)$$

where $C_{n\epsilon}^{ij}$ is the projected number density-ellipticity power spectrum between redshift bins i and j. In this work we focus on angular galaxy clustering as an individual probe, and also consider a combined clustering and shear analysis, where the analyses occur on separate patches of sky (see section 5.6.2).

5.3.1   2D power spectra

The key quantities in equations 5.4, 5.5 and 5.6 are the two-dimensional (2D) power spectra $C_{\epsilon\epsilon}$, C_{nn} and $C_{n\epsilon}$. These are the observables we model and include in our Fisher matrix theory datavector, see section 5.2.

In this work we model the 2D observable power spectra $C_{\epsilon\epsilon}$, C_{nn} and $C_{n\epsilon}$ by breaking them down into their constituent parts. The observed ellipticity of a galaxy comes from a combination of the intrinsic ellipticity of the galaxy before it is lensed ϵ_I (the intrinsic alignment, see Joachimi et al. 2015 for a review), the distortion of the shape by weak lensing shear γ_G, and a random uncorrelated component ϵ_{rnd} which accounts for the randomness in the intrinsic ellipticity of galaxies,

$$\epsilon^i(\boldsymbol{\theta}) = \gamma_G^i(\boldsymbol{\theta}) + \epsilon_I^i(\boldsymbol{\theta}) + \epsilon_{rnd}^i(\boldsymbol{\theta}) , \qquad (5.7)$$

where i denotes the redshift bin. The observed number density of galaxies comes from a combination of the number density fluctuation of galaxies as a result of galaxy clustering n_g, the distortion to the number density from weak lensing magnification n_m, and a random component n_{rnd} which accounts for the shot noise contribution,

$$n^i(\boldsymbol{\theta}) = n_g^i(\boldsymbol{\theta}) + n_m^i(\boldsymbol{\theta}) + n_{rnd}^i(\boldsymbol{\theta}) . \qquad (5.8)$$

In terms of the Fourier space 2D power spectra the uncorrelated random components lead to noise power spectra, and separating out the remaining contributions gives:

$$
\begin{aligned}
C_{\epsilon\epsilon}^{ij}(\ell) &= C_{GG}^{ij}(\ell) + C_{IG}^{ij}(\ell) + C_{IG}^{ji}(\ell) + C_{II}^{ij}(\ell) , \\
C_{nn}^{ij}(\ell) &= C_{gg}^{ij}(\ell) + C_{gm}^{ij}(\ell) + C_{gm}^{ji}(\ell) + C_{mm}^{ij}(\ell) , \\
C_{n\epsilon}^{ij}(\ell) &= C_{gG}^{ij}(\ell) + C_{gI}^{ij}(\ell) + C_{mG}^{ij}(\ell) + C_{mI}^{ij}(\ell) ,
\end{aligned}
\qquad (5.9)
$$

where G represents ellipticity from weak lensing shear, I ellipticity from the intrinsic alignment of galaxies, g number density fluctuations as a results of intrinsic galaxy clustering and m number density fluctuations as a result of weak lensing magnification.

We compute all these two-dimensional power spectra C_{ab} from their associated three-dimensional power spectra P_{ab} using the Limber approximation in Fourier space (Kaiser 1992):

$$
\begin{aligned}
C_{\mathrm{GG}}^{ij}(\ell) &= \int_0^{\chi_{\mathrm{hor}}} \mathrm{d}\chi \frac{q^i(\chi)q^j(\chi)}{f_K^2(\chi)} P_{\delta\delta}\left(k = \frac{\ell+1/2}{f_K(\chi)}, \chi\right), \\
C_{\mathrm{IG}}^{ij}(\ell) &= \int_0^{\chi_{\mathrm{hor}}} \mathrm{d}\chi \frac{p^i(\chi)q^j(\chi)}{f_K^2(\chi)} P_{\mathrm{I}\delta}\left(k = \frac{\ell+1/2}{f_K(\chi)}, \chi\right), \\
C_{\mathrm{II}}^{ij}(\ell) &= \int_0^{\chi_{\mathrm{hor}}} \mathrm{d}\chi \frac{p^i(\chi)p^j(\chi)}{f_K^2(\chi)} P_{\mathrm{II}}\left(k = \frac{\ell+1/2}{f_K(\chi)}, \chi\right), \\
C_{\mathrm{gg}}^{ij}(\ell) &= \int_0^{\chi_{\mathrm{hor}}} \mathrm{d}\chi \frac{p^i(\chi)p^j(\chi)}{f_K^2(\chi)} P_{\mathrm{gg}}\left(k = \frac{\ell+1/2}{f_K(\chi)}, \chi\right), \\
C_{\mathrm{gm}}^{ij}(\ell) &= 2(\alpha^j-1)C_{\mathrm{gG}}^{ij}(\ell), \\
C_{\mathrm{mm}}^{ij}(\ell) &= 4(\alpha^i-1)(\alpha^j-1)C_{\mathrm{GG}}^{ij}(\ell), \\
C_{\mathrm{gG}}^{ij}(\ell) &= \int_0^{\chi_{\mathrm{hor}}} \mathrm{d}\chi \frac{p^i(\chi)q^j(\chi)}{f_K^2(\chi)} P_{\mathrm{g}\delta}\left(k = \frac{\ell+1/2}{f_K(\chi)}, \chi\right), \\
C_{\mathrm{gI}}^{ij}(\ell) &= \int_0^{\chi_{\mathrm{hor}}} \mathrm{d}\chi \frac{p^i(\chi)p^j(\chi)}{f_K^2(\chi)} P_{\mathrm{gI}}\left(k = \frac{\ell+1/2}{f_K(\chi)}, \chi\right), \\
C_{\mathrm{mG}}^{ij}(\ell) &= 2(\alpha^i-1)C_{\mathrm{GG}}^{ij}(\ell), \\
C_{\mathrm{mI}}^{ij}(\ell) &= 2(\alpha^i-1)C_{\mathrm{GI}}^{ij}(\ell),
\end{aligned}
\tag{5.10}
$$

where χ is the comoving distance, $f_K(\chi)$ is the comoving angular diameter distance and $p^i(\chi)$ is the probability distribution of galaxies in redshift bin i. $q^i(\chi)$ is a weight function given by:

$$
q^i(\chi) = \frac{3H_0^2\Omega_{\mathrm{m}}}{2c^2}\frac{f_K(\chi)}{a(\chi)}\int_\chi^{\chi_{\mathrm{hor}}} \mathrm{d}\chi' p^i(\chi')\frac{f_K(\chi'-\chi)}{f_K(\chi')}, \tag{5.11}
$$

for further details see Bartelmann & Schneider (2001). The calculation of the three-dimensional power spectra P_{ab} is detailed in the following section.

Equation (5.10) shows that the 2D power spectra associated with magnification C_{gm}, C_{mm}, C_{mG} and C_{mI} can be computed from the 2D power

spectra associated with weak lensing shear C_{gG}, C_{GG} and C_{IG} using α^i the faint end slope of the galaxy luminosity function in redshift bin i. We discuss the galaxy luminosity function in section 5.4 but detail the relationship between the magnification and shear power spectra here.

As mentioned previously, weak lensing magnification contributes to fluctuations in the number density of galaxies n. If the number density of galaxies above the flux limit f is $N_0(> f)$, magnification alters the number density of sources as:

$$N(> f) = \frac{1}{\mu} N_0(> f/\mu) \,, \tag{5.12}$$

where $N(> f)$ is the observed cumulative number density of sources and μ is the local magnification factor (Bartelmann & Schneider 2001). If the cumulative number density of galaxies is assumed to follow a power law $N_0(> f) = k f^{-\alpha}$ near the flux limit of the survey then,

$$N(> f) = \frac{1}{\mu} k \left(\frac{f}{\mu} \right)^{-\alpha} = N_0(> f) \mu^{\alpha-1}, \tag{5.13}$$

where α is equivalent to α^i mentioned in the previous paragraph. This means the fluctuation in the observed number density of galaxies as a result of magnification n_m is given by,

$$
\begin{aligned}
n_m &= \frac{N(> f) - N_0(> f)}{N_0(> f)} = \mu^{\alpha-1} - 1 \approx (1 + 2\kappa)^{\alpha-1} - 1 \\
&\approx 2(\alpha - 1)\kappa,
\end{aligned}
\tag{5.14}
$$

where the weak lensing limit $\mu \approx 1 + 2\kappa$ has been employed.

5.3.2 3D power spectra

The fundamental ingredient for the construction of all of the 3D power spectra P_{ab} in eq. (5.10) is the matter power spectrum $P_{\delta\delta}$. It summarises the clustering of matter in the universe and can be derived numerically using the Boltzmann equations and the primordial power spectrum predicted by inflation. For the other power spectra, we can only rely on an effective description, which we detail in this section.

In this work, we compute $P_{\delta\delta}^{\mathrm{lin}}$ using the Boltzmann code CAMB (Lewis et al. 2000). To include non-linear corrections we use HALOFIT (Takahashi et al. 2012). The remaining power spectra used in this analysis are $P_{\delta I}$, P_{II}, P_{gg} and $P_{g\delta}$. $P_{\delta I}$ and P_{II} are the intrinsic alignment (IA) power

spectra, which encode the tendency of galaxy shapes to point in the direction of a matter overdensity ($P_{\delta I}$) or to have an intrinsic coherent alignment with other galaxy shapes (P_{II}). P_{gg} summarises the clustering of galaxies, and $P_{g\delta}$ the cross-correlations between galaxy position and gravitational shear. $P_{g\delta}$ is linearly related to the galaxy-magnification power spectrum, which is the quantity of interest in this work.

We employ a halo model formalism to calculate P_{gg} and $P_{g\delta}$, while for the IA power spectra we use the empirical Non-linear Linear Alignment (NLA) model (Bridle & King 2007).

The halo model (e.g. Cooray & Sheth 2002) assumes that dark matter clusters into dark matter halos and that all dark matter exists within dark matter halos. We define dark matter haloes as spheres of average density $\Delta\bar{\rho}_m$, with $\Delta = 200$ and $\bar{\rho}_m$ as the present day mean matter density of the Universe. Galaxies are then assumed to form within these dark matter halos, and hence the galaxy distribution traces the distribution of dark matter. The model relies on two ingredients, the underlying distribution of dark matter and how galaxies populate dark matter halos.

The dark matter distribution is summarised by: the halo mass function, which gives the number density of dark matter halos with mass M at redshift z; the halo bias function, which accounts for dark matter halos being biased tracers of the underlying dark matter distribution; and the halo density profile, which summarises how mass is distributed within dark matter halos. In this work we use the Tinker et al. (2010) functional forms for the halo mass function and halo bias function, and assume that the density of dark matter halos follows the Navarro-Frenk-White distribution (Navarro et al. 1996). To parametrise the concentration-mass relation that enters in the NFW profile, we follow Duffy et al. (2008). We compute the halo mass function using the publicly available python package *hmf*[2] (Murray et al. 2013).

We summarise the second ingredient, how galaxies populate dark matter halos, using the conditional luminosity function (CLF) (Yang et al. 2003; Cacciato et al. 2013; van den Bosch et al. 2013). The CLF gives the average number of galaxies with a luminosity L between $L \pm dL/2$ in a halo of mass M. It is divided into two parts:

$$\Phi(L|M) = \Phi_c(L|M) + \Phi_s(L|M) , \qquad (5.15)$$

where $\Phi_c(L|M)$ is the CLF for central galaxies and $\Phi_s(L|M)$ is the CLF for satellite galaxies. Central galaxies reside at the centre of dark matter halos

---

[2]https://github.com/steven-murray/hmf

and satellite galaxies orbit around them. Following the approach detailed in Cacciato et al. (2013) we take the CLF of central galaxies to be modelled by a lognormal distribution,

$$\Phi_c(L|M)\mathrm{d}L = \frac{\log e}{\sqrt{2\pi}\sigma_c}\exp\left[-\frac{(\log L - \log L_c)^2}{2\sigma_c^2}\right]\frac{\mathrm{d}L}{L}\,, \qquad (5.16)$$

where σ_c represents the scatter in the log luminosity of central galaxies and L_c is parametrised as:

$$L_c(M) = L_0\frac{(M/M_1)^{\gamma_1}}{[1+(M/M_1)]^{\gamma_1-\gamma_2}}\,. \qquad (5.17)$$

$L_0 = 2^{\gamma_1-\gamma_2}L_c(M_1)$ is a normalisation and M_1 is a characteristic mass scale. The CLF of satellite galaxies is modelled by a modified Schechter function,

$$\Phi_s(L|M)\mathrm{d}L = \phi_s^*\left(\frac{L}{L_s^*}\right)^{\alpha_s+1}\exp\left[-\left(\frac{L}{L_s^*}\right)^2\right]\frac{\mathrm{d}L}{L}\,. \qquad (5.18)$$

where α_s is the faint end slope of the satellite luminosity function. ϕ_s^* is parametrised as:

$$\log[\phi_s^*(M)] = b_0 + b_1(\log M_{12}) + b_2(\log M_{12})^2, \qquad (5.19)$$

where $M_{12} = M/(10^{12}h^{-1}M_\odot)$ and L_s^* is parametrised as:

$$L_s^*(M) = 0.562L_c(M)\,. \qquad (5.20)$$

Both of the functional forms in eq. (5.16) and (5.18) are derived from the SDSS galaxy group catalog in Yang et al. (2008). In total we have 9 free parameters in our CLF model: $\log M_1$, $\log L_0$, γ_1, γ_2, σ_c, α_s, b_0, b_1 and b_2. We include all of these parameters in our Fisher matrix.

The Halo Occupation Distribution (HOD) can then be obtained as the integral of the CLF over the luminosity interval $[L_1, L_2]$:

$$\langle N_x|M\rangle = \int_{L_1}^{L_2}\Phi_x(L|M)\mathrm{d}L\,, \qquad (5.21)$$

where x can be c, s or g=c+s; $\langle N_c|M\rangle$ and $\langle N_s|M\rangle$ are the average number of central and satellite galaxies in a halo of mass M within the luminosity interval $[L_1, L_2]$. Similarly, we can write $\bar{n}_g$ as the average number density of galaxies across all halo masses in a given luminosity interval:

$$\bar{n}_g(z) = \int\langle N_g|M\rangle n(M,z)\mathrm{d}M\,, \qquad (5.22)$$

where $n(M, z)$ is the halo mass function mentioned above. To keep the notation compact, we have omitted the redshift dependence of the HOD: it arises as a consequence of the survey flux-limit: in this case, the luminosity limits L_1 and L_2 in eq. (5.21) depend on the specific redshift bin under consideration.

Once we have defined the HOD, we can calculate the 3D power spectra P_{gg} and $P_{g\delta}$. First, the power spectra can be split into contributions from the one-halo (1h) and two-halo (2h) terms. The 1h term describes the clustering of galaxies on small scales within the same dark matter halo and the 2h term describes the clustering of galaxies on large scales between different halos. These contributions can then be split into the contributions from central c and satellite s galaxies, as with the CLF. This gives:

$$P_{gg} = 2P_{cs}^{1h} + P_{ss}^{1h} + P_{cc}^{2h} + 2P_{cs}^{2h} + P_{ss}^{2h} ,$$
$$P_{g\delta} = P_{c\delta}^{1h} + P_{s\delta}^{1h} + P_{c\delta}^{2h} + P_{s\delta}^{2h} . \tag{5.23}$$

As shown in van den Bosch et al. (2013) these contributions can be calculated using,

$$P_{xy}^{1h}(k, z) = \int \mathcal{H}_x(k, M, z)\mathcal{H}_y(k, M, z)n(M, z)\mathrm{d}M ,$$
$$P_{xy}^{2h}(k, z) = P_{\delta\delta}^{lin}(k, z) \int \mathrm{d}M_1 \mathcal{H}_x(k, M_1, z)n(M_1, z)b(M_1, z) \tag{5.24}$$
$$\times \int \mathrm{d}M_2 \mathcal{H}_y(k, M_2, z)n(M_2, z)b(M_2, z) ,$$

where x and y can be c, s or δ, and $b(M, z)$ is the halo bias. The function $\mathcal{H}$ encodes the matter or galaxy contribution:

$$\mathcal{H}_\delta(k, M, z) = \frac{M}{\bar{\rho}_m}\tilde{u}_h(k|M, z) ,$$
$$\mathcal{H}_c(k, M, z) = \mathcal{H}_c(M, z) = \frac{\langle N_c|M\rangle}{\bar{n}_g(z)} , \tag{5.25}$$
$$\mathcal{H}_s(k, M, z) = \frac{\langle N_s|M\rangle}{\bar{n}_g(z)}\tilde{u}_s(k|M, z) .$$

where $\tilde{u}_h$ is the Fourier transform of the normalised density distribution of dark matter in a halo of mass M (mentioned above), and $\tilde{u}_s$ is the normalised number density distribution of satellite galaxies in a halo of mass M. In his work, we assume satellites to follow the spatial distribution of the underlying dark matter, i.e. $\tilde{u}_s \equiv \tilde{u}_h$.

To calculate the 3D power spectra P_{II} and $P_{\mathrm{I}\delta}$ we employ the widely used NLA model. This model links the strength of the tidal field when a galaxy forms to the intrinsic ellipticity of the galaxy. This gives,

$$P_{\delta\mathrm{I}}(k,z) = -A_{\mathrm{IA}}C_1\rho_{\mathrm{c}}\frac{\Omega_{\mathrm{m}}}{D(z)}P_{\delta\delta}\,,$$

$$P_{\mathrm{II}}(k,z) = \left(A_{\mathrm{IA}}C_1\rho_{\mathrm{c}}\frac{\Omega_{\mathrm{m}}}{D(z)}\right)^2 P_{\delta\delta}\,, \tag{5.26}$$

where C_1 is a normalisation constant, ρ_{c} the critical density of the Universe today and $D(z)$ the linear growth factor. We set $C_1 = 5\times10^{-14}M_\odot^{-1}h^{-2}\mathrm{Mpc}^3$ based on the IA amplitude measured at low redshifts using SuperCOSMOS (Hartlap, Simon & Schneider Bro), and A_{IA} captures the amplitude of the deviation from this reference case. We take A_{IA} as a free parameter in our Fisher matrix. The NLA model is sufficiently flexible for current studies but can be extended by including a redshift dependent parameter, or using a halo model formalism to calculate P_{II} and $P_{\mathrm{I}\delta}$ on small scales. Recently, Fortuna et al. (2021a) explored these options and found that the IA signal in the one halo regime can be ignored at first order, and that including an extra redshift dependent parameter is possibly sufficient for LSST. Here we consider the simplest NLA model, but implementing these models could be a future extension of this work.

5.4   Galaxy Luminosity Function

The second part of our Fisher matrix theory datavector, see section 5.2, is the galaxy luminosity function. The galaxy luminosity function describes the distribution of luminosities in a galaxy sample, the number density of galaxies with a certain luminosity, and is often directly measured from a galaxy sample. As specified in Cacciato et al. (2013) the galaxy luminosity function at a given redshift z can be calculated from the CLF detailed in section 5.3.2:

$$\Phi(L,z) = \int dM\,\Phi(L|M)n(M,z)\,, \tag{5.27}$$

where $\Phi(L|M)$ is the CLF and $n(M,z)$ is the halo mass function (see section 5.3.2). In this analysis we work with a galaxy sample divided into redshift bins (labelled i and j previously) so we wish to compute the galaxy luminosity function for each redshift bin,

$$\Phi^i(L) = \int dz\,n^i(z)\Phi(L,z)\,, \tag{5.28}$$

where $\Phi^i(L)$ denotes the luminosity function of galaxies in redshift bin i, and $n^i(z)$ the redshift distribution in bin i. We include a prediction for the galaxy luminosity function in each redshift bin in our theory datavector as it helps to constrain the 9 CLF parameters detailed in section 5.3.2, and hence is critical for obtaining information from the small scale clustering. The faint end slope of the galaxy luminosity function is also required to calculate the magnification 2D power spectra, see eq. (5.29).

5.5   Survey Modelling

We perform our Fisher forecast using the cosmological parameter estimation framework CosmoSIS (Zuntz et al. 2015). To calculate the 3D power spectra detailed in section 5.3.2 we use our own halo model code, which has been tested against other halo model codes used in the literature.

In this analysis we define two mock LSST galaxy samples; an ellipticity sample ϵ-sample and a number density sample n-sample. We use a 440 square degree mock catalog from the LSST Dark Energy Science Collaboration (DESC) Data Challenge 2 (DC2) simulations (cosmoDC2 1.1.4; Korytov et al. 2019). These simulations were designed to enable preliminary LSST DESC analyses, and the statistical distributions of galaxies have undergone a wide range of validation tests, for details see Korytov et al. (2019); Kovacs et al. (prep). The catalog includes photometric redshifts for all galaxies with an i-band magnitude less than 26.5, up to redshift 3. The photometric redshifts were calculated using the template fitting code BPZ (Benítez 2000). The n-sample is defined as all galaxies in this mock catalog with an i-band magnitude less than 26.5 and photometric redshift greater than 0.1 and less than 2.0. We set an upper limit as the photometric redshifts begin to degrade significantly beyond 1.5, see Fig. 5.1. The ϵ-sample is defined as a subset of galaxies in n-sample with $i < 25.3$. This corresponds to the LSST *gold sample*, which will be used for weak lensing (LSST Science Collaboration 2009). We do not apply a separate signal-to-noise cut but, galaxies in the n-sample have a signal-to-noise ratio > 5 and galaxies in the ϵ-sample have a signal-to-noise ratio > 20.

5.5.1   Redshift distributions

To compute the 2D power spectra in eq. (5.10) and the luminosity functions in eq. (5.28) we require the redshift distribution of galaxies in each photometric redshift bin. In this work we split both the galaxy samples, n-sample

Figure 5.1: Photometric redshift point estimate mode against true redshift

((a)) number density sample n-sample


((b)) ellipticity sample ϵ-sample
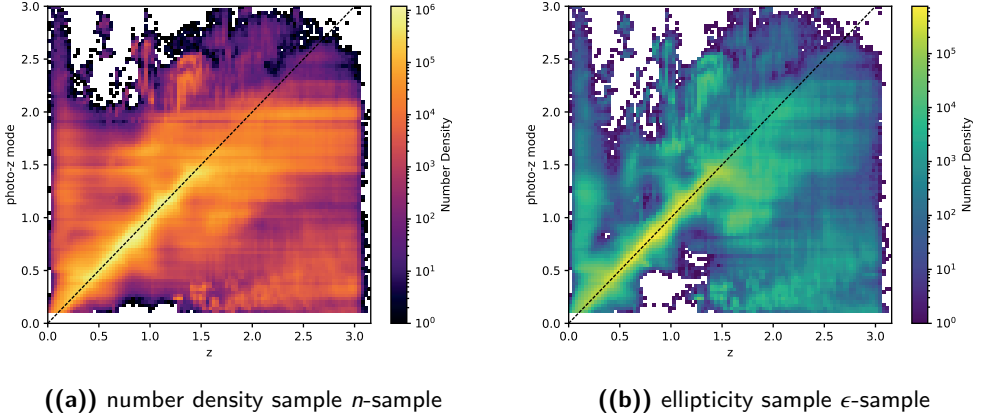
and ϵ-sample, into 10 tomographic redshift bins containing equal numbers of galaxies using their photometric redshifts. Figure 5.2 shows the resulting distribution of galaxies with redshift for each tomographic bin, as well as the tomographic bin boundaries. Figure 5.2 shows that the photometric redshifts are close to random for bin 10 of n-sample, so our maximum photometric redshift cut of 2.0 is well justified.

We compute the number density of galaxies in each tomographic bin to be $12.7 \ \mathrm{arcmin}^{-2}$ for n-sample and $4.9 \ \mathrm{arcmin}^{-2}$ for ϵ-sample. However, weak lensing shape measurements typically weight galaxies by the uncertainty or ability to calibrate the shape measurements, this would reduce the number density for ϵ-sample, especially at high redshifts. The LSST science book estimates that the number density of galaxies in the gold sample will be $55 \ \mathrm{arcmin}^{-2}$, with the number density of galaxies useful for weak lensing approximately $40 \ \mathrm{arcmin}^{-2}$ (LSST Science Collaboration 2009; Chang et al. 2013). This means that our ϵ-sample is slightly optimistic, with a galaxy number density of $49 \ \mathrm{arcmin}^{-2}$.

5.5.2 Faint end luminosity slopes

The key quantity in determining the amplitude of the fluctuation in the number density of galaxies as a result of weak lensing magnification is the faint end slope of the galaxy luminosity function α. If α is equal to 1 there is no overall fluctuation but if α does not equal 1 there is either an increase or

Figure 5.2: Number density of galaxies as a function of true redshift for each photometric bin in the galaxy sample. The dashed lines indicate the photometric bin boundaries.

((a)) n-sample

((b)) ϵ-sample
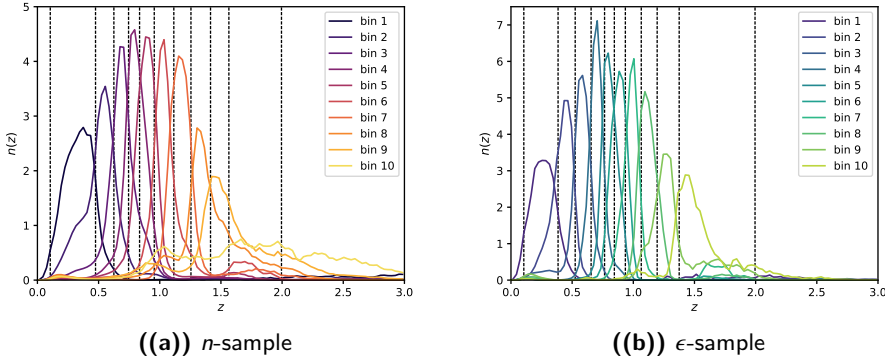
decrease in the number density of galaxies. α can be represented in terms of magnitudes as,

$$\alpha(i_{\mathrm{mag}}) = 2.5 \frac{\mathrm{d}\log_{10} N(> i_{\mathrm{mag}})}{\mathrm{d} i_{\mathrm{mag}}} \, , \tag{5.29}$$

where i_{mag} represents the i band magnitude, and $N(> i_{\mathrm{mag}})$ the unlensed cumulative number density of galaxies with an i band magnitude greater than i_{mag} (e.g. Duncan et al. 2014).

We measure the faint end slopes α from our LSST DC2 mock catalog. We compute a value α^j for each redshift bin j, in each mock sample. To compute α^j we vary the i band magnitude in eq. (5.29) and compute the cumulative number counts $N(> i_{\mathrm{mag}})$. We then fit the logarithm of $N(> i_{\mathrm{mag}})$ with a straight line, and use the slope to compute α^j. Since we are only interested in the slope at the faint end (high magnitudes) we only fit $\log_{10} N(> i_{\mathrm{mag}})$ over the last magnitude before the sample magnitude limit; 25.5-26.5 for n-sample, and 24.3-25.3 for ϵ-sample. Figure 5.3 shows that in general this lower fit limit (marked by a dotted line) captures the value of α^j at the faint end of the sample. Increasing the lower fit limit has little effect on the value of α^j obtained, whereas decreasing the fit limit in general gives a higher value of α^j.

Table 5.1 shows the α^j values obtained for each sample and their associated uncertainties. The uncertainties come from the uncertainty on the slope coefficient of the least-squares straight line fit detailed above, since
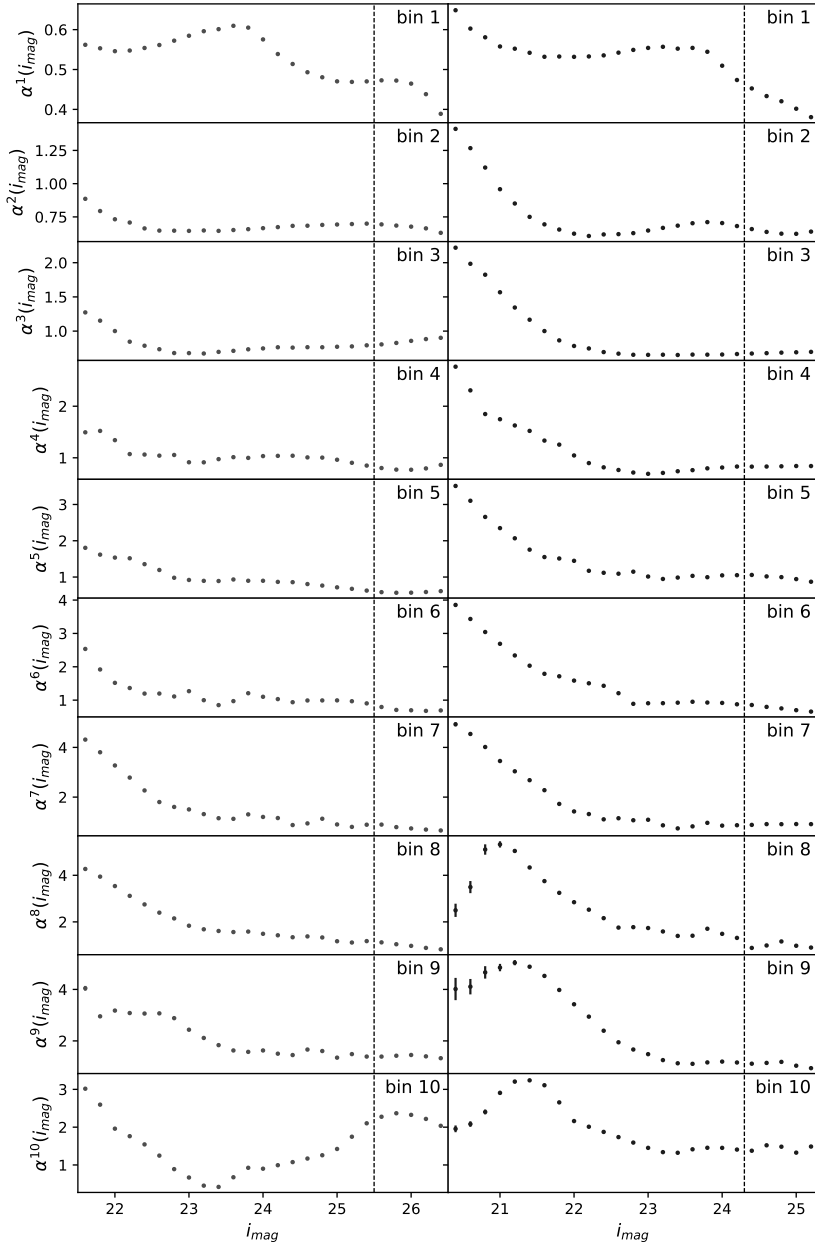
Figure 5.3: The faint end slope of the galaxy luminosity function α^i as a function of the limiting magnitude for each tomographic bin in n-sample (red) and ϵ-sample (blue). The α^i values used in this analysis were found by fitting the slope of the logarithmic cumulative number counts (see eq. (5.29)) between the vertical line and the right hand side of the figure.

Table 5.1: Faint end magnitude slopes α^j for each redshift bin j in n-sample and ϵ-sample, with their associated 1σ uncertainties.

n-sample		**ϵ-sample**	
α^1	0.445 ± 0.005	α^1	0.412 ± 0.005
α^2	0.663 ± 0.006	α^2	0.624 ± 0.004
α^3	0.848 ± 0.006	α^3	0.677 ± 0.004
α^4	0.781 ± 0.005	α^4	0.825 ± 0.006
α^5	0.573 ± 0.004	α^5	0.97 ± 0.01
α^6	0.694 ± 0.006	α^6	0.74 ± 0.01
α^7	0.74 ± 0.01	α^7	0.895 ± 0.006
α^8	0.95 ± 0.02	α^8	0.99 ± 0.01
α^9	1.39 ± 0.01	α^9	1.08 ± 0.01
α^{10}	2.24 ± 0.02	α^{10}	1.42 ± 0.01

they were found to be much larger than the uncertainties on the values of the cumulative number counts $N(> i_{\mathrm{mag}})$ due to the large number of galaxies in each sample. The uncertainties are very small, and would become even smaller when using the full 18000 square degree LSST area instead of a 440 square degree mock catalog. We therefore consider the α^j parameters as fixed in our forecast, but note that they can be difficult to measure accurately from real data due to the presence of systematics and selection effects (see conclusions for further discussion) .

We can compare the α values in Table 5.1 to those found in Duncan et al. (2014) for the Canada–France–Hawaii Lensing Survey (CFHTLenS). In both cases α^j generally increases with redshift. CFHTLenS reaches an α^j value of approximately 1 at its i band magnitude limit of 24.7, for its highest redshift bin between 1.02 and 1.3. This roughly corresponds to α^7 and α^8 in ϵ-sample, where the magnitude limit of 24.7 is included in the α^j fit. Table 5.1 shows that our α^7 and α^8 values for ϵ-sample are consistent with CFHTLenS.

5.5.3 Systematics

We include a number of systematics in our analysis using nuisance parameters. For the fiducial values of these parameters and their associated priors please see Table 5.2. To apply a Gaussian prior to a particular parameter in a Fisher matrix, one simply adds $1/\sigma^2_{\mathrm{prior}}$ to the diagonal element asso-

ciated with the parameter (Coe 2009). In conceptual terms, the priors on the Fisher matrix parameters can be summarized by a diagonal covariance matrix with elements $\sigma^2_{\mathrm{prior}}$. This covariance matrix can then be inverted into a prior Fisher matrix, giving $1/\sigma^2_{\mathrm{prior}}$ diagonal elements, and added to the experimental Fisher matrix.

Shear multiplicative bias

Systematic uncertainties in the measuring and averaging of galaxy shapes can result in a multiplicative scaling of the observed shear. These systematic effects include: noisy galaxy images, the applicability of the model used to describe the light profile of galaxies, the details of the galaxy morphology and selection biases (e.g. Heymans et al. 2006). We parametrise this multiplicative scaling using one parameter m^i per redshift bin (10 parameters in total), which scale the cosmic shear and galaxy-galaxy lensing power spectra as:

$$
\begin{aligned}
C^{ij}_{\epsilon\epsilon}(l) &\rightarrow (1+m^i)(1+m^j)C^{ij}_{\epsilon\epsilon}(l)\,, \\
C^{ij}_{\mathrm{n}\epsilon}(l) &\rightarrow (1+m^j)C^{ij}_{\mathrm{n}\epsilon}(l)\,.
\end{aligned}
\tag{5.30}
$$

We impose Gaussian priors on these multiplicative parameters, which are guided by the LSST DESC science requirements (Alonso et al. 2018). These science requirements forecast the uncertainties LSST will need to achieve in order to meet their main objectives of significantly improving the constraints on the dark energy parameters w_0 and w_a, compared to previous dark energy experiments, and obtaining dark energy constraints where the total calibratable systematic uncertainty is less than the marginalised statistical uncertainty. For the case of shear multiplicative bias the requirement is that the 'systematic uncertainty in the redshift-dependent shear calibration' should not exceed 0.003 by year 10. We therefore apply a Gaussian prior centred on zero with a standard deviation of 0.003 to each of our shear multiplicative bias parameters.

Clustering Multiplicative Bias

We parametrise uncertainties in the number count measurement using a similar approach to that for shear. Systematics which affect the number density of galaxies include: galactic dust obscuring background galaxies, variable survey depth impacting the number of sources promoted across the flux limit by magnification, and stars contaminating the galaxy sample (Hildebrandt 2015; Thiele et al. 2019). Usually these effects would be

partially absorbed by the galaxy bias (CLF) parameters, however since we include the galaxy luminosity function in our analysis the CLF parameters will be tightly constrained. We therefore felt it was important to include this multiplicative bias parameterisation for clustering as well as shear.

Analogous to shear multiplicative bias, the observed clustering power spectra are scaled by a multiplicative factor as,

$$
\begin{aligned}
C_{nn}^{ij}(l) &\rightarrow (1 + m_{eff}^i)(1 + m_{eff}^j)C_{nn}^{ij}(l) \, , \\
C_{n\epsilon}^{ij}(l) &\rightarrow (1 + m_{eff}^i)C_{n\epsilon}^{ij}(l) \, .
\end{aligned}
\tag{5.31}
$$

However, since most systematics decrease with signal to noise ratio, we assume m_{eff}^i has a power law dependence on the signal to noise of galaxies in redshift bin i. This enables us to reduce the number of clustering multiplicative bias parameters from ten parameters (one m_{eff}^i per redshift bin) to two parameters a_m and b_m. m_{eff}^i is given in terms of a_m and b_m by,

$$
\begin{aligned}
m_{eff}^i &= m_{step} - m_{fid} \\
&= \frac{1}{N_i} \left[a_m \sum_{n=1}^{N_i} \left(\frac{S}{N}\right)_n^{b_m} - a_{fid} \sum_{n=1}^{N_i} \left(\frac{S}{N}\right)_n^{b_{fid}} \right] \, ,
\end{aligned}
\tag{5.32}
$$

where N_i is the number of galaxies in tomographic bin i, the sum is over the signal-to-noise ratio S/N of all galaxies in tomographic bin i, a_{fid} is the fiducial value of a_m and b_{fid} is the fiducial value of b_m. We introduce the m_{fid} term because if $m_{eff} = m_{step}$, b_m becomes unconstrained when a_m is equal to zero, which breaks the Gaussian Likelihood assumption in the Fisher matrix prediction.

We compute the signal to noise ratio for each galaxy in our samples from the error on the i band apparent magnitude (Hainaut 2005). Using the signal to noise of every galaxy in this bias calculation is computationally expensive, since the total number of galaxies in *n-sample* and *ε-sample* is of order 10^7 and 10^8. We therefore use a randomly selected 1% subsample of galaxies in this calculation. This subsample is representative of the full galaxy sample, but prevents our bias calculation from being prohibitively slow.

Photometric redshift uncertainties

We model uncertainties in the redshift distributions shown in figure 5.2 by introducing shift factors Δ^i (Bonnett et al. 2016). Δ^i simply shifts the

redshift distribution in bin i so,

$$n^i(z) \rightarrow n^i(z - \Delta^i). \qquad (5.33)$$

Since we have two redshift distributions, one for ϵ-sample and one for n-sample, each divided into 10 bins this results in 20 shift parameters Δ^i. These parameters are likely to be correlated, so we are making a conservative choice by allowing 20 separate shift parameters, which may somewhat weaken our final constraints. We impose Gaussian priors on each of these shift parameters, once again guided by the LSST DESC science requirements (Alonso et al. 2018). The prior is centred on zero, with a standard deviation of 0.003 for the n-sample parameters and of 0.001 for the ϵ-sample parameters.

A future extension of this work could be to include other modes of redshift uncertainty, such as a change in the width or to the high redshifts tails, as in Nicola et al. (2020). These may be particularly interesting for magnification, as they change the level of overlap between different redshift bins.

5.5.4   Covariances

In this forecast we consider two component Fisher matrices. The Fisher matrix for the weak lensing observables and the Fisher matrix for the galaxy luminosity function (see section 5.2). We therefore require two covariances: the weak lensing observables covariance and the galaxy luminosity function covariance.

Weak lensing observables covariance

We compute a Gaussian covariance for the observable weak lensing power spectra ($C_{\epsilon\epsilon}, C_{\mathrm{nn}}, C_{\mathrm{n}\epsilon}$) using CosmoSIS. The covariance between two power spectra is given by,

$$\mathrm{Cov}\left[C^{ij}(\ell), \, C^{kl}(\ell')\right] = \delta_{\ell\ell'} \frac{2\pi}{A\ell\Delta\ell} \left[\bar{C}^{ik}(\ell)\bar{C}^{jl}(\ell) + \bar{C}^{il}(\ell)\bar{C}^{jk}(\ell)\right], \quad (5.34)$$

where $ijkl$ denote redshift bins, $\delta_{\ell\ell'}$ is the Kronecker delta, A is the survey area and $\Delta\ell$ the size of the angular frequency ℓ bin (Joachimi et al. 2008; Joachimi & Bridle 2010). We do not include the non-gaussian contributions to the covariance since their effect is small, and unlikely to impact our final results (Barreira et al. 2018). To account for the random terms in equations 5.7 and 5.8 we define,

$$\bar{C}^{ij}(\ell) = C^{ij}(\ell) + N^{ij}, \qquad (5.35)$$

where N^{ij} is the shot or shape noise contribution. In the case of $C_{\epsilon\epsilon}$,

$$N^{ij} = \delta_{ij} \frac{\sigma_\epsilon^2}{2\bar{n}^i} \, , \qquad (5.36)$$

in the case of C_{nn},

$$N^{ij} = \delta_{ij} \frac{1}{\bar{n}^i} \, , \qquad (5.37)$$

and in the case of $C_{n\epsilon}$, $N^{ij} = 0$. Where σ_ϵ is the total intrinsic ellipticity dispersion, and $\bar{n}^i$ is the average number density of galaxies in redshift bin i (Bartelmann & Schneider 2001). We compute the power spectra covariance for 20 log-spaced angular frequency l bins from $l_{\min} = 30$, to avoid inaccuracies in the Limber approximation, to $l_{\max} = 3000$, to avoid the very non-linear regime.

Galaxy luminosity function covariance

We compute the galaxy luminosity function covariance by measuring the galaxy luminosity functions of our mock LSST galaxy samples and then computing a bootstrap covariance. Since Fisher forecasts do not require a datavector, only a covariance, we only use the measured luminosity functions to compute the covariance and model the galaxy luminosity function in the forecast using the CLF formalism (see section 5.4).

To measure the luminosity functions for the n-sample and ϵ-sample we begin by computing the luminosity of each galaxy from its rest-frame absolute magnitude in the i band. We then divide our sample into the 10 tomographic bins described above and scale the luminosity function for each bin j by the volume of bin j, to convert the histogram to a number density. When calculating the bin volume we assume that the galaxies do not scatter beyond the tomographic bin boundaries. This is an approximation, which figure 5.2 shows, is becoming problematic for bin 10.

Ideally, we would use the full range of galaxy luminosities to compute our bootstrap covariance. However in order to use the low luminosity region we would need to correct our galaxy samples to be volume complete, for example through the $1/V_{\max}$ method (Schmidt 1968; Felten 1976; Cole 2011). High luminosity objects can be observed across the full volume of the survey, but low luminosity objects can only be observed at smaller distances. This introduces a bias referred to as Malmquist bias, and we therefore only want to include galaxies that can be observed across the whole volume of the survey. For the purposes of this work we deemed it sufficient to simply cut out the low luminosity galaxies to make the sample volume

limited, since this is still a significant step forward compared to previous analyses. For details of how we determine the volume complete cut see appendix A1.

We then compute a bootstrap covariance for our measured galaxy luminosity functions. First, we sample our dataset with replacement 100 times and compute the associated datavectors. We then assume that each luminosity bin in each tomographic bin is independent (each of our datapoints is independent) and calculate the variance of these 100 samples. This gives us a diagonal covariance. The variance of the 100 samples is in general small, due to the very large numbers of galaxies in each sample.

5.5.5 Fiducial values

The Fisher matrix gives the curvature of the log-Likelihood function around its peak. It does not find the location of the peak, this is defined with a set of fiducial values (shown in Table 5.2). The set of parameters required to calculate the 3D power spectra in section 5.3.2 are the cosmological parameters and the CLF parameters. In this work we consider the constraints on a flat ΛCDM cosmology, and vary the cosmological parameters Ω_{m}, h_0, Ω_{b}, n_{s}, $A_{\mathrm{s}}/10^{-9}$, w and w_{a}. We take their fiducial values from the input values used to generate the simulation for the LSST DESC mock catalog, or from the values obtained by the *Planck* satellite (Aghanim et al. 2018).

We also vary the full set of CLF parameters $\log M_1$, $\log L_0$, γ_1, γ_2, σ_{c}, α_{s}, b_0, b_1 and b_2, detailed in section 5.3.2. Here we use the fiducial values found for SDSS by Cacciato et al. (2013), which have been shown to also be applicable to higher redshift surveys (Cacciato et al. 2014; van Uitert et al. 2016b).

5.6 Results

5.6.1 Clustering

Figure 5.4 shows the forecast constraints on the cosmological parameters from C_{nn} with and without including magnification terms for n-sample. In the case of including magnification the observable is $C_{\mathrm{nn}} = C_{\mathrm{gg}} + C_{\mathrm{gm}} + C_{\mathrm{mm}}$ instead of $C_{\mathrm{nn}} = C_{\mathrm{gg}}$. Including magnification has only a small impact on the cosmological parameter constraints. The greatest change is the 1σ constraint on Ω_m, which is improved by a factor of 1.3 from 0.003 to 0.0023.

Table 5.2: Fiducial values and priors for the model parameters used to compute the fisher matrices in this work.

Parameter	Fiducial Value	Prior
Survey		
Area	$18000 \, \mathrm{deg}^2$	fixed
σ_e	0.35	fixed
Cosmology		
Ω_m	0.265	flat
h_0	0.71	flat
Ω_b	0.0448	flat
n_s	0.963	flat
$A_\mathrm{s}/10^{-9}$	2.1	flat
w	-1.0	flat
w_a	0.0	flat
Ω_k	0.0	fixed
CLF		
$\log(M_1)$	11.24	flat
$\log(L_0)$	9.95	flat
γ_1	3.18	flat
γ_2	0.245	flat
σ_c	0.157	flat
α_s	-1.18	flat
b_0	-1.17	flat
b_1	1.53	flat
b_2	-0.217	flat
Intrinsic Alignments		
A_IA	1.0	flat
n-sample Photo-z		
Δ_n^i	0.0	Gauss(0.0, 0.003)
ϵ-sample Photo-z		
Δ_ϵ^i	0.0	Gauss(0.0, 0.001)
Shear Bias		
m^i	0.0	Gauss(0.0, 0.003)
Clustering Bias		
a_m	0.001	flat
b_m	0.0	flat
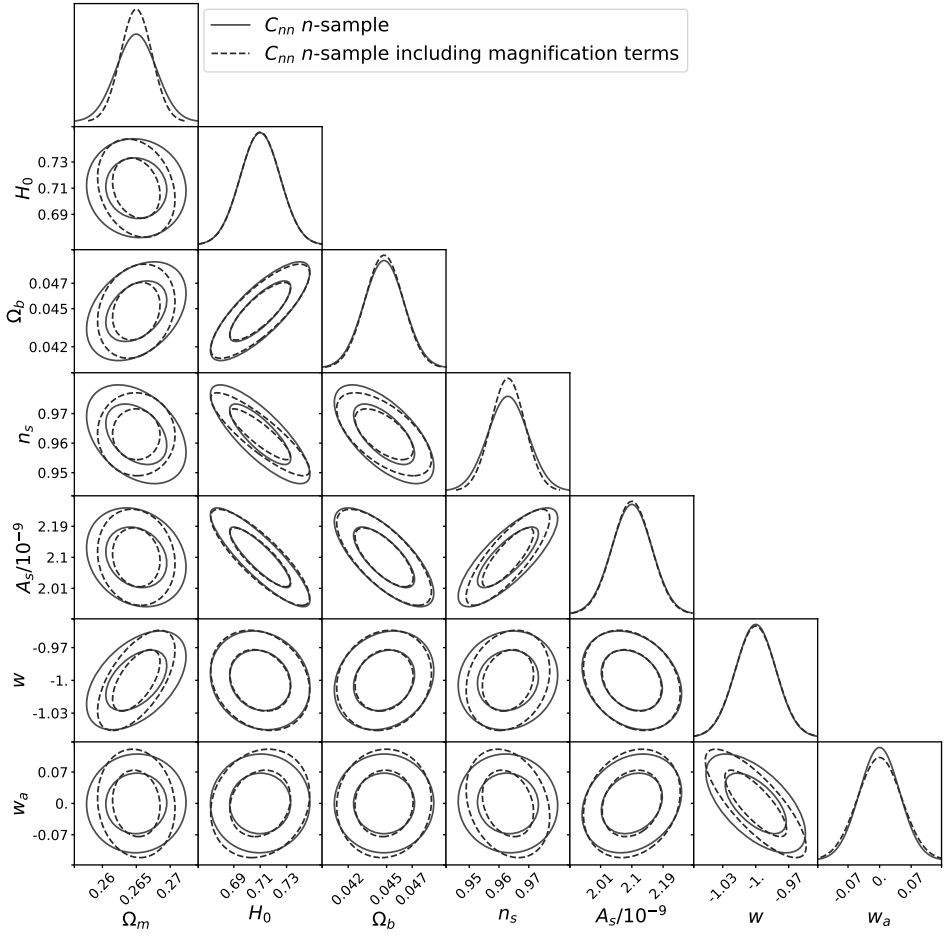
Figure 5.4: Constraints on the cosmological parameters used in this analysis from C_{nn} and C_{nn} including magnification terms for n-sample. Including magnification has only a small impact on the constraints.

The forecast constraints on the cosmological parameters from C_{nn} and C_{nn} including magnification terms for ϵ-sample show that the impact of magnification is further reduced compared to the deeper n-sample. The 1σ constraint on Ω_m is only improved by a factor of 1.03 from 0.0032 to 0.0031, instead of a factor of 1.3 with the deeper n-sample. This shows that including magnification has a greater, albeit modest, impact for deeper samples.

Figure 5.5 shows the forecast constraints on the CLF parameters from C_{nn} with and without including magnification terms for the n-sample. Including magnification has little effect on the constraints on the CLF parameters. This is expected because the CLF constraints are predominantly determined by the galaxy luminosity function. We focus on the cosmological and CLF parameters, instead of presenting the full 28 parameter space, for clarity. The steps taken to ensure the stability of our Fisher matrix are detailed in appendix A2.

A useful measure of the constraining power of an analysis is the Figure of Merit (FoM) defined as,

$$\mathrm{FoM} = \det([\mathrm{F}^{-1}]_q)^{\frac{1}{N_q}} \; , \tag{5.38}$$

where $[\mathrm{F}^{-1}]_q$ is the inverse Fisher matrix for the set of parameters q and N_q is the number of parameters q in the set. In this work we define q as the full set of cosmological parameters, so the FoM represents the power of the constraints on the cosmological parameters. It is also common to define a Dark Energy FoM where $q = \{w, w_a\}$ (Albrecht et al. 2006).

When magnification is included in the clustering analysis for the deeper n-sample the FoM is increased by a factor of 1.45. However, when magnification is included in the clustering analysis for ϵ-sample (the LSST gold sample) the FoM is increased by a factor of 1.08. This mirrors the conclusions from looking at the parameter constraints on Ω_m – magnification is more beneficial for deeper samples with greater numbers of low signal-to-noise ratio galaxies. Interestingly, there is no increase in the FoM for clustering without magnification when using the deeper n-sample instead of ϵ-sample. This implies that it is more beneficial to have a smaller sample of high signal-to-noise objects than a larger sample including lower signal-to-noise objects. This is likely due to the additional fainter objects having poorer photometric redshifts and therefore largely contributing to the tails of the redshift distribution. Looking back at figure 5.2 we can see that the redshift distribution for the shallower ϵ-sample is much cleaner.
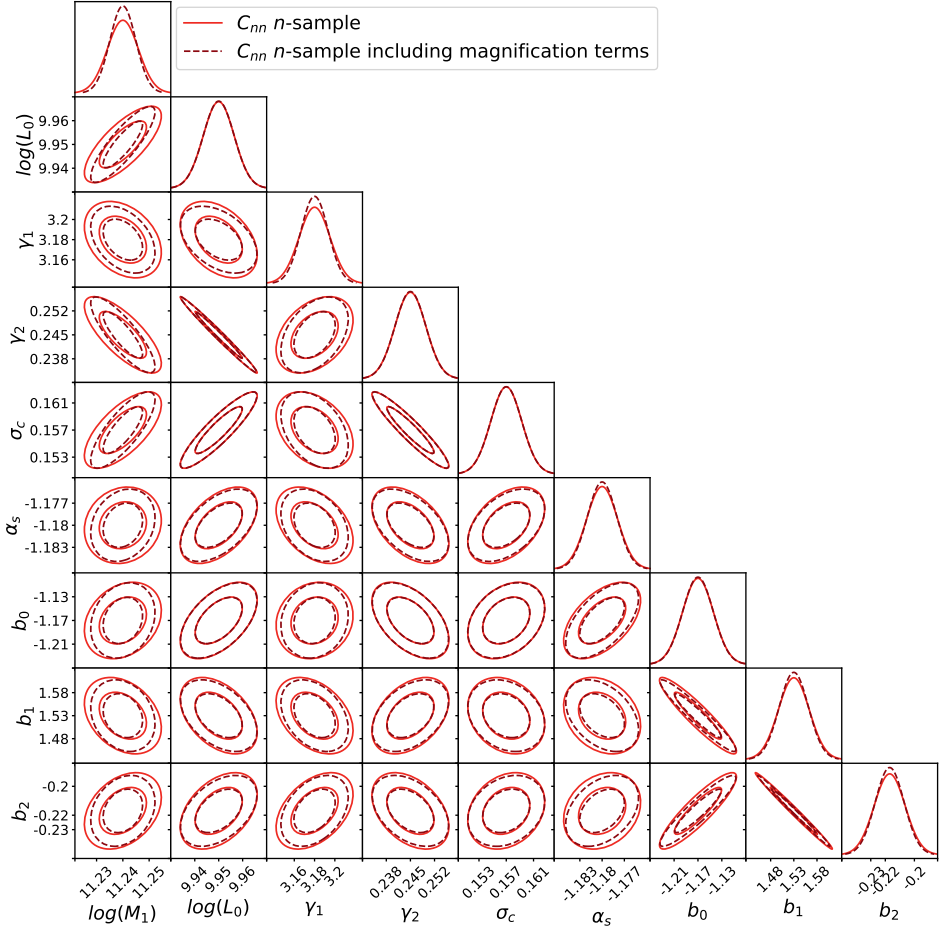
Figure 5.5: Constraints on the Conditional Luminosity Function (CLF) parameters used in this analysis from C_{nn} and C_{nn} including magnification terms for *n*-sample. Including magnification has little effect on the constraints, since they are driven by the galaxy luminosity function not the weak lensing or clustering observables.

5.6.2 Shear calibration

The previous section showed that including weak lensing magnification only has a small effect on the cosmological parameter constraints from an LSST-like angular galaxy clustering analysis. In a combined clustering and cosmic shear analysis the impact of magnification on the cosmological parameter constraints can only be reduced. This is because magnification predominantly contributes to the clustering signal and provides very similar information to shear. We therefore focus on the effect of magnification on the shear multiplicative bias parameters.

We examine the impact of including magnification on the shear multiplicative bias parameters for a combined LSST clustering C_{nn} and shear $C_{\epsilon\epsilon}$ analysis, where the analyses occur on separate patches of sky. This is because the full '3x2pt' (C_{nn}, $C_{n\epsilon}$, $C_{\epsilon\epsilon}$) analysis requires careful treatment of the cross terms, which is beyond the scope of this work. We are therefore investigating whether the improved cosmological constraints from magnification translate into an improved calibration.

Figure 5.6 shows the forecast constraints on the shear multiplicative bias parameters from our C_{nn} and $C_{\epsilon\epsilon}$ analysis, with and without magnification terms, where $C_{\epsilon\epsilon}$ is calculated for ϵ-sample and C_{nn} for the deeper n-sample. Including magnification only slightly improves the constraints on the shear calibration parameters, with a greater effect at higher redshift. The 1σ constraint on m^1 is improved by a factor of 1.06, m^6 by 1.3 and m^{10} by 1.34 when including magnification. When C_{nn} is calculated using the shallower ϵ-sample the impact is similar, but less pronounced. These results show that including magnification is not particularly helpful for calibrating the shear measurement. However, the impact of magnification may be slightly improved when performing a full '3x2pt' analysis, where the clustering and shear are measured on the same patch of sky.

5.6.3 Bias

Recent works have shown that cosmological results from upcoming surveys such as LSST will be biased if the effects of weak lensing magnification are not included, due to improvements in statistical precision (Duncan et al. 2014; Cardona et al. 2016; Lorenz et al. 2018; Thiele et al. 2019). To examine this for our forecast, figure 5.7 shows the absolute difference between the clustering power spectra C_{nn} with and without magnification in terms of the 1σ uncertainty on the clustering power spectra without magnification. In this case the clustering power spectra have been calculated using

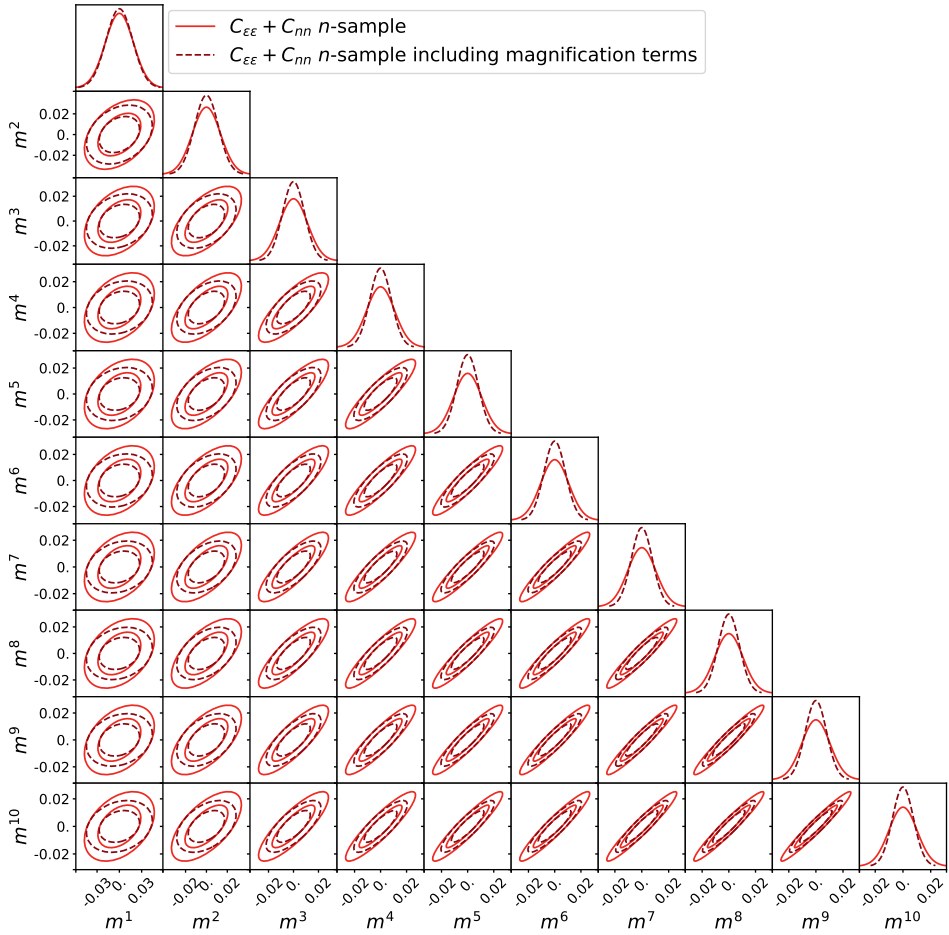**Figure 5.6:** Constraints on the shear multiplicative bias parameters from a joint analysis of $C_{\epsilon\epsilon}$ and C_{nn} (not including $C_{\mathrm{n}\epsilon}$) with and without magnification terms, where we have not applied the Gaussian prior detailed in Table 5.2. $C_{\epsilon\epsilon}$ is calculated for ϵ-sample and C_{nn} is calculated for n-sample. Including magnification only slightly improves the constraints, with a greater impact at higher redshift.

n-sample. The grey shaded region indicates where C_{nn} including magnification is more than 2σ away from C_{nn} without magnification. Particularly at high ℓ (small scales) C_{nn} including magnification significantly diverges from C_{nn} without magnification.

For comparison, we have also shown the impact of changing Ω_m and A_s by 5σ in Fig. 5.7. In all of the redshift bin combinations shown, the difference from including magnification is larger than or comparable to the difference from changing Ω_m and A_s by 5σ. This clearly indicates that not including magnification terms will catastrophically bias cosmological constraints from LSST. Additionally, the difference from not including magnification seems to mimic the behaviour of biasing A_s by 5σ. This implies that not including magnification could particularly bias the constraints for A_s, one of the parameters weak lensing is most sensitive to.

Figure 5.8 shows the absolute difference between the clustering power spectra C_{nn} with and without magnification in terms of the 1σ uncertainty on the clustering power spectra without magnification, where the clustering power spectra have been calculated using the shallower ϵ-sample. In this case the difference from including magnification is not as large as for n-sample, however in most redshift bin combinations is still comparable or larger than the differences from changing Ω_m and A_s by 5σ.

5.7   Conclusions

Previous works have shown that upcoming results from surveys such as LSST and *Euclid* will be biased if the effects of weak lensing magnification are not included (Duncan et al. 2014; Cardona et al. 2016; Lorenz et al. 2018; Thiele et al. 2019). In this work we forecast whether including weak lensing magnification as a complementary probe can additionally improve the precision of the LSST weak lensing constraints. We determined this using the Fisher matrix formalism, where our theory datavector included the weak lensing observables and the galaxy luminosity function. To calculate the weak lensing observables and the galaxy luminosity function, we employed a halo model, detailed in Cacciato et al. (2013). We defined two mock LSST galaxy samples from the LSST DC2 simulations (Korytov et al. 2019) for use in our forecast; a sample which corresponds to the LSST gold sample where the i band magnitude is less than 25.3 (intended to be used for the weak lensing shear measurement), and a deeper sample where the i band magnitude is less than 26.5.

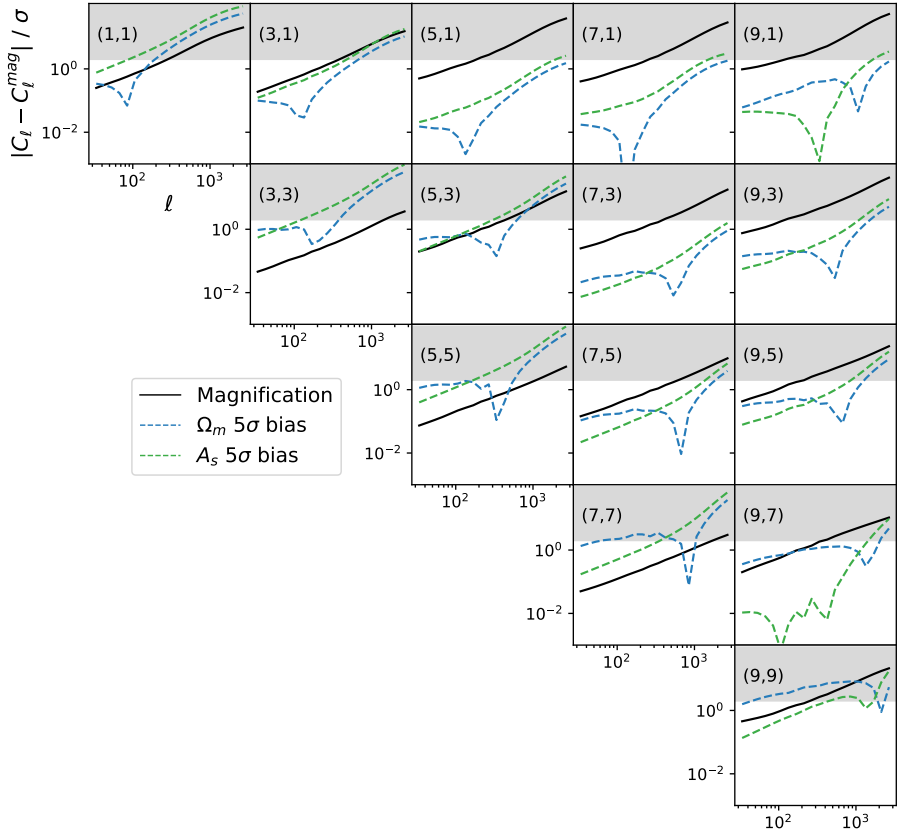We found that weak lensing magnification provides little additional in-
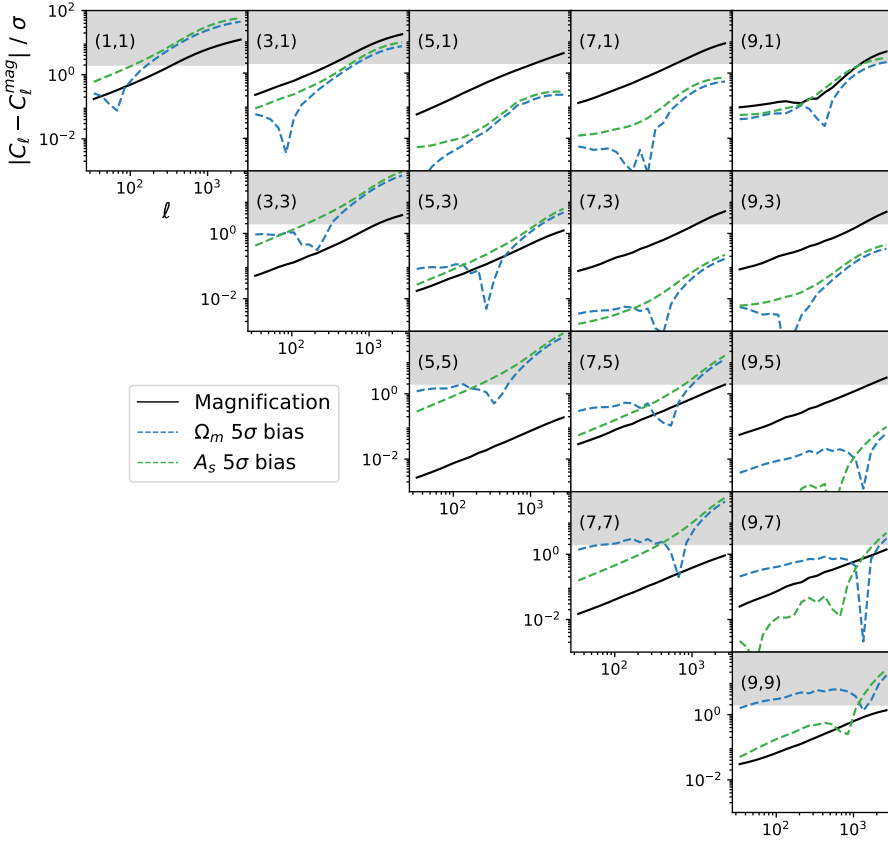
Figure 5.7: Absolute difference between C_{nn} with and without magnification, in terms of the uncertainty on C_{nn} with magnification, for n-sample. The grey shaded region indicates where C_{nn} including magnification is more than 2σ away from C_{nn} without magnification. The dashed lines show the difference in C_{nn} when Ω_{m} and A_{s} are altered by 5σ.

Figure 5.8: Absolute difference between C_{nn} with and without magnification, in terms of the uncertainty on C_{nn} with magnification, for ϵ-sample. The grey shaded region indicates where C_{nn} including magnification is more than 2σ away from C_{nn} without magnification. The dashed lines show the difference in C_{nn} when Ω_m and A_s are altered by 5σ.

formation as a complementary probe for LSST. For a galaxy clustering analysis using the LSST gold sample we found that including magnification increased the Figure of Merit (FoM) for the set of cosmological parameters $\Omega_{\rm m}$, h_0, $\Omega_{\rm b}$, $n_{\rm s}$, $A_{\rm s}/10^{-9}$, w and $w_{\rm a}$ by a factor of 1.08. When using the deeper galaxy sample we found that magnification increased the FoM by a factor of 1.45. In terms of the precision of the Ω_m constraints, we found for a galaxy clustering analysis using the LSST gold sample that including magnification increased the 1σ precision by a factor of 1.03, using the deeper sample we found a factor increase of 1.3. These results show that including magnification is more beneficial for deeper samples, but still has a fairly small impact.

The effect of including magnification would be even smaller in a combined galaxy clustering and cosmic shear analysis because magnification provides similar information to that of cosmic shear. However, we investigated the impact of including magnification on the calibration of the shear measurement. We found that including magnification only slightly improves the constraints on the shear calibration parameters.

While this forecast is more realistic than many to date, as it includes LSST mock catalog data and a flexible galaxy bias model, it still relies on a number of simplified assumptions about magnification. Firstly, the magnification modelling assumes that the galaxy sample is purely flux limited. Often galaxies are also selected based on their signal-to-noise ratio, colours and morphology which complicates the magnification modelling (Hildebrandt 2015). Secondly, there are a large number of systematics associated with the magnification measurement such as dust attenuation, variable survey depth, star-galaxy separation and the blending of galaxy images (Hildebrandt et al. 2013; Morrison & Hildebrandt 2015; Thiele et al. 2019). We included a multiplicative factor in our modelling of the clustering power spectra in order to incorporate these effects, but more detailed modelling is likely required. For example, we could have marginalised over the faint end luminosity slopes α^i, which are required to compute the magnification power spectra. We chose to fix them, since at least for the gold sample it should be comparatively easy to explore the luminosity function beyond the magnitude limit, so measurement errors on α^i can be expected to be very small. This forecast could therefore be considered a best case scenario for magnification, and even in this scenario we found that including magnification has little impact. However, we also confirmed that not including magnification will strongly bias cosmological results from LSST, so must be modelled.

Acknowledgements

A1 Volume Complete Cut for Galaxy Luminosity Function Covariance

A deeper galaxy sample will be volume complete to lower luminosities, so when the luminosity function of a shallower sample diverges from the luminosity function of a deeper sample, we know the shallower sample has ceased to be volume complete. We can therefore determine the volume complete luminosity cut for the ϵ-sample by finding where it diverges from the n-sample. Our divergence condition is

$$\frac{|\Phi_\epsilon^i(L) - \Phi_{n(\epsilon)}^i(L)|}{\Phi_\epsilon^i(L)} > 0.2 \,, \tag{39}$$

where Φ_ϵ^i is the luminosity function for the ϵ-sample and $\Phi_{n(\epsilon)}^i$ is the luminosity function for the n-sample, where the n-sample has been binned using the ϵ-sample tomographic bins. We cut Φ_ϵ^i when there is a difference of 20% from the deeper sample $\Phi_{n(\epsilon)}^i$. This value was found to cut Φ_ϵ^i before it significantly diverged from the deeper sample whilst allowing for small deviations, see the right panel of Fig. 9.

Since we did not have a sample deeper than the n-sample available to us, we made a more stringent volume complete cut on the n-sample luminosity function based on where the luminosity function of our shallower sample ϵ-sample diverged. If the shallower sample is volume complete we can be sure that the deeper sample is also volume complete. In this case our divergence condition is

$$\frac{|\Phi_n^i(L) - \Phi_{\epsilon(n)}^i(L)|}{\Phi_n^i} > 0.2 \,, \tag{40}$$
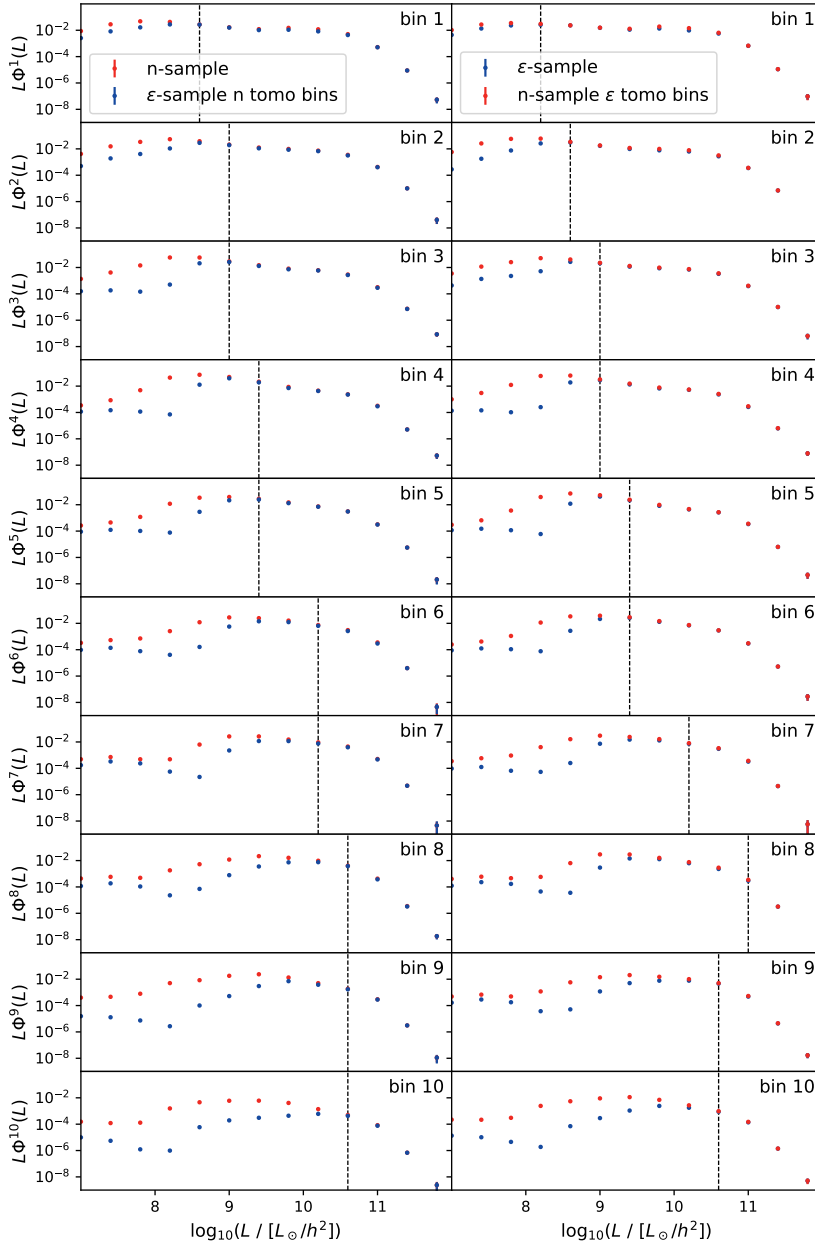
Figure 9: Measured luminosity functions $\Phi^i(L)$ for each photometric redshift bin in n-sample (left) and ϵ-sample (right), with associated bootstap errors. The dotted lines show the location of the luminosity cuts to n-sample (left) and ϵ-sample (right) to make sure they are volume complete, and do not introduce a bias. ϵ-sample n tomo bins refers to the ϵ-sample being binned into the n-sample redshift bins, and n-sample ϵ tomo bins refers to the n-sample being binned into ϵ-sample redshift bins. $L\Phi^i(L)$ has units of h^3/Mpc^3.

where Φ_n^i is the luminosity function for n-sample and $\Phi_{\epsilon(n)}^i$ is the luminosity function for ϵ-sample, where ϵ-sample has been binned using the n-sample tomographic bins. While this luminosity cut enforces that n-sample is volume complete, using a shallower sample means that the cut is much more conservative than necessary.

A2   Fisher Matrix Stability

High-dimensional Fisher matrices can be unstable. Here we detail the steps taken to ensure the stability of our Fisher matrices and hence the robustness of our results.

The derivatives in eq. (5.3) are calculated numerically using a method of numerical differentiation called a 5-pt stencil. This method requires the pipeline to be evaluated at 4 points around the model parameter's fiducial value (5 points including the fiducial value). The separation between these points is referred to as the step size. If the step size is too large the Fisher matrix fails to capture the curvature of the likelihood function about the peak and if it is too small numerical difficulties can arise. Therefore when using Fisher matrices it is vital to verify whether the step size is appropriate, otherwise any results are meaningless.

We verify our step sizes in 1 dimension by fixing all but one model parameter. We then calculate the 1D likelihood using a Fisher matrix with a specified step size and by sampling the likelihood function directly. If the 1D likelihoods match we know we are using a reasonable step size when calculating our Fisher matrix. We sample the likelihood function directly using a simulated datavector generated at the Fisher matrix fiducial values and a grid sampler. Grid samplers evaluate the likelihood at a specified set of grid points. Since we are assuming a Gaussian Likelihood when calculating our Fisher matrix (eq. (5.3)) we are only interested in whether the standard deviation σ of the likelihood calculated using the Fisher matrix matches the σ of the likelihood from sampling directly using a grid sampler.

Figure 10 shows the σ of the 1D likelihood calculated using the Fisher matrix for different choices of step size. These plots show that as the step size decreases the σ of the 1D likelihood reaches a plateau, where the step size is actually capturing the shape of the likelihood, before becoming unstable (see subplot for the photometric redshift bias parameter for redshift bin 10). We therefore select a step size in the range where the σ of the Fisher likelihood is stable. Figure 11 shows the Fisher likelihoods gener-

ated using the selected step sizes overlaid with the likelihood from the grid sampler to verify that they match. For the case of the magnification bias parameter b_{m} the Fisher and grid likelihoods do not match. This is because when calculating the Fisher matrix we assume that the likelihood is Gaussian, and the likelihood of b_{m} from direct sampling is clearly not Gaussian. This is a limitation of the Fisher matrix approach.

We additionally check the Fisher step sizes for the cosmological parameters, by varying all the cosmological parameters at once and exploring the multivariate posterior with Markov Chain Monte Carlo (MCMC) sampling[3]. Figure 12 shows a comparison between the constraints obtained from the MCMC and the Fisher matrix. They match well and show that our Fisher matrix is adequately capturing the shape of the likelihood.

Figures 10 and 11 show only an example case for the parameters used to generate the C_{nn} Fisher matrix for ϵ-sample. However, the step sizes have been verified using this method for every Fisher matrix referred to in the results section.

---

[3]the MCMC we use is emcee (Foreman-Mackey et al. 2013)
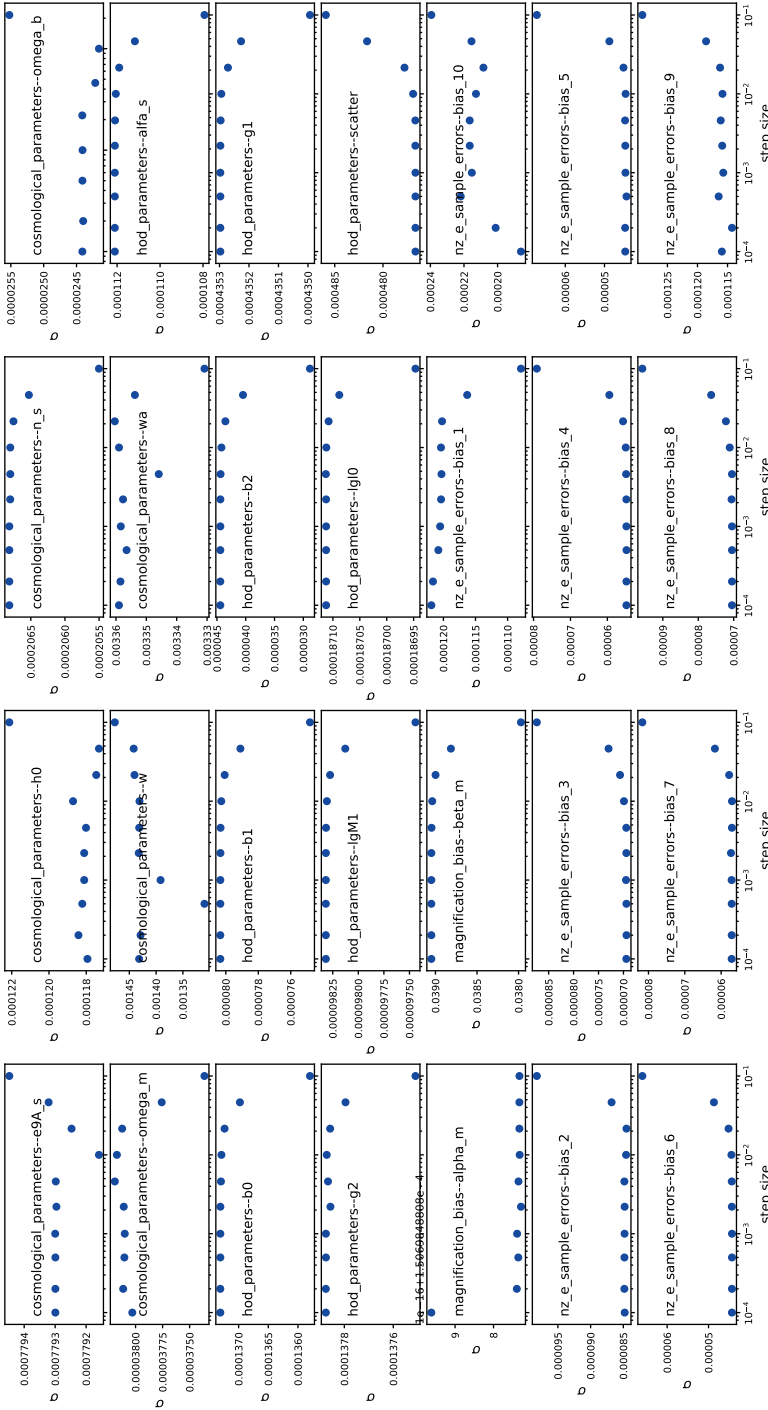
Figure 10: Standard deviation of the 1D Fisher likelihoods against the step size used to calculate the derivatives in the Fisher matrix. The chosen step size should be in the plateau region where the Fisher matrix is actually capturing the shape of the likelihood.
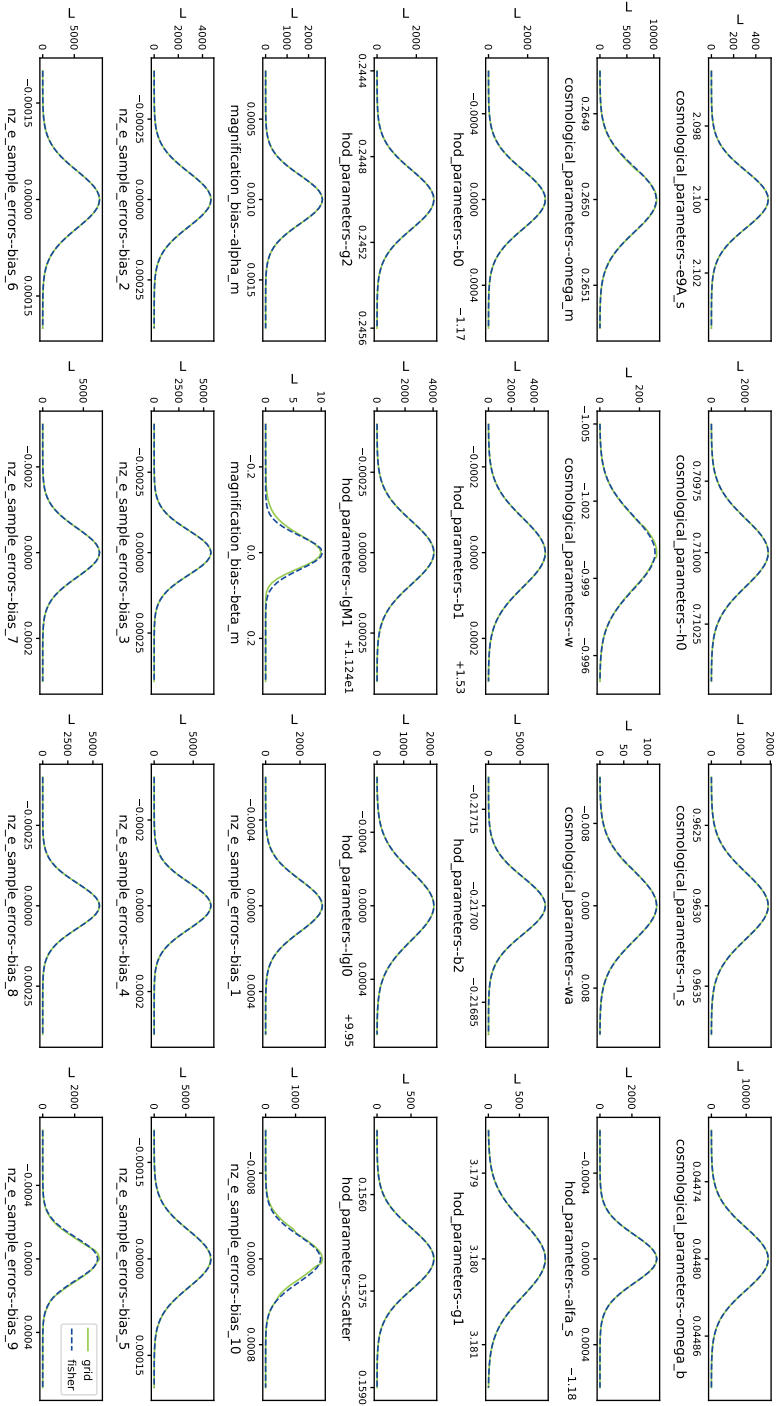
Figure 11: Comparison of the 1D likelihoods from the Fisher matrix calculated using the selected step size against the 1D likelihoods from sampling the likelihood directly using a grid sampler.
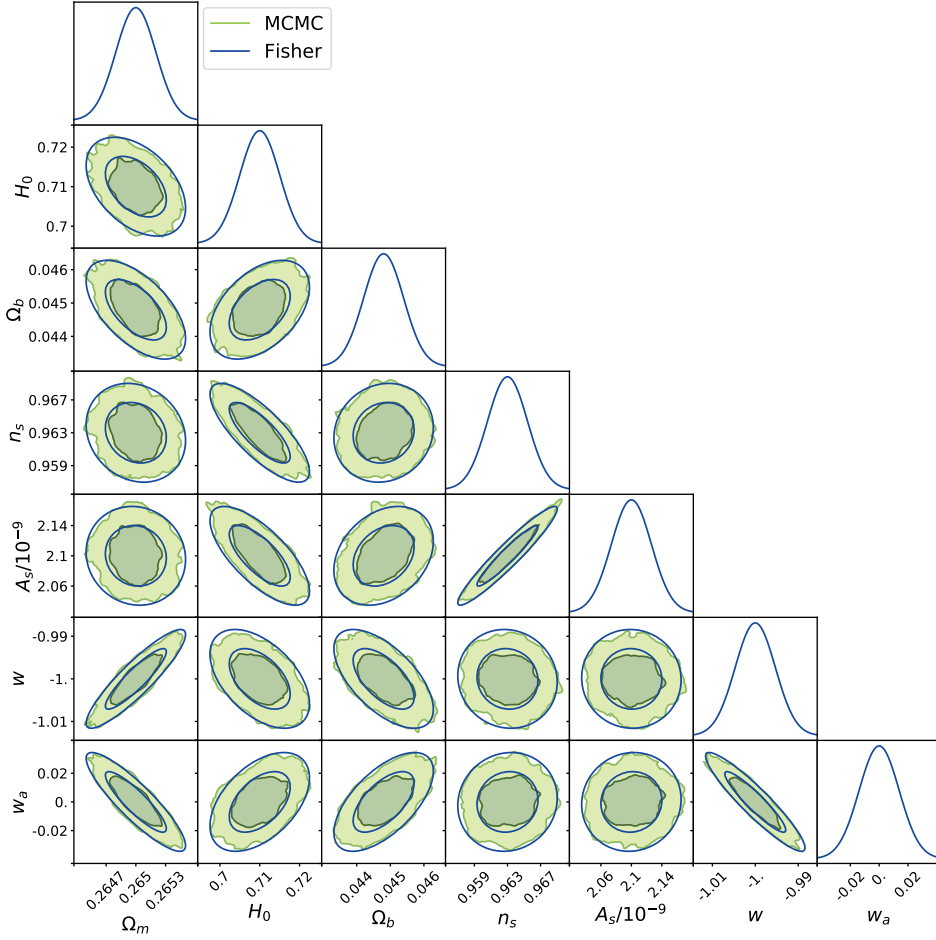
Figure 12: Comparison of the constraints on the cosmological parameters used in this analysis when found using and MCMC or a Fisher matrix. All other parameters have been fixed.

Bibliography

Abbott T. M. C., et al., 2018, Phys. Rev., D98, 043526

Abbott T., et al., 2019, Phys. Rev. D, 99, 123505

Abbott T. M. C., et al., 2021, arXiv e-prints, p. arXiv:2101.05765

Abell P. A., et al., 2009

Aghanim N., et al., 2018, arXiv:1807.06209

Aihara H., et al., 2018, PASJ, 70, S4

Albareti F. D., et al., 2017, ApJS, 233, 25

Albrecht A., et al., 2006, arXiv:astro-ph/0609591

Alonso D., et al., 2018, arXiv:1809.01669

Alpher R. A., Herman R. C., 1948, Physical Review, 74, 1737

Alpher R. A., Bethe H., Gamow G., 1948, Physical Review, 73, 803

Amara A., Réfrégier A., 2007, MNRAS, 381, 1018

Arnouts S., Ilbert O., 2011, LePHARE: Photometric Analysis for Redshift Estimate (ascl:1108.009)

Arun K., Gudennavar S. B., Sivaram C., 2017, Advances in Space Research, 60, 166

Asgari M., et al., 2021, A&A, 645, A104

Bailin J., Power C., Norberg P., Zaritsky D., Gibson B. K., 2008, MNRAS, 390, 1133

Barreira A., Krause E., Schmidt F., 2018, JCAP, 10, 053

Bartelmann M., 2010, Class. Quant. Grav., 27, 233001

Bartelmann M., Schneider P., 2001, Phys. Rep., 340, 291

Benítez N., 2000, ApJ, 536, 571

Bertin E., Arnouts S., 1996, A&AS, 117, 393

Bhowmick A. K., Chen Y., Tenneti A., Di Matteo T., Mandelbaum R., 2020, MN-RAS, 491, 4116

Bilicki M., et al., 2021, arXiv e-prints, p. arXiv:2101.06010

Blake C., et al., 2016, Monthly Notices of the Royal Astronomical Society, 462, 4240–4265

Blanton M. R., et al., 2003, ApJ, 592, 819

Blanton M. R., et al., 2005, AJ, 129, 2562

Blazek J., McQuinn M., Seljak U., 2011, J. Cosmology Astropart. Phys., 2011, 010

Blazek J., Mandelbaum R., Seljak U., Nakajima R., 2012, J. Cosmology Astropart. Phys., 2012, 041

Blazek J. A., MacCrann N., Troxel M. A., Fang X., 2019, Phys. Rev. D, 100, 103506

Boerner G., Ehlers J., 1988, A&A, 204, 1

Bonnett C., et al., 2016, Phys. Rev. D, 94, 042005

Bridle S., King L., 2007, New Journal of Physics, 9, 444

Bridle S., et al., 2009, Annals of Applied Statistics, 3, 6

Brown M. L., Taylor A. N., Hambly N. C., Dye S., 2002, MNRAS, 333, 501

Bruzual G., Charlot S., 2003, MNRAS, 344, 1000

Cacciato M., van den Bosch F. C., More S., Li R., Mo H. J., Yang X., 2009, MNRAS, 394, 929

Cacciato M., van den Bosch F. C., More S., Mo H., Yang X., 2013, MNRAS, 430, 767

Cacciato M., van Uitert E., Hoekstra H., 2014, MNRAS, 437, 377

Calzetti D., Kinney A. L., Storchi-Bergmann T., 1994, ApJ, 429, 582

Capaccioli M., et al., 2012, in Science from the Next Generation Imaging and Spectroscopic Surveys. p. 1

Cardona W., Durrer R., Kunz M., Montanari F., 2016, Phys. Rev., D94, 043007

Carretero J., Castander F. J., Gaztañaga E., Crocce M., Fosalba P., 2015, MNRAS, 447, 646

Carretero J., et al., 2017, PoS, EPS-HEP2017, 488

Catelan P., Kamionkowski M., Blandford R. D., 2001, MNRAS, 320, L7

Chabrier G., 2003, PASP, 115, 763

Chang C., et al., 2013, MNRAS, 434, 2121

Chen G. C. F., et al., 2019, MNRAS, 490, 1743

Chisari N. E., Mandelbaum R., Strauss M. A., Huff E. M., Bahcall N. A., 2014, MNRAS, 445, 726

Chisari N. E., Dunkley J., Miller L., Allison R., 2015a, MNRAS, 453, 682

Chisari N., et al., 2015b, MNRAS, 454, 2736

Chisari N. E., et al., 2019, ApJS, 242, 2

Codis S., Jindal A., Chisari N. E., Vibert D., Dubois Y., Pichon C., Devriendt J., 2018, MNRAS, 481, 4753

Coe D., 2009, arXiv:0906.4123

Coe D., Benítez N., Sánchez S. F., Jee M., Bouwens R., Ford H., 2006, AJ, 132, 926

Cole S., 2011, MNRAS, 416, 739

Cooray A., Sheth R., 2002, Phys. Rep., 372, 1

Crittenden R. G., Natarajan P., Pen U.-L., Theuns T., 2001, ApJ, 559, 552

Crocce M., Castander F. J., Gaztañaga E., Fosalba P., Carretero J., 2015, MNRAS,

453, 1513

Croft R. A. C., Metzler C. A., 2000, ApJ, 545, 561

DES Collaboration et al., 2021, arXiv e-prints, p. arXiv:2105.13549

Davies L. J. M., et al., 2015, MNRAS, 447, 1014

Despali G., Giocoli C., Angulo R. E., Tormen G., Sheth R. K., Baso G., Moscardini L., 2016, MNRAS, 456, 2486

Di Valentino E., et al., 2021, arXiv e-prints, p. arXiv:2103.01183

Dodelson S., 2003, Modern cosmology. Academic Press

Driver S. P., et al., 2009, Astronomy and Geophysics, 50, 5.12

Driver S. P., et al., 2011, MNRAS, 413, 971

Dubinski J., 1992, ApJ, 401, 441

Duffy A. R., Schaye J., Kay S. T., Dalla Vecchia C., 2008, MNRAS, 390, L64

Duncan C., Joachimi B., Heavens A., Heymans C., Hildebrandt H., 2014, Mon. Not. Roy. Astron. Soc., 437, 2471

Dvornik A., et al., 2018, MNRAS, 479, 1240

Dvornik A., et al., 2020, A&A, 642, A83

Edge A., Sutherland W., Kuijken K., Driver S., McMahon R., Eales S., Emerson J. P., 2013, The Messenger, 154, 32

Eriksen M., et al., 2019, MNRAS, 484, 4200

Faltenbacher A., Li C., Mao S., van den Bosch F. C., Yang X., Jing Y. P., Pasquali A., Mo H. J., 2007, ApJ, 662, L71

Faltenbacher A., Li C., White S. D. M., Jing Y.-P., Shu-DeMao Wang J., 2009, Research in Astronomy and Astrophysics, 9, 41

Felten J. E., 1976, ApJ, 207, 700

Fenech Conti I., Herbonnet R., Hoekstra H., Merten J., Miller L., Viola M., 2017, MNRAS, 467, 1627

Foreman-Mackey D., Hogg D. W., Lang D., Goodman J., 2013, PASP, 125, 306

Forero-Romero J. E., Contreras S., Padilla N., 2014, MNRAS, 443, 1090

Fortuna M. C., Hoekstra H., Joachimi B., Johnston H., Chisari N. E., Georgiou C., Mahony C., 2021a, MNRAS, 501, 2983

Fortuna M. C., et al., 2021b, A&A, 654, A76

Fosalba P., Gaztañaga E., Castander F. J., Crocce M., 2015a, MNRAS, 447, 1319

Fosalba P., Crocce M., Gaztañaga E., Castander F. J., 2015b, MNRAS, 448, 2987

Freedman W. L., et al., 2020, ApJ, 891, 57

Freudenburg J. K., Huff E. M., Hirata C. M., 2019, arXiv:1910.02906

Friedmann A., 1922, Zeitschrift fur Physik, 10, 377

Friedmann A., 1924, Zeitschrift fur Physik, 21, 326

Gabor J. M., Davé R., Finlator K., Oppenheimer B. D., 2010, MNRAS, 407, 749

Gaia Collaboration et al., 2018, A&A, 616, A1

Gamow G., 1946, Physical Review, 70, 572

Gamow G., 1948, Nature, 162, 680

Gao L., Navarro J. F., Cole S., Frenk C. S., White S. D. M., Springel V., Jenkins A., Neto A. F., 2008, MNRAS, 387, 536

Georgiou C., et al., 2019a, A&A, 622, A90

Georgiou C., et al., 2019b, A&A, 628, A31

Giblin B., et al., 2021, A&A, 645, A105

Górski K. M., Hivon E., Banday A. J., Wandelt B. D., Hansen F. K., Reinecke M., Bartelmann M., 2005, ApJ, 622, 759

Guth A. H., 1981, Phys. Rev. D, 23, 347

Hahn O., Porciani C., Carollo C. M., Dekel A., 2007, MNRAS, 375, 489

Hainaut O., 2005, Signal, Noise and Detection, https://www.eso.org/~ohainaut/ccd/sn.html

Haridasu B. S., Luković V. V., Moresco M., Vittorio N., 2018, J. Cosmology Astropart. Phys., 2018, 015

Hartlap J., Simon P., Schneider P., 2007, A&A, 464, 399

Heavens A., Refregier A., Heymans C., 2000, MNRAS, 319, 649

Heymans C., et al., 2006, MNRAS, 368, 1323

Heymans C., et al., 2013, MNRAS, 432, 2433

Hikage C., et al., 2019, PASJ, 71, 43

Hildebrandt H., 2015, MNRAS, 455, 3943

Hildebrandt H., van Waerbeke L., Erben T., 2009, A&A, 507, 683

Hildebrandt H., et al., 2013, MNRAS, 429, 3230

Hildebrandt H., et al., 2017, MNRAS, 465, 1454

Hildebrandt H., et al., 2020, A&A, 633, A69

Hildebrandt H., et al., 2021, A&A, 647, A124

Hirata C. M., Seljak U., 2004, Phys. Rev. D, 70, 063526

Hirata C. M., Mandelbaum R., Ishak M., Seljak U., Nichol R., Pimbblet K. A., Ross N. P., Wake D., 2007, MNRAS, 381, 1197

Hoekstra H., Hsieh B. C., Yee H. K. C., Lin H., Gladders M. D., 2005, ApJ, 635, 73

Hoekstra H., Viola M., Herbonnet R., 2017, MNRAS, 468, 3295

Hoffmann K., Bel J., Gaztañaga E., Crocce M., Fosalba P., Castander F. J., 2015, MNRAS, 447, 1724

Hopkins P. F., Bahcall N. A., Bode P., 2005, ApJ, 618, 1

Huang H.-J., Mandelbaum R., Freeman P. E., Chen Y.-C., Rozo E., Rykoff E., Baxter E. J., 2016, MNRAS, 463, 222

Huang H.-J., Mandelbaum R., Freeman P. E., Chen Y.-C., Rozo E., Rykoff E., 2018, MNRAS, 474, 4772

Hubble E., 1929, Proceedings of the National Academy of Science, 15, 168

Hubble E., Humason M. L., 1931, ApJ, 74, 43

Huff E. M., Graves G. J., 2013, The Astrophysical Journal, 780, L16

Jarvis M., Bernstein G., Jain B., 2004, MNRAS, 352, 338

Jenkins A., Frenk C. S., White S. D. M., Colberg J. M., Cole S., Evrard A. E., Couchman H. M. P., Yoshida N., 2001, MNRAS, 321, 372

Jimenez R., Loeb A., 2002, ApJ, 573, 37

Joachimi B., Bridle S. L., 2010, A&A, 523, A1

Joachimi B., Schneider P., Eifler T., 2008, Astron. Astrophys., 477, 43

Joachimi B., Mandelbaum R., Abdalla F. B., Bridle S. L., 2011, A&A, 527

Joachimi B., et al., 2015, Space Sci. Rev., 193, 1

Johnston H., et al., 2019, A&A, 624, A30

Joudaki S., et al., 2018, Mon. Not. Roy. Astron. Soc., 474, 4894

Kafedžić-Briga A., Džaferović-Mašić E., 2021, in Journal of Physics Conference Series. p. 012007, doi:10.1088/1742-6596/1814/1/012007

Kaiser N., 1992, ApJ, 388, 272

Kaiser N., Squires G., Broadhurst T., 1995, ApJ, 449, 460

Kannawadi A., et al., 2019, A&A, 624, A92

Kiessling A., et al., 2015, Space Sci. Rev., 193, 67

Kilbinger M., 2015, Reports on Progress in Physics, 78, 086901

Kilbinger M., et al., 2009, A&A, 497, 677

Kirk D., Bridle S., Schneider M., 2010, MNRAS, 408, 1502

Kirk D., et al., 2015, Space Sci. Rev., 193, 139

Knebe A., Gill S. P. D., Gibson B. K., Lewis G. F., Ibata R. A., Dopita M. A., 2004, ApJ, 603, 7

Korytov D., et al., 2019, Astrophys. J. Suppl., 245, 26

Kovacs E., et al., "in prep.", Title

Kraljic K., Davé R., Pichon C., 2020, MNRAS, 493, 362

Krause E., Eifler T., Blazek J., 2016, MNRAS, 456, 207

Kravtsov A. V., Berlind A. A., Wechsler R. H., Klypin A. A., Gottlöber S., Allgood B. o., Primack J. R., 2004, ApJ, 609, 35

Kuijken K., 2011, The Messenger, 146, 8

Kuijken K., et al., 2019, A&A, 625, A2

LSST Science Collaboration 2009, arXiv:0902.0201

Landy S. D., Szalay A. S., 1993, ApJ, 412, 64

Laureijs R., et al., 2011, arXiv e-prints, p. arXiv:1110.3193

Leauthaud A., et al., 2017, MNRAS, 467, 3024

Lee J., Springel V., Pen U.-L., Lemson G., 2008, MNRAS, 389, 1266

Lemaître G., 1931, MNRAS, 91, 490

Leonard C. D., Mandelbaum R., LSST Dark Energy Science Collaboration 2018, MNRAS, 479, 1412

Lewis A., Bridle S., 2002, Phys. Rev. D, 66, 103511

Lewis A., Challinor A., Lasenby A., 2000, ApJ, 538, 473

Li S.-S., Kuijken K., Hoekstra H., Hildebrandt H., Joachimi B., Kannawadi A., 2021, A&A, 646, A175

Liske J., et al., 2015, MNRAS, 452, 2087

Lorenz C. S., Alonso D., Ferreira P. G., 2018, Phys. Rev., D97, 023537

Lukić Z., Heitmann K., Habib S., Bashinsky S., Ricker P. M., 2007, ApJ, 671, 1160

Ma C.-P., Fry J. N., 2000, The Astrophysical Journal, 543, 503

MacCrann N., et al., 2020, arXiv e-prints, p. arXiv:2012.08567

Mancone C. L., Gonzalez A. H., 2012, PASP, 124, 606

Mandelbaum R., 2018, Annual Review of Astronomy and Astrophysics, 56, 393

Mandelbaum R., et al., 2005, MNRAS, 361, 1287

Mandelbaum R., Hirata C. M., Ishak M., Seljak U., Brinkmann J., 2006, Mon. Not. R. Astron. Soc, 367, 611

Mandelbaum R., Seljak U., Hirata C. M., 2008, J. Cosmology Astropart. Phys., 2008, 006

Mandelbaum R., et al., 2011, MNRAS, 410, 844

Melchior P., Viola M., Schäfer B. M., Bartelmann M., 2011, MNRAS, 412, 1552

Miller L., Kitching T. D., Heymans C., Heavens A. F., van Waerbeke L., 2007, MN-RAS, 382, 315

Miller L., et al., 2013, MNRAS, 429, 2858

Miyatake H., et al., 2015, ApJ, 806, 1

More S., van den Bosch F. C., Cacciato M., Skibba R., Mo H. J., Yang X., 2011, MNRAS, 410, 210

Morrison C. B., Hildebrandt H., 2015, Mon. Not. Roy. Astron. Soc., 454, 3121

Murray S., 2014, HMF: Halo Mass Function calculator (ascl:1412.006)

Murray S. G., Power C., Robotham A. S. G., 2013, Astronomy and Computing, 3, 23

Myers A. D., Outram P., Shanks T., Boyle B., Croom S., Loaring N., Miller L., Smith R., 2005, Mon. Not. Roy. Astron. Soc., 359, 741

Myles J., et al., 2020, arXiv e-prints, p. arXiv:2012.08566

Navarro J. F., Frenk C. S., White S. D. M., 1996, ApJ, 462, 563

Nicola A., et al., 2020, JCAP, 03, 044

Okumura T., Jing Y. P., 2009, ApJ, 694, L83

Padilla C., et al., 2019, AJ, 157, 246

Penzias A. A., Wilson R. W., 1965, ApJ, 142, 419

Pereira M. J., Bryan G. L., 2010, ApJ, 721, 939

Pereira M. J., Kuhn J. R., 2005, ApJ, 627, L21

Pereira M. J., Bryan G. L., Gill S. P. D., 2008, ApJ, 672, 825

Perlmutter S., et al., 1999, ApJ, 517, 565

Piras D., Joachimi B., Schäfer B. M., Bonamigo M., Hilbert S., van Uitert E., 2018, MNRAS, 474, 1165

Planck Collaboration et al., 2020, A&A, 641, A6

Press W. H., Schechter P., 1974, ApJ, 187, 425

Riess A. G., et al., 1998, AJ, 116, 1009

Riess A. G., Casertano S., Yuan W., Macri L. M., Scolnic D., 2019, ApJ, 876, 85

Robertson N. C., et al., 2020, arXiv e-prints, p. arXiv:2011.11613

Robotham A. S. G., et al., 2011, MNRAS, 416, 2640

Roche N., Eales S. A., 1999, MNRAS, 307, 703

Rozo E., et al., 2016, MNRAS, 461, 1431

Rubin V. C., Ford W. K. J., . Thonnard N., 1980, ApJ, 238, 471

Rykoff E. S., et al., 2014, ApJ, 785, 104

Samuroff S., et al., 2018, MNRAS, 475, 4524

Samuroff S., et al., 2019, MNRAS, 489, 5453

Samuroff S., Mandelbaum R., Blazek J., 2020a, arXiv e-prints, p. arXiv:2009.10735

Samuroff S., Mandelbaum R., Di Matteo T., 2020b, MNRAS, 491, 5330

Sargent M. T., et al., 2007, ApJS, 172, 434

Scarlata C., et al., 2007, ApJS, 172, 406

Schechter P., 1976, ApJ, 203, 297

Schmidt M., 1968, ApJ, 151, 393

Schmidt F., Leauthaud A., Massey R., Rhodes J., George M. R., Koekemoer A. M., Finoguenov A., Tanaka M., 2011, The Astrophysical Journal, 744, L22

Schneider P., 2005, arXiv e-prints, pp astro−ph/0509252

Schneider M. D., Bridle S., 2010, MNRAS, 402, 2127

Schöneberg N., Lesgourgues J., Hooper D. C., 2019, J. Cosmology Astropart. Phys., 2019, 029

Scoville N., et al., 2007, ApJS, 172, 1

Scranton R., et al., 2005, Astrophys. J., 633, 589

Seljak U., 2000, MNRAS, 318, 203

Shapley H., 1918, PASP, 30, 42

Shapley H., 1919, JRASC, 13, 438

Shapley H., Curtis H. D., 1921, Bulletin of the National Research Council, 2, 171

Sheldon E. S., et al., 2004, AJ, 127, 2544

Sifón C., Hoekstra H., Cacciato M., Viola M., Köhlinger F., van der Burg R. F. J., Sand D. J., Graham M. L., 2015, A&A, 575, A48

Sifón C., Herbonnet R., Hoekstra H., van der Burg R. F. J., Viola M., 2018, MNRAS, 478, 1244

Singh S., Mandelbaum R., 2016, MNRAS, 457, 2301

Singh S., Mandelbaum R., More S., 2015, MNRAS, 450, 2195

Singh S., Mandelbaum R., Seljak U., Slosar A., Vazquez Gonzalez J., 2017, MNRAS, 471, 3827

Skibba R., Sheth R., 2009, Monthly Notices of the Royal Astronomical Soc, v.392, 1080-1091 (2009), 392

Smith R. W., 1979, Journal for the History of Astronomy, 10, 133

Smith J. A., et al., 2002, AJ, 123, 2121

Soussana A., et al., 2020, MNRAS, p. 58

Spergel D., et al., 2015, arXiv e-prints, p. arXiv:1503.03757

Springel V., et al., 2005, Nature, 435, 629

Takahashi R., Sato M., Nishimichi T., Taruya A., Oguri M., 2012, ApJ, 761, 152

Tegmark M., Taylor A., Heavens A., 1997, Astrophys. J., 480, 22

Tenneti A., Mandelbaum R., Di Matteo T., 2016, MNRAS, 462, 2668

Tenneti A., Gnedin N. Y., Feng Y., 2017, ApJ, 834, 169

Thiele L., Duncan C. A. J., Alonso D., 2019, arXiv:1907.13205

Tinker J. L., Robertson B. E., Kravtsov A. V., Klypin A., Warren M. S., Yepes G., Gottloeber S., 2010, The Astrophysical Journal, 724, 878

Tonegawa M., Okumura T., Totani T., Dalton G., Glazebrook K., Yabe K., 2018, PASJ, 70, 41

Troxel M. A., Ishak M., 2015, Phys. Rep., 558, 1

Troxel M. A., et al., 2018, Phys. Rev. D, 98, 043528

Tudorica A., et al., 2017, Astron. Astrophys., 608, A141

Unruh S., Schneider P., Hilbert S., Simon P., Martin S., Puertas J. C., 2020, A&A, 638, A96

Vakili M., et al., 2019, MNRAS, 487, 3715

Vakili M., et al., 2020, arXiv e-prints, p. arXiv:2008.13154

Velander M., et al., 2014, MNRAS, 437, 2111

Velliscig M., et al., 2015a, MNRAS, 453, 721

Velliscig M., et al., 2015b, MNRAS, 454, 3328

Vlah Z., Chisari N. E., Schmidt F., 2020, J. Cosmology Astropart. Phys., 2020, 025

Weinmann S. M., van den Bosch F. C., Yang X., Mo H. J., 2006, MNRAS, 366, 2

West M. J., Blakeslee J. P., 2000, ApJ, 543, L27

White S. D. M., Rees M. J., 1978, MNRAS, 183, 341

Wright A. H., et al., 2019, A&A, 632, A34

Wright A. H., Hildebrandt H., van den Busch J. L., Heymans C., Joachimi B., Kannawadi A., Kuijken K., 2020, A&A, 640, L14

Xia Q., Kang X., Wang P., Luo Y., Yang X., Jing Y., Wang H., Mo H., 2017, ApJ, 848, 22

Yang X., Mo H. J., van den Bosch F. C., 2003, MNRAS, 339, 1057

Yang X., Mo H. J., van den Bosch F. C., Pasquali A., Li C., Barden M., 2007, ApJ, 671, 153

Yang X., Mo H. J., van den Bosch F. C., 2008, ApJ, 676, 248

Zehavi I., et al., 2011, ApJ, 736, 59

Zentner A. R., Kravtsov A. V., Gnedin O. Y., Klypin A. A., 2005, ApJ, 629, 219

Zheng Z., et al., 2005, The Astrophysical Journal, 633

Zheng Z., Coil A. L., Zehavi I., 2007, ApJ, 667, 760

Zinger E., Dekel A., Kravtsov A. V., Nagai D., 2018, MNRAS, 475, 3654

Zonca A., Singer L., Lenz D., Reinecke M., Rosset C., Hivon E., Gorski K., 2019, Journal of Open Source Software, 4, 1298

Zuntz J., et al., 2015, Astronomy and Computing, 12, 45

Zwicky F., 1933, Helvetica Physica Acta, 6, 110

de Jong J. T. A., Verdoes Kleijn G. A., Kuijken K. H., Valentijn E. A., 2013, Experimental Astronomy, 35, 25

van Uitert E., Joachimi B., 2017, MNRAS, 468, 4502

van Uitert E., Hoekstra H., Schrabback T., Gilbank D. G., Gladders M. D., Yee H. K. C., 2012, A&A, 545, A71

van Uitert E., Cacciato M., Hoekstra H., Herbonnet R., 2015, A&A, 579, A26

van Uitert E., et al., 2016a, MNRAS, 459, 3251

van Uitert E., Gilbank D. G., Hoekstra H., Semboloni E., Gladders M. D., Yee H. K. C., 2016b, A&A, 586, A43

van Uitert E., et al., 2018, Mon. Not. Roy. Astron. Soc., 476, 4662

van den Bosch F. C., More S., Cacciato M., Mo H., Yang X., 2013, MNRAS, 430, 725

van den Busch J. L., et al., 2020, A&A, 642, A200

von Wietersheim-Kramsta M., et al., 2021, MNRAS, 504, 1452

Nederlandse Samenvatting

Ons huidige begrip van het Heelal berust op de grote doorbraken van de vorige eeuw: de uitwerking van de Algemene Relativiteitstheorie, het postulaat van een "donkere", onzichtbare materie om de spreiding in de waargenomen snelheden van sterrenstelsels in clusters te verklaren, net als de waargenomen rotatiesnelheid in de sterrenstelsels zelf, en ten slotte de ontdekking van de versnellende uitdijing van het Heelal. Theoretisch gezien zijn we nu in staat om de groei van structuur op grote schalen te verbinden met het vroege Heelal en om diverse waarnemingen op verschillende schalen en tijden te beschrijven met één enkel model. Dit model vereist het bestaan van twee "donkere" ingrediënten: donkere materie die de extra waargenomen zwaartekracht rondom sterrenstelsels verklaart en ook leidt tot het ontstaan van structuur, en donkere energie die de versnelde uitdijing veroorzaakt. De totale hoeveelheid energie in het Heelal bestaat voor meer dan 95% uit deze twee bestanddelen. Het is duidelijk dat niettegenstaande het succes van dit model, er een enorme open vraag resteert: wat is de ware aard van de twee voornaamste ingrediënten van het Heelal?

Naast de directe zoektocht naar het donkere materiedeeltje in het lab, kunnen we ook waarnemingen van het Heelal op grote schaal gebruiken om mogelijke afwijkingen van dit standaardmodel te onderzoeken. Specifiek willen we weten of donkere energie evolueert in de tijd, wat de vorming van structuur in verschillende tijdperken zou beïnvloeden, en ook of de zwaartekracht van de donkere materie te onderscheiden valt van een mogelijke aanpassing aan de Algemene Relativiteitstheorie. Hiervoor hebben we grootschalige waarnemingen nodig om met de enorme hoeveelheid data die zij leveren, mogelijke afwijkingen van het standaardmodel van de kosmologie met grotere statistische zekerheid te meten. Een grote precisie moet echter ook gepaard gaan met een grote nauwkeurigheid: we moeten mogelijke systematische fouten, zowel in de waarnemingstechnieken als in de interpretatie van de data, tot op een ongezien niveau begrijpen. Dit is

het voornaamste doel van deze thesis.

Zwakke zwaartekrachtslenzen zijn een van de krachtigste methodes om de donkere kant van het Heelal te onderzoeken. Lichtstralen volgen de lokale kromming van de ruimtetijd veroorzaakt door een nabije massaverdeling, wat resulteert in een gecorreleerde vervorming van de afbeelding van achterliggende sterrenstelsels. Uit deze vervorming kan de hoeveelheid donkere materie langs de gezichtslijn bepaald worden.

De interpretatie van dit signaal wordt bemoeilijkt door intrinsieke uitlijningen (*intrinsic alignment*, IA) van sterrenstelsels. Naburige sterrenstelsels hebben intrinsiek een gecorreleerde oriëntatie omdat ze ontstaan binnenin ophopingen van donkere materie, ook wel halo's genoemd, en onderhevig zijn aan de getijdenvelden van de omliggende massaverdeling. Dit laat een voorkeursoriëntatie na in de vorm van sterrenstelsels voordat hun licht doorheen de tussenliggende zwaartekrachtslens naar ons propageert. Vanwege de correlatie tussen de verschillende overdichtheden die verantwoordelijk zijn voor het zwaartekrachtsveld nabij de sterrenstelsels, is de uitlijning van de sterrenstelsels ook gecorreleerd, zowel op middelgrote als op grote schalen. Op kleine schaal is de uitlijning daarentegen het gevolg van de getijdenvelden binnenin de halo.

De intrinsieke uitlijning van sterrenstelsels is dus niet enkel een belangrijke bron van onzekerheid die zorgvuldig gemodelleerd moet worden: ze gunt ook een unieke blik op het vormingsproces van sterrenstelsels en de mogelijkheid om het verband tussen sterrenstelsels en hun donkere materiehalo's te begrijpen.

In deze thesis focussen we op het begrip van hoe intrinsieke uitlijningen afhangen van de eigenschappen van sterrenstelsels om de variatie in de sterkte van het signaal in zwakke zwaartekrachtslenzen te verklaren. We gebruiken waarnemingen om het uitlijningssignaal direct te bepalen voor specifieke deelverzamelingen van de data. We introduceren een enkel model dat de complexe afhankelijkheid van het uitlijningssignaal van de waargenomen sterrenstelseleigenschappen meeneemt en de impact van het uitlijningssignaal op de waarnemingen kan voorspellen. Hier is een tweevoudige winst: enerzijds kan het model direct gerelateerd worden aan waarnemingen en zodoende kunnen zwaartekrachtslensanalyses waarden uit de literatuur gebruiken voor de a priori aannames van de parameters van het model, anderzijds kan de verwachte sterkte van het uitlijningssignaal in een specifieke dataset bepaald worden om simpele modellen een betere voorkennis te leveren over de beste a priori aanname voor de verwachte signaalsterkte.

We vatten de inhoud van de hoofdstukken van deze thesis samen.

In **Hoofdstuk 2** introduceren we een model dat de diversiteit van het IA-signaal van verschillende soorten sterrenstelsels kan beschrijven, inclusief de afhankelijkheid van hun morfologie (meegenomen via de kleur van de sterrenstelsels) en type (centraal of satelliet). Met dit model en een gesimuleerde populatie sterrenstelsels die de verdeling in kleur en type van de willekeurige dataset reproduceert, kan het IA-signaal voorspeld worden. We hebben deze methode toegepast op gesimuleerde zwakke gravitatielenswaarnemingen en zo het totale IA-signaal en de schaalafhankelijkheid bestudeerd. We gebruiken dit gesimuleerde signaal om de impact van IA op huidige en toekomstige waarnemingen te voorspellen, met als specifieke interesse het onderzoeken of simplistische IA-modellen een systematische fout in de afgeleide kosmologische parameters introduceren. We concluderen dat dit effect verwaarloosbaar is voor huidige waarnemingen maar dat in de toekomst ten minste een effectieve roodverschuivingsafhankelijkheid moet meegenomen worden in simpele IA-modellen om de juiste kosmologie te bekomen.

In **Hoofdstuk 3** bepalen we de amplitude van het IA-signaal voor de heldere rode sterrenstelsels (*luminous red galaxies*, LRGs) van de vierde data-uitgave van de Kilo Degree Survey. We meten de vormen van de sterrenstelsels met twee verschillende methodes en vergelijken het resulterende IA-signaal om een mogelijke afhankelijkheid van de methode te onderzoeken. Beide methodes zijn in overeenkomst. Vervolgens onderzoeken we de lichtkrachtsafhankelijkheid van het signaal door de sterrenstelsels te groeperen volgens hun lichtkracht. In combinatie met voorgaande metingen in de literatuur, vinden we dat de afhankelijkheid goed beschreven kan worden met behulp van een functie met een dubbele machtsschaling. Bij lage lichtkracht hangt het signaal significant minder af van de lichtkracht dan voor heldere sterrenstelsels. We hebben de roodverschuivingsafhankelijkheid van het signaal onderzocht en vinden geen bewijs voor enige evolutie in het roodverschuivingsbereik $0.2 < z < 0.8$.

In **Hoofdstuk 4** gebruiken we de LRGs van Hoofdstuk 3 als lens voor achterliggende sterrenstelsels om hun totale massa te bepalen. We modelleren het signaal met een halo-model in combinatie met de voorwaardelijke lichtkrachtsfunctie (*conditional luminosity function*) om sterrenstelsels met donkere materiehalo's te verbinden. We groeperen de sterrenstelsels volgens

hun lichtkracht en beschrijven de vervorming door de zwaartekrachtslens met één model. Hierdoor verkrijgen we de relatie tussen de massa en de lichtkracht van de LRGs die we gebruiken om het gemeten IA-signaal in Hoofdstuk 3 te heranalyseren. De massa-afhankelijkheid van het IA-signaal kan goed beschreven worden met een enkele machtsafhankelijkheid over een massabereik van meer dan drie ordes van grootte. We onderzoeken ook de neiging van naburige sterrenstelsels om in de richting van de LRG te wijzen: in dit geval meten we geen signaal.

Ten slotte, in **Hoofdstuk 5**, bestuderen we de invloed van de vergroting van afbeeldingen door de zwaartekrachtslens voor de Large Synoptic Survey Telescope (LSST). We onderzoeken of het meenemen van deze vergroting in een analyse van het clusteren van sterrenstelsels de bepaling van de kosmologische parameters kan verbeteren. We vinden slechts een klein effect. Daarnaast probeerden we ook de vergroting mee te nemen een gelijktijdige meting van het clusteren en het vervormingssignaal van de zwaartekrachtslenzen aan verschillende delen van de hemel om zo de ijking van het vervormingssignaal te verbeteren. Ook in dit geval is de verbetering klein. Tot slot vinden we een significante systematische fout in het signaal wanneer de vergroting niet wordt meegenomen in de analyse. We concluderen dus dat het cruciaal is om de vergroting mee te nemen in een kosmologische analyse om systematische fouten te voorkomen, maar dit leidt echter niet tot een grote verbetering in de precisie waarmee de kosmologische parameters bepaald kunnen worden.

Summary

Our current view of the Universe relies on the great discoveries that characterised the last century: from the formulation of the theory of General Relativity to the postulation of a 'dark', invisible matter to account for the velocity dispersion and the rotational curves of galaxy clusters and galaxies, to the discovery of the accelerated expansion of the Universe. From a theoretical point of view, we are now able to link the very early Universe to the formation of structures at large scales and provide a single model to describe multiple observations that invoke different scales and epochs. This model postulates the existence of two 'dark' components, the dark matter, which accounts for the extra gravity observed around galaxies and it is also expected to provide the seeds for structure formation, and a dark energy, responsible for the accelerated expansion. Those two ingredients account together for more than 95% of the total energy budget of the Universe. It is thus clear that, although successful in so many aspects, this model leaves open an enormous question: What is the true nature of the two main ingredients of the Universe?

While searching for a dark matter particle in the laboratories, we can also use observations of the Universe at large scales to investigate possible deviations from the standard paradigm of this model. In particular, we aim to know whether the dark energy has evolved over time, affecting the structure formation over the epochs, and to discriminate the gravitational effect of dark matter from a possible extension of general relativity. To do so, we need wide surveys that can collect an enormous amount of data: in this way, statistical uncertainties are reduced and we can capture deviations from the standard cosmological model. However, high precision needs to be paired with great accuracy: We need to control all the possible systematics, both observational and in the interpretation of the data to an unprecedented level. This is the main goal of this thesis.

One of the most powerful probes to investigate the dark sector of the

Universe is weak lensing, a phenomenon caused by the distortion of space-time by a mass distribution, which forces the light-rays to travel bent in the proximity of the mass. This generates correlated distortions of the images of background galaxies that can be used to infer the properties of dark matter along the line-of-sight.

Intrinsic alignment (IA) complicates the interpretation of this signal by adding a correlation between the orientation of galaxy shapes before being lensed. This is caused by the fact that galaxies form inside dark matter haloes and are subjected to the surrounding tidal fields: this imprints a preferred direction to their shapes. Since the overdensities responsible for the gravitational fields where the galaxies form are correlated, the alignment of galaxies is also correlated both at intermediate scales and at large scales. At small scales, the alignment is instead sourced by the intra-halo tidal fields.

Intrinsic alignment is thus not only an important contaminant to lensing that needs to be carefully modelled, but it is also a unique window to understand better the processes of galaxy formation and the dark matter-galaxy connection.

In this work, we mainly focus on understanding how IA depends on galaxy properties to capture the variation of amplitudes that the signal carries in a weak lensing analysis. We use observations to directly constrain the IA in specific subsets of data. We combine the observed complexity of IA signal on galaxy sample into a single model to forecast the impact on lensing. The gain is twofold: on one hand, we provide a model that can directly be linked to observations, such that the weak lensing analyses can use priors from the literature (which are always based on specific galaxy samples); on the other hand, this can be used to study the effective IA content in a specific data-set, and then learn the level of contamination expected, to inform effective models on which amplitude should be adopted as a prior.

In the following, we summarise in more detail the content of each chapter.

In **Chapter 2** we provide a model to account for the diversity of the IA signal as sourced by different kinds of galaxies, including the dependence on morphology (here accounted via galaxy colour) and type (central/satellite). This model allows predicting the total IA in any kind of data-set, given a mock for the galaxy population that includes colour and type. We applied such a method to a simulated weak lensing survey and studied the total signal and its scale dependence. We use this simulated signal to forecast the

impact of IA on ongoing and upcoming surveys, with a particular interest in investigating whether the use of simplistic models for IA would bias the inferred cosmological parameters. We found this to be negligible for ongoing surveys, but upcoming ones need to at least include an effective redshift dependence in their modelling to recover the correct cosmology.

In **Chapter 3** we constrain the IA amplitude of the luminous red galaxy (LRG) sample in the 4th data release of the Kilo Degree Survey. We measure the shapes with two different shape measurement algorithms and compare the resulting IA signal to investigate a possible dependence on the IA amplitude on the shape method adopted. We found the methods to be compatible. We then investigate the luminosity dependence by binning the sample in luminosity bins: when analysing these in combination with previous measurements from the literature, we found that these could be well described by a double power law. At low-luminosity we found the signal to be significantly less luminosity dependent than for bright objects. We explored the redshift dependence of the signal finding no support in the data for any evolution in the redshift range $0.2 < z < 0.8$.

In **Chapter 4** we use galaxy-galaxy lensing to infer the total masses of the LRGs used in Chapter 3. We model the signal using a halo model combined with a conditional luminosity function to populate the haloes: We bin our data in luminosity and fit all the resulting lensing signals with a single model. This provides a luminosity-mass relation that we use to re-analyse the IA signal measured in Chapter 3. We find that the IA dependence on halo mass is well described by a single power law, in a mass range that spans more than three orders of magnitude. We also investigate the tendency of the surrounding galaxies to point in the direction of the LRGs: in this case, we do not detect any signal.

Finally, in **Chapter 5** we investigate the impact of weak lensing magnification in the Large Synoptic Survey Telescope (LSST). We study how much the inclusion of magnification can improve the cosmological parameter constrain in a clustering analysis: We found it to be very mild. We also considered the combined case of clustering and shear signals on separate patches of the sky and investigated whether magnification could improve the shear calibration, but also in this case the improvement was small. Finally, we considered the effect of ignoring magnification in these analyses, and this time we found a significant deviation in the signal: We thus conclude that although the improvement by the including magnification is not

significant, it is crucial to include it in the analysis to avoid biasing the cosmological parameters.

List of Publications

First author

Fortuna, M.C.; Hoekstra, H.; Dvornik, A.; *KiDS-1000: weak lensing and intrinsic alignment around luminous red galaxies*, to be submitted in A&A

Fortuna, M.C.; Hoekstra, H.; Johnston, H.; Vakili, M.; Kannawadi, A.; Georgiou, C.; Joachimi, B.; Weight, A.H.; Asgari, M.; Bilicki, M.; Heymans, C.; Hildebrandt, H.; Kuijken, K.; Von Wietersheim-Kramsta, M.; *KiDS-1000: Constraints on the intrinsic alignment of luminous red galaxies*, A&A, 654, A76 (2021)

Fortuna M.C.; Hoekstra, H.; Joachimi, B.; Johnston, H.; Chisari, N. E.; Georgiou, C.; Mahony, C.; *The halo model as a versatile tool to predict intrinsic alignments*, MNRAS, 501, 2, 2983-3002 (2021)

Contributing author

Mahony, C.; **Fortuna, M.C.**; Joachimi, J.; Korn, A.; Hoekstra, H. *Forecasting the potential of weak lensing magnification to enhance LSST large-scale structure analyses*, to be submitted in MNRAS

Robertson, N. C.; Alonso, D.; Harnois-Déraps, J.; Darwish, O.; Kannawad, A.; Amon, A.; Asgari, M.; Bilicki, M.; Calabrese, E.; Choi, S. K.; Devlin, M. J.; Dunkley, J.; Dvornik, A.; Erben, T.; Ferraro, S.; **Fortuna, M. C.**; Giblin, B.; Han, D.; Heymans, C.; Hildebrandt, H.; Hill, J. C.; Hilton, M.; Ho, S. P.; Hoekstra, H.; Hubmayr, J.; Hughes, J.; Joachimi, B.; Joudaki, S.; Knowles, K.; Kuijken, K.; Madhavacheril, M. S.; Moodley, K.; Miller, L.; Namikawa, T.; Nati, F.; Niemack, M. D.; Page, L. A.; Partridge, B.;

Schaan, E.; Schillaci, A.; Schneider, P.; Sehgal, N.; Sherwin, B. D.; Sifón, C.; Staggs, S. T.; Tröster, T.; van Engelen, A.; Valentijn, E.; Wollack, E. J.; Wright, A. H.; Xu, Z.; *Strong detection of the CMB lensingxgalaxy weak lensingcross-correlation from ACT-DR4,PlanckLegacy and KiDS-1000*, A&A 649, A146 (2021)

Johnston, H.; Joachimi, B.; Norberg, P.; Hoekstra, H.; Eriksen, M.; **Fortuna, M.C.**; Manzoni, G.; Serrano, S.; Siudek, M.; Tortorelli, L.; Cabayol, L.; Carretero, J.; Casas, R.; Castander, F.; Fernandez, E.; García-Bellido, J.; Gaztanaga, E.; Hildebrandt, H.; Miquel, R.; Padilla, C. Sanchez, E.; Sevilla-Noarbe, I.; Tallada-Crespí, P.; *The PAU Survey: Intrinsic alignments and clustering of narrow-band photometric galaxies*, A&A 646, A147 (2021)

Vakili, M.; Hoekstra, H.; Bilicki, M.; **Fortuna, M. C.**; Kuijken, K.; Wright, A. H.; Asgari, M.; Brown, M.; Dombrovskij, E.; Erben, T.; Giblin, B.; Heymans, C.; Hildebrandt, H.; Johnston, H.; Joudaki, S.; Kannawadi, A.; *Clustering of red-sequence galaxies in the fourth data release of the Kilo-Degree Survey*, submitted to A&A, eprint arXiv:2008.13154

Heymans, C.; Tröster, T.; Asgari, M.; Blake, C.; Hildebrandt, H.; Joachimi, B.; Kuijken, K.; Lin, C.; Sánchez, A. G.; van den Busch, J.L.; Wright, A. H.; Amon, A.; Bilicki, M.; de Jong, J.; Crocce, M.; Dvornik, A.; Erben, T.; **Fortuna, M.C.**; Getman, F.; Giblin, B.; Glazebrook, K.; Hoekstra, H.; Joudaki, S.; Kannawadi, A.; Köhlinger, F.; Lidman, C.; Miller, L.; Napolitano, N. R.; Parkinson, D.; Schneider, P.; Shan, H.; Valentijn, E.; Verdoes K., Gijs; Wolf, C.; *KiDS-1000 Cosmology: Multi-probe weak gravitational lensing and spectroscopic galaxy clustering constraints*, A&A 646, A140 (2021)

Georgiou, C.; Chisari, N. E.; **Fortuna, M. C.**; Hoekstra, H.; Kuijken, K.; Joachimi, B.; Vakili, M.; Bilicki, M.; Dvornik, A.; Erben, T.; Giblin, B.; Heymans, C.; Napolitano, N. R.; Shan, H. Y.; *GAMA+KiDS: Alignment of galaxies in galaxy groups and its dependence on galaxy scale*, A&A 628, A31 (2019).

Johnston, H.; Georgiou, C.; Joachimi, B.; Hoekstra, H.; Chisari, N. E.; Farrow, D.; **Fortuna, M. C.**; Heymans, C.; Joudaki, S.; Kuijken, K.; Wright, A.; *KiDS+GAMA: Intrinsic alignment model constraints for current and*

future weak lensing cosmology, A&A 624, A30 (2019)

Curriculum Vitae

I was born in Assisi on the 7th of March 1991 and I spent my early childhood in Perugia. I moved with my family to Reggio Calabria in 1997, where I attended almost my entire school time. Growing up in different cities had an important impact on me and helped me to always have the curiosity to change cities and the environment.

My passion for science emerged during middle school: I was extremely fascinated by both natural science and physics, and this motivated me to enrol in the Scientific Liceum. I was very lucky and I had great teachers in all of my schools: this built up my passion and I started reading lots of outreach books about physics. My interest in cosmology was mainly sourced by the conversations with my grandfather, who was the first to introduce me to the Big Bang theory, the cosmic expansion and all the suggestive pictures from the Hubble Telescope. Nevertheless, it was still difficult to choose which university I wanted to attend. I have always been extremely attracted to arts and I love to paint and draw. During high school, I had the great luck to meet Nietta D'Atena, an artist from Reggio Calabria, and to attend her evening art laboratory, where she was teaching sculpture and painting. My passion for science convinced me to enrol in Physics, but with the aim to go back to art any time possible. I kept attending evening courses on art during my whole University time.

I studied at the University of Milano-Bicocca: I got my Bachelor Degree in Physics in 2013 with a thesis on Active Galactic Nuclei, supervised by Dr Massimo Dotti and co-supervised by Dr Alessandro Lupi. I then enrolled in the Master course in Astrophysics and Space Physics at the same university. During it, I joined the Technical University of Vienna with the Erasmus Programme. There I followed courses in Theoretical Physics and experienced for the first time what it meant to live in a different country. Back in Italy, I did my Master Thesis under the supervision of Prof. Luigi Guzzo and Dr Adam Hawken at the Observatory of Brera-Merate, joining

the ERC group Darklight. The international environment of the group further encouraged me to apply for the PhD position at Leiden Observatory. I graduated in March 2016 with a thesis titled 'Constraining the Halo Occupation Distribution by combining galaxy surveys and numerical simulations'.

I started my PhD at the Leiden Observatory in September 2016, under the supervision of Prof.Dr.Henk Hoekstra, and I joined the weak lensing group of the Observatory. My research mainly focused on studying the intrinsic alignment of galaxies using both modelling and observational approaches. I worked on a model to incorporate the small scale signal as well as its dependence on galaxy properties and constrained these latter directly on data from KiDS. The model and the pipeline I developed are currently used in ongoing projects in the Kilo Degree Survey (KiDS) and Euclid collaborations. Since the beginning of my PhD, I became a member of KiDS, the Physics of the Accelerated Universe Survey (PAUS), Euclid, and in the later years also of the Large Synoptic Survey Telescope (LSST). All these collaborations were great experiences of scientific exchange and coordination. Thanks to PAUS, I was able to go several times to observe at the William Herschel Telescope at La Palma, in the Canary Islands. In 2016 I attended the winter school in Cosmology in Tonale, Italy. During my PhD, I visited the University College of London (UCL) several times, I attended conferences and collaborations meetings, and I presented my work on many occasions in different countries: the US, UK, France, Finland, Germany. I was invited to give a review talk at the annual Euclid Italy meeting in February 2020. For three years, I served as an assistant to the course 'Galaxies and Cosmology' taught by Dr J.Hodge. I also participated in non-scientific activities of the Leiden Observatory: for one year (2017/2018), I was one of the four organisers of the 'borrel', a social event that takes place every Friday and is meant to create a friendly environment and socialise with the colleagues outside work; I have also been a member of the social committee for three years (2016-2019), and I volunteer to the 'Discovery Club', an outreach programme coordinated by the UNAWE team to teach and play with Astronomy with the children in the refugee centres near Leiden, during summer 2018.

Now that this part of the journey is turning to an end, I will serve science in a new way: I want to become an illustrator for science communication. This will finally bring together my two main passions and, somehow, the two halves of me.

Acknowledgements

This PhD has been an incredible experience and this was thanks to all the people that have been a part of it. From the scientific to the social side: some people have been very close to me, some have been important even if more tangential. I want to thank you all. During the multiple attempts to write these acknowledgements, I always realised I had forgotten someone, so I am pretty sure I still have. I hope you will feel my thanks in between these lines anyway!

I would like to thank Henk for having been a stimulating and supportive supervisor. I greatly enjoyed the scientific conversations and your ability to always keep in mind the big picture. I think you really communicate your passion for science, and this is something I will bring with me after this PhD.

During these years many people have crossed the Weak Lensing Group, leaving their personal touch. I have learnt from you all. Ricardo, Margot, Christos, Andrej, Stijn, Omar, Lammim, Shun-Sheng, Marcello, Massimo, Martin, Maciek, Patricia, Mohammadjavad, Arun, Alessandro, Matthieu, Yannick, David, Koen. Thank you for your mentoring and the stimulating discussions. It was always nice to interact with you, both scientifically and not, and to share experiences at conferences.

I would like to especially thank the KiDS team as a whole: I enjoyed our time together enormously. I was always looking forward to the KiDS busy weeks. I do not think this is the standard: you made it a great environment, managing to combine tough science and fun. Harry, Constance and Andrej, I really enjoyed collaborating with you. I also want to express my gratitude to Benjamin and Elisa: I considered you as second supervisors. Thank you for your guidance.

sional joiners.

Fraser, thank you for checking my English when I was in doubt! I will miss your big smile and our Sunday runs together!
Kirsty, living together was so much fun! Thanks for taking care of my plants so many times (and forever). I will miss the K-fam!

Christos: thank you for your direct and sincere friendship, for the work and non-related work chats in the office and outside; for the conferences, the trips, and all the rest. Jit: for your rudeness and your kindness: it is so much less fun when you are not around! For complaining about my continuous saving (it's coming in handy uh), for your great vodka and your sincerity. I am just sorry I can't complain anymore about you not cooking for us. Ele: we did so many things together! I couldn't have hoped for a better partner for all of my hobbies and activities. Thank you for the chats, the dress consultancies and your contagious enthusiasm and sociality. Gabriella: you came last but you imposed yourself like a truck :D For the laughs and the trash, and for all the times together cooking, eating and drinking, as it should be: thanks! You guys are one of the most precious takeaways of this PhD!

Per i Mellon non ci sono parole adatte a descrivervi né per ringraziarvi della vostra presenza nella mia vita: siete qualcosa di speciale ed unico. È anche grazie alla vostra vicinanza che in tanti momenti ho trovato la grinta giusta per affrontare le sfide che mi si presentavano. In ordine casuale: Marco G., Iaco, la Fra, Enrica, Mirko, Edoardo, Giulia F., Ghil, Marta B., Marco A. e Giulia, Marco B., Nicco e Olivia, Alberto e Judith, Yasir. E ancora: Marta M., Nadine, Mitch, Maria Cristina: grazie di tutto! Chiara, Richard: voi ci siete stati nel momento più difficile. Vi voglio bene.

Alla mia famiglia va un grazie particolare. Si dice sempre, ma lo penso davvero: siete sempre stati di supporto ed incoraggianti in tutte le mie scelte. Se ho imboccato questo percorso è certamente merito dell'atmosfera stimolante che si respirava a casa, del sostegno nelle sfide, della curiosità a cui ci avete educato. Siete chiassosi, a volte un po' intensi, sempre in grado di far sentire la vostra vicinanza nella distanza, e sempre, sempre presenti in tutto. Grazie!

Tommaso, questo dottorato è anche merito tuo, del tuo infaticabile sosteg-

no e della pazienza con cui mi sei stato vicino. Con te al mio fianco ho scoperto il coraggio di fare passi azzardati. Se questa nuova avventura lavorativa si affaccia davanti a me è anche grazie al tuo incredibile incoraggiamento. So che di grazie ce ne saranno ancora tanti: e andiamo!